학위기간 업적자료 사본
[연구개발 실적]

2025년 한국고분자학회 추계 학회상
권순기 우수학위논문상 지원자

이 윤 경

ADVANCED MATERIALS

www.advmat.de

A Water-Soluble Organic Photocatalyst Discovered for Highly Efficient Additive-Free Visible-Light-Driven Grafting of Polymers from Proteins at Ambient and Aqueous Environments

Yungyeong Lee, Yonghwan Kwon, Youngmu Kim, Changhoon Yu, Siyang Feng, Jeehun Park, Junsang Doh, Reinhold Wannemacher, Byungjin Koo, Johannes Gierschner,* and Min Sang Kwon**

Since the pioneering discovery of a protein bound to poly(ethylene glycol), the utility of protein–polymer conjugates (PPCs) is rapidly expanding to currently emerging applications. Photoinduced energy/electron-transfer reversible addition–fragmentation chain-transfer (PET-RAFT) polymerization is a very promising method to prepare structurally well-defined PPCs, as it eliminates high-cost and time-consuming deoxygenation processes due to its oxygen tolerance. However, the oxygen-tolerance behavior of PET-RAFT polymerization is not well-investigated in aqueous environments, and thereby the preparation of PPCs using PET-RAFT polymerization needs a substantial amount of sacrificial reducing agents or inert-gas purging processes. Herein a novel water-soluble and biocompatible organic photocatalyst (PC) is reported, which enables visible-light-driven additive-free "grafting-from" polymerizations of a protein in ambient and aqueous environments. Interestingly, the developed PC shows unconventional "oxygen-acceleration" behavior for a variety of acrylic and acrylamide monomers in aqueous conditions without any additives, which are apparently distinct from previously reported systems. With such a PC, "grafting-from" polymerizations are successfully performed from protein in ambient buffer conditions under green light-emitting diode (LED) irradiation, which result in various PPCs that have neutral, anionic, cationic, and zwitterionic polyacrylates, and polyacrylamides. It is believed that this PC will be widely employed for a variety of photocatalysis processes in aqueous environments, including the living cell system.

1. Introduction

Post-translational modification of proteins with a synthetic polymer largely influences their properties.[1–3] From a therapeutic point of view, in the case of a protein attached to poly(ethylene glycol) (i.e., PEGylation), stability, bioavailability, and pharmacokinetic/dynamic properties of the protein are enhanced, and immunogenicity is reduced.[4–6] As a result, more than 16 PEGylated protein drugs have received approval from the US Food and Drug Administration (FDA) and have been used clinically worldwide.[7] In addition to conventional PEGylated proteins, protein–polymer conjugates (PPCs) are expected to play an essential role for a variety of emerging applications such as nanomedicine,[8,9] plastics degradation,[10] protein-based membranes/columns for precious metal capture,[11,12] and enzyme catalysis in chemical synthesis via manipulating catalytic activity of enzymes in organic media.[13]

Efficient and site-selective conjugation of a structurally well-defined polymer with

Y. Lee, Y. Kwon, Y. Kim, C. Yu, J. Doh, M. S. Kwon
Department of Materials Science and Engineering
Seoul National University
Seoul 08826, Republic of Korea
E-mail: minsang@snu.ac.kr

Y. Kwon, Y. Kim
Department of Materials Science and Engineering
Ulsan National Institute of Science and Technology (UNIST)
Ulsan 44919, Republic of Korea

The ORCID identification number(s) for the author(s) of this article can be found under https://doi.org/10.1002/adma.202108446.

DOI: 10.1002/adma.202108446

S. Feng, R. Wannemacher, J. Gierschner
Madrid Institute for Advanced Studies
IMDEA Nanoscience, Calle Faraday 9, Campus Cantoblanco, Madrid 28049, Spain
E-mail: johannes.gierschner@imdea.org

J. Park, J. Doh, M. S. Kwon
Research Institute of Advanced Materials
Seoul National University
Seoul 08826, Republic of Korea

B. Koo
Department of Polymer Science and Engineering
Dankook University
Gyeonggi-do 16890, Republic of Korea
E-mail: bkoo@dankook.ac.kr

a narrow molecular weight distribution greatly enhances the preparation efficiency of PPCs, and also reduces the difficulties in purification as well as the unpredictable side effects caused by nonspecifically modified proteins and by-/side products.[6,14] Moreover, this enables precise studies of "structure–property–performance" relationships of PPCs, which accelerate the development of new areas of applications based on PPCs. Therefore, PPCs with a well-defined architecture and high uniformity would be highly beneficial.

Combination of site-selective protein modification and "grafting-from" reversible-deactivation radical polymerization (RDRP) process has been regarded as one of the most promising ways to afford well-defined PPCs with a high uniformity.[6,15] Since the seminal works by the groups of Lewis and Leppard,[16,17] Maynard and co-workers,[18,19] Matyjaszewski and co-workers,[20] precise modification of various proteins with well-defined polymers has been realized by RDRP such as atom-transfer radical polymerization (ATRP) and reversible addition–fragmentation chain-transfer (RAFT) polymerization.[21,22] However, these methods mostly require time-consuming and expensive pre-deoxygenation processes including freeze–pump–thaw and/or inert gas purging that also might cause protein denaturation and/or cell destruction (in the case of in situ preparation of PPCs in living cells).[23–25]

From a merger of RDRP with photochemistry, photomediated RDRP (photo-RDRP) has become even more advantageous in terms of mildness in reaction conditions and versatility of the method.[26–29] Photo-RDRP harnesses visible light as an energy source and thus excludes heat that is used in conventional thermally induced reactions, which prevents denaturation and consequent loss of activity of protein. Particularly, photoinduced electron/energy-transfer-RAFT (PET-RAFT) polymerization does not require a prior deoxygenation process due to its unique feature of "oxygen tolerance,"[30,31] which eliminates the need for external deoxygenation processes for PPCs' syntheses. However, while "oxygen-tolerance" behavior of PET-RAFT polymerization has been well-investigated in organic solvents (i.e., dimethyl sulfoxide (DMSO)), the studies in aqueous environments are still scarce.[32–36] Therefore, the preparation of PPCs by PET-RAFT polymerization requires a substantial amount of sacrificial reducing agents such as tertiary amines and ascorbic acids or an inert gas purging process, which limits the practicability of this method;[37–40] it is noted in this context that PPCs should be prepared in an aqueous environment to prevent the denaturation of a protein. The development of new photocatalysts (PCs) that afford an intrinsically "oxygen-tolerant" photocatalytic system would resolve this problem; however, aqueous PET-RAFT polymerization is substantially limited to several specific PCs such as $Ru(bpy)_3Cl_2$, Eosin Y (and its derivatives), and inorganic PCs that require external additives (previously reported systems on aqueous PET-RAFT are summarized in Figure S1 in the Supporting Information).[37,40–42]

Here, we report a new water-soluble and biocompatible organic PC (i.e., "3DP-MSDP-IPN"; **Figure 1**a), which successfully proceeds visible-light-driven "grafting-from" PET-RAFT polymerizations of a protein at ambient and aqueous environments without additives. To achieve this, water-soluble and weakly electron-donating sulfonate moiety was introduced in one of four donor groups of "4DP-IPN" with a strongly twisted donor–acceptor structure that has been known for highly efficient organic PC for various organic reactions and polymerizations.[43–51] Most excitingly, the discovered PC exhibited unique "oxygen-acceleration" behavior in PET-RAFT polymerizations of a variety of acrylates and acrylamides in both DMSO and aqueous conditions without any additives, which is apparently distinct from previously reported systems.[30,31] Combined experimental and theoretical studies suggested that molecular oxygen acts as an electron shuttle to catalyze the electron transfer between the PC in the excited state and the chain-transfer agent (CTA) (Figure 1d). Here, the PC is expected to play a critical role i) to generate singlet oxygen that is a better oxidant as compared to triplet oxygen and ii) to form superoxide radical anion ($O_2^{\bullet-}$) through electron transfer with singlet and/or triplet oxygen, which is derived from the unique photophysical and electrochemical characteristics of 3DP-MSDP-IPN. With the developed PC, we successfully performed "grafting-from" polymerizations from a protein in ambient buffer conditions under 515 nm green light-emitting diode (LED) irradiation (≈10 mW cm^{-2}), which results in a variety of PPCs having neutral, anionic, cationic, and zwitterionic polyacrylates and polyacrylamides that have rarely been reported before (vide infra). Our water-soluble and biocompatible PC will be applicable to various aqueous photocatalytic and photo-electrocatalytic reactions besides preparation of PPCs.

2. Results and Discussion

2.1. Design Strategy

An ideal PC for visible-light-driven "grafting-from" polymerization of a protein would be a water-soluble and biocompatible molecule exhibiting high catalytic efficiency at ambient and aqueous conditions without any additives that might result in negative consequences for protein functions[52–54] and/or biological systems.[55–57] In particular, intrinsic tolerance of a catalyst system for oxygen is in high demand due to the high-cost, time-consuming, and bio-incompatible pre-deoxygenation processes required.

In order to achieve oxygen tolerance in aqueous PET-RAFT polymerization, the reductive quenching pathway has mostly been used so far, instead of the oxidative quenching pathway (Figure S1, Supporting Information). While the reductive quenching pathway shows great oxygen tolerance, it should require substantial amount of sacrificial reducing agents such as tertiary amines and ascorbic acid;[58,59] according to very recent reports from Boyer's group, "oxygen acceleration," in which oxygen acts as an electron shuttle, could also be attained in organic solvents through the carefully chosen phthalocyanine PCs in the presence of tertiary amines (vide infra).[60] Moreover, the reductive quenching cycle often affords undesired side reactions and less controllability of the polymerization,[40] which originates from the longer lifetime of one-electron-reduced PC ($PC^{\bullet-}$) being an active PC species in a reductive quenching cycle as compared to that of the excited PC species ($^{1/3}PC^*$) being an active PC intermediate in an oxidative quenching cycle.

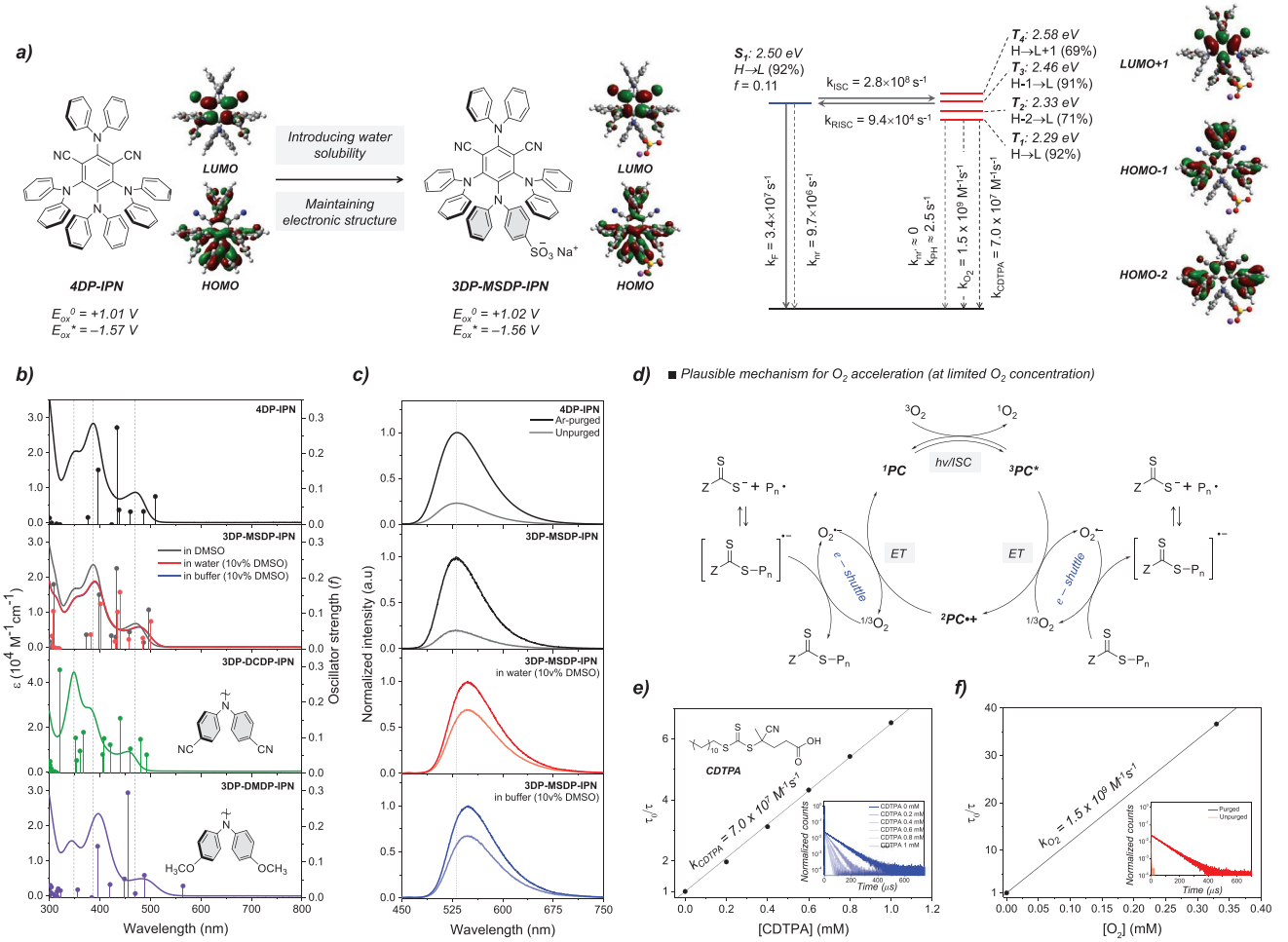

Figure 1. Characterization of 3DP-MSDP-IPN. a) Molecular structure and calculated highest occupied molecular orbital (HOMO) and lowest unoccupied molecular orbital (LUMO) topologies of 4DP-IPN and 3DP-MSDP-IPN with experimentally evaluated E_{ox}^0 and E_{ox}^* values (left). Jablonski diagram of 3DP-MSDP-IPN in DMSO (right). b) UV–vis absorption spectra of 4DP-IPN, 3DP-MSDP-IPN, 3DP-DCDP-IPN, and 3DP-DMDP-IPN each dissolved in the solvent indicated (10×10^{-6} M). The sticks represent oscillator strengths obtained by TD-DFT. c) Photoluminescence (PL) spectra of 4DP-IPN and 3DP-MSDP-IPN in varying solvents (10×10^{-6} M) at room temperature before (dark line) and after (bright line) being degassed with Ar for 10 min. d) Plausible mechanism for PET-RAFT polymerization facilitated by oxygen of limited concentration. e) Stern–Volmer plots for the PL quenching of 3DP-MSDP-IPN in DMSO (10×10^{-6} M) by CDTPA at room temperature. f) Stern–Volmer plots for the PL quenching of 3DP-MSDP-IPN in DMSO (10×10^{-6} M) by oxygen at room temperature (dissolved oxygen concentration in DMSO at room temperature is known to be 0.33×10^{-3} M[69]).

Recently, we reported that cyanoarene-based PC, 4DP-IPN, enabled the oxygen-tolerant PET-RAFT polymerization of methyl methacrylate (MMA) without additives in organic solvent, DMSO (Figure 1a).[45] It has been suggested that a key factor for the excellent oxygen tolerance of this system is the efficient generation of long-lived triplet excited states of the PC. The generated triplet excitons react with molecular oxygen to produce reactive oxygen species (ROS) through a type I and/or type II mechanism, which are subsequently consumed by quencher (here, oxidation of DMSO to dimethyl sulfone), thereby largely decreasing the concentration of dissolved oxygen and consequently furnishing oxygen tolerance (i.e., "pre-deoxygenation" mechanism). Given all these facts, we hypothesized that a water-soluble analog of 4DP-IPN would be a suitable PC candidate for visible-light-driven "grafting-from" polymerization of a protein. Surely, at the beginning, we did not expect "oxygen-tolerance" behavior in aqueous environments without additives, because there are no ROS quenchers in aqueous PET-RAFT polymerization conditions (vide infra).

In order to confer water solubility without perturbing the electronic structures of 4DP-IPN, 3DP-MSDP-IPN was carefully designed, where one of the four donor groups was replaced with sulfonate-substituted diphenylamine while retaining the acceptor moiety (Figure 1a). Sulfonate substitution of diphenylamine was chosen because the sulfonate group is known to be water-soluble, biocompatible, highly stable in aqueous environments, and weakly electron-donating that may not influence the electronic structure;[61–63] in fact, our density functional theory (DFT) calculations show that the highest occupied molecular orbital (HOMO) energy of diphenylamine-4-sulfonate is almost equal to that of diphenylamine (−5.45 and −5.43 eV, respectively; Figure S2, Supporting Information). Full details of the syntheses and characterizations including ^{1}H(^{13}C) NMR and mass spectrometry are shown in Figures S21–S23 (Supporting Information).

2.2. Biocompatibility and Photophysical/Electrochemical Characterizations of 3DP-MSDP-IPN

We first investigated the water solubility of 3DP-MSDP-IPN as compared to that of 4DP-IPN. As expected, 3DP-MSDP-IPN showed greatly enhanced solubility in water in the presence of small amount of DMSO (as low as 1.0 vol%) compared to that of 4DP-IPN (Figure S3, Supporting Information), which is enough for aqueous photocatalysis of interest; since the different amounts of DMSO were used depending on the situation, a vol% of DMSO to the total volume was given where necessary. 3DP-MSDP-IPN was then studied in vitro in cells to evaluate its biocompatibility. 3DP-MSDP-IPN in the absence of light illumination showed no toxicity to HeLa cells up to a concentration of 100×10^{-6} M ($IC_{50} > 200 \times 10^{-6}$ M; Figure S4, Supporting Information) after 48 h of incubation, implying that 3DP-MSDP-IPN could be utilized as a PC for engineering proteins and cell surfaces of living cells[64] as well as for in situ synthesizing polymeric architectures inside living cells.[65]

We then performed photophysical and electrochemical studies, which are the basis for the photocatalytic performance. To perform an accurate comparison with 4DP-IPN, which has very low solubility in water (Figure S3, Supporting Information), photophysical and electrical measurements of 3DP-MSDP-IPN were carried out in DMSO (and CH_3CN). As we anticipated, UV–vis absorption and photoluminescence (PL) spectra and cyclic voltammetry (CV) patterns of 3DP-MSDP-IPN were almost perfectly overlapped with those of 4DP-IPN in DMSO (Figure 1b,c and **Table 1**; Figure S5, Supporting Information). Also, they gave very similar values of PL quantum yields (Φ_F) and prompt and delayed fluorescence lifetimes (τ, Table 1), consequently providing nearly the same excited-state dynamics, i.e., rate constants for radiative and nonradiative singlet state deactivation (k_F, $k_{nr,S}$) and (reverse) intersystem-crossing (k_{ISC}, k_{RISC}).[66] The Jablonski diagrams in Figure 1a (for 3DP-MSDP-IPN) and Figure S6 (Supporting Information) (for 4DP-IPN) sum up the kinetics with the relevant excited-state energies (and compositions), as well as molecular orbital (MO) topologies as calculated by time-dependent (TD) DFT calculations. To validate the effect of substitution, 4,4′-dicyano- and 4,4′-dimethoxydiphenylamine-substituted derivatives of 4DP-IPN (i.e., 3DP-DCDP-IPN and 3DP-DMDP-IPN) were prepared as model compounds. Whereas substitution with diphenylamine-4-sulfonate moiety gave no effect on the overall electronic structure, substitution of diphenylamine with strongly electron-accepting (−CN) and electron-donating ($-OCH_3$) groups resulted in substantial changes in photophysical properties as presented in Figure 1b,c and Table S1 (Supporting Information). More detailed investigations of this aspect are currently underway.

2.3. PET-RAFT Polymerization in DMSO

We next investigated the catalytic performance of 3DP-MSDP-IPN. For a proper comparison, the PET-RAFT polymerization of methyl acrylate (MA) was chosen as a model system. DMSO and 4-cyano-4-[(dodecylsulfanylthiocarbonyl)sulfanyl]-pentanoic acid (CDTPA) were selected as a solvent and CTA, respectively, as they are widely used in PET-RAFT polymerization (**Figure 2**a).[33,45,67] Also, 515 nm green LED was used as an excitation light source. As a negative control, polymerization of MA was conducted in the absence of either a PC or CTA under N_2 or air atmosphere (Figure S7, Supporting Information). These control experiments clearly suggested that the photoiniferter process does not occur under these conditions, and both PC and CTA are essential for the controlled polymerization. Catalytic performance of 4DP-IPN and 3DP-MSDP-IPN was then compared. The polymerizations of MA were successful for both PCs (5 ppm) under N_2 atmosphere and 2 W green LED irradiation (≈1.7 mW cm^{-2}) conditions (Figure S7, Supporting Information). As hypothesized, the results were very similar in terms of conversion and controllability, confirming that the catalytic performance in DMSO of 3DP-MSDP-IPN is comparable to that of 4DP-IPN.

We then tested the oxygen tolerance of 3DP-MSDP-IPN for the PET-RAFT polymerization of MA in DMSO with and without N_2 purging. Very surprisingly, the polymerization of

Table 1. Photophysical and electrochemical properties of 4DP-IPN and 3DP-MSDP-IPN in varying solvents. Ground-state redox potentials were measured in CH_3CN (0.2×10^{-3}M) versus Ag/AgCl. E_{00} was evaluated from onset of gated PL spectrum at room temperature. Excited-state redox potentials were calculated from the Rehm–Weller equation ($E_{ox/red}^{*} = -E_{00} + E_{ox/red}^{0}$).

PC	Solvent	$\lambda_{max,abs}$ [nm]	$\lambda_{max,em}$ [nm]	E_{red}^{0} [V]	E_{ox}^{0} [V]	E_{00} [eV]	E_{red}^{*} [V]	E_{ox}^{*} [V]	Atmosphere	ϕ_F [%]	τ_{prompt} [ns]	$\tau_{delayed}$ [μs]
4DP-IPN	DMSO	471	536	–1.66	+1.01	2.58	0.92	–1.57	N_2	85	3.3	82
									Air	14	3.2	4.0
3DP-MSDP-IPN	DMSO	470	536	–1.60	+1.02	2.58	0.98	–1.56	N_2	78	3.1	79
									Air	13	3.1	2.9
	Water (10 vol% DMSO)	476	554	–1.60	+1.02	2.50	0.90	–1.48	N_2	9	2.2	21
									Air	7	2.2	2.5
	Buffer (10 vol% DMSO)	476	547	–1.60	+1.02	2.50	0.90	–1.48	N_2	9	2.1	20.2
									Air	7	2.1	3.0

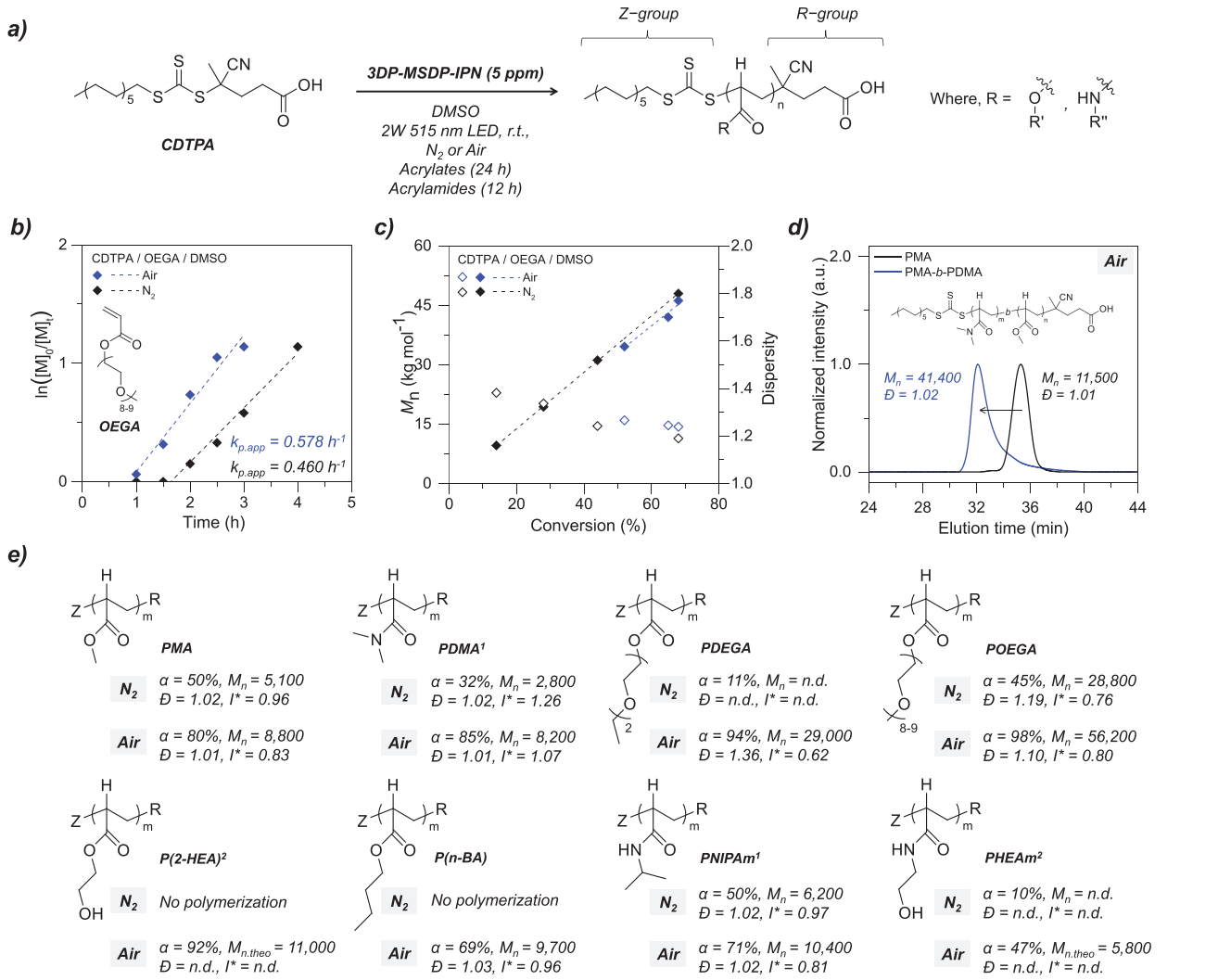

Figure 2. Results of PET-RAFT polymerizations in DMSO. a) Reaction scheme of PET-RAFT polymerization using CDTPA as CTA. b) Kinetic plots for PET-RAFT polymerization of OEGA under air and N_2 using 3DP-MSDP-IPN (5 ppm): $\ln([M]_0/[M]_t)$ versus reaction time. c) M_n (filled) and dispersity (empty) versus conversion. d) GPC traces of poly(methyl acrylate) (PMA, black) and poly(methyl acrylate)-*b*-poly(*N*,*N*-dimethyl acrylamide) (PMA-*b*-PDMA, blue). e) Summary of polymers prepared from various acrylate and acrylamide monomers. 1) The reaction was conducted for 3 h (PDMA) or 4 h (PNIPAm) instead of 12 h to clearly observe the "oxygen-acceleration" behavior; 2) the polymers could not be analyzed by GPC in tetrahydrofuran (THF) due to insolubility and in water due to incompatibility of the polymers containing residual DMSO.

MA gave substantially higher conversion ($\alpha = 80\%$) in the presence of oxygen (without N_2 purging) than after purging with N_2 (α = 50%) while maintaining the excellent controllability (Figure 2e). Such "oxygen-acceleration" behavior was observed indeed in Boyer's group as stated above, however, in a reductive quenching cycle in the presence of sacrificial reducing agents.[60] This rather counterintuitive "oxygen-acceleration" behavior was similarly observed for a variety of acrylate and acrylamide monomers (Figure 2e). To understand the origin of this phenomenon, kinetics of PET-RAFT polymerizations of oligo(ethylene glycol) methyl ether acrylate (OEGA) were monitored by ^{1}H NMR and gel-permeation chromatography (GPC) for 3DP-MSDP-IPN (5 ppm) under air and N_2 atmosphere (Figure 2b,c; Figure S8, Supporting Information); here, OEGA was chosen as a model system of the kinetics studies for the comparison to PET-RAFT polymerizations in aqueous environment. A linear relation of conversion versus time, and of M_n versus conversion, was observed for both cases, suggesting the living characters of these polymerizations being also supported by successful synthesis of block copolymer (Figure 2d). Good temporal control in polymerization was observed in a light "ON"/"OFF" experiment (Figure S9, Supporting Information). Moreover, the apparent rate of propagation ($k_{p,app}$) and inhibition period were evaluated from kinetic plots (Figure 2b). Obvious increase in $k_{p,app}$ (from 0.460 to 0.578 h^{-1}) and decrease in inhibition period (from 98 to 57 min) were found for the polymerization under air, suggesting that the activation step in PET-RAFT polymerization (i.e., electron transfer from PC in the excited states ($^{1/3}PC^*$) to dormant species) could be facilitated in the presence of oxygen. In other words, oxygen might

catalyze the electron-transfer process between $^{1/3}PC^*$ and dormant species (Figure 1d), which rather contradicts the previously proposed mechanism of "oxygen tolerance" (vide supra, i.e., "pre-deoxygenation mechanism").

In order to clarify the role of oxygen in "oxygen-acceleration" behavior, we performed PL quenching studies in the presence of CDTPA and oxygen (Figure 1e,f). In the quenching experiments, no lifetime changes were observed in the prompt PL, but very significant changes were observed in the delayed PL; see Figure 1e,f and Table 1; this clearly evidences that the long-lived lowest triplet excited state (T_1) is mainly affected by quenching. This can be directly seen in the evaluated kinetic constants related to excited-state dynamics and electron-transfer kinetics (Figure 1a, vide infra). In fact, quenching constants were evaluated to be $\approx 7.0 \times 10^7$ M^{-1} s^{-1} (for CDTPA) and $\approx 1.5 \times 10^9$ M^{-1} s^{-1} (for oxygen) by Stern–Volmer analysis;[68,69] it is noted that the quenching constant for oxygen is very fast, reaching the diffusion limit in DMSO ($\approx 3 \times 10^9$ M^{-1} s^{-1}, as obtained from the Stokes–Einstein equation).[70] Given the concentration of CDTPA and oxygen in the polymerization conditions (11.3×10^{-3} and 0.67×10^{-3} M, respectively; here, dissolved oxygen concentration was calculated for the mixed solutions of DMSO and monomers with a 1:1 volume ratio), the rate of electron/energy transfer between $^3PC^*$ and oxygen is calculated to be $\approx 1.0 \times 10^6$ s^{-1}, which is faster than that between $^3PC^*$ and CDTPA ($\approx 7.9 \times 10^5$ s^{-1}), implying that direct electron transfer from $^3PC^*$ to CDTPA (and/or dormant species) might not be favored in the presence of oxygen. Very recently, Boyer and co-workers proposed the oxygen-mediated reductive quenching pathway (O-RQP) as a new mechanism to rationalize the "oxygen-acceleration" behavior observed for carefully chosen PCs in the presence of triethylamine (TEA) as a sacrificial reducing agent,[60] where the author demonstrated the thermodynamic feasibility of O-RQP through quantum-chemical (QC) calculations and studies of structure–property–performance relationships. Here, oxygen acts as an electron shuttle to catalyze the electron transfer between TEA and CTA (and/or dormant species) in the overall reductive quenching cycle. The role of PC is rather limited to be a singlet oxygen generator. All those things considered; we propose the "oxygen-acceleration" mechanism, as presented in Figure 1d. While oxygen acts as an electron shuttle between $^{1/3}PC^*$ and CTA as in the O-RQP, the PC plays a more essential role: i) as a generator of singlet oxygen, which is far stronger oxidant than triplet oxygen and ii) as a photoreductant to form the superoxide radical ion ($O_2^{\bullet -}$), which originates from the photophysical and electrochemical features of 3DP-MSDP-IPN—i) ultraefficient generation of long-lived triplet excited states (according to our simulations, triplet concentration in photostationary state of 3DP-MSDP-IPN is ≈2 orders of magnitude higher than that of $Ir(ppy)_3$ and $Ru(bpy)_3^{2+}$; see Figure S10 in the Supporting Information), ii) substantially negative excited-state oxidation potential ($E_{ox}^* = -1.56$ V), and iii) highly stable radical cation as evidenced by reversible waves in CV. Given the singlet–triplet energy gap and reduction potential of molecular oxygen ($\Delta E_{ST} \approx 0.98$ eV and $E_{red}^0 \approx -0.60$–1.00 V vs saturated calomel electrode (SCE)),[71–74] overall processes following the proposed mechanism are thermodynamically feasible. The half-life and diffusion length of $O_2^{\bullet -}$, which is known to be rather long (≈1 µs and 1 µm (in water), respectively),[74,75] also support our proposed mechanism. Nevertheless, more in-depth studies are currently on-going in our laboratory.

2.4. PET-RAFT Polymerization in Water

We then expanded our studies to aqueous PET-RAFT polymerizations. Here, 4-((((2-Carboxyethyl)thio)carbonothioyl)thio)-4-cyanopentanoic acid (CETCPA) was used as a CTA instead of CDTPA due to its excellent water solubility (**Figure 3**). For the comparison of PET-RAFT polymerization in DMSO, OEGA was selected as a monomer. Apart from the change in solvent, all other conditions were exactly the same as those in the DMSO experiment. As a negative control, the polymerization of OEGA was performed in the absence of PC or CTA, providing no polymers, as we expected (Figure S11, Supporting Information). Interestingly, no polymerization took place in inert atmosphere, while 98% conversion was obtained in air with an excellent control ($Đ = 1.10$, $I^* = 0.83$), implying that the "oxygen-acceleration" effect is more pronounced in aqueous conditions. As shown in Figure 3e, similar behaviors were found in a variety of water-soluble acrylates and acrylamides. It may be noted that the catalytic performance of the PC developed here exceeded, without any additives, that of the previously reported water-soluble PCs including $Ru(bpy)_3Cl_2$ and Eosin Y disodium salt in the presence of additives (Figure S12, Supporting Information).

Kinetics of the aqueous PET-RAFT polymerization of OEGA was monitored under air to investigate the "oxygen-acceleration" effect as well as the livingness of the polymerization. Again, no polymerization was seen in the kinetics monitoring under N_2 atmosphere (Figure 3b,c; Figure S13, Supporting Information). A clear linear relationship of conversion versus time, and of M_n versus conversion, was found, indicating the livingness of the polymerization, which is also supported by the fact that the synthesis of a block copolymer was successful (Figure 3d). Polymerization was observed only when light is turned on, reflecting good temporal control (Figure S14, Supporting Information). From the kinetics plot, $k_{p,app}$ was calculated to be 0.167 h^{-1}, which is smaller than that in DMSO conditions.

In order to further understand the pronounced "oxygen-acceleration" behavior and rate retardation in aqueous conditions, photophysical properties of the aqueous solution of 3DP-MSDP-IPN were studied (Figure 1b,c and Table 1). The absorption and emission spectra in water show a small but distinct bathochromic shift (0.04 eV) versus that in DMSO. According to the TD-DFT calculations, this is not due to a polarizability effect, but is ascribed to dissociation of the sodium ion in water (Figure 1b; Figure S6, Supporting Information). Strikingly, the overall Φ_F decreases from 78% in DMSO to 9% in water under N_2 purged conditions, despite careful deaeration by applying a repeated freeze–pump–thaw procedure. According to our kinetic analysis (Figure S6, Supporting Information), this is mainly ascribed to a strong increase of nonradiative deactivation for the S_1 state ($k_{nr,S}$; see Figure 1a and also Figure S6 in the Supporting Information), while the other rates are very similar to DMSO. In fact, $k_{nr,S}$ in solution combines internal conversion (IC) and vibrational relaxation (VR). While PL quenching in water is sometimes ascribed to high-energy vibrations, which slows down VR,[76] the very pronounced

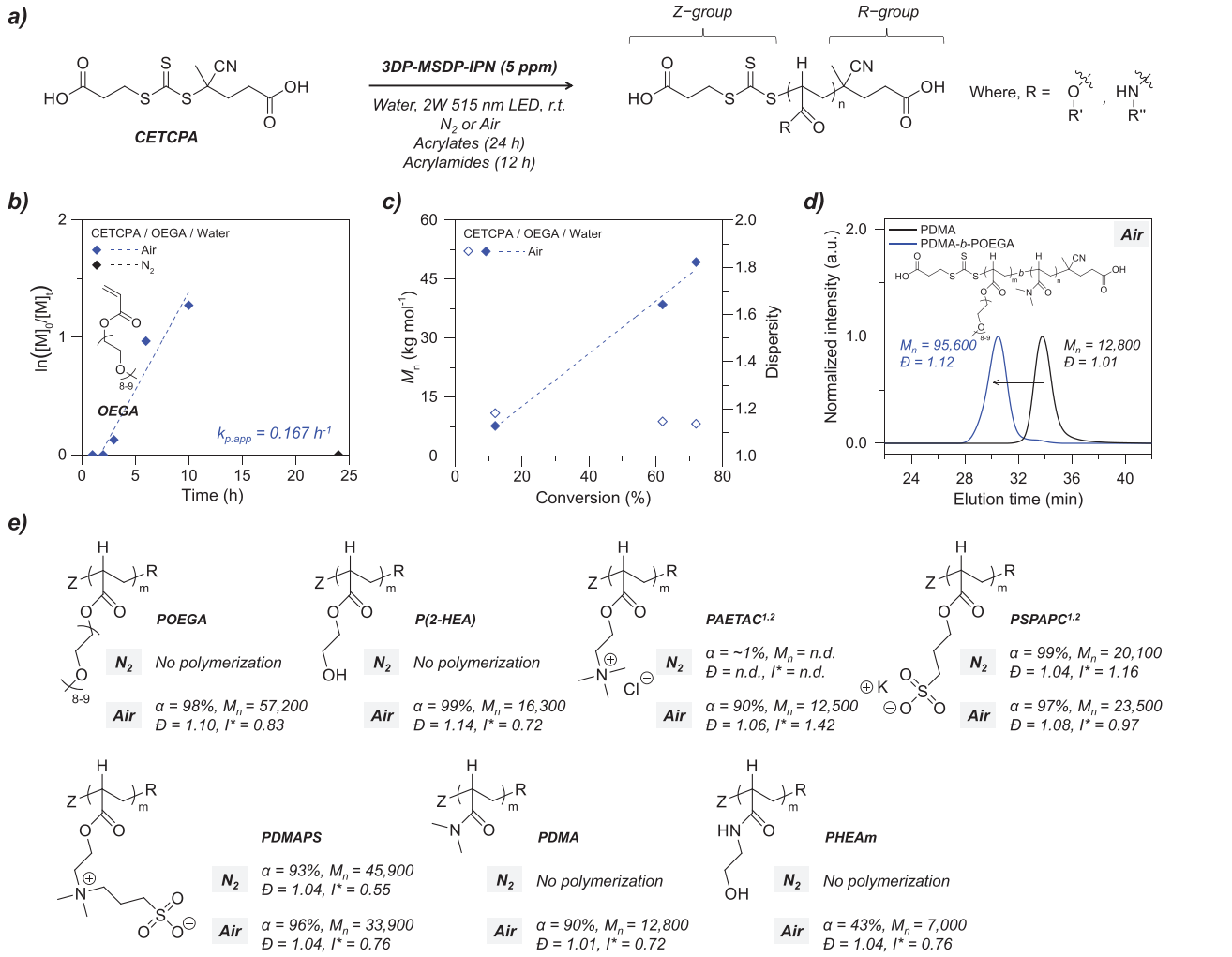

Figure 3. Results of PET-RAFT polymerizations in water. a) Reaction scheme of PET-RAFT polymerization using CETCPA as CTA. b) Kinetic plots for PET-RAFT polymerization of OEGA under air and N_2 using 3DP-MSDP-IPN (5 ppm): $\ln([M]_0/[M]_t)$ versus reaction time. c) M_n (filled) and dispersity (empty) versus conversion. d) GPC traces of poly(*N*,*N*-dimethyl acrylamide) (PDMA, black) and poly(*N*,*N*-dimethyl acrylamide)-*b*-poly(oligo(ethylene glycol) methyl ether acrylate) (PDMA-*b*-POEGA, blue). e) Summary of polymers prepared from various acrylate and acrylamide monomers. 1) The reaction was conducted for 1.5 h (PAETAC) instead of 24 h to clearly observe the "oxygen-acceleration" behavior. In case of PSPAPC, the higher catalyst loading of 50 ppm was used for reproducibility; 2) the GPC analysis was done using an refractive index (RI) detector instead of MALLS.

increase of $k_{nr,S}$ may rather suggest an enhanced IC process, possibly by the formation of specific hydrogen bonds with the surrounding water molecules.[77] The increase in $k_{nr,S}$ affects the delayed emission much more than the prompt one, as seen in the significant decrease in $\tau_{delayed}$ from ≈80 µs in DMSO to ≈20 µs in water; see Table 1. Under air atmosphere, the delayed component shortens to ≈3 µs, which is evidently sufficient to maintain the photocatalytic activity, however, retarding the reaction rate.

Given all experiments and theoretical calculations presented so far, the mechanistic origin of "oxygen-acceleration" behavior in water and DMSO is expected to be the same. Thus, the pronounced effect in aqueous environments seems to be due to the differences in singlet oxygen quenching ability between water and DMSO. However, DMSO is known as a good singlet oxygen quencher, and water does not act as a quencher.[34,60,67] Therefore, substantial oxygen consumption takes place in DMSO as compared to water, which reduces the catalytic role of oxygen and, hence, the "oxygen-acceleration" behavior. For poly(3-sulfopropyl acrylate potassium salt) (PSPAPC) and poly(3-[[2-(acryloyloxy)ethyl]dimethylammonio]propane-1-sulfonate) (PDMAPS) (Figure 3e), the reaction time was too long to observe the behavior and, thereby, more investigations are planned for this interesting "oxygen-acceleration" behavior.

2.5. "Grafting-From" PET-RAFT Polymerization from BSA

We finally conducted "grafting-from" PET-RAFT polymerization of a protein. Bovine serum albumin (BSA) was selected, as a model protein since modification of a free thiol at the Cys-34 residue of BSA is well established.[18,19,37,78] Following

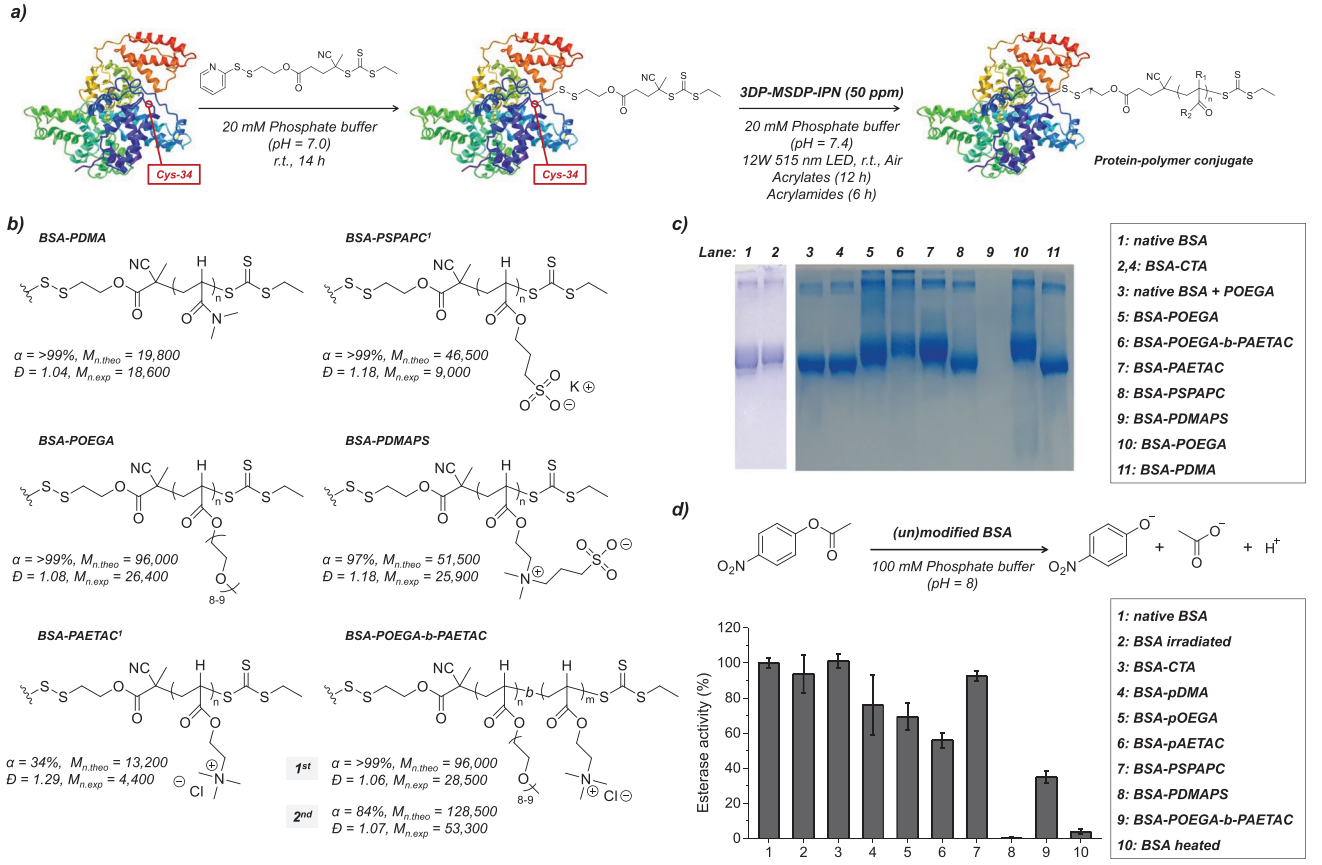

Figure 4. Results of "grafting-from" PET-RAFT polymerization from BSA. a) Reaction scheme of synthesis of BSA–macroinitiator and "grafting-from" PET-RAFT polymerization thereafter. b) Summary of grafted polymers prepared from various acrylate and acrylamide monomers. c) SDS-PAGE analysis of native BSA, BSA–macroinitiator, and various BSA–polymer conjugates. d) Esterase activity of BSA (and its derivatives) and various BSA–polymer conjugates.1) The GPC analysis was done using an RI detector instead of MALLS. In case of PSPAPC, the higher catalyst loading of 500 ppm was used.

the previous reports,[79] a trithiocarbonate-based CTA (4-cyano-4-(((ethylthio)carbonothioyl)thio)pentanoic acid, CETPA) with a pyridyl disulfide moiety (P-CETPA) was prepared (**Figure 4**a). The conjugation of P-CETPA to BSA was carried out in 20×10^{-3} M phosphate buffer (pH = 7.0) with an excess amount of P-CETPA at ambient conditions. After 14 h, the mixture solution was then purified to remove excess P-CETPA by dialysis against water followed by freeze-drying to afford BSA–macroinitiator in powder form. Matrix-assisted laser desorption ionization time-of-flight (MALDI-TOF) analysis further confirmed the successful formation of the BSA–macroinitiator (Figure S15, Supporting Information).

We first tried to perform PET-RAFT polymerization from BSA–macroinitiator in ambient buffer environments. Here, we used *N*,*N*-dimethylacrylamide (DMA) as a model monomer for the "grafting-from" preparation of PPCs due to its simplicity and wide utility. In order to prevent protein denaturation, polymerization conditions were optimized (with DMA) in more diluted conditions and reduced reaction time with higher PC loadings (50 ppm) and higher light intensity (12 W green LED irradiation (≈10 mW cm^{-2}); see Figure 4a and also Figure S16 in the Supporting Information). Polymerizations of the other acrylate and acrylamide monomers were then conducted in the same conditions. Conjugation of a polymer to a BSA–macroinitiator was characterized by ^{1}H-NMR, GPC–multi-angle laser light scattering (MALLS), and sodium dodecyl sulfate-poly(acrylamide) gel electrophoresis (SDS-PAGE) analyses of the reaction aliquot (Figure 4b–d).

Most monomers gave a quantitative conversion confirmed by ^{1}H-NMR, but not all conjugates showed a clear shift in GPC traces presumably due to the limited solubility of the resulting protein–polymer conjugates in eluent of our GPC system (Figure S17, Supporting Information). We assume that the appearance of a substantially wide range of monomers with different characteristics complicates the analysis of their resulting protein conjugates. For example, the successful conjugation of DMAPS polymers (PDMAPS) could be clearly observed both in NMR and aqueous GPC, albeit not in SDS-PAGE (no trace was seen) (Figure 4c; Figure S17, Supporting Information). Addition of an excess amount of tris(2-carboxyethyl)phosphine hydrochloride (TCEP) to the resulting PPCs provided polymers with a narrow dispersity, cleaved from the protein, which further validates that the polymerization proceeded in a controlled manner. To summarize, as listed in Figure 4b, the polymerizations of a variety of water-soluble monomers having neutral, anionic, cationic, and zwitterionic acrylates/acrylamides gave successful syntheses of PPCs. Notably, poly(oligo(ethylene glycol) methyl ether acrylate)-poly([2-(acryloyloxy)ethyl]trimethylammonium chloride) (POEGA–PAETAC) block copolymer was also successfully prepared from the BSA–macroinitiator

with a continuous monomer feeding process at ambient conditions, which has not been demonstrated before.

However, the molecular weight of the grown polymers from the protein was shown to be smaller as compared to the theoretical molecular weight calculated from the conversion, which has not been observed in the PET-RAFT polymerizations in the absence of protein (Figure 4b, vide supra). This phenomenon was seen for the most of monomers (the only exception here was DMA), implying that additional initiation sites might exist in our experimental conditions. In order to understand this behavior, a series of negative control experiments was conducted with OEGA (Figure S19, Supporting Information). Surprisingly, the use of native BSA instead of BSA–macroinitiator resulted in the formation of "hydrogel." Considering the structural feature of BSA that there are 17 disulfide bonds,[80] disulfide bonds might generate thiyl radicals by PC-mediated energy/electron-transfer reactions[81] followed by thiyl-radical-mediated polymerizations and thereby, network formation; it is here noted that native BSA gave negligible polymerization in the absence of PC, indicating that PC plays an essential role for native BSA-initiated gelation. However, the reaction for thiyl radical formation might be far slower than the radical generation from a trithiocarbonate moiety, which is supported by the fact that BSA–macroinitiator provided the successful syntheses of PPCs. In particular, for a monomer with a high rate of propagation (i.e., DMA), the molecular weight obtained from GPC–MALLS is in well accordance to a theoretical molecular weight, further confirming our argument; it is presumed that a substantial amount of DMA monomers was consumed before the activation of disulfide bonds.

The effect of a variety of polymers on the enzymatic activity of BSA was then studied (Figure 4d). BSA is known to show an esterase-like activity, which can be evaluated from the hydrolysis experiments of *p*-nitrophenyl acetate where the absorbance at 405 nm of the hydrolyzed product, *p*-nitrophenol, was measured. Native BSA with or without irradiation and BSA–macroinitiator retained the esterase-like activity in contrast to BSA heated at 80 °C for 5 h, indicating that the polymerization condition does not cause protein denaturation. The synthesized PPCs with a variety of polymers showed activity in varying degrees, clearly indicating that the enzymatic activity could be tailored by the structure of polymers conjugated to the protein. Although the modification with the grown polymers lowered the activity in some cases, BSA–PSPAPC conjugates indicated the similar BSA activity to the native BSA with an additional benefit of tuning the surface changes of BSA, which is often hard to achieve by chemistries with small molecules. Moreover, interestingly, almost no activity was retained for BSA–PDMAPS conjugates, which might enable "activity-switching behavior" of the enzyme by introducing external stimuli–responsive moiety into the polymers. The related researches are currently underway.

3. Conclusion

A highly efficient water-soluble and biocompatible organic PC was discovered, which enables the syntheses of well-defined PPCs through a "grafting-from" PET-RAFT polymerization at ambient/aqueous conditions without additives. Incorporation of water-soluble and weakly electron-donating sulfonate moiety into one of four donor groups of the well-known highly efficient organic PC, 4DP-IPN, yields 3DP-MSDP-IPN with the same electronic structure, but, largely enhanced water solubility. Unconventional "oxygen-acceleration" behavior was observed for the PET-RAFT polymerization of acrylic and acrylamide monomers in the presence of 3DP-MSDP-IPN in which oxygen acts as an electron shuttle between $^3PC^*$ and CTA. Here, the PC plays an important role: i) singlet oxygen generator and ii) photoreductant to form superoxide radical ion ($O_2^{\bullet-}$), which originates from the photophysical and electrochemical features of 3DP-MSDP-IPN. With 50 ppm of 3DP-MSDP-IPN, we successfully performed "grafting-from" polymerizations from BSA in biorelevant conditions under green LED irradiation, which allows for preparation of various types of PPCs with neutral, anionic, cationic, and zwitterionic polyacrylates and polyacrylamides. We believe that our PC system will be actively utilized for a variety of photocatalysis processes in aqueous environments including the living cell system.

Supporting Information

Supporting Information is available from the Wiley Online Library or from the author.

Acknowledgements

This work was supported by Creative-Pioneering Researchers Program through Seoul National University (0417-20200126) and by the Basic Science Research Program through the National Research Foundation of Korea (NRF), which was funded by the Ministry of Education (2019R1I1A2A01059288) and the Ministry of Science and ICT (MSIT) (2021R1A5A1030054). The work at IMDEA was supported by the Spanish Ministry for Science (MINECO/MICINN–FEDER projects CTQ2017–87054, and RTI2018-097508-B-I00) by the "Severo Ochoa" programme for Centers of Excellence in Research and Development (MINECO; grant SEV-2016-0686 and MICINN CEX2020-001039-S), European Union structural funds and Comunidad de Madrid NMAT2D-CM Program (P2018/NMT-4511), and Campus of International Excellence UAM + CSIC.

Conflict of Interest

The authors declare no conflict of interest.

Data Availability Statement

The data that support the findings of this study are available from the corresponding author upon reasonable request.

Keywords

organic photocatalysts, photocatalyzed RAFT, photoredox catalysis, protein–polymer conjugates, reversible-deactivation radical polymerization

Received: October 21, 2021
Revised: January 11, 2022
Published online: February 23, 2022

[1] J. Y. Shu, B. Panganiban, T. Xu, *Annu. Rev. Phys. Chem.* **2013**, *64*, 631.
[2] I. Cobo, M. Li, B. S. Sumerlin, S. Perrier, *Nat. Mater.* **2015**, *14*, 143.
[3] T. A. Wright, R. C. Page, D. Konkolewicz, *Polym. Chem.* **2019**, *10*, 434.
[4] A. Abuchowski, T. van Es, N. C. Palczuk, F. F. Davis, *J. Biol. Chem.* **1977**, *252*, 3578.
[5] J. M. Harris, R. B. Chess, *Nat. Rev. Drug Discovery* **2003**, *2*, 214.
[6] E. M. Pelegri-O'Day, E.-W. Lin, H. D. Maynard, *J. Am. Chem. Soc.* **2014**, *136*, 14323.
[7] I. Ekladious, Y. L. Colson, M. W. Grinstaff, *Nat. Rev. Drug Discovery* **2019**, *18*, 273.
[8] C. A. Stevens, K. Kaur, H.-A. Klok, *Adv. Drug Delivery Rev.* **2009**, *61*, 1203.
[9] A. Grigoletto, T. Tedeschini, E. Canato, G. Pasut, *WIREs Nanomed. Nanobiotechnol.* **2021**, *13*, e1689.
[10] C. DelRe, Y. Jiang, P. Kang, J. Kwon, A. Hall, I. Jayapurna, Z. Ruan, L. Ma, K. Zolkin, T. Li, C. D. Scown, R. O. Ritchie, T. P. Russell, T. Xu, *Nature* **2021**, *592*, 558.
[11] W.-H. Leung, P.-K. So, W.-T. Wong, W.-H. Loa, P.-H. Chan, *RSC Adv.* **2016**, *6*, 106837.
[12] M. Liu, L. Jia, Z. Zhao, Y. Han, Y. Li, Q. Peng, Q. Zhang, *Chem. Eng. J.* **2020**, *390*, 124667.
[13] J. Zhu, Y. Zhang, D. Lu, R. N. Zare, J. Ge, Z. Liu, *Chem. Commun.* **2013**, *49*, 6090.
[14] J. C. M. van Hest, *Polym. Rev.* **2007**, *47*, 63.
[15] B. S. Sumerlin, *ACS Macro Lett.* **2012**, *1*, 141.
[16] A. L. Lewis, S. W. Leppard, *US 8053520*, **2011**.
[17] A. L. Lewis, *US 8431113*, **2013**.
[18] D. Bontempo, K. L. Heredia, B. A. Fish, H. D. Maynard, *J. Am. Chem. Soc.* **2004**, *126*, 15372.
[19] K. L. Heredia, D. Bontempo, T. Ly, J. T. Byers, S. Halstenberg, H. D. Maynard, *J. Am. Chem. Soc.* **2005**, *127*, 16955.
[20] B. S. Lele, H. Murata, K. Matyjaszewski, A. J. Russell, *Biomacromolecules* **2005**, *6*, 3380.
[21] E. M. Pelegri-O'Day, H. D. Maynard, *Acc. Chem. Res.* **2016**, *49*, 1777.
[22] M. S. Messina, K. M. M. Messina, A. Bhattacharya, H. R. Montgomery, H. D. Maynard, *Prog. Polym. Sci.* **2020**, *100*, 101186.
[23] L. Zhao, L. Li, G. Liu, L. Chen, X. Liu, J. Zhu, B. Li, *Food Res. Int.* **2013**, *53*, 409.
[24] L. Zhang, Y. Zhang, J. Cheng, L. Wang, X. Wang, M. Zhang, Y. Gao, J. Hu, X. Zhang, J. L. Lü, G. Li, R. Tai, H. Fang, *Sci. Rep.* **2017**, *7*, 10176.
[25] K. A. Pikal-Cleland, N. Rodríguez-Hornedo, G. L. Amidon, J. F. Carpenter, *Arch. Biochem. Biophys.* **2000**, *384*, 398.
[26] M. Chen, M. Zhong, J. A. Johnson, *Chem. Rev.* **2016**, *116*, 10167.
[27] N. Corrigan, S. Shanmugam, J. Xu, C. Boyer, *Chem. Soc. Rev.* **2016**, *45*, 6165.
[28] X. Pan, M. A. Tasdelen, J. Laun, T. Junkers, Y. Yagci, K. Matyjaszewski, *Prog. Polym. Sci.* **2016**, *62*, 73.
[29] Y. Lee, C. Boyer, M. S. Kwon, *Nat. Rev. Mater.* **2022**, *7*, 74.
[30] J. Yeo, R. Chapman, A. J. Gormley, C. Boyer, *Chem. Soc. Rev.* **2018**, *47*, 4357.
[31] M. D. Nothling, Q. Fu, A. Reyhani, S. Allison-Logan, K. Jung, J. Zhu, M. Kamigaito, C. Boyer, G. G. Qiao, *Adv. Sci.* **2020**, *7*, 2001656.
[32] J. Xu, K. Jung, C. Boyer, *Macromolecules* **2014**, *47*, 4217.
[33] S. Shanmugam, J. Xu, C. Boyer, *J. Am. Chem. Soc.* **2015**, *137*, 9174.
[34] N. Corrigan, D. Rosli, J. W. J. Jones, J. Xu, C. Boyer, *Macromolecules* **2016**, *49*, 6779.
[35] C. Wu, S. Shanmugam, J. Xu, J. Zhu, C. Boyer, *Chem. Commun.* **2017**, *53*, 12560.
[36] C. Wu, N. Corrigan, C.-H. Lim, K. Jung, J. Zhu, G. Miyake, J. Xu, C. Boyer, *Macromolecules* **2019**, *52*, 236.
[37] J. Xu, K. Jung, N. A. Corrigan, C. Boyer, *Chem. Sci.* **2014**, *5*, 3568.
[38] B. S. Tucker, M. L. Coughlin, C. A. Figg, B. S. Sumerlin, *ACS Macro Lett.* **2017**, *6*, 452.
[39] C. Fu, B. Demir, S. Alcantara, V. Kumar, F. Han, H. G. Kelly, X. Tan, Y. Yu, W. Xu, J. Zhao, C. Zhang, H. Peng, C. Boyer, T. M. Woodruff, S. J. Kent, D. J. Searles, A. K. Whittaker, *Angew. Chem., Int. Ed.* **2020**, *59*, 4729.
[40] R. A. Olson, J. S. Levi, G. M. Scheutz, J. J. Lessard, C. A. Figg, M. N. Kamat, K. B. Basso, B. S. Sumerlin, *Macromolecules* **2021**, *54*, 4880.
[41] J. Xu, S. Shanmugam, H. T. Duonga, C. Boyer, *Polym. Chem.* **2015**, *6*, 5615.
[42] S. Allison-Logan, Q. Fu, Y. Sun, M. Liu, J. Xie, J. Tang, G. G. Qiao, *Angew. Chem., Int. Ed.* **2020**, *59*, 21392.
[43] V. K. Singh, C. Yu, S. Badgujar, Y. Kim, Y. Kwon, D. Kim, J. Lee, T. Akhter, G. Thangavel, L. S. Park, J. Lee, P. C. Nandajan, R. Wannemacher, B. Milián-Medina, L. Lüer, K. S. Kim, J. Gierschner, M. S. Kwon, *Nat. Catal.* **2018**, *1*, 794.
[44] M. Garreau, F. L. Vaillant, J. Waser, *Angew. Chem., Int. Ed.* **2019**, *58*, 8182.
[45] Y. Song, Y. Kim, Y. Noh, V. K. Singh, S. K. Behera, A. Abudulimu, K. Chung, R. Wannemacher, J. Gierschner, L. Lüer, M. S. Kwon, *Macromolecules* **2019**, *52*, 5538.
[46] J.-H. Back, Y. Kwon, J. C. Roldao, Y. Yu, H.-J. Kim, J. Gierschner, W. Lee, M. S. Kwon, *Green Chem.* **2020**, *22*, 8289.
[47] J.-H. Back, Y. Kwon, H.-J. Kim, Y. Yu, W. Lee, M. S. Kwon, *Molecules* **2021**, *26*, 385.
[48] Y. Lee, M. S. Kwon, *Eur. J. Org. Chem.* **2020**, *38*, 6028.
[49] M. A. Bryden, E. Zysman-Colman, *Chem. Soc. Rev.* **2021**, *50*, 7587.
[50] C. Wu, N. Corrigan, C.-H. Lim, W. Liu, G. Miyake, C. Boyer, *Chem. Rev.* **2022**, https://doi.org/10.1021/acs.chemrev.1c00409.
[51] H. Uoyama, K. Goushi, K. Shizu, H. Nomura, C. Adachi, *Nature* **2012**, *492*, 234.
[52] O. Boutureira, G. J. L. Bernardes, *Chem. Rev.* **2015**, *115*, 2174.
[53] J. H. Ko, H. D. Maynard, *Chem. Soc. Rev.* **2018**, *47*, 8998.
[54] K. M. Burridge, R. C. Page, D. Konkolewicz, *Polymer* **2020**, *211*, 123062.
[55] S. J. Bryant, C. R. Nuttelman, K. S. Anseth, *J. Biomater. Sci., Polym. Ed.* **2012**, *11*, 439.
[56] C. S. Bahney, T. J. Lujan, C. W. Hsu, M. Bottlang, J. L. West, B. Johnstone, *Eur. Cells Mater.* **2011**, *22*, 43.
[57] R. A. Olson, A. B. Korpusika, B. S. Sumerlin, *Chem. Sci.* **2020**, *11*, 5142.
[58] Q. Fu, Q. Ruan, T. G. McKenzie, A. Reyhani, J. Tang, G. G. Qiao, *Macromolecules* **2017**, *50*, 7509.
[59] J. Yeow, R. Chapman, J. Xu, C. Boyer, *Polym. Chem.* **2017**, *8*, 5012.
[60] C. Wu, K. Jung, Y. Ma, W. Liu, C. Boyer, *Nat. Commun.* **2021**, *12*, 478.
[61] C. Kerzig, X. Guo, O. S. Wenger, *J. Am. Chem. Soc.* **2019**, *141*, 2122.
[62] A. M. Mansour, K. Radacki, O. R. Shehab, *Dalton Trans.* **2021**, *50*, 10701.
[63] D. Kand, P. Liu, M. X. Navarro, L. J. Fischer, L. Rousso-Noori, D. Friedmann-Morvinski, A. H. Winter, E. W. Miller, R. Weinstain, *J. Am. Chem. Soc.* **2020**, *142*, 4970.
[64] J. Niu, D. J. Lunn, A. Pusuluri, J. I. Yoo, M. A. O'Malley, S. Mitragotri, H. T. Soh, C. J. Hawker, *Nat. Chem.* **2017**, *9*, 537.
[65] J. Geng, W. Li, Y. Zhang, N. Thottappillil, J. Clavadetscher, A. Liliana, M. Bradley, *Nat. Chem.* **2019**, *11*, 578.
[66] All rates are obtained by fitting the experimental data to the behavior derived from the rate equations for the occupation of the singlet and triplet states using the following approximations: $k_{ISC} \gg k_F, k_{nr,S}, k_{PH}, k_{RISC} \gg k_{nr,T}$.
[67] G. Ng, J. Yeow, J. Xu, C. Boyer, *Polym. Chem.* **2017**, *8*, 2841.
[68] The Stern–Volmer equation can be applied for triplet quenching in thermally activated delayed fluorescence (TADF)-type materials under the condition that $k_{RISC} \ll k_{ISC}$, which is usually valid for most TADF molecules, including the current systems, see the rates in the

Jablonski diagrams of Figure 1a and Figure S6 (Supporting Information). Details will be discussed in a forthcoming paper.
[69] C. Franco, J. OlmstedIII, *Talanta* **1990**, *37*, 905.
[70] N. J. Turro, V. Ramamurthy, J. C. Scaiano, *Principles of Molecular Photochemistry: An Introduction*, University Science Books, Sausalito, CA **2008**.
[71] P. S. Rao, E. Hayon, *J. Phys. Chem.* **1975**, *79*, 397.
[72] D. Vasudevan, H. Wendt, *J. Electroanal. Chem.* **1995**, *392*, 69.
[73] J. P. Cole, D.-F. Chen, M. Kudisch, R. M. Pearson, C.-H. Lim, G. M. Miyake, *J. Am. Chem. Soc.* **2020**, *142*, 13573.
[74] M. Hayyan, M. A. Hashim, I. M. AlNashef, *Chem. Rev.* **2016**, *116*, 3029.
[75] M. Levy, P. P. Chowdhury, P. Nagpal, *J. Biol. Eng.* **2019**, *13*, 48.
[76] J. Maillard, K. Klehs, C. Rumble, E. Vauthey, M. Heilemann, A. Fürstenberg, *Chem. Sci.* **2021**, *12*, 1352.
[77] G. E. Dobretsov, T. I. Syrejschikova, N. V. Smolina, *Biophysics* **2014**, *59*, 183.
[78] C. Boyer, V. Bulmus, J. Liu, T. P. Davis, M. H. Stenzel, C. Barner-Kowollik, *J. Am. Chem. Soc.* **2007**, *129*, 7145.
[79] W. Hou, L. Wei, L. Liu, H. Zhao, *Biomacromolecules* **2018**, *19*, 4463.
[80] T. Peters, *All About Albumin: Biochemistry, Genetics, and Medical Applications*, Academic Press, New York **1996**.
[81] J. Kim, B. Kang, S. H. Hong, *ACS Catal.* **2020**, *10*, 6013.

Visible-light-driven polymerization towards the green synthesis of plastics

Yungyeong Lee[1], *Cyrille Boyer*[2]✉ *and Min Sang Kwon*[1]✉

Environmentally benign and sustainable chemistry has the potential to address negative environmental impacts associated with the production and degradation of synthetic polymers. In particular, green synthesis of plastics could be achieved by the convergence of visible-light-driven photocatalysis and reversible-deactivation radical polymerization.

Since the emergence of the first commercialized synthetic plastic Bakelite, a variety of synthetic polymers have been designed into plastic products, which are now ubiquitous in our daily life. However, the increasing production of plastics and the lack of adequate recycling have led to the increasing generation of plastic waste that negatively impacts our environment, motivating research into mechanical and/or chemical recycling methods to increase the recovery rate of plastics and reduce plastic waste[1]. In addition to recycling polymers after their use, the development of green synthetic methods can advance the sustainability of polymeric materials. Green synthesis of plastics could be achieved by designing polymeric materials that are degradable and/or prepared from environmentally benign reagents. Alternatively, reaction processes can be developed that attain high energy efficacy and atom economy under mild reaction conditions. For example, plants apply photosynthesis to convert light energy into chemical energy, which is then stored in the form of carbohydrates. Giacomo Ciamician already suggested in 1912 that the same photochemical process could be applied to synthetic organic chemistry: "And if in a distant future the supply of coal becomes completely exhausted, civilization will not be checked by that, for life and civilization will continue as long as the sun shines!"[2]

The 2021 Nobel Prize in Chemistry was awarded to Benjamin List and David MacMillan, who pioneered the development of organic catalysis as a new toolbox for the effective synthesis of (asymmetrical) molecules. Not only is this strategy powerful in terms of unprecedented chemical reactivity, but it also makes the chemistry greener by replacing potentially toxic metal-based catalysts with organic molecules. Moreover, merging organic catalysis with photoredox catalysis has allowed organic chemists to use visible light as the energy source in organic transformations, resembling biological photosynthesis. Visible light is abundant and a sustainable energy source, and thus visible-light-driven photocatalysis is of great interest from a green chemistry perspective. Visible light can also be applied to polymerization reactions for the synthesis of well-defined polymeric materials with desired properties. Here, we discuss visible-light-driven polymerization reactions, highlighting how this approach could enable the green synthesis of plastics.

Visible light in reversible-deactivation radical polymerization

Reversible-deactivation radical polymerization (RDRP) applies a chain-growth mechanism to produce well-defined polymers with controlled molecular weight and narrow dispersity[3]. Reversible activation of the dormant chain end keeps the concentration of unstable and reactive radicals low, which would otherwise cause undesired termination and chain transfer reactions. The preserved living end affords polymers the aforementioned controllability and allows complex architecture design. For example, in atom transfer radical polymerization (ATRP), polymer chains only grow if the carbon–halide bond at the end of the initiator or propagating chain is reduced to form a reactive radical. Inspired by the use of $Ir(ppy)_3$ in photocatalysed atom transfer radical addition, which includes the reduction of a carbon–halide bond, the first photomediated ATRP of methyl methacrylate was achieved using $Ir(ppy)_3$ and 50 W fluorescent lamps[4]. $Ir(ppy)_3$ has also been introduced in reversible addition–fragmentation chain transfer polymerization (RAFT) (that is, photoinduced electron/energy transfer-RAFT (PET-RAFT))[5]. The environmental compatibility of photomediated RDRP has since been improved by the development of non-toxic or less toxic organic photoredox catalysts, highly reactive photoredox catalysts that allow efficient polymerization with low catalyst loading, and photoredox catalysts, such as porphyrins, that can absorb visible light at longer wavelengths[6].

Visible light is more than a green energy source

In addition to being a green energy source, visible light provides controlled features to reactions; for example, reactions can be controlled in a spatiotemporal manner, they can be orthogonally regulated by multiple external

[1]*Department of Materials Science Engineering, Seoul National University, Seoul, South Korea.*

[2]*Centre for Advanced Macromolecular Design (CAMD), School of Chemical Engineering, and Australian Centre for NanoMedicine, School of Chemical Engineering, UNSW Australia, Sydney, New South Wales, Australia.*

✉*e-mail: cboyer@unsw.edu.au; minsang@snu.ac.kr*

https://doi.org/10.1038/s41578-021-00409-6

stimuli, and they can be proceeded in mild and ambient conditions (for example, in the presence of oxygen and water)[3,7]. As the chain end becomes active for propagation, after entering the photocatalytic cycle, polymerization can only occur if and where light is irradiated. The photocatalytic process relies on the absorption of visible light and the photoexcitation of photoredox catalysts, and, subsequently, on electron and/or energy transfer to the reagent. Benefitting from these photophysical aspects, molecular weight, monomer sequence, architecture and even the tacticity of polymers can be exquisitely controlled through finely designed reaction systems. Moreover, the reaction system is tolerant to oxygen and water, and the reaction can thus be conducted in a user-friendly and sustainable fashion[7]; there is no need for degassing the reaction mixture, and thus the reactor setup is simpler and accessible to non-experts in polymer chemistry.

Challenges

Several challenges remain to be overcome for the real-world use of photomediated RDRP in industrial applications.

Monomer scope. The monomer scope is currently limited to (meth)acrylates and (meth)acrylamides, but could be expanded to other vinylic monomers. Incorporation of cyclic ketene acetal monomers, for example, allows the introduction of a heteroatom within polymer backbones, which would enable the biological or chemical degradation of the resulting polymers. Commodity polymers with carbon-only backbones, such as high- and low-density polyethylene, polypropylene or polyvinyl chlorides, have beneficial material properties, but very low recovery rates[1]. Therefore, it is important to design polymers that have similar material properties to polymers with carbon-only backbones, such as elastic modulus and tensile strength, but that are also recyclable. Expanding the monomer pool would allow the design of polymers with various monomeric compositions and functionalities; however, the reaction system (for example, photoredox catalyst, chain transfer agent, additives and irradiation conditions) would need to be carefully optimized for each monomer. High-throughput combinatorial and automated polymer chemistry combined with machine learning would aid this process and enable the development of new polymeric materials[8].

Reactor design. Reactors need to be designed in order to scale-up photomediated RDRP to industry standards. The penetration of light into the reaction mixture becomes more inefficient in larger reactors, which considerably decreases the efficiency of the photocatalyst and the photocatalysed reaction. According to the Beer–Lambert law, the path length of light should be short and the concentration of the reaction mixture should be kept low. This can be achieved by a continuous-flow reactor setup that contains a light irradiation source (that is, a photoflow reactor). In the case of multiblock copolymer synthesis, this setup eliminates the purification step and can further increase the reaction efficiency. We envisage that photoflow reactors may also be capable of directly harvesting sunlight, as imagined by Ciamician.

Mechanistic understanding. The controllability and sustainability of photomediated RDRP originate from the underlying photochemistry. However, our understanding of photochemical mechanisms remains limited. A better insight into the mechanism would aid in improving the design of reaction systems. For example, combinatorial chemistry could be applied to study structure–property–performance relationships of photoredox catalysts to gain mechanistic insight into specific reactions and to systematically design new photoredox catalysts[9].

Outlook and future opportunities

Visible-light-driven polymerization, together with advances in photophysics, polymer chemistry, combinatorial chemistry and machine learning, offers a sustainable route to designing polymeric materials; however, to efficiently harvest light for the large-scale production of polymers and to replace conventional (free radical) polymerization in industry, a deeper understanding of the reactions and proper design of reactors are needed. In addition to providing green energy for the production of polymeric materials, visible light could also induce photomediated depolymerization[10], thus offering an alternative approach to plastics degradation and waste management. Therefore, visible-light-driven (de) polymerization has the potential to resolve environmental issues associated with synthetic polymeric materials, and may ultimately deliver on the promise of green and more sustainable plastics.

1. Rahimi, A. & García, J. M. Chemical recycling of waste plastics for new materials production. *Nat. Rev. Chem.* **1**, 0046 (2017).
2. Ciamician, G. The photochemistry of the future. *Science* **36**, 385–394 (1912).
3. Corrigan, N. et al. Reversible-deactivation radical polymerization (controlled/living radical polymerization): from discovery to materials design and applications. *Prog. Polym. Sci.* **111**, 101311 (2020).
4. Fors, B. P. & Hawker, C. J. Control of a living radical polymerization of methacrylates by light. *Angew. Chem. Int. Ed.* **51**, 8850–8853 (2012).
5. Xu, J., Jung, K., Atme, A., Shanmugam, S. & Boyer, C. A robust and versatile photoinduced living polymerization of conjugated and unconjugated monomers and its oxygen tolerance. *J. Am. Chem. Soc.* **136**, 5508–5519 (2014).
6. Lee, Y. & Kwon, M. S. Emerging organic photoredox catalysts for organic transformations. *Eur. J. Org. Chem.* **38**, 6028–6043 (2020).
7. Yeow, J., Chapman, R., Gormley, A. J. & Boyer, C. Up in the air: oxygen tolerance in controlled/living radical polymerization. *Chem. Soc. Rev.* **47**, 4357–4387 (2018).
8. Gormley, A. J. & Webb, M. A. Machine learning in combinatorial polymer chemistry. *Nat. Rev. Mater.* **6**, 642–644 (2021).
9. Singh, V. K. et al. Highly efficient organic photocatalysts discovered via a computer-aided-design strategy for visible-light-driven atom transfer radical polymerization. *Nat. Catal.* **1**, 794–804 (2018).
10. Nguyen, S. T., McLoughlin, E. A., Cox, J. H., Fors, B. P. & Knowles, R. R. Depolymerization of hydroxylated polymers via light-driven C–C bond cleavage. *J. Am. Chem. Soc.* **143**, 12268–12277 (2021).

Acknowledgements

This work was supported by the Basic Science Research Program through the National Research Foundation of Korea (NRF) funded by the Ministry of Education (2019R1I1A2A01059288).

Competing interests

The authors declare no competing interests.

Chem Soc Rev

REVIEW ARTICLE

View Article Online
View Journal | View Issue

Cite this: *Chem. Soc. Rev.*, 2023, **52**, 3035

Photocontrolled RAFT polymerization: past, present, and future

Yungyeong Lee,[a] Cyrille Boyer *[c] and Min Sang Kwon *[ab]

In this review, we provide a brief history, progress, and applications, and discuss the remaining challenges of photocontrolled reversible addition–fragmentation chain transfer (RAFT) polymerization (*i.e.*, photoinduced electron/energy transfer-RAFT (PET-RAFT), photoiniferter, and photomediated cationic RAFT polymerization). Among these, visible-light-driven RAFT polymerization has attracted particular attention in recent years due to its benefits, including low energy consumption and the safe reaction procedure. Moreover, the incorporation of visible-light photocatalysis in the polymerization has conferred attractive features, such as spatiotemporal control and oxygen tolerance; however, a clear understanding of the reaction mechanism has not been completely provided. We also present recent research efforts to elucidate the polymerization mechanisms with the aid of quantum chemical calculations combined with experimental evidence. This review offers an insight into the better design of polymerization systems for desired applications and helps realize the full potential of photocontrolled RAFT polymerization in both academic- and industrial-scale applications.

Received 7th December 2022

DOI: 10.1039/d1cs00069a

rsc.li/chem-soc-rev

1. Introduction

1.1. Visible light as an energy source for photomediated reactions

Visible light refers to electromagnetic waves with wavelengths in the range of approximately 400–750 nm that are detectable by the human eye.[1] As visible light constitutes approximately half of the solar energy reaching the surface of earth, tremendous efforts have been devoted to utilize visible light as an energy source in the field of solar energy utilization including photovoltaics and solar

[a] *Department of Materials Science and Engineering, Seoul National University, Seoul 08826, Republic of Korea. E-mail: minsang@snu.ac.kr*
[b] *Research Institute of Advanced Materials, Seoul National University, Seoul 08826, Republic of Korea*
[c] *Cluster for Advanced Macromolecular Design (CAMD), School of Chemical Engineering, and Australian Centre for NanoMedicine, UNSW Sydney, Kensington, NSW 2052, Australia. E-mail: cboyer@unsw.edu.au*

Yungyeong Lee

Yungyeong Lee received her B.S. and M.S. degrees in Chemistry from Ulsan National Institute of Science and Technology (UNIST) in 2017 and 2019, respectively. Since 2021, she has been pursuing a PhD in Materials Science and Engineering (MSE) at Seoul National University (SNU) under the supervision of Prof. Min Sang Kwon. Her research interest focuses on the development of organic photocatalysts, investigation of their photophysical and electrochemical properties, and application to visible-light-mediated polymerization reactions particularly in aqueous systems.

Cyrille Boyer

Prof Cyrille Boyer is a Full Professor in the School of Chemical Engineering, Deputy Head of School, and Co-Director of Australian Centre for Nanomedicine. In 2022, he was awarded an Australian Laureate Fellowship. Cyrille's research interests mainly cover the preparation of functional macromolecules using photocatalysts, which find applications in various areas, including in nanomedicine and in energy storage. The research of his group has been recognized by several research awards, including 2018 IUPAC-Polymer International Young Researcher award, 2016 ACS Biomacromolecules/Macromolecules Young Researcher Award, Le Fevre Memorial Prize for Chemistry; and 2015 Malcolm McIntosh Prize for Physical Science.

fuels. Owing to Ciamician's pioneering insight, influenced by photosynthesis in nature,[2] light has been consistently used as an energy source for organic reactions.[3] Because most organic molecules do not absorb light in the visible range, ultraviolet (UV) light has long been employed as the primary energy source for photochemical reactions. However, due to its high energy, UV light often causes substantial side reactions and thereby reduces the reaction efficiency, which consequently limits the scope of photochemical reactions. Therefore, compared to conventional thermal reactions, photochemical reactions have been considerably underexplored.

In 2008, MacMillan,[4] Yoon,[5] and Stephenson[6] and coworkers reported that complex organic reactions proceed very efficiently in the presence of photoredox catalysts (PCs) under visible light irradiation. From these pioneering studies, organic chemists recognized that low-energy visible light could be a suitable energy source for various organic reactions, which led to the origin of a new field called "visible-light photocatalysis".[7–9] Thereafter, for more than a decade, visible-light photocatalysis has indeed been used as a mild and efficient method to activate molecules for a wide range of organic transformations that cannot be realized by other methodologies of chemical catalysis.[10–13] Under irradiation, excited-state PCs engage in electron or energy transfer and consequently generate highly reactive radical species from the corresponding stable substrates. These previously inaccessible reaction scaffolds have enabled significant development of radical chemistry in organic synthesis.

1.2. Visible-light-driven reversible deactivation radical polymerization

Reversible deactivation radical polymerization (RDRP) is a powerful technique to prepare polymers with controlled molecular weights, narrow molecular weight distributions (MWDs), compositions, functionalities, and architectures that impact the properties of polymers.[14,15] As this method provides appropriate controllability and compatibility with various monomers under mild conditions, it has been employed in numerous applications such as coatings, adhesives, cosmetics, ink materials for printing, detergents, paints, and surfactants.[16] In RDRP, heat is typically utilized as an energy source for polymerization in the presence of an initiator or a catalyst.[17,18]

Consistent efforts have been made to utilize light as an energy source for RDRP because of the potential benefits, including spatiotemporal control over polymerization and fast kinetics at ambient temperature as compared to conventional thermal processes.[19–21] Early systems for photomediated RDRP, which utilized high-energy UV light, had mostly relied on (i) a traditional photoinitiating system based on Norrish type I/II reactions,[22] (ii) a catalytic species with absorption only in the UV range,[23,24] or (iii) a chain transfer agent (CTA) (*i.e.*, RAFT agent) that undergoes photolysis under UV light irradiation.[25–27] However, these processes typically exhibited insufficient controllability of polymerization, side reactions and/or too fast kinetics due to the high energy of UV light. Nevertheless, it should be noted that in the field of polymer chemistry, a variety of UV-light-induced photoinitiating systems had been actively investigated before the emergence of visible-light photocatalysis owing to their utility in industrial applications such as photoresists and/or photocuring systems.

With regard to the milder reaction conditions of polymerization, visible light has been introduced as an energy source for RDRP since the early 2010. Inspired by visible-light photocatalysis, in 2012 Hawker and Fors demonstrated atom transfer radical polymerization (ATRP) of methacrylates using tris(2-phenylpyridine)iridium ($Ir(ppy)_3$) as a PC and a 50 W fluorescent lamp.[28] Matyjaszewski and coworkers reported another photomediated ATRP using a copper (Cu) complex under violet and blue light irradiation (392 and 450 nm, respectively),[29] where photoinduced reduction of the Cu^{2+} complex and subsequent activation of the alkyl halide initiator were achieved by irradiation rather than heating. By the addition of visible-light-absorbing dyes to indirectly reduce the Cu^{2+} complex and generate initiating radicals, Yagci and coworkers further expanded the polymerization wavelength to 400–500 nm.[30] In the case of RAFT polymerization, in 2014, Boyer and coworkers employed $Ir(ppy)_3$ to activate the reversible addition–fragmentation chain transfer (RAFT) polymerization of various vinylic monomers (including (meth)acrylamides, (meth) acrylates, styrene, and vinyl esters) under blue light irradiation (435 nm).[31] In 2015, Boyer,[32] Qiao,[33] and coworkers separately reported the successful RAFT polymerization of (meth)acrylates under blue or green light irradiation (435 and 530 nm, respectively) in the absence of PCs. These visible-light-driven RDRPs retained excellent controllability of polymerization similar to conventional thermal RDRPs. Since these initial studies, various types of visible-light-driven RDRPs have been extensively studied from different perspectives such as (i) reaction optimization, (ii) mechanistic studies, (iii) understanding the unique features of each polymerization, (iv) catalyst/reagent developments, (v) syntheses of polymers with a novel structure, and (vi) new applications.[19,20,34–36]

1.3. Visible-light-driven RAFT polymerization

In conventional RAFT polymerization, an initiator generates radicals typically by thermal decomposition and a CTA ensures

Min Sang Kwon

Min Sang Kwon received his B.S. degrees in Chemistry and MSE from SNU. Then, he did his PhD in Chemistry at SNU under the guidance of Prof. Eun Lee. After finishing his postdoctoral studies at SNU with Prof. Soo Young Park, he moved to University of Michigan to work with Prof. Jinsang Kim. In 2016, he began his independent career at UNIST as an Assistant Professor. In 2020, he moved back to his alma mater, SNU, where he is currently an Associate Professor of MSE. He has a broad interest in organic chemistry, photochemistry, and polymer chemistry.

the controllability of polymerization *via* RAFT equilibrium.[37] In contrast, in photomediated RAFT polymerization, a photoinitiating system mostly driven by UV light has replaced the conventional thermal initiator. Despite the simplicity and convenience of photomediated polymerization, which proceeds by irradiation rather than heating, the high energy of UV light caused undesired side reactions and lowered the controllability of polymerization.[38] Boyer and coworkers pioneered the use of low-energy visible light for photomediated RAFT polymerization in 2014 by the incorporation of PCs, named photoinduced electron/energy transfer-RAFT (PET-RAFT) polymerization.[31] In 2015, Boyer,[32] Qiao,[33] and coworkers separately reported visible-light-driven photoiniferter polymerization of specific (meth)acrylates. The proposed PET-RAFT polymerization was based on electron/energy transfer between a visible-light-absorbing PC and a CTA,[31] whereas photoiniferter polymerization was based on visible-light-driven photolysis of a CTA in the absence of PCs and had been previously demonstrated only under UV light.[39,40] More recently, cationic RAFT polymerization, which involves the formation of carbocations as propagating species,[41,42] was realized under visible light in the presence of a PC, as reported by Fors and coworkers.[43] Since then, numerous studies have improved the utility of reaction systems, for example, by investigating PCs and/or CTAs to enhance the rate of polymerization under a broad range of irradiation wavelengths. It has also been revealed that these visible-light-driven RAFT polymerizations exhibit decent controllability of polymerization as well as attractive features including spatiotemporal control, oxygen tolerance, and unique selectivity of polymerization, which are dependent on reaction conditions (*i.e.*, irradiation wavelengths and the combination of a CTA, monomer, and PC if employed), and high compatibility with other polymerization methods, which was not observed in conventional RDRP.[44] Therefore, visible-light-driven RAFT polymerization has enabled the preparation of polymers with high levels of structural complexities and functionalities and reached a wide range of advanced applications, such as advanced manufacturing, nanomedicine, and energy. Fig. 1 depicts the timeline of milestones toward the development of visible-light-driven RAFT polymerization.

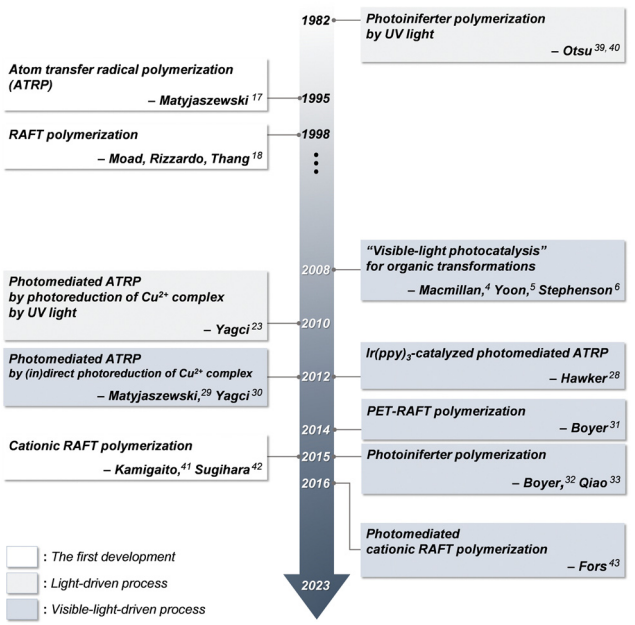

Fig. 1 Timeline of milestones toward the development of photocontrolled RAFT polymerization.

1.4. Scope of this review

Given these attractive and unique features, several highly cited review articles have already discussed photocontrolled RAFT polymerization either as a part of photomediated RDRP or photoredox catalysis,[19,20,45–47] or as an independent topic with a particular emphasis on mechanistic studies,[48] oxygen tolerance,[49] spatiotemporal regulation of the reaction system by light,[50,51] fabrication of advanced materials,[52] and environmental compatibility of polymerization.[44] The recent review articles have provided an insight into the remaining challenges and underscored the promising future of photomediated RAFT polymerization for its wide applicability in the industry.[34,53] However, as compared to PET-RAFT polymerization, only a few articles[54,55] have paid considerable attention to photoiniferter polymerization until Hartlieb in 2022 outlined the progress of photoiniferter polymerization from early systems to the current state.[56] It was because photoiniferter polymerization has mostly utilized UV light thus far, in contrast to PET-RAFT polymerization which utilized the milder visible light.

Visible light is more than an energetically mild and environmentally benign energy source. Convergence of visible-light photocatalysis and photomediated RDRP has also brought decent controllability of polymerization and distinct features such as oxygen tolerance. Furthermore, visible and near-infrared (NIR) light allows utilizing wavelength-orthogonal chemistry for activating wavelength-selective photoinduced reactions in an orthogonal manner. In this regard, it is timely to provide a detailed review on photocontrolled RAFT polymerization reactions (*i.e.*, PET-RAFT, photoiniferter, and photomediated cationic RAFT polymerization) with a particular emphasis on visible-light-driven systems, and summarize their concept, method, mechanism, and applications. In addition to the unprecedently wide versatility of the polymerization ranging from precision polymer synthesis in academic fields to 3D/4D printing technologies in industrial fields, we describe the recent increasing efforts to uncover and elucidate the underlying mechanistic backgrounds from a photophysical point of view with the help of computational studies. As the broad applicability of the polymerization originates from the mechanism, this review provides an overview of the current status and the remaining challenges in photocontrolled RAFT polymerization.

2. Mechanism

In this section, the basic mechanisms and current studies related to the mechanistic understanding of various visible-light-driven RAFT polymerizations are described. The methods mostly do not require exogenous initiators and share a RAFT process, which underpins the controllability similar to that in conventional

thermal RAFT polymerization. Based on the initiation mechanism, the methods can be categorized as follows.

In PET-RAFT polymerization, an initiating radical is generated by the interaction between an excited-state PC and a CTA followed by (i) fragmentation of the reduced CTA *via* either an oxidative[31] or a reductive quenching cycle,[57] and/or (ii) homolysis of the CTA *via* energy transfer.[46] The CTA can be oxidized as in the case of photomediated cationic RAFT polymerization.[43] Photoiniferter polymerization includes direct homolysis of the CTA under irradiation in the absence of a PC.[40,58] Very recently, the RAFT process has been combined with inner-sphere electron transfer (ISET)[59] and hydrogen atom transfer (HAT).[60]

Despite the burgeoning applications of visible-light-driven RAFT polymerization in numerous fields, several questions, such as whether it is electron or energy transferred from the excited-state PC to the CTA, still remain unsolved. It is also noteworthy that the electron/energy transfer processes may also depend on the type of PC and CTA. Herein, the importance of enhancing fundamental understanding of the mechanism and thereby the recent efforts utilizing quantum chemical (QC) calculations, kinetic modeling, laser flash photolysis, or transient absorption spectroscopy to answer these unsolved questions are summarized.

2.1. Conventional RAFT polymerization (RAFT process)

RAFT polymerization, which was firstly developed by Rizzardo, Moad, Thang, and coworkers in 1998,[18] relies on degenerative chain transfer to reversibly deactivate active propagating radicals. By the addition of a CTA possessing a thiocarbonylthio (TCT) group to conventional radical polymerization, the RAFT process successfully realized RAFT polymerization with controlled and living behavior (Scheme 1). Firstly, an external initiator is fragmented, typically by heat or light, to generate initiating radicals. After several additions of monomers, the propagating radical is added to the CTA. The resulting TCT intermediate radical undergoes fragmentation to liberate the R group as another propagating radical. These two propagating radicals are reversibly added and fragmented to become dormant and active species for polymerization, respectively, which is called RAFT main equilibrium. *Via* this RAFT main equilibrium, the propagating radicals share equal probabilities for chain growth. It is noted that addition and fragmentation occur faster than propagation, which prevents bimolecular termination between two radical species. Therefore, polymers possessing TCT groups exhibit low dispersity and can be reactivated by adding new monomers. As controlled and living radical polymerization is realized through an efficient RAFT process, for each monomer family, a CTA with appropriate R and Z groups must be chosen to ensure energetically favorable addition, fragmentation, and propagation. Dithiobenzoates (DTBs), dithiocarbamates (DTCs), trithiocarbonates (TTCs), and xanthates are representative classes of CTAs categorized based on the Z groups. Since the development of RAFT polymerization, the influence of R and Z groups on polymerization control has been thoroughly studied. The well-established general guidelines for the selection of CTAs for a certain monomer are well described

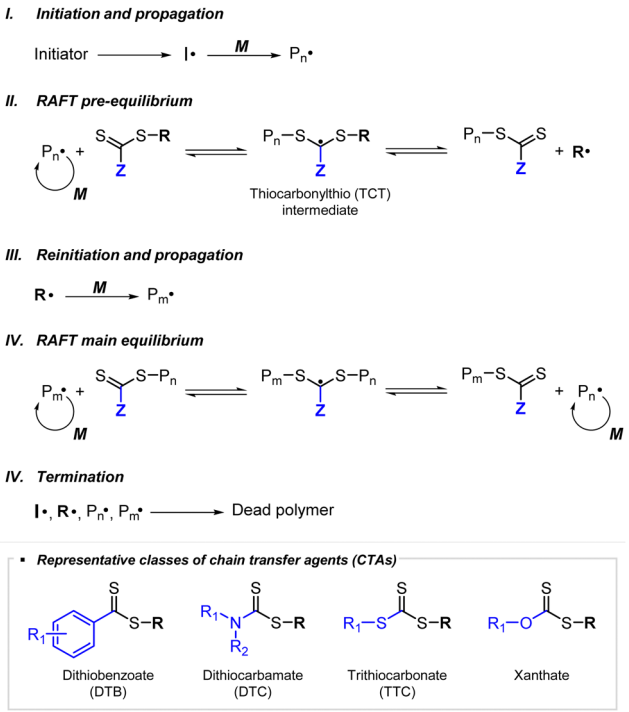

Scheme 1 Mechanism of conventional RAFT polymerization.

in the review articles by the inventors of RAFT polymerization in the Commonwealth Scientific and Industrial Research Organization (CSIRO)[61] and Perrier.[37]

2.2. Visible-light-driven RAFT polymerization

2.2.1. PET-RAFT polymerization. Despite the recent remarkable advancements of PET-RAFT polymerization, its mechanism remains elusive as it involves multiple competing pathways (*i.e.*, electron and/or energy transfer; see below). The complexity of the PET-RAFT polymerization mechanism primarily arises from the fact that CTAs have relatively high oxidizing powers and hence high ground-state reduction potentials (-1.0 V $< E^0_{red} < -0.4$ V; *vs.* saturated calomel electrode (SCE)), low energies at the lowest triplet excited state (T_1) (1.5 eV $< E_{00}(T_1) <$ 1.8 eV), and moderate visible-light absorption abilities. The high E^0_{red}s allow the reduction of the CTA by PC intermediates *via* electron transfer, whereas the low T_1 energies allow energy transfer from an excited-state PC to the CTA. Finally, several visible-light-absorbing CTAs can be directly excited by absorbing visible light ($<$530 nm) by themselves in the absence of a PC (please see Section 2.2.2). Among the different pathways, three pathways involving PCs are depicted in Scheme 2: one energy transfer pathway and two electron transfer pathways which are divided into the oxidative quenching pathway (OQP) and the reductive quenching pathway (RQP) depending on the fate of excited-state PCs during the photocatalytic cycle. Most PCs can, in principle, induce polymerization *via* all the pathways, which greatly limits the complete understanding of the precise mechanism. Propagating radical species are generated regardless of the pathways, but their reaction intermediates (*i.e.*, TCT anion and TCT radical) are different.

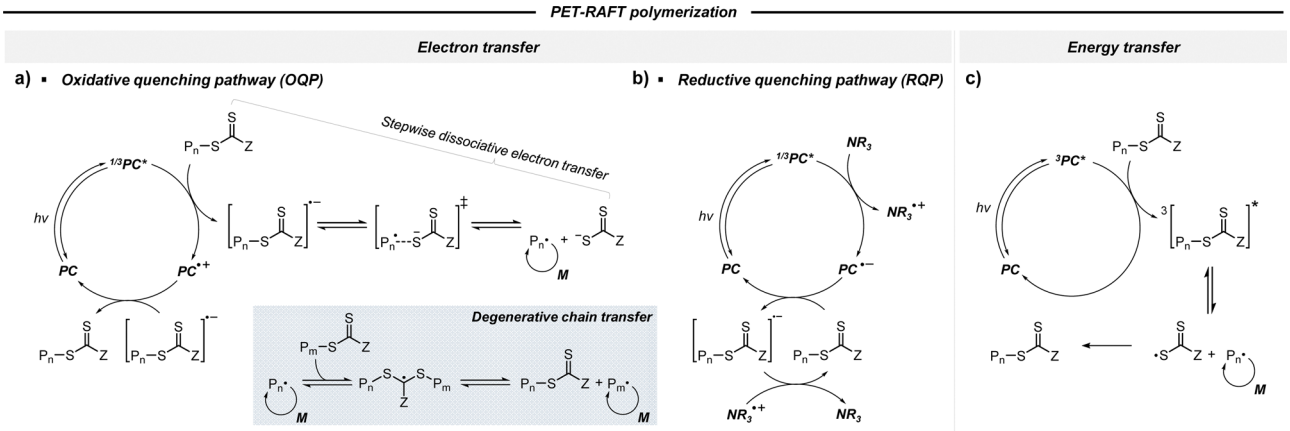

Scheme 2 Mechanism of PET-RAFT polymerization. Electron transfer *via* (a) oxidative quenching pathway (OQP) and (b) reductive quenching pathway (RQP) in the presence of a reducing agent (*e.g.*, tertiary amine). (c) Energy transfer.

2.2.1.1. Electron transfer: oxidative quenching pathway (OQP). The OQP involves oxidation of an excited-state PC. Electron transfer from an excited-state PC to a ground-state CTA leads to the formation of a one-electron-oxidized PC ($PC^{\bullet+}$) and an anionic intermediate of the CTA, which then undergoes fragmentation to afford a propagating radical and a TCT anion. Stepwise dissociative electron transfer (DET) is considered to occur during the activation step (Scheme 2a). Based on the transfer coefficient (α) measured by cyclic voltammetry (CV), Moad, Strover, and coworkers claimed that electron transfer from the excited-state PC to the CTA and dissociation of the C–S bond occur in a stepwise manner.[62] More recently, Denifl, Moad, Coote, and coworkers thoroughly investigated the reduction of the selected CTAs (cyanomethyl benzodithioate and dimethyl trithiocarbonate) and their subsequent chemical reactions by performing low-energy electron attachment experiments in the gas phase (Fig. 2).[63] Interestingly, in these experiments, the authors observed that anion intermediates were (i) generated and (ii) selectively dissociated into TCT anions and carbon radicals through C–S bond cleavage. These observations strongly supported the involvement of stepwise DET in the electron-transfer-driven RAFT process.

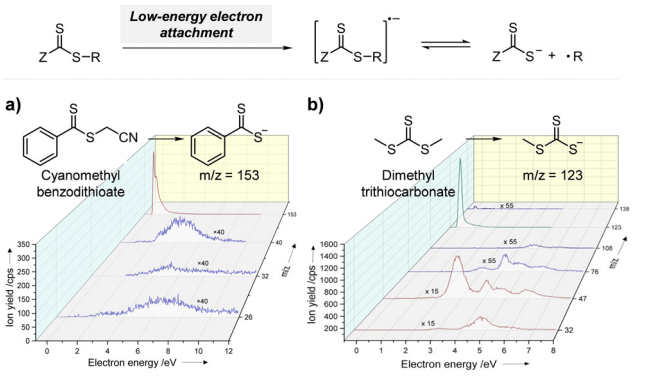

Fig. 2 Electrochemical activation of the CTA by low-energy electron attachment and intensity map of TCT anions generated from subsequent dissociation of (a) cyanomethyl benzodithioate and (b) dimethyl trithiocarbonate. Adapted with permission from ref. 63 (Copyright 2021 John Wiley & Sons, Inc.).

Recently, the research groups of Boyer and Liu,[64] and Kwon[65] separately reported that the selectivity for the CTA in PET-RAFT polymerization is closely related to the stepwise DET mechanism. Boyer and coworkers observed that metal naphthalocyanine (MNC)-catalyzed PET-RAFT polymerization of methyl acrylate (MA) under NIR light irradiation (780 nm) showed substantial monomer conversion and decent control for TTCs with a tertiary R group, whereas no polymerization occurred for TTCs with a secondary R group.[64] QC calculations combined with experiments revealed that an activation barrier exists for the dissociation of the C–S bond of a CTA anion intermediate, depending on the R group. Similar results were also reported by Kwon and coworkers.[65] Using Ag_2S nanocrystals (NCs) as a PC under red light irradiation (635 nm), PET-RAFT polymerization of methacrylates was achieved for TTCs (CDTPA), whereas no polymers were obtained for DTBs (CPADB). According to QC calculations, a significantly higher activation energy was obtained for the stepwise dissociation of the anion intermediate of CPADB compared to that of CDTPA (45.47 *vs.* 21.86 kJ mol^{-1}), implying that anion intermediates generated by photoinduced electron transfer play an essential role in the observed Z-group selectivity (Fig. 3).

Although OQPs mostly rely on photoinduced outer-sphere electron transfer (OSET) between the PC and CTA, Pan and coworkers recently reported PET-RAFT polymerization based on photoinduced ion-pair ISET (IP-ISET) (Scheme 3).[59] The authors demonstrated successful PET-RAFT polymerization of various vinylic monomers under visible-light irradiation in the presence of a zwitterionic borane catalyst ($[L_2B]^+X^-$) and CTA. Based on QC calculations combined with experiments, $[L_2B]^+[ZCS_2]^-$ generated *in situ* from $[L_2B]^+X^-$ and CTA was considered to be an active catalytic species. The stability of $[L_2B]^\bullet$ formed by ion-pair electron transfer and the very long excited-state lifetime of $[L_2B]^{+}*$ allowed the reaction to proceed well even at extremely low catalyst concentrations as low as 1 ppb, which is approximately three orders of magnitude lower than those of OSET-based systems. Unlike the

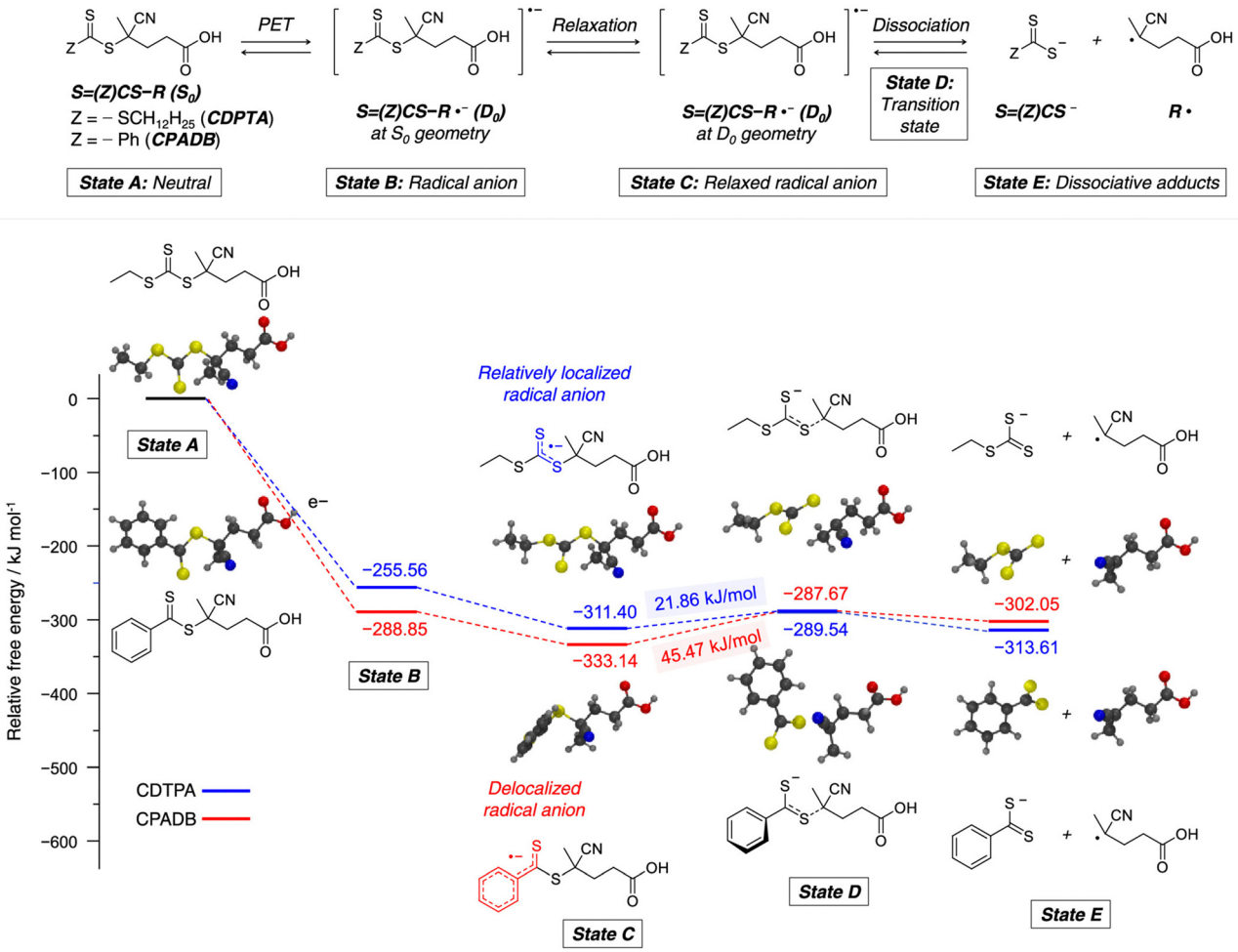

Fig. 3 Calculated energy profiles for stepwise dissociation of anion intermediates of CDTPA (blue) and CPADB (red). Adapted with permission from ref. 65 (Copyright 2023 American Chemical Society).

reported PET-RAFT polymerization, this method showed excellent tolerance to phenolic radical inhibitors, owing to the strong hydrogen bond between the phenolic group of the inhibitor and X^- of $[L_2B]^+X^-$.

2.2.1.2. Electron transfer: reductive quenching pathway (RQP). The RQP involves reduction of an excited-state PC by adding a sacrificial reducing agent (Scheme 2b). A one-electron-reduced PC ($PC^{\bullet-}$) is initially formed through electron transfer from a sacrificial reducing agent to an excited-state PC. Subsequently, one electron was transmitted from $PC^{\bullet-}$ to the CTA, generating propagating radical species and a TCT anion through a TCT anionic intermediate. In 2015, Boyer and coworkers proposed PET-RAFT polymerization *via* RQP using a tertiary amine as a sacrificial reducing agent.[66] This protocol provided faster kinetics and enhanced oxygen tolerance without severely sacrificing controllability compared to PET-RAFT polymerization *via* OQP (*i.e.*, in the absence of tertiary amines). Since this report, PET-RAFT polymerization *via* RQP has been widely used when fast polymerization kinetics under ambient conditions, such as polymerization under biorelevant conditions, are required.[67–70]

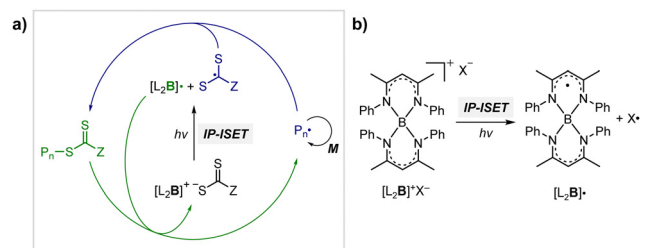

Scheme 3 (a) Mechanism of PET-RAFT polymerization based on photoinduced inner-sphere electron transfer (ISET). (b) Chemical structures of $[L_2B]^+$ and $[L_2B]^{\bullet}$.[59]

At approximately the same time in 2015, the use of tertiary amines in photocontrolled RAFT polymerization in the absence of PCs was proposed by Qiao and coworkers (Scheme 4).[71] Herein, the CTA directly absorbed light and tertiary amines, as a catalyst, reduced the excited-state CTA. This electron transfer from the tertiary amine to the excited-state CTA generated the anionic intermediate of the CTA, which then underwent fragmentation to provide a propagating radical and a TCT anion. Qiao and coworkers used 365 nm UV LEDs as the light source, and Konkolewicz and coworkers later demonstrated that the polymerization could proceed properly under visible light

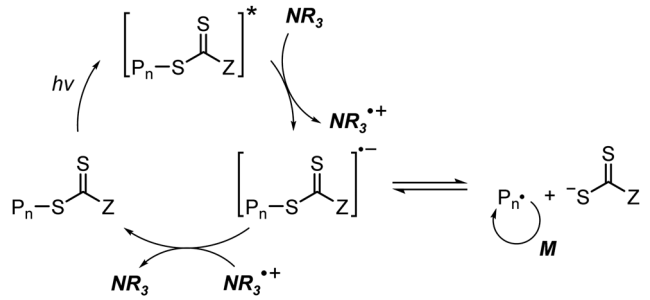

Scheme 4 Mechanism of tertiary amine-catalyzed generation of the TCT anion in the absence of a PC.

(<530 nm).[72] It is noted that this mechanism of tertiary amine-catalyzed generation of the TCT anion in the absence of a PC cannot be excluded in PET-RAFT polymerization *via* RQP, which complicates a complete understanding of the polymerization results.

In PET-RAFT polymerization *via* RQP, the polymerization features, such as the rate of polymerization, oxygen tolerance, and controllability, were found to be sensitive to the type[73] and amount of tertiary amines,[71,72] as well as the irradiation wavelength.[57] This sensitivity likely arises because the rate of electron transfer from a tertiary amine to an excited-state PC (or an excited-state CTA) relies on the amount and redox potentials of the amine. Furthermore, one-electron-oxidized tertiary amines may cause various side reactions by providing hydrogen and/or generating reactive α-amino radical species,[74,75] leading to poor controllability. However, the effects of tertiary amine intermediates on the polymerization have not been thoroughly analyzed and hence, combined efforts involving QC calculations, kinetics simulations, and chromatographic analyses are required.

2.2.1.3. Energy transfer. An alternative pathway involves photoinduced energy transfer, in which energy is transferred from an excited-state PC to a CTA, promoting the CTA to an electronically excited state. Then, active propagating radicals are generated *via* homolytic C–S bond cleavage of the excited-state CTA (Scheme 2c). Energy transfer is likely to occur from the T_1 state of the PC to the triplet excited states of the CTA.

Energy transfer is a photophysical process by which energy is transferred from one molecular entity (donor, D) in an excited state to another molecular entity (acceptor, A) to be raised to a higher energy state. The process can be distinguished into three types:[76,77] primitive energy transfer by emission-reabsorption, Förster resonance energy transfer, and Dexter energy transfer. In photocatalysis of organic molecules, Dexter energy transfer is of predominant relevance.[77] As Dexter energy transfer is based on simultaneous electron exchange between D and A, which requires the overlap of the wavefunctions, the energy transfer occurs over very short distances within approximately 10 Å, which approaches the collisional diameter.[78,79] In addition, the electron exchange is governed by the Wigner spin conservation rule and hence, the spin-allowed processes are single–singlet and triplet–triplet energy transfer. Among these, triplet–triplet energy transfer is preferred owing to the typically longer lifetime of triplet states compared to singlet states. The longer lifetime increases the probability of collisions. Because this is essentially an electron transfer process, the kinetics can be described using Marcus theory.[80] Therefore, the rate of Dexter energy transfer is strongly influenced by the thermodynamic driving force, reorganization energy, and electronic coupling between D and A; nevertheless, in the synthetic community, the thermodynamic driving force (*i.e.*, the energy gap between the lowest triplet state of D and A) is mostly utilized to estimate the energy transfer efficiency because the reorganization energy and electronic coupling are rather difficult to measure. When the thermodynamic driving force is large as in exergonic energy transfer, the energy transfer gets faster close to the diffusion limit. The studies on the energy transfer pathway in PET-RAFT polymerization are discussed in the next section.

2.2.1.4. Mechanistic understanding of PET-RAFT polymerization. The important debate with respect to the mechanism of PET-RAFT polymerization is how an excited-state PC interacts with a CTA: *via* either electron transfer or energy transfer. Substantial research efforts to answer this difficult question have been continuously made until recently, and these efforts are well summarized in a recent review article by Konkolowicz and coworkers.[48] Smith and coworkers supported an electron transfer mechanism based on calculations of the energetics of selected PCs (ZnTPP and pheophorbide A (PheoA)), various CTAs, and charge-transfer complexes that can be formed between them.[81] Falvey and coworkers also supported an electron transfer mechanism based on studies using laser flash photolysis for (i) triplet–triplet energy transfer between a triplet sensitizer (*e.g.*, anthraquinone, Rose Bengal, and benzophenone) and a CTA, and (ii) subsequent decomposition of an excited-state CTA.[82] Although energy transfer from the sensitizer to the CTA was efficient, decomposition of the CTA was rarely observed, suggesting that radical generation by energy transfer is rather limited compared to radical generation by electron transfer. Very recently, Kwon and coworkers successfully resolved the mechanistic complexity of PET-RAFT polymerization by using appropriately designed Ag_2S NCs as a PC.[65] Owing to the small bandgap and moderate E^*_{ox} of the Ag_2S NCs, PET-RAFT polymerization proceeded solely through electron transfer. Successful polymerization of methyl methacrylate (MMA) in the presence of Ag_2S NCs confirmed that the electron transfer readily occurs in PET-RAFT polymerization. However, it is noteworthy that the mechanism depends on the type of PCs. In the case of $[Ru(bpy)_3]^{2+}$ and $Ir(ppy)_3$, the research groups of Allonas and Boyer[83,84] and Konkolewicz[85] provided evidence for an energy transfer process. Allonas, Boyer, and coworkers calculated the Gibbs free energy change during electron transfer (ΔG_{ET}) and triplet–triplet energy transfer (ΔG_{EnT}) based on the redox potentials and triplet energies of PCs and a series of CTAs obtained from QC calculations and CV measurements.[83,84] ΔG_{ET} and ΔG_{EnT} were then plotted against the rate constant for quenching (k_q) of an excited-state PC obtained from laser flash photolysis experiments. A substantial correlation was observed between k_q and ΔG_{EnT}, whereas no relationship was found between k_q and ΔG_{ET}, suggesting that energy transfer likely

occurs between an excited-state PC and a CTA. Konkolewicz and coworkers also supported an energy transfer mechanism based on the simulation results of polymerization kinetics.[85] Using PET-RAFT polymerization of MA using $Ir(ppy)_3$ and TTC as a model system, the kinetics data obtained by experiment were compared with the data simulated using kinetic models of possible PET-RAFT mechanisms. Among them, the energy transfer mechanism was found to be the best fit.

In addition to the abovementioned issue, several issues remain unsolved, as introduced by Konkolewicz and coworkers.[48] First, the mechanism of electron transfer during OQP needs to be reconsidered. According to the current mechanism where the TCT anion is mainly involved in the regeneration of the ground-state PC, PET-RAFT polymerization could be significantly retarded or even stop at very low catalytic loading of the PC, as demonstrated by Konkolewicz and coworkers.[85] This finding is inconsistent with the previously reported experimental results. As such, in-depth studies are required to determine which pathways are involved in the reduction of oxidized cationic PC intermediates. Second, more in-depth understanding of the overall picture of what drives electron or energy transfer is required. The experimental results thus far suggest that the mechanism is dependent on the reaction system composition (*i.e.*, combination of PC, CTA, and monomer), whereas the exact mechanistic background remains unknown. Third, the fate of TCT radicals, which can be generated in PET-RAFT polymerization *via* energy transfer or photoiniferter polymerization, needs to be understood better. Herein, excessive TCT radicals could be accumulated by the termination of propagating radical species, as observed for TCT radicals generated by electron transfer, consequently leading to significant rate retardation. However, this retardation was not observed in the experimental studies and could be related to the formation of disulfide compounds that have not been much investigated. Fourth, the process of C–S bond dissociation in the energy transfer process remains unclear. As studied by Falvey and coworkers, C–S bond dissociation of the CTA in the triplet excited state was not sufficiently efficient to drive polymerization.[82] However, the study was performed in the absence of a monomer and thus, additional experiments in the presence of a monomer are necessary to draw a clear conclusion. Last, the direct spectroscopic observation of essential intermediates such as one-electron-oxidized/reduced PC, TCT anions, and TCT radicals would help to unambiguously identify the underlying mechanisms.

2.2.2. Photoiniferter polymerization

2.2.2.1. Basic mechanism. Photoiniferter polymerization under UV light irradiation, firstly proposed by Otsu and coworkers in 1982 as a type of RDRP,[39,86] has garnered renewed interest since Boyer,[32] Qiao,[33] and coworkers separately expanded the energy source of polymerization to visible light. Herein, a TCT-based CTA is a key agent that simultaneously acts as an initiator, a transfer agent, and a reversible terminator (ini-ferter), thereby eliminating the need for a PC or an exogenous initiator. As depicted in Scheme 5, the CTA directly absorbs light to become an excited state, which is followed by the homolysis of the C–S bond to produce an active initiating/propagating radical and a persistent TCT radical.[56] The propagating radicals can participate in degenerative chain transfer, a key mechanistic aspect of RAFT polymerization, and the TCT radical can deactivate active radical species in a reversible fashion as seen in ATRP. As this process requires the absorption of light by the CTA, the irradiation wavelength for photoiniferter polymerization is quite limited in contrast to PET-RAFT polymerization.

2.2.2.2. Mechanistic understanding of photoiniferter polymerization. The most essential issue in photoiniferter polymerization is to clearly understand the mechanism of photolysis of the C–S bond, an important process that determines the concentrations of radicals and CTAs during polymerization. Recently, Konkolewicz and coworkers reported that the rate of photoiniferter polymerization of MMA was significantly affected by the Z group of DTBs.[87] The rate of polymerization was nicely correlated with the redox potentials of CTAs, implying that the homolysis of the C–S bond is closely related to the electronic properties of CTAs. Falvey and coworkers suggested that higher singlet excited states such as S_2 states are involved more in the photolysis than S_1 or T_1 states based on energetics considerations.[82] Although these studies provided useful mechanistic insights into photolysis of the C–S bond, a precise understanding of the entire process of photoiniferter polymerization is still lacking and is expected to be provided through advanced QC calculations combined with well-designed experiments. For example, Kwon, Min, and coworkers very recently proposed that S_1/S_0 conical intersection (CI) acted as an activation barrier for photolysis of the C–S bond.[88] CDTPA under 515 nm irradiation (10 mW cm^{-2}) led to controlled and quantitative polymerization of MMA, whereas polymerization of MA provided adducts of $(MA)_n$–CDTPA rather than polymers. QC calculations of reaction intermediates proposed that relative

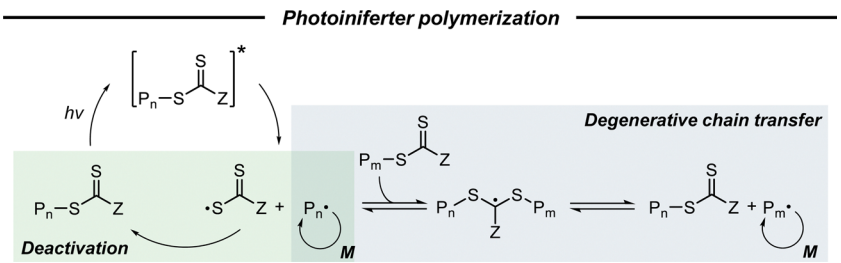

Scheme 5 Mechanism of photoiniferter polymerization.

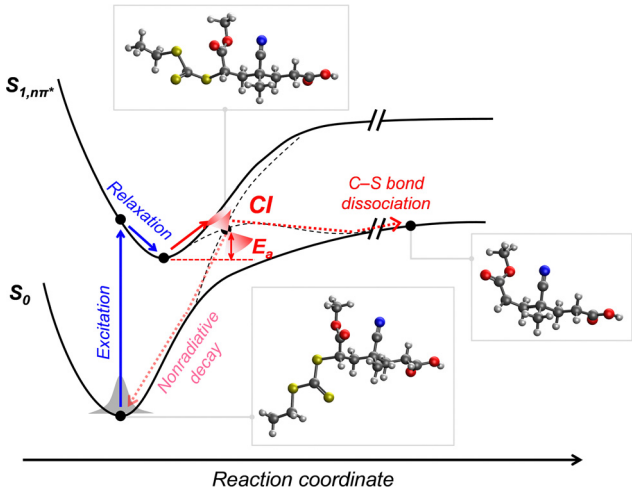

Fig. 4 Pathway for photolysis of the C–S bond in MA–CDTPA proposed by QC calculations.[88]

energies at the adiabatic S_1 state, CI, and after dissociation were critical for the observed monomer–CTA selectivity (Fig. 4). Energy profiles for the process from Frank–Condon excitation, structural relaxation, and CI were similar for adducts of both monomers, whereas energy profiles for the process from CI to bond dissociation were more favorable in MMA–CDTPA due to the large stabilization energy of generated radicals. Other possible processes from CI include nonradiative decay channels, hindering the C–S bond photolysis and subsequent polymerization.

Next, two different mechanisms (*i.e.*, degenerative chain transfer and reversible deactivation) can affect the control of RAFT polymerization, depending on the type of CTA employed in the reaction. These two mechanisms could jointly operate in the case of xanthate (with a low transfer constant).[56] In contrast, in the other study using TTC (with a higher transfer constant), preliminary calculations suggested that the reversible deactivation did not contribute primarily to the control over polymerization.[89] Quantitative analysis of the contribution of two mechanisms needs to be provided by further investigation using experimental and theoretical studies.

Lastly, as in PET-RAFT polymerization, the fates of the CTA and the corresponding TCT radical need to be clarified. Although the photodegradation of TCT groups under UV light irradiation with high energy has been reported,[19,26] the case under visible-light irradiation with low energy has not been observed.

2.2.3. Photomediated cationic RAFT polymerization and others

2.2.3.1. Photomediated cationic RAFT polymerization. Cationic RAFT polymerization was firstly reported by the research group of Kamigato[41] and Sugihara.[42] Herein, in the presence of protonic acid initiators to protonate a CTA, the fragmentation of the CTA cation generated carbocations as propagating species, which were polymerized in a controlled fashion *via* degenerative chain transfer. Fors and coworkers then developed a photomediated version of cationic RAFT polymerization by introducing highly oxidizing 2,4,6-tris(*p*-methoxyphenyl)pyrylium tetrafluoroborate as a PC to oxidize a CTA and generate a carbocation (Scheme 6).[43] One-electron oxidation of the CTA by the excited-state PC upon irradiation was followed by mesolytic cleavage of the resulting CTA radical cation to yield the CTA radical and carbocation as propagating intermediates. Similar to conventional cationic RAFT polymerization, the polymerization was controlled *via* degenerative chain transfer. The use of a PC provided additional regulation over the propagation step by photo-reversible generation of the carbocation. Reduction of the CTA radical by the one-electron-reduced PC generated the CTA anion and PC, which capped the carbocation chain-end and closed the catalytic cycle. Therefore, the photocontrolled behavior of polymerization (*i.e.*, the generation of the propagating carbocation and thus polymerization only proceed under light irradiation) could only be provided by a PC that possessed proper E^*_{ox} and E^0_{red} for favored one-electron oxidation of the CTA and reduction of the CTA radical, respectively.[90] Based on the investigation of the detailed mechanism using selected PCs and CTAs, Fors and coworkers concluded that in the case of pyrylium derivatives, a singlet excited state might involve electron transfer as the low fluorescence quantum yield (Φ_{FL}) of the PC led to a lower polymerization rate. The concern over the direct oxidation of the monomer instead of the

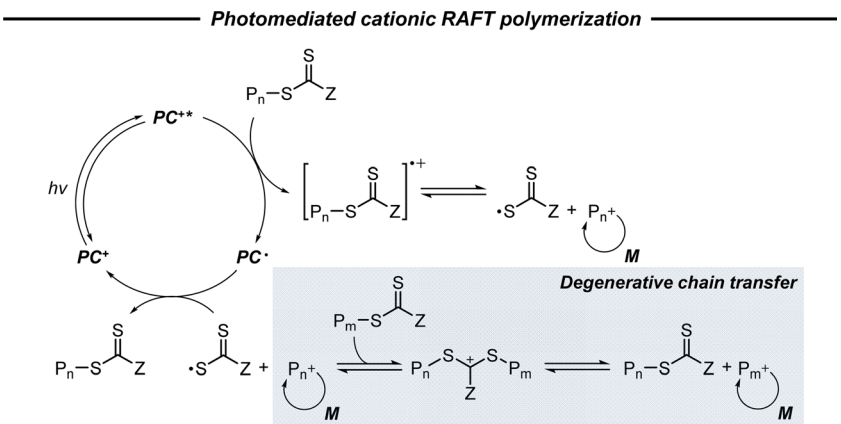

Scheme 6 Mechanism of photomediated cationic RAFT polymerization.

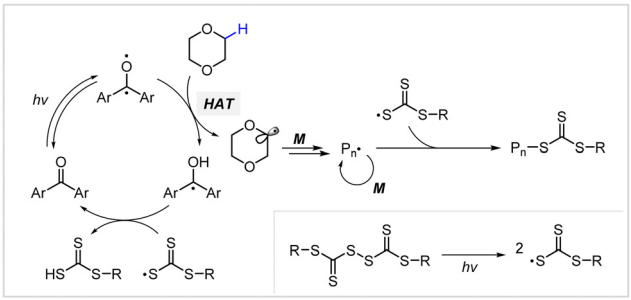

Scheme 7 Mechanism of hydrogen atom transfer (HAT)-mediated photomediated cationic RAFT polymerization.[60]

CTA by the excited-state PC was also resolved by Stern–Volmer analysis and CV measurements. Both the CTA and isobutyl vinyl ether (iBVE) monomer could be oxidized, but it was revealed that the oxidation of the CTA was favored by lower E^0_{ox}. The bimolecular quenching constant between the excited-state PC and CTA determined by Stern–Volmer analysis was two orders of magnitude higher than that between the PC and iBVE. Lastly, E^0_{red} of the PC was important for efficient capping of the propagating chain-end and deactivation of polymerization, providing perfect temporal control.

2.2.3.2. Hydrogen atom transfer (HAT)-mediated photomediated RAFT polymerization. Fors and coworkers introduced a HAT manifold into photomediated RAFT polymerization.[60] Herein, a benzophenone analogue capable of Norrish type II reaction was used as a PC and TTC-derived disulfide was used as a CTA precursor, unlike in conventional PET-RAFT polymerization. Under irradiation using a compact fluorescent lamp (CFL), the PC absorbed light to generate a PC intermediate with diradical character (Scheme 7). This PC intermediate abstracted the C–H bond of the substrate through hydrogen abstraction, and the resulting radical intermediates of the substrate initiated the polymerization. On the other hand, the disulfide generated two TCT radicals through S–S bond homolysis. One TCT radical was combined with the propagating radical to generate a macro-CTA, whereas the other TCT radical reacted with the PC intermediate, ketyl radical derived from benzophenone, to generate trithiocarbonic acid and regenerate the PC. As stated by the authors, this method will be useful to graft CTA moieties into hydridic C–H bonds of substrates (*e.g.*, biomolecules and backbone of commodity polymers) for subsequent polymerization.

3. Distinct features

In addition to the use of green and abundant visible light as an energy source, the distinct features of visible-light-driven RAFT polymerization endow the reaction system with controllability and the synthesized polymers with structural diversity, functionality, and excellent livingness, which otherwise are not realizable *via* conventional thermally initiated reactions. These features are attributed to the abovementioned mechanisms and can be primarily categorized into (i) spatiotemporal control, (ii) selectivity, (iii) orthogonality, and (iv) oxygen tolerance. It is noted that PET-RAFT polymerization distinctly demonstrates all four features. As active species are generated by light irradiation, spatiotemporal control is commonly achieved regardless of the polymerization mechanism (Section 3.1). Except for photomediated cationic RAFT polymerization, in PET-RAFT and photoiniferter polymerizations, active species are radicals so that the reactions can simultaneously occur with other reactions possessing different (such as ionic) intermediates and can be orthogonally controlled by turning the light on/off (Section 3.3). Meanwhile, the other two features (*i.e.*, selectivity and oxygen tolerance) have mainly been examined for PET-RAFT polymerization and still remain elusive for other methods.

3.1. Spatiotemporal control

Every photomediated RAFT polymerization operates by the absorption of light by either a PC or a CTA, and is therefore inherently a spatiotemporally controlled process that only occurs where and when the light is irradiated. Perfect temporal control directs the mechanism of the reaction toward a photocontrolled process necessitating the use of light and compounds that appropriately absorb light and play the role. For example, imperfect control or increase in monomer conversion even without light irradiation, which has been observed in some photomediated cationic RAFT polymerizations, has been ascribed to the decomposition of the PC or slow deactivation of the CTA owing to improper balance between ground- and excited-state redox potentials of the PC and CTA.[43,90–92] Slow deactivation of the CTA results in longer lifetime of active propagating species such that these species remain after the cessation of irradiation and consume monomers. This loss of control caused by the remaining radicals, however, can be utilized to induce latent RAFT polymerization in the dark using the energy stored during precedent irradiation.[93] Here, eosin Y (EY)-mediated photoinduced conversion of triplet oxygen into singlet oxygen which was then reduced by ascorbic acid in the dark generated the initiating hydroxyl radical.

On the other hand, PET-RAFT polymerization can be temporally switched by other stimuli (*e.g.*, temperature, pH, atmosphere, external magnetic field, and chemical reagents) in combination with light under which the photocatalytic activity of the PC is reversibly controllable (Fig. 5). The listed examples of dual-gated polymerizations have significant prospects for industrial applications as they offer additional means of control other than light and/or easy separation of PCs from the polymerization mixture for reuse.

Johnson and coworkers embedded 10-phenylphenothiazine (PTH) in a poly(*N*-isopropylacrylamide (NIPAm))-based gel in which at temperatures above the lower critical solution temperature (LCST), the PC could not be accessed by light and other reagents, and consequently the polymerization could not proceed (Fig. 5a).[94] Polymerization only proceeded at temperatures below the LCST and under light irradiation. In contrast, in nanocomposites composed of cross-linked hyperbranched polyglycerol, polyfluorene backbones decorated with poly(NIPAm)

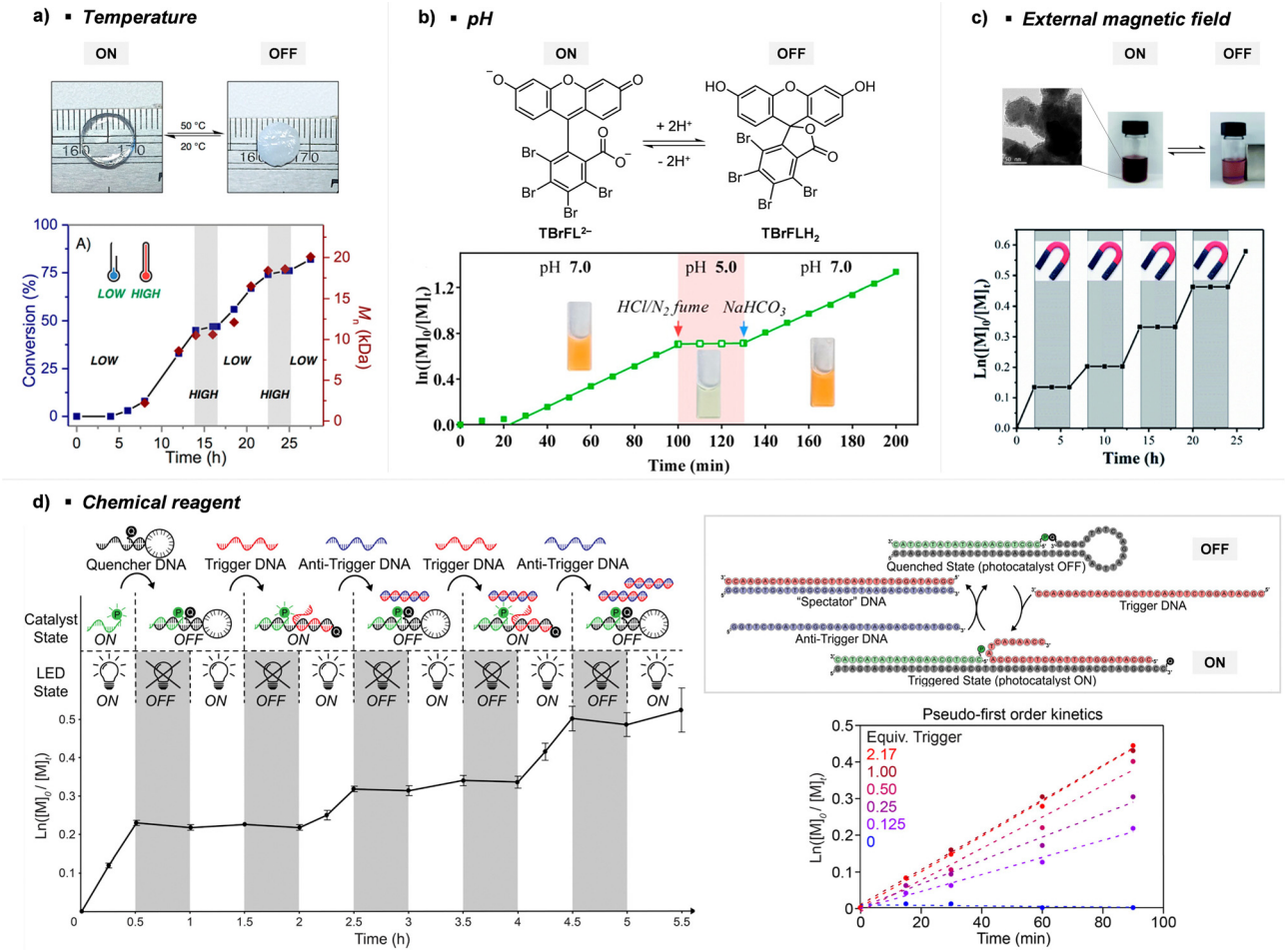

Fig. 5 Temporal control of PET-RAFT polymerization by various stimuli other than light: (a) heat, (b) pH, (c) external magnetic field, and (d) chemical reagents. Adapted with permission from (a) ref. 94 (Copyright 2017 American Chemical Society), (b) ref. 96 (Copyright 2019 American Chemical Society), (c) ref. 103 (Copyright 2020 The Royal Society of Chemistry), and (d) ref. 104 (Copyright 2023 American Chemical Society).

brushes, and $Ru(bpy)_3Cl_2$, heat-driven shrinkage of poly(NIPAm) chains generated open pores for reagents to enter and polymerization proceeded.[95]

Boyer and coworkers discovered a pH-switchable xanthene-based PC TBrFL (Fig. 5b).[96] Because of the pH-responsiveness of xanthene dyes, at pH = 5, TBrFL became colorless and inactive to catalyze PET-RAFT polymerization, whereas at pH = 7, the original visible-light absorption property was restored to turn on the reaction. pH was lowered by adding gaseous HCl/N_2 or CO_2 and was recovered by $NaHCO_3$ or N_2, respectively. This pH-responsive photocatalytic performance of xanthene dyes was retained in heterogeneous PCs where Erythrosin B (EB) and Rose Bengal were conjugated to porous polymers.[97] $ZnTPPS_4^-$ demonstrated pH-dependent polymerization kinetics.[98] The polymerization kinetics were retarded by lowering the pH of the reaction mixture from 8.6 to 3.5. This was presumably because higher concentration of the hydroxide ion at higher pH weakened the coordination of the zinc core of $ZnTPPS_4^-$ with the CTA or monomer and promoted the absorption of light by $ZnTPPS_4^-$ and subsequent polymerization, as evidenced by the higher molar absorption coefficient of the reaction mixture at irradiation wavelength. In contrast, ZnOETPP exceptionally utilized oxygen for the polymerization process so that polymerization did not occur in the presence of CO_2 or N_2.[99] This role of oxygen contradicted its conventionally recognized role of inhibiting polymerization by scavenging the propagating radicals (for a detailed explanation, please see Section 3.4). Copolymerization of macrocyclic allylic sulfones with acrylate and acrylamide monomers was reversibly switched by alternate introduction of Ar and SO_2.[100] During radical ring-opening cascade polymerization, macrocyclic allylic sulfones release SO_2 and the resulting secondary alkyl radicals participate in propagation. However, the gradually accumulated SO_2 in the reaction system recombined with the alkyl propagating radicals and inhibited polymerization in the late stages particularly at low reaction temperature. Density functional theory (DFT) calculations and electron paramagnetic resonance (EPR) spectroscopy evidenced that Gibbs free energy change upon extrusion and recombination of SO_2 from the monomer was relatively small such that SO_2 could negatively affect the polymerization behavior. Thus, the introduction of Ar re-initiated the SO_2-inhibited polymerization, whereas the introduction of exogenous SO_2 switched off the polymerization.

The hybrid nanocomposites of magnetic Fe_3O_4, silica, and PCs ($Ir(ppy)_3$[101] and ZnTPP[102]) reported by Cai, Zhang, and coworkers or γ-Fe_2O_3 nanoparticles (NPs) doped with carbon dots reported by Qiao, Pang, and coworkers[103] were responsive to an external magnetic field. Upon applying a magnetic field, these nanohybrid PCs exhibited agglomeration and could not catalyze polymerization. This was attributed to the reduced visible-light absorption and limited access and electron transfer between PCs (bound to the surface of the nanocomposites) and CTA (Fig. 5c).

Lastly, Martell and coworkers conjugated DNA aptamers and a quencher dye with EY to switch on the photocatalytic activity of EY by adding chemical reagents that could be hybridized with the DNA (Fig. 5d).[104] As absorption of the quencher dye overlaps with emission of EY, fluorescence and photocatalytic activity of EY were switched off when the quencher dye and EY were in proximity through static quenching and Förster resonance energy transfer (FRET). The added chemical reagent noncovalently hybridized with the DNA to induce a conformational change, remove the proximity between the quencher dye and EY, and switch on the photocatalytic activity of EY. In particular, when trigger DNA was used as the chemical reagent, anti-trigger DNA with complementary sequences could inactivate the trigger DNA resulting in double-stranded spectator-DNA and a photocatalytically inactivate PC. Therefore, the activity of the PC could be reversibly switched, and the polymerization rate could be modulated by the amount of trigger-DNA relative to that of quencher-DNA. As sequences and secondary structures of DNA aptamers can be designed to specifically fit diverse trigger molecules such as glucose, hydrocortisone, and zinc ions, these switchable DNA–PC conjugates were expected to be expanded to various PCs and chemical reagents, only if appropriate pair of PC and quencher dye possessing overlapping emission and absorption spectra could be identified.

3.2. Selectivity

For successful photocontrolled RAFT polymerization, effective photolysis of the CTA (activation), insertion of the monomer, and deactivation of the CTA are required. It has been shown that each step is highly selective toward reagents and reaction conditions. First of all, the irradiation wavelength should match the absorption profile of either PC or CTA (depending on the type of polymerization) for their excitation. In PET-RAFT polymerization the (de)activation of the CTA by the PC at the initiation stage and that of the CTA with monomers inserted at the propagation stage are mainly governed by thermodynamic constraints where the reactivity of the excited-state PC is determined by the energy absorbed at the irradiation wavelength. In addition to irradiation at the appropriate wavelength, selectivity of the PC toward the CTA and selective insertion of the monomer into the CTA have been observed. These selectivity issues can be leveraged to prepare polymers with desired sequences and complex architectures.

3.2.1. Selectivity of the PC toward the CTA. After successful excitation of the PC, selectivity in the transfer of electron or energy from the excited-state PC to the CTA arises from selective interaction between the PC and the CTA. Specific coordination of zinc of ZnTPP to a TTC resulted in photoinduced reduction of BTPA (a TTC) than CPADB (a DTB) despite the lower E^0_{red} of BTPA.[105] Upon changing the solvent from dimethyl sulfoxide (DMSO) to *N*,*N*-dimethylformamide (DMF) which competes with BTPA for the coordination, the coordination between ZnTPP and BTPA was reduced to retard the polymerization. On the other hand, interaction of CPADB with PheoA probably due to hydrogen bonding between its acid group and pyrrole of PheoA was evidenced by NMR and UV/Vis spectroscopy.[106] These selective interactions were considered to enhance electron transfer by the proximity effect. Later, Smith, Seal, and coworkers theoretically investigated these experimentally observed selectivity trends based on QC calculations using DMSO as a model solvent.[81] The authors ruled out the energy transfer pathway and considered that electron/charge transfer from the S_1 state of the PC to CTA was the crucial step for CTA activation, which would be facilitated by the favored precomplexation of the PC and CTA. From the analysis of the excited-state molecular orbitals of PC–CTA complexes, the selectivity of ZnTPP toward TTC and that of PheoA toward CPADB were indicated by the lowest energy gap between the initial optically excited state and the charge-transfer state along with the facilitated perturbative coupling between these two states, which enhanced electron transfer. Combined with the intrinsic monomer compatibility of the given CTA,[37] careful design of the reaction system using a mixture of multiple pairs of PC, CTA, and monomer that could be selectively activated at distinct irradiation wavelengths (Scheme 8) enabled the facile

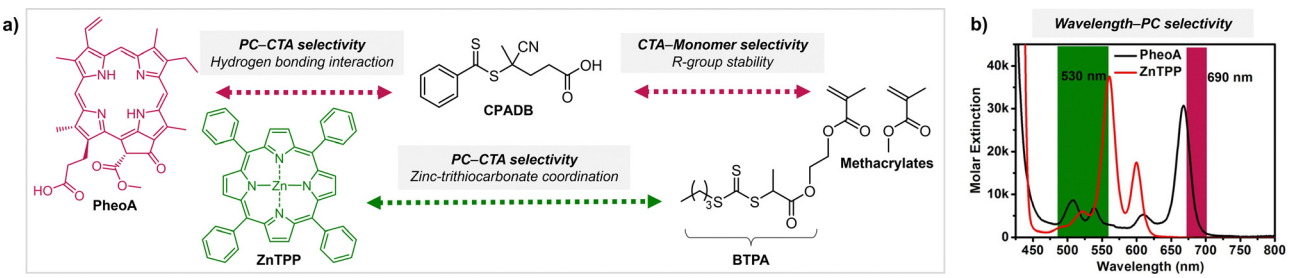

Scheme 8 (a) Selectivity issues in PET-RAFT polymerization from a reaction mixture of two PCs (PheoA and ZnTPP), two CTAs (CPADB and BTPA), and methacrylate monomers. The two PCs can be selectively activated at different wavelengths as per (b) UV-vis absorption profiles. Adapted with permission from (b) ref. 106 (Copyright 2016 American Chemical Society).

synthesis of well-defined graft copolymers,[106] as discussed in Section 4.3.2. For selective activation, irradiation wavelengths at which the absorption profiles of two PCs do not overlap are required. Selective activation of a certain PC and concomitant selective polymerization of the monomer that is compatible with a certain CTA can be achieved even in a mixture of all reagents. However, it is noted that the time of monomer addition should be carefully considered, as certain monomers, once reacted, block the successive insertion of the other type of monomers, leading to failed polymerization.

3.2.2. Selective insertion of the monomer into the CTA. Such blocking of further propagation prevents the subsequent incorporation of upcoming monomers into the CTA, and thus is called single unit monomer insertion (SUMI). For successive polymerization, fragmentation of the propagating radical from the RAFT intermediate and additional insertion of the monomer are required. For example, after the insertion of MA into CPADB, the tertiary carbon radical of the R group of CPADB transformed into a less stable secondary radical that could no longer be activated by PheoA, whereas MMA with a tertiary carbon radical had no problem in polymerization.[106]

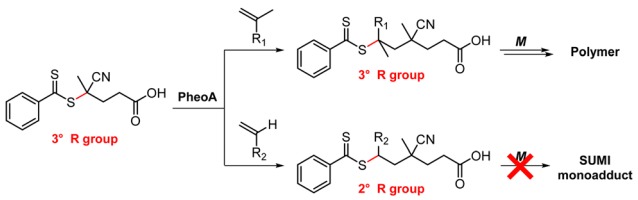

Scheme 9 Monomer-dependent selective photoactivation of CPADB.[106]

PheoA-catalyzed PET-RAFT polymerization for 20 hours of different monomers (typically 20 equivalents to CPADB) that yielded propagating radicals with secondary radicals, including styrene, acrylates, and acrylamides, other than methacrylates, all provided the same results (Scheme 9).[106] In contrast, AIBN-initiated RAFT polymerization afforded oligomeric products under otherwise identical reaction conditions, which was consistent with the previous studies which reported that AIBN was not a suitable initiator due to the possible formation of initiator-derived byproducts.[107] Furthermore, a very short reaction time was essential to prevent multiple insertions of monomers and to ensure high end-group fidelity if a certain number of SUMI reactions of different monomers had to be repeated.[108] Therefore, the unique selectivity of PET-RAFT and photoiniferter polymerizations even with mild reaction conditions and the absence of an exogenous initiator successfully afforded polymers with controlled monomer sequences of precisely positioned functionalities *via* SUMI.[109]

CTAs possessing the same Z group but different R groups can also be selectively fragmented. Matyjaszewski and coworkers in collaboration with Boyer reported that during photoiniferter polymerization of MMA in the presence of CDTPA and BTPA, only CDTPA was consumed for polymerization.[110] This was because the photolysis of CDTPA was favored owing to the higher stability and radical stabilization energy (RSE) of the tertiary R group, whereas BTPA with the secondary R group did not undergo fragmentation or participate in chain transfer with the poly(MMA) radical (Scheme 10a). The retarded polymerization rate upon the addition of an excess amount of BTPA or DTPA evidenced that both CTAs participated in the formation of the intermediate adduct radical, whereas only the adduct with CDTPA resulted in the fragmentation and release of the R group

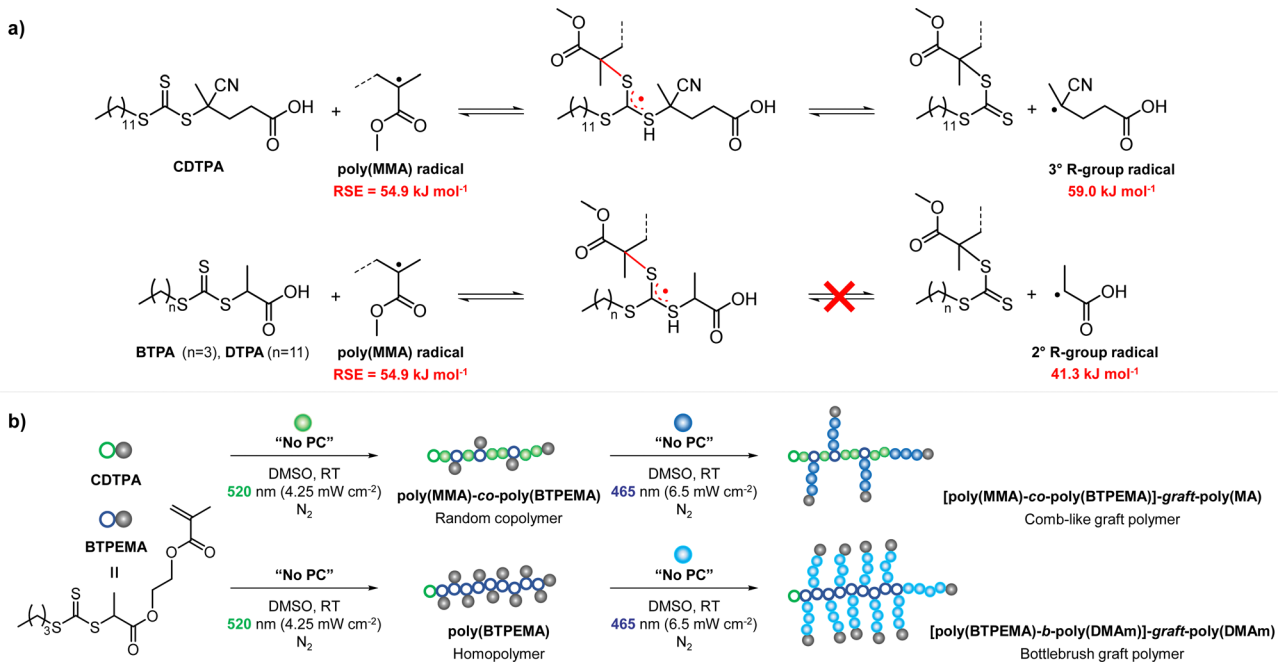

Scheme 10 (a) Selective fragmentation of CTAs after the addition of the poly(MMA) radical. (b) Stepwise synthesis of comb-like and bottlebrush polymers *via* selective fragmentation of CTAs under irradiation at different wavelengths.[110]

for propagation. By changing the irradiation wavelength from green (520 nm, 4.25 mW cm^{-2}) to blue (465 nm, 6.5 mW cm^{-2}), the remaining intact BTPA could be consumed for polymerization of MA or *N*,*N*-dimethyl acrylamide (DMAm) in which both the R group of the CTA and the monomer generated secondary R groups (Scheme 10b).

As it is the change in C–S bond stability and balance among the various possible reactions (*e.g.*, chain transfer, dissociation, propagation, and recombination) within the RAFT equilibrium that dictate the selectivity in the activation of the CTA to add a monomer, the existence of a PC is not necessary for the selective activation of the CTA and subsequent polymerization; nevertheless, the PC facilitates the reaction or allows upscale of the reaction system because of oxygen tolerance. For further discussion on SUMI and utilization of the unique selectivity of photocontrolled RAFT polymerization to confer polymers with complex architectures, please see Sections 4.3.1.2 and 4.3.2, respectively.

3.2.3. Overcoming the selectivity issue by heat. Very recently, Boyer, Liu, and coworkers reported that the selectivity issue could be overcome by heat.[64] In PET-RAFT polymerization of (meth)acrylates under NIR light irradiation (780 nm), MNCs selectively activated TTCs with tertiary R groups over TTCs with secondary R groups (Fig. 6a). Computational chemistry suggested that the oxidation capabilities of MNCs in their excited states were too low to transfer an electron to DTPA, a model CTA with the secondary R group. The leaving ability of the R group depends on bond dissociation energy and RSE. From intrinsic reaction coordinate (IRC) simulation to compare the energy barrier between either before or after the fragmentation of the CTA radical anion, and the transition state, DTPA, compared to CDTPA and DDMAT with the tertiary R group, was unlikely to favor the formation of the transition state and thus the fragmentation to initiate the polymerization (Fig. 6b). In contrast, poly(MA)$_{59}$-DTPA prepared by thermally initiated RAFT polymerization successfully underwent PET-RAFT polymerization along with a decrease in the Gibbs free energy of ~1 kcal mol^{-1} during one-electron reduction of the CTA, as the inserted monomer units did decrease the effect of the original R group. The authors further postulated that this energy barrier could be overcome by increasing the reaction temperature by 15 °C using a hot plate. The MNC-catalyzed PET-RAFT polymerization of MA from DTPA, which could not be realized, was achieved only after the heat-promoted photoactivation of DTPA in the initial state (Fig. 6c). It is noted that the revealed mechanistic origin of the unique selectivity of MNCs to a certain CTA would help overcome the abovementioned energy barrier, and consequently expand the applicability of PCs *via* the combined use of light and thermal energy.

3.2.4. Overcoming the selectivity issue by oxygen. Likewise, the energy barrier and thermodynamic constraints within the photocatalytic cycle limit the applicability of a certain PC for successful polymerization. PCs that absorb at long wavelengths particularly suffer from weak excited-state redox properties which thermodynamically restricts PET-RAFT polymerization *via* OQP or RQP. Therefore, it has been difficult to find

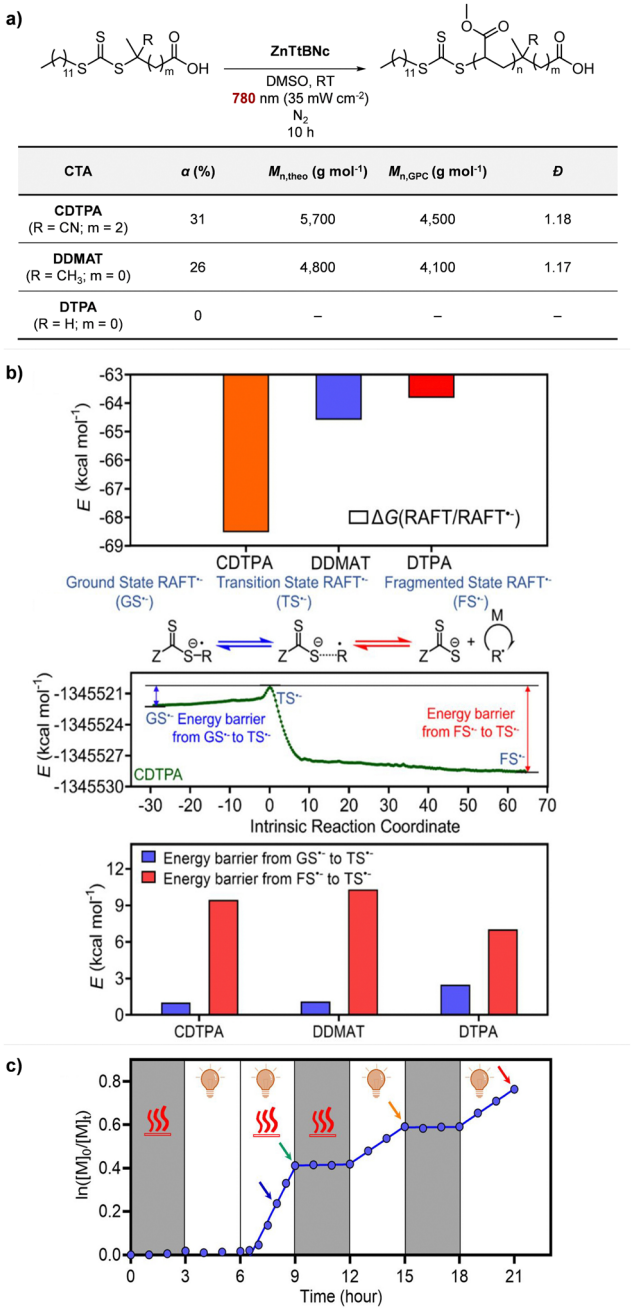

CTA	α (%)	$M_{n,theo}$ (g mol^{-1})	$M_{n,GPC}$ (g mol^{-1})	$Đ$
CDTPA (R = CN; m = 2)	31	5,700	4,500	1.18
DDMAT (R = CH_3; m = 0)	26	4,800	4,100	1.17
DTPA (R = H; m = 0)	0	–	–	–

Fig. 6 (a) PET-RAFT polymerization of MA. (b) Comparison of Gibbs free energy change, reaction path calculated by the IRC method, and energy barriers in CTA$^{\bullet-}$ fragmentation. (c) Heat-assisted photoactivation (at 52 °C) of DTPA for PET-RAFT polymerization of MA. Adapted with permission from ref. 64 (Copyright 2022 American Chemical Society).

appropriate PC candidates for polymerization under NIR light irradiation. In this regard, Boyer, Liu, and coworkers proposed a new oxygen-mediated pathway for PET-RAFT polymerization using NIR-light-absorbing (metallo)porphyrin and phthalocyanines as a PC, where the PC, oxygen, and triethylamine (TEA) synergistically provide thermodynamically favored electron transfer for one-electron-reduction of the CTA and subsequent polymerization.[111] This necessity of oxygen for successful and

well-controlled polymerization was contradictory to the conventional role of oxygen in inhibiting the reaction (for a detailed explanation, please see Section 3.4.3).

3.3. Orthogonality

Multiple reactions that can occur either individually or simultaneously in one pot without interfering with each other are said to be orthogonal. For example, in terms of the type of reactive species, PET-RAFT or photoiniferter polymerization with radical intermediates is orthogonal to the reactions, including (photomediated) cationic RAFT or anionic or cationic ring-opening polymerization (ROP), involving ionic intermediates. In terms of the energy source, light can be turned on and off without interrupting other stimuli. Moreover, light at certain wavelengths that can selectively activate one of the several combined organic photochemical reactions has paved the way for efficient synthesis of advanced functional materials through, for example, formation and post-modification of the polymer network and programmed patterning of given surfaces.[112–114] Therefore, researchers either orthogonally turned on and off the photomediated reversible (de)activation of the radicals produced from the PC and/or CTA to ionic polymerizations mediated by other stimuli (*e.g.*, heat,[115] electricity,[116,117] and the presence of specific reagents[118–122]) or selectively activated two photomediated polymerizations *via* irradiation at disparate wavelengths.[123–126]

This orthogonality that allows on-demand control of each polymerization system has been applied to the one-pot synthesis of polymers with complex architectures and compositions as discussed in Sections 4.3.1.1 and 4.3.2. By combining two orthogonal polymerizations, the scope of the monomers incorporated along the single backbone has widened. The microstructure of multiblock copolymers (*e.g.*, order, length, and number of blocks) could also be facilely manipulated by tuning the order and length of the applied external stimuli, and the number of switching between two polymerizations.

3.4. Oxygen tolerance

Due to its radical scavenging effect, oxygen is detrimental to radical polymerization and thus needs to be removed before the reaction. To conduct the reaction in the presence of oxygen, oxygen tolerance is of significant interest as the degassing process is time-consuming and limits the practicability of polymerization from both biological and industrial perspectives. Among the various photomediated RAFT polymerizations discussed herein, oxygen tolerance of PET-RAFT polymerization has been extensively recognized,[49,127] as compared to the cases of photoiniferter and photomediated cationic RAFT polymerizations. It is because inactivation of oxygen occurs *via* a photoinduced electron or energy transfer mechanism in the presence of the PC and/or any additives that play a supporting role (Section 3.4.1.1). In contrast, photoiniferter polymerization involving direct photolysis of the CTA lacks the ability to consume oxygen, and thus is intrinsically sensitive to oxygen. Therefore, in the reported studies, alternative approaches such as not stirring the reaction mixture or use of solvent with high viscosity and low oxygen solubility, to physically block the diffusion of oxygen into the polymerization mixture, or additives were employed. Every reported photomediated cationic RAFT polymerization has been performed in deoxygenated media, providing no hint towards oxygen tolerance of the reaction system. As cationic reaction intermediates are not affected by radical-scavenging oxygen, cationic polymerization is known to be insensitive to oxygen;[22,128] nevertheless, the impact of oxygen on photocatalytic systems needs to be investigated.

Meanwhile, in some cases, oxygen could in turn be transformed into an initiating source or even facilitate the activation of the CTA, which contradicts its known inhibitory role. These examples of oxygen-initiated or -accelerated polymerizations are discussed in Section 3.4.2. This section describes the three categories of oxygen tolerance reported to date in various polymerization reactions (Scheme 11).

It should be noted that, regardless of the type of mechanism, 'the presence of oxygen' can refer to the reaction being performed in either a completely 'open-to-air', 'sealed but not degassed' container or other containers where the volume of the remaining head space substantially affects the amount of oxygen and controllability of polymerization. In any case, oxygen tolerance has extended the applications of photocontrolled RAFT polymerization to 3D/4D printing or surface functionalization of given surfaces or biomolecules in which the deoxygenation

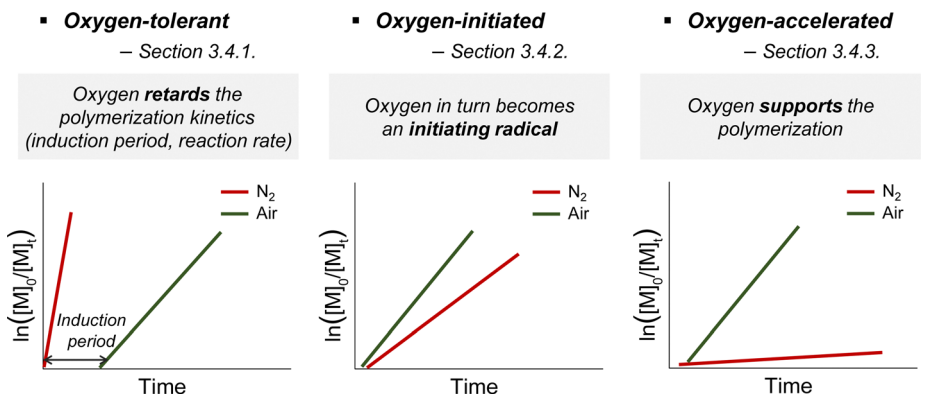

Scheme 11 Three categories of oxygen tolerance. Schematic representation of the kinetic plot of $\ln([M]_0/[M]_t)$ *vs.* reaction time in (a) oxygen-tolerant, (b) oxygen-initiated, and (c) oxygen-accelerated PET-RAFT polymerizations.

process can be time-consuming, cumbersome, or harsh to the substrate.

3.4.1. Oxygen-tolerant polymerization

3.4.1.1. PET-RAFT polymerization. Although the consumption of oxygen accompanies the induction period or slower polymerization kinetics as compared to the case in the absence of oxygen, the polymerization reaction would eventually proceed. Thus, well-defined polymers with high end-group fidelity in the presence of oxygen could be realized. The mechanism to achieve oxygen tolerance depends on the reaction system composition and the concomitant role of the excited-state PC as a reductant (*via* OQP) or an oxidant (*via* RQP). In brief, oxygen is reduced by the excited-state PC in OQP and by the ground-state anion of the PC in RQP. Photoinduced energy transfer from the triplet excited-state PC to triplet oxygen is another route for oxygen tolerance (Scheme 12).

Electron transfer: oxidative quenching pathway (OQP). Oxygen tolerance of PET-RAFT polymerization was discovered by Boyer and coworkers in 2014 in their first study of PET-RAFT polymerization using $Ir(ppy)_3$ as a PC.[31] Strongly reducing excited-state $Ir(ppy)_3$ was expected to reduce oxygen into a superoxide radical anion, which allows the polymerization in a non-degassed sealed vessel. The kinetics of the polymerization of MMA and MA in DMSO were almost identical to that in a degassed vessel after the induction period to consume oxygen, indicating no degradation of the PC or CTA. With the preserved photocatalytic activity and chain ends, a di- or tri-block copolymer was successfully synthesized by simply adding the monomer and solvent to the reaction mixture. $Ru(bpy)_3Cl_2$ with reducing property (E^*_{ox} = −0.81 V *vs.* SCE) similar to that of $Ir(ppy)_3$ (E^*_{ox} = −1.73 V *vs.* SCE) also exhibited oxygen tolerance for the polymerization of MA and DMAm in DMSO despite the retardation in polymerization kinetics in the presence of air.[129] It was attributed to the sluggish consumption of oxygen by the PC. Whereas the induction period was decreased with an increase in the catalyst loading, the polymerization rate was not significantly affected.

Electron transfer: reductive quenching pathway (RQP). In their first study of PET-RAFT polymerization using organic dyes, Boyer and coworkers observed that EY and fluorescein with lower $E^*_{ox}(PC^*/PC^{\bullet+})$ than $E^0_{red}(CTA/CTA^{\bullet-})$ and sufficiently low Φ_{FL} allowed effective PET and polymerization of methacrylates in DMSO under blue light irradiation.[66] The apparent propagation rate (k_p^{app}) which was lowered by oxygen was restored by adding TEA. The shortened inhibition period suggested that *via* RQP, the one-electron-reduced EY, generated by the reduction of excited-state EY by TEA, concurrently reduced oxygen to a superoxide radical anion and activated the CTA to allow polymerization without degassing. TEA of at least one equivalent to the CTA was required to completely reduce dissolved oxygen in the reaction vessel. The concentrations of TEA and EY were also important as the highly increased polymerization rate (*i.e.*, high radical flux and high catalyst turnover) led to an increase in polymer dispersity ($Đ$ = 1.4).[130] In addition to the tertiary amine, ascorbic acid (or ascorbate)[131–133] was added to the reaction system to induce reductive quenching of other PCs including $ZnTPPS_4^-$ [131,133] and poly(boron dipyrromethene-*alt*-fluorene),[132] and concomitant oxygen tolerance in the reaction system.

The study of the effect of tertiary amines on PET-RAFT polymerization using EY by Ferji and coworkers revealed that the stability of the amine radical cation impacted the efficiency of the reduction of excited-state EY, subsequent reduction of the CTA, and polymerization in DMSO in the presence of air.[73] Herein, the authors concluded that (i) oxygen tolerance originated from photoinduced conversion of oxygen to inactive singlet oxygen rather than from the reduction of oxygen to the superoxide radical anion and (ii) the tertiary amine facilitated the reduction of the CTA by preferably generating the EY radical anion. Among five amines (TEA, triethanolamine (TEOA), tributylamine, *N*,*N*,*N*′,*N*″,*N*″-pentamethyldiethylenetriamine (PMDETA), and 4-(dimethylamino)pyridine (DMAP)), tributylamine and DMAP increased the amine radical stability and conferred oxygen tolerance because of the long alkyl chain and π-bond conjugation, respectively, whereas TEOA in combination with EY produced an initiating radical even in the absence of a CTA to provide polymers with high dispersity.

To date, a variety of amines such as TEA,[134] TEOA,[67,135–140] *N*,*N*,*N*′,*N*′-tetramethylethylenediamine (TEMED)[141] and PMDETA[68–70] have been employed as cocatalysts with EY in various solvents for 3D printing resin, surface-initiated polymerization from proteins

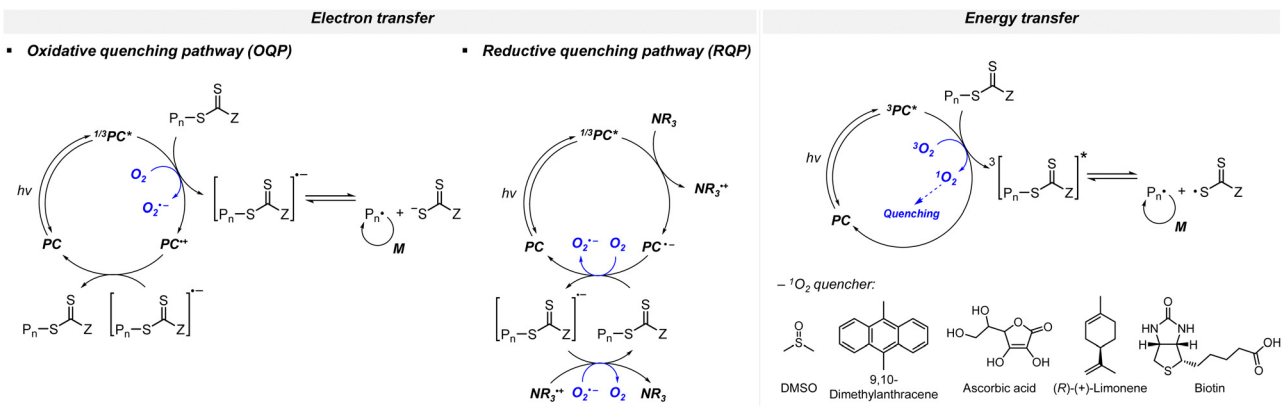

Scheme 12 Mechanisms of the three categories of oxygen tolerance in PET-RAFT polymerization.

and DNA, and polymerization in continuous flow reactors, where oxygen tolerance and accelerated polymerization kinetics are highly advantageous. Another xanthene-based organic PC EB/TEOA system was also employed for 3D printing in aqueous solutions without prior deoxygenation.[142] However, some reaction systems were still degassed despite the use of amines, and the reason for degassing and the results of negative controls such as polymerization without a PC, amine, or CTA were not provided, which hampered the elucidation of the exact role of an amine additive. Moreover, Boyer, Sumerlin and coworkers reported that the reaction mechanism became complicated depending on the reaction conditions (*e.g.*, irradiation wavelength, reagents, concentration, and solution pH) and concomitantly generated different reaction intermediates.[57]

Amine-facilitated reduction of oxygen was also reported for graphitic carbon nitride (g-C_3N_4).[143,144] Qiao and coworkers observed a significant decrease in the inhibition period (from 3 hours to 30 minutes) after the addition of TEOA into PET-RAFT polymerization of MA under UV light irradiation (365 nm, 3.5 mW cm^{-2}).[143] The efficient deoxygenation was ascribed to an additional pathway to reduce dissolved oxygen *via* g-C_3N_4-mediated electron transfer from TEA. Ferji and coworkers again examined the influence of the amount of amine on polymerization control.[144] In g-C_3N_4-catalyzed PET-RAFT polymerization of MMA as a model monomer in the presence of tributylamine under irradiation at 405 nm (60 mW cm^{-2}), loss of polymerization control was noticed when five equivalents of tributylamine relative to TTC were added. It was attributed to the production of species that could initiate free radical polymerization *via* the interaction of the oxidized amine with another amine. The authors thus set the appropriate molar ratio of amine to CTA as one.

Energy transfer. Oxygen can also be inactivated *via* the photoinduced energy transfer mechanism. Owing to the excitation of triplet oxygen to the singlet state *via* triplet–triplet annihilation with excited-state ZnTPP and subsequent consumption of singlet oxygen by DMSO to form dimethyl sulfone, the concentration of dissolved oxygen was kept sufficiently low to continue the polymerization of DMAm even under fully open conditions.[145] However, in other solvents with properties (*i.e.*, boiling point, molecular weight, and dielectric constant) similar to those of DMSO, polymerization became considerably slower with longer inhibition time, implying the intrinsic role of DMSO in the consumption of singlet oxygen. Therefore, to realize oxygen tolerance in other solvents, additives as singlet oxygen quenchers were necessary.[146] Among 9,10-dimethylanthracene, ascorbic acid, and (*R*)-(+)-limonene, 9,10-dimethylanthracene was the most effective additive, demonstrating similar kinetics to the polymerization with deoxygenation, a very short inhibition period, and excellent temporal control. ZnTMPyP, another water-soluble analogue of ZnTPP, with biotin was employed in the oxygen-tolerant aqueous dispersion polymerization of hydroxypropyl methacrylate (HPMA) for photoinitiated polymerization-induced self-assembly (photo-PISA) in a 96-well plate without deoxygenation.[147] Herein, the thioether group of biotin was oxidized to sulfoxide upon trapping of singlet oxygen. When the thioether group was a part of the monomer, polymerization of 2-(methylthio)ethyl methacrylate (MTEMA) bearing the thioether group using ZnTPP was oxygen-tolerant without any additives.[148] This oxygen tolerance of ZnTPP was also retained when embedded in 2D metal–organic framework (MOF) nanosheets.[149] Similarly, sodium ascorbate significantly reduced singlet oxygen in $Ru(bpy)_3Cl_2$-catalyzed rapid and controlled polymerization of acrylamides in water and enabled the facile preparation of triblock copolymers within an hour without deoxygenation.[150]

3.4.1.2. Photoiniferter polymerization. In the abovementioned mechanisms of conferring oxygen tolerance to PET-RAFT polymerization, oxygen is commonly consumed and inactivated *via* additional reaction pathways mediated by a PC with or without additives. In contrast, photoiniferter polymerization in which a reactive radical can only be generated by direct photolysis of the CTA innately suffers from rather slow reaction kinetics and is not tolerant to oxygen. Thus, oxygen tolerance has rarely been achieved.

For instance, TTC-based CTAs in the presence of tertiary amines could mediate polymerization under UV[71] or blue light irradiation[151,152] to prepare polymers in the absence of a PC. Energetically favored photoinduced electron transfer from the amine to the excited-state CTA and then from the resulting CTA anion to oxygen led to *in situ* removal of oxygen such that polymerization without prior deoxygenation proceeded after the induction period (Scheme 13).[151] Regarding the mechanistic origin of oxygen tolerance, photoinduced energy transfer (*i.e.*, generation of singlet oxygen) was excluded by the similar monomer conversions of MA in DMSO and in toluene despite the different abilities of the solvents to scavenge singlet oxygen. Very recently, Zhang, Weng, and coworkers reported an oxygen-tolerant polymerization system using CPADB under irradiation with a household lamp (14 W, 2.4 mW cm^{-2}) where the amine was incorporated as a part of 2-(dimethylamino)-, 2-(diethylamino)-, or 1-(dipropylamino)ethyl methacrylate monomers.[153] However, with a target degree of polymerization (DP) of 400, the relatively high dispersity (1.42–2.12), deviation of molecular weight from theoretical values, and/or the color change of solution from red to yellow (*i.e.*, degradation of CPADB) suggested the need for further optimization of reaction conditions. Gibson and coworkers disregarded the high dispersities of

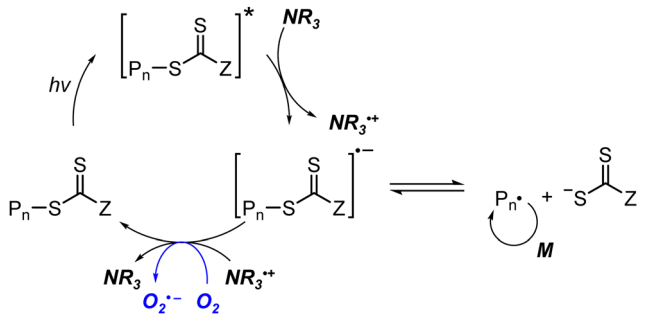

Scheme 13 Tertiary amine-assisted oxygen-tolerant polymerization in the absence of a PC.

polymers synthesized *via* amine-catalyzed photolysis of TTC and only focused on the quick preparation of large libraries of polymers *via* high-throughput (HTP) synthesis in a 96-well plate. Dioxane with degassing ability inferior to that of DMSO was thus used as a solvent owing to the ease of purification of polymers by simple evaporation of solvent under vacuum.[152] It has to be noted that categorizing these reports which harnessed amine additives as photoiniferter polymerization might be controversial because herein amine-catalyzed electron transfer instead of the direct photolysis of the CTA initiated the polymerization, which was similar to PC-catalyzed electron transfer in PET-RAFT polymerization. Meanwhile, Chen and coworkers introduced $Zn_{0.64}Fe_{2.36}O_4$ into DMSO[154,155] or ZnO NPs into aqueous medium[156] to reduce oxygen to a hydroxyl radical *via* photoinduced generation of electron–hole pairs under sunlight irradiation, and enabled open-to-air photoiniferter polymerization from various CTAs despite the poor controllability ($Đ$ = 1.35–1.56).

Oxygen tolerance was also achieved without additives. The so-called ''polymerization through oxygen'' was reported by Johnson and coworkers even in a completely open vial, where the diffusion of oxygen into the polymerization site was substantially restricted by the high viscosity and low solubility of oxygen in DMSO and not stirring the reaction mixture.[157] Polymerization of acrylates and acrylamides from TTCs was thus conducted at the bottom of the reaction vessel directly above the high-intensity irradiation source (450 nm, $\geq$503 mW cm^{-2}) to ensure a high radical flux and a short inhibition period arising from high light intensity. Although this oxygen-tolerant and rapid polymerization retained the controlled and living nature, the molecular weight of the polymer was larger than the theoretical value due to partial degradation of the CTA located near the solution/air interface. The use of deep eutectic solvents (DES) instead of DMSO improved the ''polymerization through oxygen'' approach.[158] DES, composed of hydrogen-bonding-accepting tetrabutylammonium chloride and hydrogen-bonding-donating ethylene glycol, provided an enhanced polymerization rate and higher stability of the end group of TTCs and DTBs against photodegradation under 465 nm irradiation (0.7 or 3.1 mW cm^{-2}). In addition, oxygen tolerance behavior was more pronounced such that stirring the reaction mixture in an open vial did not affect the polymerization rate. Similar results were observed with PET-RAFT polymerization using Ir(ppy)$_3$, EY, and ZnTPP as a PC, although the exact role of DES needs to be elucidated. The effects of composition of DES, solubility of monomers and polymers in DES, and propagation rate constants (k_ps) of monomers in DES should also be considered.

Meanwhile, oxidative decomposition of xanthates and concomitant molecular weight discrepancy were also observed during additive-free polymerization of *n*-butyl acrylate (*n*-BA) under violet light irradiation in a closed non-degassed reaction vessel.[159] Subsequently, Konkolewicz and coworkers filled the remaining headspace in the reaction vessel with an inert solvent rather than air to block the diffusion of oxygen.[160] The combination of two immiscible liquids (water and mineral oil) allowed the preparation of aqueous- or organic-soluble polymers after the induction period to consume the already dissolved oxygen.

Benefitting from the simple system composition, photoiniferter polymerization has recently been applied to 3D printing where rapidness and efficiency of polymerization may have higher significances than precise controllability of polymerization. Zhu, Li, and coworkers conducted open-to-air rapid 3D printing using a commercial digital light processing (DLP) technique-based 3D printer, where the oxygen was consumed by the radicals generated after the photolysis of xanthate EXEP under violet light irradiation (405 nm, 2.0 mW cm^{-2}).[161] Herein, xanthate was employed because of its favored photolysis due to lower stability of the intermediate radical and the weaker C–S bond as compared to those of TTCs. The radicals generated after photolysis consumed oxygen thereby affording oxygen tolerance to the reaction system. It is noted that in the preparation of a linear polymer under blue light irradiation (460–470 nm), deviation of molecular weight because of the oxidation of some portion of EXEP was observed with a long induction period.[162]

3.4.1.3. Photomediated cationic RAFT polymerization and others. Oxygen tolerance in PET-RAFT and photoiniferter polymerization is achieved by converting oxygen to reactive oxygen species which is then trapped or deactivating oxygen by coupling with excess radicals. For example, DMSO acts as both a solvent and a singlet oxygen quencher, and thus it is extensively used for oxygen-tolerant polymerization. In contrast, oxygen tolerance of photomediated cationic RAFT polymerization remains elusive presumably because cationic propagating species cannot capture oxygen and this polymerization method is not compatible with DMSO due to the high Lewis basicity of DMSO.[121] Cationic reaction intermediates are insensitive to oxygen, but oxygen tolerance of photomediated cationic RAFT polymerization has not been studied.

In other polymerizations, enzymes are utilized. This enzymatic degassing strategy harnesses the intrinsic enzymatic activity to reduce oxygen, so the oxygen tolerance is achieved regardless of irradiation and decoupled from light. Glucose oxidase (GOx) or pyranose oxidase (P2Ox) in the presence of glucose reduces oxygen to hydrogen peroxide. Thus, *in situ* removal of oxygen was leveraged for EY-catalyzed surface-initiated PET-RAFT polymerization from CTA-tethered substrates under ambient conditions.[163] Nanopure water had to be used as a solvent as the enzymatic stability of GOx and the polymerization rate could be influenced by residual minerals and salts in deionized water. Flavin adenine dinucleotide (FAD), a cofactor within GOx, was reduced to FADH$^-$ by glucose. Upon violet light irradiation (405 nm, 11.5 W), FADH$^-$ was excited, became a highly reducing state, and initiated polymerization by transferring an electron to a monomer or CTA. In addition to the deoxygenation capability by GOx, oxygen was consumed by FADH$^-$ regenerating FAD. Therefore, an excess of glucose was necessary initially for GOx and then for FAD to continuously generate FADH$^-$ that played a catalytic role. This photoenzymatic RAFT polymerization was employed for ultrahigh-molecular-weight (UHMW) polymer synthesis in an

aqueous solution from *N*-vinylcaprolactam,[164] oligo(ethylene glycol) methyl ether methacrylate (OEGMA), and other monomers.[165]

In conventional photomediated radical polymerization based on Type II visible-light-sensitive photoinitiating systems, oxygen tolerance is achieved by coinitiators and additives (*e.g.*, amine, thiol, silane, germane, borane, phosphine, and phosphite).[128,166,167] These hydrogen donors quench inactive peroxyl radicals by hydrogen abstraction and generate new initiating radicals. Page and coworkers recently reported rapid visible-light-driven thiol–ene reaction-based 3D printing of acrylic resin under ambient conditions using a three-component photoinitiating system (ZnTPP as a PC, and electron-donating and electron-accepting coinitiators) (Scheme 14).[168,169] The thiol quenched a peroxyl radical which was formed by the addition of oxygen to the propagating radical. The resulting thiyl radical was substantially reactive than the peroxyl radical, so consequently decreased the oxygen inhibition period and continued the polymer network formation. Moreover, the thiol reduced excited-state ZnTPP to yield a thiyl radical which in turn was incorporated as a thioether within the network. The thioether also contributed to oxygen tolerance by scavenging singlet oxygen which was generated by TTA between excited-state ZnTPP and triplet oxygen. Only 1 wt% thiol was sufficient to achieve oxygen tolerance, and the mechanical properties of the printed objects were adjustable by the thiol content.

3.4.2. Oxygen-initiated polymerization. As mentioned above, oxygen acts as an inhibitor or a scavenger of propagating radicals, so it needs to be physically removed or inactivated using PCs or additives for successful polymerization. However, if oxygen in turn could become an initiating species (*i.e.*, hydroxyl radical), the reaction would proceed without prior deoxygenation; however, the reaction can be accompanied by imperfect temporal control due to latent radical generation. Hydroxyl radicals are generated from oxygen in the presence of ascorbic acid or water.

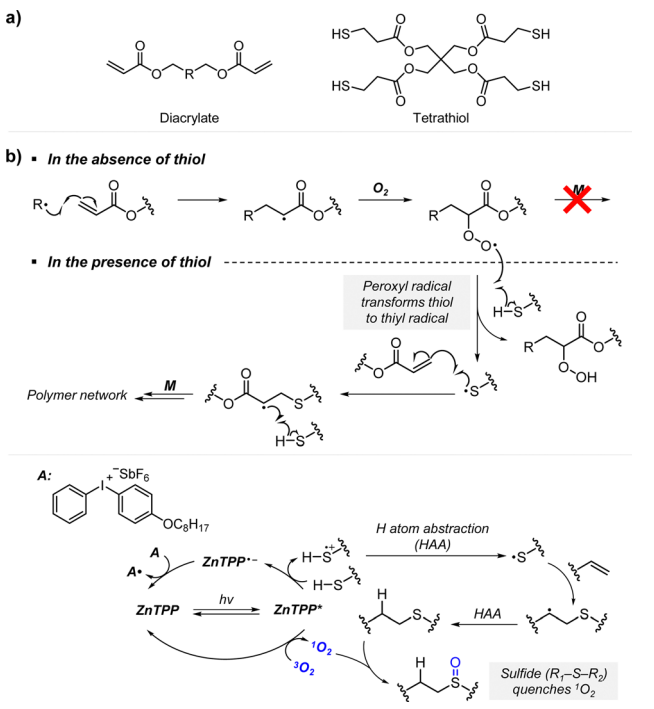

Scheme 14 Oxygen-tolerant thiol–ene reaction-based visible-light-driven 3D printing of acrylic resin.[169] (a) Structure of diacrylate and tetrathiol monomers. (b) Mechanism of oxygen tolerance in the presence of ZnTPP and thiol.

Ascorbic acid converts singlet oxygen into hydrogen peroxide and then reduces hydrogen peroxide into hydroxyl radicals. Hydroxyl radicals enable polymerization in ultralow volumes (μL scale) where deoxygenation is difficult.[170] On the other hand, hydroxyl radical-initiated polymerization could also proceed in the dark *via* the hydroxyl radicals after a brief irradiation period.[93] Hydrogen peroxide, a precursor of hydroxyl radicals, was generated during irradiation. Under near neutral and basic conditions where hydrogen peroxide remained stable, the temporal control was restored as in the case of $ZnTPPS_4^-$/ascorbic acid-catalyzed PET-RAFT polymerization of DMAm in water.[131] Inferior temporal control of polymerization was also observed for a fluorescein/ascorbic acid system.[171] Only the prior deoxygenation prevented the generation of the latent radicals and stopped the reaction in the dark, but the polymerization rate accordingly decreased owing to lowered amount of radicals.

Oxygen in the presence of water can also generate hydroxyl radicals. Very recently, Hou, Xiao, Zhao, and coworkers reported that 1,3,6,8-tetrakis(4-formylphenyl)pyrene (TFPPy)-azine based covalent organic frameworks (COFs) generated initiating hydroxyl radicals from water and atmospheric air under white light irradiation (15 mW cm^{-2}).[172] Photoinduced production of the superoxide radical anion followed by reaction with water generated hydroxyl radicals. Thus, in a completely open vial, the polymerization rate increased with an increase in the volumetric ratio of water to dioxane, whereas polymerization did not proceed in the absence of water. Nonpolar solvents were not appropriate reaction media due to inefficient stabilization of photogenerated carriers. Adding methylene blue or benzoquinone to scavenge the hydroxyl radical or superoxide radical anion, respectively, led to no polymerization, supporting the initiation mechanism. TEA promoted polymerization by enhancing charge separation in the COF and the capability to transform singlet oxygen into a superoxide radical anion.

3.4.3. Oxygen-accelerated polymerization. Even the peculiar role of oxygen in supporting and accelerating the PET-RAFT polymerization was observed very recently in several reports. Herein, oxygen is directly involved in the photocatalytic cycle for activation of the CTA (Scheme 15). In the examples discussed below, the significantly improved polymerization kinetics were ascribed to the reduction of the CTA by the superoxide radical anion. The superoxide radical anion was generated either in the presence or absence of a tertiary amine.

Boyer and coworkers firstly reported the surprisingly supportive role of oxygen in ZnOETPP/TEA-catalyzed PET-RAFT polymerization under far-red light irradiation (690 nm, 3.0 mW cm^{-2}).[99] DMAm and MA could be polymerized in the presence of PC, TEA, and oxygen. "On/off" switchability of the

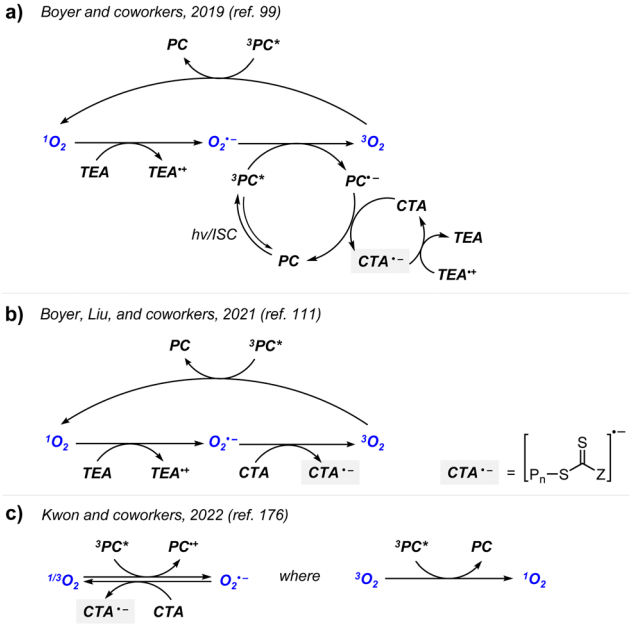

Scheme 15 Three distinct mechanisms proposed for oxygen-accelerated PET-RAFT polymerization. Generation of the superoxide radical anion to reduce the CTA was achieved as described in (a) ref. 99 and (b) ref. 111 in the presence or (c) absence of TEA as an additive.[176] It is noted that to emphasize the participation of oxygen, the complete catalytic cycles of reagents are not described for clarity.

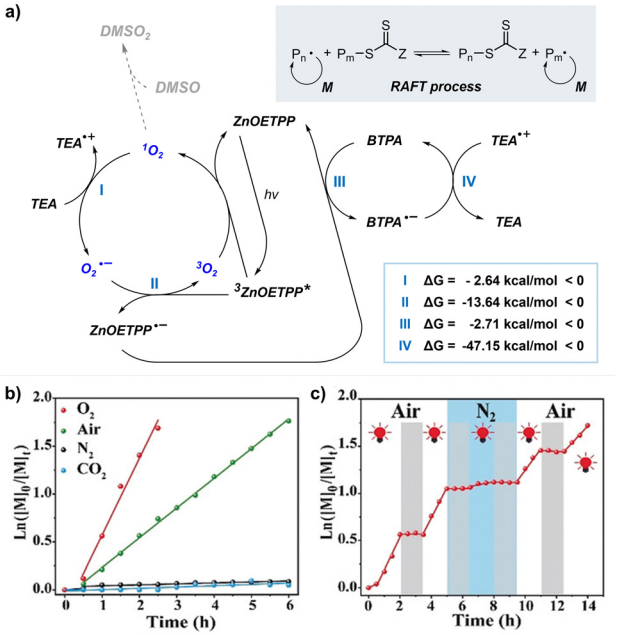

Fig. 7 (a) The proposed mechanism of ZnOETPP/TEA-catalyzed PET-RAFT polymerization accelerated by oxygen. Kinetic plots of $\ln([M]_0/[M]_t)$ *vs.* reaction time (b) under different atmospheres and (c) in gas and light dual-gated polymerization. Monomer: MA; CTA: BTPA; additive: TEA (one equivalent relative to the CTA). Adapted with permission from ref. 99 (Copyright 2019 John Wiley & Sons, Inc.).

reaction by the introduction and removal of oxygen combined with a constant polymerization rate in the "on" state implied the essential role of oxygen as a catalyst. Moreover, pure oxygen, when compared to atmospheric air, further increased the polymerization kinetics. Based on the experimental investigation and DFT calculations of the formation of singlet oxygen and the superoxide radical anion, the authors proposed the mechanism of oxygen-catalyzed PET-RAFT polymerization. The superoxide radical anion, which was generated *via* the reduction of singlet oxygen by TEA, reduced excited-state ZnOETPP to proceed PET-RAFT polymerization *via* RQP (Scheme 15a and Fig. 7).

The peculiar role of oxygen, namely the 'oxygen-mediated reductive quenching pathway (O-RQP)', was also reported by Boyer, Liu, and coworkers.[111] Herein, oxygen allowed the activation of the CTA, which otherwise was restricted by the unfavorable thermodynamics of the PC exhibiting long wavelength absorption either *via* conventional OQP or RQP. The excited-state PC generates singlet oxygen, which is reduced to a superoxide radical anion by TEA. It was this superoxide radical anion that directly activated the CTA *via* single-electron transfer and activated the polymerization (Scheme 15b and Fig. 8). Combined experimental and theoretical investigations of the PET-RAFT polymerization of MA in DMSO using four model (metallo)porphyrin-based PCs revealed that the thermodynamic viability of O-RQP predominantly depended on the singlet oxygen generation ability of the PC, rather than the electron transfer ability. In particular, *via* O-RQP in the presence of oxygen, the fastest kinetics was achieved as compared to that *via* other pathways. Finally, as expected, four phthalocyanines that were previously considered inactive for PET-RAFT polymerization *via* the conventional mechanisms became successful PC candidates for well-controlled PET-RAFT polymerization under red to NIR light irradiation (590, 660, 730, and 780 nm depending on PCs, 10 mW cm^{-2}) *via* the newly proposed O-RQP (Scheme 16a). This mechanism was partially valid for aqueous polymerization in water using a water-soluble phthalocyanine $ZnPCS_4^-$ (Scheme 16b).[173] Herein, reactive oxygen species did not directly activate the CTA, but participated in the generation of other initiating radicals. Water as a hydrogen donor transformed the superoxide radical anion into a hydrogen peroxyl radical, which is a precursor of hydrogen peroxide. Hydrogen peroxide was then activated by excited-state $ZnPCS_4^-$ to form an initiating hydroxyl radical. Based on experimental and DFT calculations, this proposed pathway was more favored than OQP and RQP, leading to successful demonstration of polymerization in water under NIR irradiation (730 nm, 12 mW cm^{-2}). Another water-soluble phthalocyanine possessing several ethylene glycol units could also catalyze PET-RAFT polymerization under NIR irradiation (730 nm, 75.7 mW cm^{-2}) only in the presence of hydrogen peroxide under a N_2 atmosphere,[174] supporting the proposed mechanism for initiation. This newly proposed O-RQP is thus promising to widen the scope of PCs in catalyzing PET-RAFT polymerization at longer wavelengths; nevertheless, the stability of PC candidates in the presence of reactive oxygen species must be considered. Hou, Xiao, and coworkers reported a similar system for heterogeneous PCs involving porphyrins.[175] As the head space or amount of oxygen in the sealed reaction vessel increased, the polymerization rate was accelerated albeit with the lengthened induction period. TEA-catalyzed depletion of

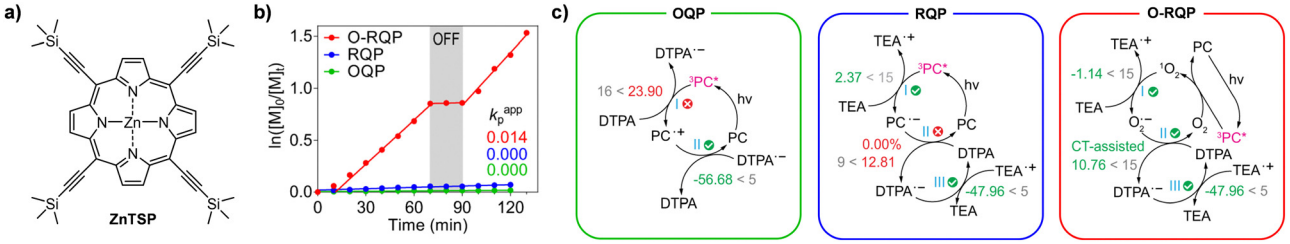

Fig. 8 (a) Chemical structure of ZnTSP. (b) Kinetic plot of $\ln([M]_0/[M]_t)$ *vs.* reaction time and temporal control of model PET-RAFT polymerization *via* OQP (green), RQP (blue), and O-RQP (red). (c) Schematic representation of thermodynamic viability (denoted by Gibbs free energy change [kcal mol^{-1}]) for each mechanism. Written in grey are threshold values for each step. Monomer: MA; CTA: DTPA; additive: TEA (0.5 equivalent relative to the CTA). Adapted with permission from ref. 111 (open access).

singlet oxygen and the formation of the superoxide radical anion were experimentally confirmed by UV/Vis and electron spin resonance (ESR) spectroscopy.

Very recently, Kwon and coworkers in collaboration with Gierschner and Koo reported 3DP-MSDP-IPN as a novel organic PC for additive-free oxygen-accelerated polymerization in ambient and aqueous environments.[176] The mechanism was similar to O-RQP[111] in terms of generation of singlet oxygen by the excited-state PC and activation of the CTA by the superoxide radical anion. However, Stern–Volmer analysis suggested that the excited-state PC was likely to be quenched by oxygen rather than by the CTA, which means that in the presence of a PC possessing a suitable redox potential, the superoxide radical anion could be generated without an external reductant (Scheme 15c). Ag_2S NCs also exhibited a similar phenomenon.[65] Using potassium superoxide as a source of the superoxide radical anion, the polymerization still proceeded in the absence of Ag_2S NCs, confirming the proposed mechanism for oxygen-accelerated polymerization.

Nevertheless, it should be noted that the abovementioned oxygen-accelerated polymerization, such as *via* O-RQP, is mechanically distinct from the previously reported oxygen-demanding polymerization using alkylborane (complex) as a precursor of the initiating radical. For example, triethylborane reacts with oxygen to liberate an ethyl radical, which reacts with another oxygen to generate a peroxyl radical. The peroxyl radical then reacts with triethylborane to generate an ethyl radical as an initiating species (Scheme 17a). Therefore, polymerization can be initiated and externally regulated by the presence of oxygen.[177] If alkylboranes are complexed, the complex first needs to be decomplexed for further processes.[178] Wu and coworkers reported both oxygen-demanding and photocontrolled polymerization based on light-induced decomplexation of the alkylborane complex.[179] Upon UV light irradiation, the photoacid in the triethylborane-amine/photoacid complex 1,3-diaminopropane-triethylborane (DAPTB)/Ph_2I^+ generated a proton which subsequently released ethylborane to consecutively initiate polymerization (Scheme 17b).

4. PET-RAFT polymerization

4.1. Overview

This section aims to summarize the research on PET-RAFT polymerization. First of all, the reported PCs are outlined in Section 4.2. The next sections summarize the applications of PET-RAFT polymerization such as for preparation of polymers with precise control over their characteristics (*e.g.*, sequence, architecture, polymer tacticity, and dispersity). PET-RAFT polymerization has been widely applied to various applications owing to its uniquely distinct features in contrast to the conventional RAFT polymerization. In particular, surface-initiated polymerization to functionalize a given surface, 3D/4D printing technologies, and stereolithography along with the advent of advanced techniques, such as flow chemistry and high-throughput (HTP) synthesis, would pave the way to the industrial applications. If worth mentioning, the newly designed functional monomers are also introduced.

4.2. PCs for polymerization

Since the first employment of Ir(ppy)$_3$ as a PC in 2014,[31] along with the increasing number of applications, the scope of PCs has

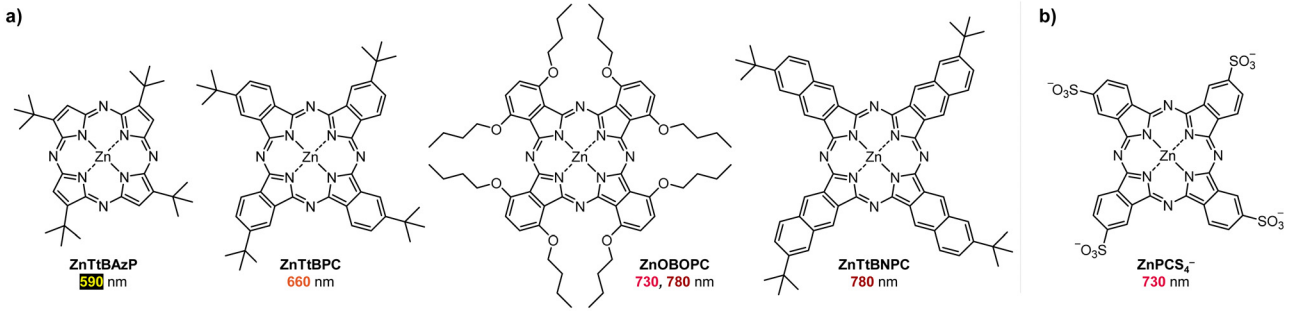

Scheme 16 Chemical structures of the phthalocyanines discovered for PET-RAFT polymerization at longer wavelengths (>590 nm) *via* O-RQP.[111]

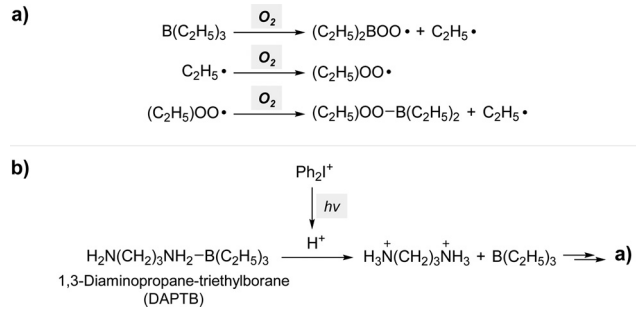

Scheme 17 Mechanism of (a) oxygen-mediated generation of an initiating radical from triethylborane[177] and (b) photomediated decomplexation of 1,3-diaminopropane-triethylborane (DAPTB) to triethylborane.[179]

been accordingly widened to realize PET-RAFT polymerization of various monomers under a wide range of wavelengths. In brief, the development of PCs has been directed as follows. Concerns regarding environmental issues of transition metals have led to development of metal-free (in)organic alternatives, which increased the environmental compatibility of PCs and eliminated the potential harm in applying the prepared polymeric materials in electronic and/or biomedical fields.[180,181] In the case of biomedical applications, PCs that can be activated under irradiation at longer wavelengths are desired as deeper penetration length and lower energy would allow polymerization in the presence of biomolecules and eventually enable *in vivo* polymerization in the near future. Last but not least, heterogeneous PCs that can be easily purified and reused for the next polymerizations have also gained interest. In any case, highly efficient photocatalytic performance of a PC that realizes polymerization at low catalytic loading and/or endows the reaction system with oxygen tolerance is desired.

During the search of PCs, researchers initially adapted PCs that were efficient for other types of visible-light-driven organic transformations including RDRPs, solar energy conversion, or water splitting, and successfully demonstrated PET-RAFT polymerization using a wide range of PCs. Apart from these trial-and-error strategies, recently emerging approaches are based on investigation of the structure–property/performance relationship of conventional PCs and computer-guided design of novel PCs.[96,182] These general design strategies have been quite well established and allow efficient, systematic, and rational design of novel PCs. For details on the rational design of PCs, please refer to the review articles by Boyer, Miyake, Liu, and coworkers, who have summarized the effects of the structures of PCs on their photocatalytic activities (light absorption, quantum yield, and redox properties) in various photocontrolled polymerizations (including PET-RAFT and photomediated cationic RAFT polymerizations),[183] and Kwon and coworkers, who have particularly focused on the recently emerged purely organic PCs since 2016.[184]

In the following sections, the reported PCs are categorized into metal-based, organic, inorganic, and modified PCs. The types of PCs are briefly described, while the detailed applications are mentioned throughout Sections 4.3 and 4.4. For representative PCs, structures of the PCs are provided with the used wavelengths and monomers reported for polymerization (Table 1). It is noted that PET-RAFT polymerization provided high tolerance of functional groups incorporated into monomers (Scheme 18). For example, by PET-RAFT polymerization using $Ir(ppy)_3$[100] or EY,[185] macrocyclic allylic sulfones, which introduce degradable ester bonds along the polymer backbone, could be evenly distributed within a nearly ideal random copolymer of macrocyclic allylic sulfones and acrylic monomers, which otherwise is not achieved by thermally initiated RAFT polymerization. The even distribution of degradable moieties along the copolymers led to significantly improved degradation behaviors.

4.2.1. Metal-based PCs. $Ir(ppy)_3$, as the PC employed for PET-RAFT polymerization for the first time,[31] is one of the most extensively applied PCs. A wide range of monomers ranging from challenging unconjugated monomers (*i.e.*, vinyl acetate (VAc), *N*-vinylpyrrolidinone (NVP), and vinyl benzoate (VBz)),[31,186] vinyl ketones,[130,187] to monomers bearing various functional groups (*e.g.*, metallocene,[188] amino acids,[189] and fluorine[190,191]) were successfully polymerized. Another transition metal-based $Ru(bpy)_3Cl_2$ exhibited less efficient photocatalytic performance than $Ir(ppy)_3$,[129] but expanded the scope of solvent of PET-RAFT polymerization to alcoholic dispersion[192] and aqueous systems[129,193] owing to its water-solubility. Moreover, owing to its traditional usage as an electrochemiluminescence (ECL) probe, after the $Ru(bpy)_3Cl_2$-catalyzed polymerization to synthesize surface-modified gold NPs as a solid substrate of ECL sensors, $Ru(bpy)_3Cl_2$ need not be purified. Based on these wide utilities, $Ir(ppy)_3$[84,85] and $Ru(bpy)_3Cl_2$[83,84] have been a model PC in the recently emerging field of systematic investigation of the PET-RAFT polymerization mechanism.

Chlorophyll a, a naturally occurring visible-light-absorbing PC for photosynthesis in green plants, is considered the first non-transition metal-based PC and it allowed utilization of low-energy red light (635 nm) for PET-RAFT polymerization for the first time.[194,195] Bacteriochlorophyll a, which is present in purple bacteria and absorbs at even longer wavelength (>900 nm), further expanded the wavelength range of PET-RAFT polymerization to the far-red (780 nm) and NIR region (850 nm).[196] Metalloporphyrins were also effective under red light irradiation (635 nm).[105] Among the metalloporphyrins embedded with different core metals (Zn^{2+}, Ni^{2+}, Co^{2+}, and Fe^{3+}), only ZnTPP catalyzed the polymerization as its high triplet state quantum yield (0.88) and low Φ_{FL} (0.04) increased the probability of photoinduced electron transfer at the triplet excited state. Aluminum (Al^{3+}) porphyrin complexes were recently discovered for polymerization under blue light irradiation (460 nm, 5 mW cm^{-2}).[197] On the other hand, free base porphyrin without the core metal still retained photocatalytic ability albeit with a slow polymerization rate, owing to ineffective collision between free base porphyrin and CTA.[198] The polymerization rate was significantly enhanced by covalently tethering the CTA to free base porphyrin.

ZnTPP demonstrated a wide absorption profile, so PET-RAFT polymerization could be performed under blue, green,

Table 1 Representative PCs employed for PET-RAFT polymerization

PC	Irradiation wavelengths	CTA–monomer pair		
		Dithiobenzoates	Trithiocarbonates	Xanthates
Metal-based PCs – Section 4.2.1				
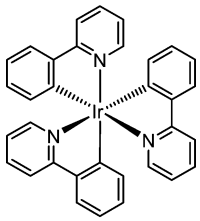 $Ir(ppy)_3$	Blue (435–470 nm)	MMA, OEGMA, TFEMA	CoAEMA, MAEFe	←(*Methacrylates*)
			t-BA, BzA, MA, OEGA, TFEA	←(*Acrylates*)
		HPMAm		←(*Methacrylamides*)
			DEAm, DMAm, NAM, NIPAm, *N*-acryloyl amino acids	←(*Acrylamides*)
		(*Others*)→	Isoprene, St, VAc, vinyl ketones, macrocyclic allylic sulfone	DVP, NVP, VAc, VBz, VCz, VP
	White		Fluorinated monomers	VDF
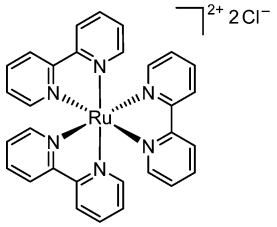 $Ru(bpy)_3Cl_2$	Blue (435–470 nm)	BzMA, MMA, OEGMA	HPMA, MAA	
			DEGA, MA, NASS, OEGA	
			DEAm, DMAm, NAM, NIPAm	
			St	
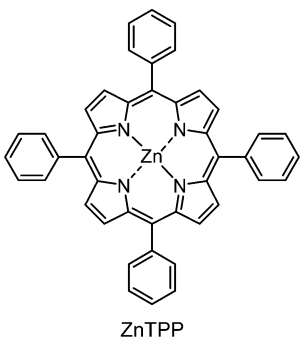 ZnTPP	Red (635 nm) Yellow (560 nm) Green (530 nm)		BzMA, DMAPS-MA, GMA, HEMA, HPMA, MMA, MPC, MTEMA, NBMA, NHSMA, OEGMA, TFEMA	
			n-BA, *t*-BA, Boc-AEA, BzA, CHA, DEGA, DMAEA, EA, EHA, *n*-HA, HEA, HPA, IBOA, MA, MSEA, OEGA, TEGDA, TFEA	
			AAm, AAPTAC, *t*-BAm, Boc-AEAm, Cp-DIBAC, DAAm, DEAm, DMAm, HEAm, NAM, NIPAm, PEAm	
			St, VBA	
	White		DEAm, DMAm, HEAm, NAM	
Organic PCs – Section 4.2.2				
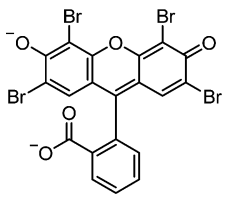 Eosin Y	Blue (450–483 nm) Green (520–530 nm)	BzMA, DMAEMA, GMA, HEMA, MAA, MMA, OEGMA, PFPMA	HFBMA, MMA	
			n-BA, *t*-BA, HEA, MA, OEGA, PEGDA	
		CBMAm, HPMAm		
			AMPS, DAAm, DEAm, DMAm, FSAm, HEAm, NAM, NIPAm, PEG-based monomers, saccharide- and peptide-based monomers	
			BTP, NaSS, St, vinyl ketones, macrocyclic allylic sulfone	

yellow, orange, and red light irradiation (460, 522, 565, 595, and 635 nm, respectively).[105] Nevertheless, red light has been typically used in subsequent studies. Several ZnTPP derivatives were employed as well. Water-soluble analogues including $ZnTPPS_4$[−98,131,133,199] and ZnTMPyP[147,200,201] or supramolecular ZnTPOR/cucurbit[7]uril which exhibited improved water-solubility compared to ZnTPOR[202] catalyzed polymerization in aqueous systems. In the case of supramolecular ZnTPOR/cucurbit[7]uril, host–guest complexation between cucurbit[7]uril and TPOR also prevented self-aggregation-induced quenching of excited-state ZnTPOR in water and reduction of photocatalytic performance. Similarly, self-aggregation of ZnTPP at high concentration in DMSO was reduced by linking polyhedral oligomeric silsesquioxane (POSS) to ZnTPP.[203] ZnOETPP could absorb far-red light (690 nm), but could catalyze polymerization only in the presence of oxygen and TEA, which is contradictory to the common role of oxygen in inhibiting the polymerization[99]

Very recently, phthalocyanines were discovered for PET-RAFT polymerization under red to NIR light irradiation (Scheme 16).[111,173] These molecules exhibiting long wavelength absorption were inactive for polymerization *via* OQP and RQP owing to the unfavorable thermodynamics, but became active for polymerization *via* O-RQP in the presence of oxygen and tertiary amines. For a detailed explanation on the role of oxygen in the case of ZnOETPP and phthalocyanines, please see Section 3.4.2.2.

4.2.2. Organic PCs. Organic PCs reduce the potential negative impacts of residual transition metal components on polymeric materials for electronicand biological applications.[36,180,181]

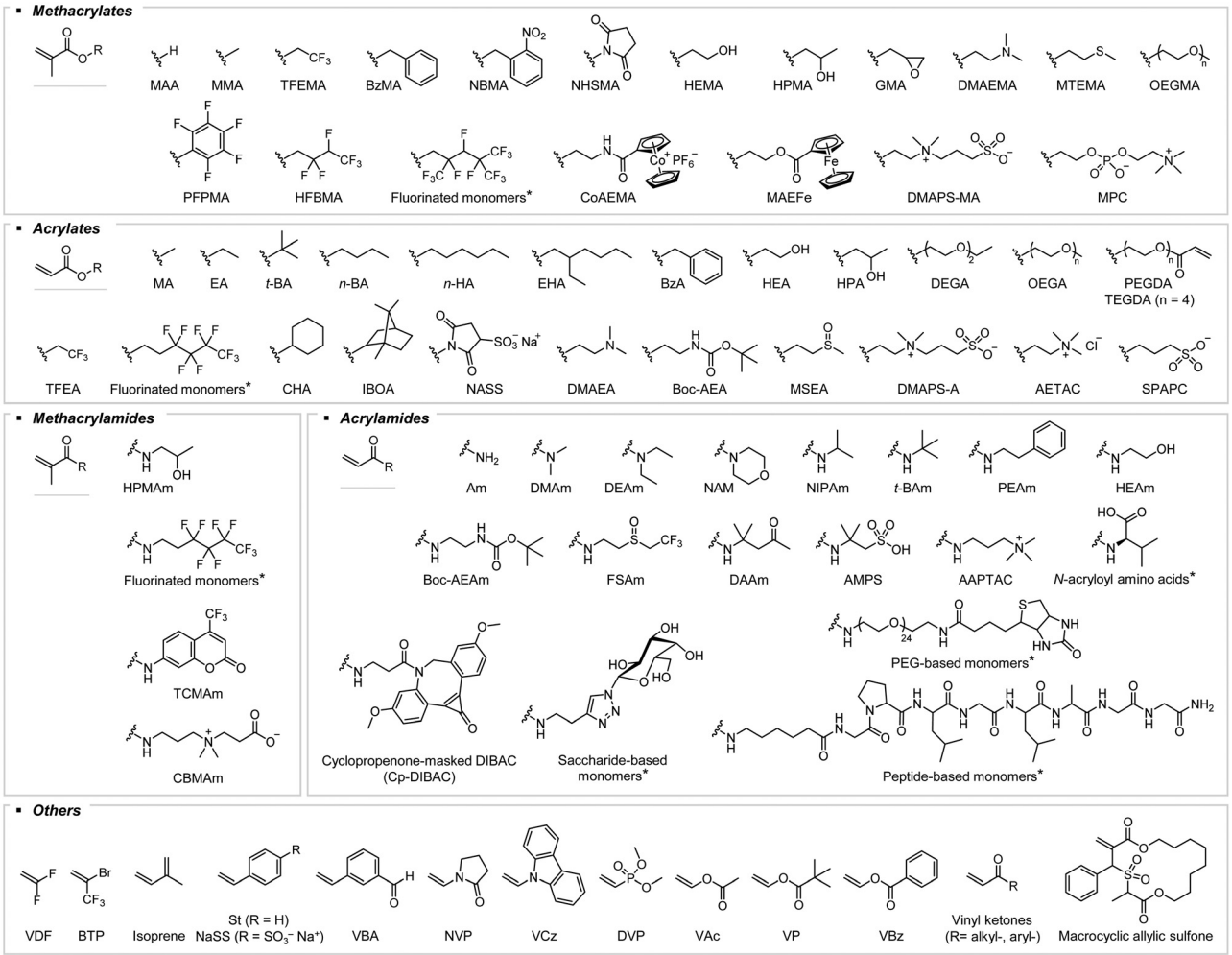

Scheme 18 Chemical structures and abbreviations of monomers employed for PET-RAFT polymerization. The asterisk denotes that only a selected monomer is shown.

In the initial investigations of the photocatalytic capabilities of commercially available and non-toxic organic dyes (*i.e.*, EY, fluorescein, methylene blue, Nile red, and rhodamine 6G) in PET-RAFT polymerization, EY and fluorescein were found to be efficient.[66] Since then, EY has been extensively utilized as a PC under green and blue light irradiation, owing to its adequate catalytic efficiency and water-solubility. Later studies revealed that Rose Bengal,[93] EB,[204] and Phloxine B,[204] which share the common fluorescein scaffolds (Scheme 19), could also catalyze the polymerization.

EY has been widely applied as a PC in various organic transformation reactions *via* photoredox catalysis.[205] In this regard, researchers have employed other classes of previously reported organic PCs (*e.g.*, phenothiazines, phenazines, and cyanoarenes) for PET-RAFT polymerization (Scheme 19). For example, PTH, which realized photoinduced organocatalyzed ATRP (O-ATRP) for the first time,[206] promoted the PET-RAFT polymerization of acrylates and acrylamides under irradiation using a CFL[207] or at 400 nm.[208] Incorporation of electron withdrawing groups (*i.e.*, *n*-butylphenyl and hydrofluorocarbons) into PTH caused a red-shift in absorption profiles, and thus enhanced visible-light-absorbing abilities in the case of PTH-2,[209] PTH-3,[210,211] and PTH-4.[212] Moreover, fluorinated PTH-4 provided better control over the polymerization of fluorinated polymers as compared to non-fluorinated PTH-3, owing to the fluorine–fluorine interaction between the PC and the propagating chain-end.[212] PTH-5 with the extended conjugation exhibited lower E^*_{red} and higher E^0_{ox} than PTH-3, which led to favored initial electron transfer from the excited-state PC to xanthate and subsequent electron transfer from the xanthate anion to the one-electron-oxidized PC.[213] A series of phenazine-based PCs developed by structural modification of 5,10-diphenyl-5,10-dihydrophenazine exhibited disparate photocatalytic activities in PET-RAFT polymerization under blue light irradiation (460 nm).[125] Likewise, covalent structural modification of the known PC scaffolds, including extension of the conjugated structure or change of substituents, has been widely applied to modulate the performance of PCs in polymerization under desired reaction conditions (*e.g.*, irradiation wavelengths and chemical properties of reagents).

As the structures of PCs affect their catalytic abilities for PET-RAFT polymerization, a comprehensive investigation of commercial fluorescein derivatives guided the development of

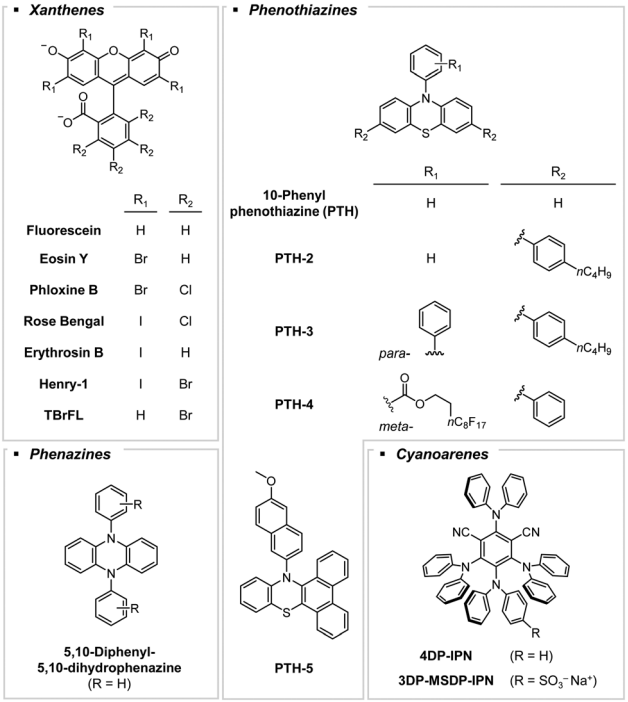

Scheme 19 Four representative scaffolds of organic PCs discovered for PET-RAFT polymerization.

a novel PC Henry-1.[214] Herein, the photophysical properties studied by DFT calculations were compared with the experimental results of the polymerization. On the other hand, the discovery of TBrFL was fully guided by DFT calculations.[96] In a similar vein, *via* a synthetic platform proposed for the design of organic PCs based on strongly twisted donor–acceptor scaffolds,[182] a combination of various donors and acceptors provided a large number of PC candidates with predictable photophysical and electrochemical characteristics. Thus, highly efficient cyanoarene derivatives 4DP-IPN[215] and 3DP-MSDP-IPN[176] were newly designed for PET-RAFT polymerization in an organic and aqueous system, respectively. The outstanding photocatalytic performances of all systematically designed PCs (*i.e.*, Henry-1, TBrFL, 4DP-IPN, and 3DP-MSDP-IPN) were ascribed to efficient generation of a triplet excited state and appropriate excited-state redox potentials, proposing the key design principle of next-generation PCs for PET-RAFT polymerization.

Thus far, perylene,[216] benzaldehyde,[217–219] benzothiadiazole,[220] PheoA,[106] reduced free base porphyrin,[221] fluorophenyl bacteriochlorin,[222] self-assembled carboxylated porphyrin (SA-TCPP),[223] g-C_3N_4,[143,144,224,225] poly(1,4-diphenylbutadiyne)-nanofibers (PDNB-NF),[226] imine-based COFs,[227] and (heteroatom-doped) carbon dots[228] have been reported as organic PCs. Among them, SA-TCPP, g-C_3N_4, imine-based COFs, and PDPB-NF were heterogeneous, so they can be separated after the polymerization and reused several times. Moreover, biomolecules such as flavin mononucleotide[229] and FAD cofactor[164,165] were employed. FAD is a cofactor of GOx and is reduced to $FADH^-$ in the presence of glucose. $FADH^-$ exhibits a high excited-state reducing power, so could catalyze photoenzymatic RAFT polymerization under violet light irradiation (405 nm).

4.2.3. Inorganic PCs. Numerous inorganic materials including Ag_3PO_4,[230] Ag_2S NCs,[65] semi-conducting nanomaterials (*i.e.*, ZnO,[231] $Zn_{0.64}Fe_{2.36}O_4$,[154,155] Bi_2O_3,[232] and CdSe-[233–235] and Si-based quantum dots (QDs)[236]), and upconversion nanoparticles (UCNPs) (*i.e.*, $CsPbBr_xI_{3-x}$ perovskite NCs[237] and $NaYF_4$:Yb^{3+}/Tm^{3+} and $NaYF_4$:Yb^{3+}/Er^{3+} NPs[238]) have been employed for PET-RAFT polymerization (Table 2).[239] Several studies showed that the catalytic performance of PCs was affected by size[234] and morphology[230] of the prepared PCs.

It is noted that Ag_3PO_4 could be activated in the NIR region (940 nm) owing to the localized surface plasmon resonance effect.[230] $NaYF_4$:Yb^{3+}/Tm^{3+} and $NaYF_4$:Yb^{3+}/Er^{3+} NPs,[238] and $CsPbBr_xI_{3-x}$ perovskite NCs[237] could also utilize NIR light owing to their upconversion properties and an extremely large two-photon absorption cross-section, respectively. $NaYF_4$:Yb^{3+}/Tm^{3+} and $NaYF_4$:Yb^{3+}/Er^{3+} NPs absorbed NIR light (980 nm) and emitted light at 325–380 and 425–500 nm *via* upconversion.[238]

Moreover, based on the heterogeneity of inorganic PCs, recovery and reusability of the used PCs for the next polymerizations were demonstrated for several PCs such as CdSe-based QDs,[233] $Zn_{0.64}Fe_{2.36}O_4$,[154] and Bi_2O_3.[232] These PCs were typically retrieved by simple centrifugation, whereas magnetic $Zn_{0.64}Fe_{2.36}O_4$ could be recovered with a magnet.

4.2.4. Modified PCs. Besides the structural modification strategies, small molecule PCs have been modified by their immobilization on heterogeneous supports. The resulting PCs became heterogeneous, allowing the simple catalyst recovery from the polymerization mixtures through centrifugation or filtration. For example, free base porphyrin and ZnTPP were immobilized onto cotton thread (Fig. 9a),[240] sponges,[241] and silica microspheres.[242] EY was conjugated to cotton thread[243] and silica NPs.[244] Surface-initiated copolymerization of acrylate-

Table 2 Operational irradiation wavelengths of reported inorganic PCs for PET-RAFT polymerization

PC	Irradiation wavelengths				
Ag_3PO_4	Blue (465 nm)	Green (525 nm)	Red (625 nm)	NIR (780, 940 nm)	Sunlight
Ag_2S NCs	Blue (455 nm)	Green (515 nm)	Red (630 nm)		Sunlight
$Zn_{0.64}Fe_{2.36}O_4$					Sunlight
Bi_2O_3					White
CdSe QDs	Blue (465 nm)	Green (532 nm)			White, sunlight
Si QDs	Blue (460 nm)				White
$CsPbBr_xI_{3-x}$ NCs	Blue (460 nm)	Green (535 nm)	Red (635 nm)		
$NaYF_4$:Yb^{3+}/Tm^{3+} and $NaYF_4$:Yb^{3+}/Er^{3+} NPs				NIR (980 nm)	

functionalized fluorescein with MA from glass beads provided fluorescein-immobilized glass beads (Fig. 9b).[245,246] The catalytic performance was comparable to that of their small molecule counterparts and was preserved after repeated recoveries. Moreover, after its conjugation to silica NPs, the stability of EY against photodegradation was enhanced.[244] Immobilization of $Ir(ppy)_3$,[101] ZnTPP,[102] and carbon dots[103] on functional materials such as magnetic nanocomposites led to switchable catalytic performance in response to an external magnetic field. Agglomeration of the modified PCs limited the access and electron transfer between PC and CTA, and subsequent polymerization.

PCs can be covalently incorporated into a macromolecular network. *Via* the introduction of polymerizable vinyl moieties into PCs, followed by copolymerization with different monomers, macromolecular versions of PTH[94] and EY[247,248] were prepared. Copolymerization with NIPAm resulted in PC-embedded poly(NIPAm)s with thermoresponsive behavior, allowing the purification of macromolecular PCs by heating the reaction mixture at temperatures above the LCST (Fig. 9c).[94,247] Amine-functionalized EY served as a monomer for ROP between diglycidyl and diamine monomers for the preparation of an interpenetrating polymer network.[249] The prepared PC-based copolymers could be grafted onto the commercial ultrafiltration membranes.[250,251] These PC-tethered membranes served as an integrated synthesis-separation system by catalyzing the polymerization and efficiently filtering unreacted monomers and other reagents after the polymerization. On the other hand, Sonogashira–Hagihara reactions between halogen substituents of xanthene dyes (*i.e.*, EB and Rose Bengal) and dialkynes[97] and Debus–Radziszewski reactions between amine-terminated porphyrins and imidazolium bromides[252] generated PC-conjugated porous polymer frameworks. Cross-linking between hydroxy-terminated porphyrins and dichlorodimethylsilanes provided twisted 3D structures with open catalytic sites.[253,254] The effective catalytic performance was ascribed to the large surface area of catalytically active sites, prevention of aggregation of porphyrins and concomitant reduction of quenching of excited-state porphyrins.

COFs or MOFs also served as heterogeneous platforms. 2D porphyrinic COFs were synthesized through polycondensation reactions between amine-terminated porphyrins and multivalent aldehydes.[255,256] 3D MOFs synthesized from zirconium-based clusters and porphyrins showed catalytic activities dependent on their crystal structures (Fig. 9d).[257] During the synthesis of 3D MOFs from free base- or zinc-embedded porphyrins as organic ligands and zinc-based clusters as metal

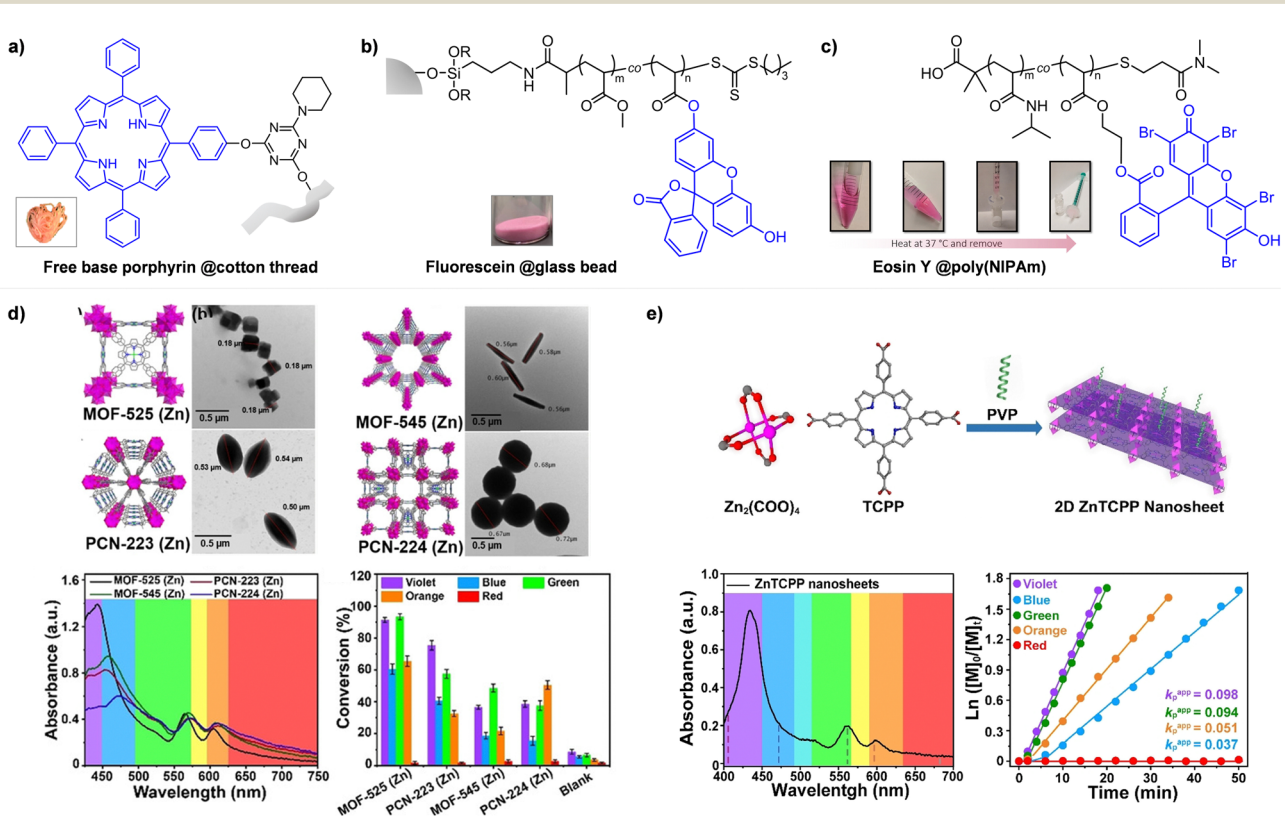

Fig. 9 Chemical structures and photographs of (a) free base porphyrin, (b) fluorescein, and (c) EY immobilized on heterogeneous supports or polymers. (d) Crystal structures, TEM images (top) and UV/Vis absorption spectra of 3D zinc porphyrinic MOFs, and monomer conversions in the polymerization of MA from BTPA using various 3D zinc porphyrinic MOFs under irradiation (9 mW cm^{-2}) (bottom). (e) Schematic representation and UV/Vis absorption spectrum of the 2D zinc porphyrinic MOF, and kinetic plots of $ln([M]_0/[M]_t)$ *vs.* reaction time in the polymerization of MA from BTPA using the 2D zinc porphyrinic MOF under irradiation (10 mW cm^{-2}). Adapted with permission from (a) ref. 240 (Copyright 2018 American Chemical Society), (b) ref. 245 (Copyright 2022 The Royal Society of Chemistry), (c) ref. 247 (Copyright 2021 American Chemical Society), (d) ref. 257 (Copyright 2020 John Wiley & Sons, Inc.), and (e) ref. 258 (Copyright 2021 John Wiley & Sons, Inc.).

nodes, addition of polyvinylpyrrolidone (PVP) induced anisotropic growth of the frameworks and generation of ultrathin 2D nanosheets (Fig. 9e).[258] Ultrathin 2D nanosheets demonstrated more rapid polymerization kinetics than 3D MOFs owing to the higher aspect ratio, larger surface area, and more accessible catalytically active sites.[149,258,259]

4.3. Applications

High end-group fidelity in PET-RAFT polymerization allows the one-pot synthesis of multiblock copolymers comprised of vinyl monomers with various side chains *via* chain extension with subsequently added monomers. Multiple extensions technically would lead to the preparation of (ultra)high-molecular-weight polymers (Section 4.3.5). Vinyl ethers and cyclic monomers (*e.g.*, cyclic esters, thiiranes, and epoxides) which are ionically (not radically) polymerized can also be manually incorporated into the polymers at the designated positions with tunable lengths and numbers of blocks. This is owing to the orthogonality and compatibility of PET-RAFT polymerization with other polymerizations (Section 4.3.1.2). Moreover, by introducing specially designed monomers, CTA, or any additives, the control of architecture (Section 4.3.2), stereochemistry (Section 4.3.3), and dispersity (Section 4.3.4) has been achieved. It is noted that to fully demonstrate the versatility of PET-RAFT polymerization, strategies that include "click" reactions to synthesize structurally diverse polymers by linking multiple polymers possessing pre- or post-functionalized chain ends into a single chain are not discussed here. Becer and coworkers described various methodologies for multiblock copolymer synthesis.[260]

4.3.1. Sequence control

4.3.1.1. Multiblock copolymer synthesis. Multiblock copolymers are synthesized by a number of successful chain extensions. After each step, end-group fidelity should remain high, and the reactivity of the PC should be retained to restart polymerization reaction upon addition of new monomers. In their first discovery of PET-RAFT polymerization using $Ir(ppy)_3$ as a PC in 2014, Boyer and coworkers leveraged the effective retention of the DTB end group of the polymer to demonstrate whether chain extension could yield di-, tri-, or even deca-block copolymers.[31] The decablock copolymer of MA ($[poly(MA)]_{10}$, $M_{n,GPC}$ = ~82 000 g mol^{-1} and $Đ$ = ~1.40) was synthesized from BTPA by ten repeated quantitative polymerizations of MA (58–144 equivalents to the macroinitiator) dissolved in degassed DMSO as the viscosity of the reaction mixture increased with the number of polymerizations. Neither isolation of the macroinitiators nor an additional amount of PC was required. The tailing of GPC traces at the low molecular weight region was attributed to dead polymers and the gradual decrease in end-group fidelity (Fig. 10a). The final end-group fidelity after the tenth polymerization was calculated to be 68% from the deconvolution of the MWD. Similarly, the pentablock copolymer of five different monomers (methyl, ethyl, *n*-propyl, *n*-butyl, and *n*-pentyl acrylate) with the target DP of 50 for each monomer was synthesized from BSTP ($M_{n,GPC}$ = 28 390 g mol^{-1}, $Đ$ = 1.14, and end-group fidelity = ~80%).[261] By adding $Ir(ppy)_3$ of 10 ppm relative to the monomer in the polymerization of the first monomer, >89% monomer conversion was achieved in 24 hours and 48 hours for the first three and rest two reactions, respectively. The authors decided to increase the reaction time instead of the catalytic loading to avoid the loss of the end group which appeared in the GPC traces. A functional triblock copolymer of the monomers possessing ketone and trimethylsilyl-protected alkynes could also be synthesized although the fast reactivity of the latter monomer was considered to increase the dispersity to 1.24.

$Ru(bpy)_3Cl_2$ was the first reported PC that enabled the synthesis of $[poly(MA)_{70}]_{10}$-*b*-$poly(MA)_{90}$ and $[poly(DMAm)_{60}]_5$-

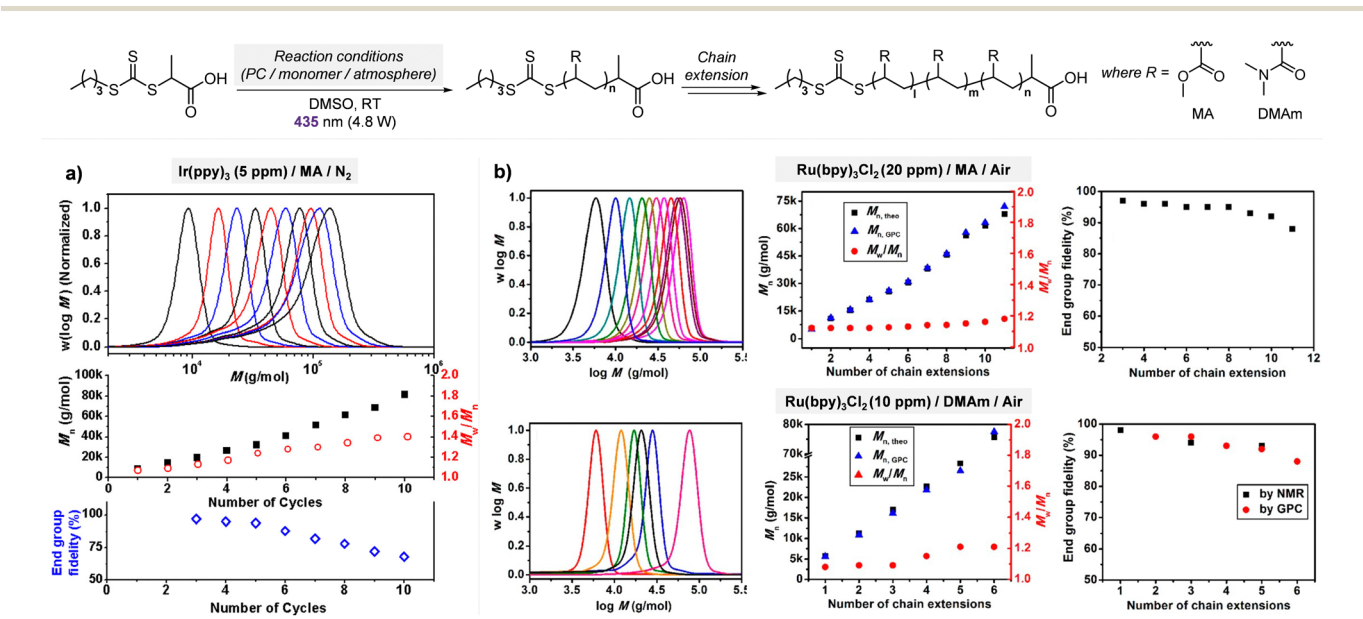

Fig. 10 Multiblock polymers of MA and DMAm obtained by PET-RAFT polymerization. Evolution of MWDs, M_n, M_w/M_n, and end-group fidelity *vs.* number of cycles of chain extensions for (a) $Ir(ppy)_3$- and (b) $Ru(bpy)_3Cl_2$-catalyzed reactions. Adapted with permission from (a) ref. 31 (Copyright 2014 American Chemical Society) and (b) ref. 129 (Copyright 2014 American Chemical Society).

b-poly(DMAm)$_{300}$ in DMSO in the presence of oxygen when used at 20 ppm and 10 ppm, respectively, under blue light irradiation (435 nm, 4.8 W) (Fig. 10b).[129] Herein, neither the reaction vessel nor the monomer solution was degassed, but polymerization was controlled such that the end-group fidelity determined by GPC remained higher than 86% and dispersity did not exceed 1.2. Owing to its aqueous solubility, Ru(bpy)$_3$Cl$_2$ was also employed for the oxygen-tolerant and rapid synthesis of a water-soluble triblock copolymer.[150] Ru(bpy)$_3$Cl$_2$ (25 ppm relative to the monomer) with ascorbate (two equivalents relative to BTPA) was employed to prepare poly(*N*-acryloylmorpholine (NAM))$_{40}$-*b*-poly(*N*,*N*-diethylacrylamide (DEAm))$_{40}$-*b*-poly(DMAm)$_{40}$ in water within an hour under blue light irradiation (470 nm, 26 mW cm^{-2}). Employment of a continuous flow reactor further enhanced the polymerization kinetics. EY disodium salt in combination with TEOA (0.01 and one equivalent relative to the CTA, respectively) allowed the rapid oxygen-tolerant synthesis of the triblock copolymer poly(DMAm)$_{100}$-*b*-poly(DMAm)$_{50}$-*b*-poly(DMAm)$_{50}$ ($Đ$ = 1.39) and [poly(DMAm)$_{10}$]$_3$ ($Đ$ = 1.24) within 15 minutes without prior deoxygenation.[136] Meanwhile, ZnTPP that could achieve oxygen tolerance in DMSO without any additives solely pushed the limit to HTP polymerization in a 96-well plate. At diluted monomer concentration (1.0 M), 400 ppm of ZnTPP under yellow light irradiation (560 nm, 9.7 mW cm^{-2}) provided [poly(NAM)$_{25}$]$_6$ ($M_{n,GPC}$ = 20 900 g mol^{-1} and $Đ$ = 1.19) with low molecular weight tailing.[262] This simple and efficient ZnTPP-catalyzed HTP polymerization has enabled the simple and efficient synthesis of high-order block copolymers to construct a library of polymers with varying sequences, compositions, molar ratios between different monomer functionalities (*e.g.*, cationic, hydrophobic, and hydrophilic), or structures, which revealed the relationship between the structures and properties of polymers in antimicrobial activities[263,264] and polymer–protein binding interactions.[265,266]

Liao, Lalevée, and coworkers developed a novel organic PC oxygen-doped anthanthrene (ODA) for metal-free synthesis of [poly(*n*-BA)]$_{10}$ ($M_{n,GPC}$ = ∼143.2 kg mol^{-1} and $Đ$ = ∼1.31) (Fig. 11).[267] The polymerization of the first block with ODA (5 ppm), BTPA as the CTA, and *n*-BA as the monomer (100 equivalents relative to BTPA) under blue light irradiation (455 nm, 3 mW cm^{-2}) was followed by multiple chain extensions with degassed *n*-BA (100 equivalents relative to the macroinitiator) for four hours per step.

4.3.1.2. Incorporation of various monomers into a single polymer chain. PET-RAFT polymerization with radical intermediates is orthogonal to other polymerizations with ionic intermediates. Moreover, the use of light as an energy source allows selective activation of PET-RAFT polymerization and consumption of radically polymerizable vinyl monomers (*e.g.*, (meth)acrylates and (meth)acrylamides) from the reaction mixture in which ionically polymerizable monomers (*e.g.*, vinyl ether and cyclic monomers) also exist. The remaining monomers can be independently polymerized in the presence of corresponding initiators. Therefore, using appropriately designed initiators, various monomers can be incorporated into a single polymer chain *via* dual polymerization processes.

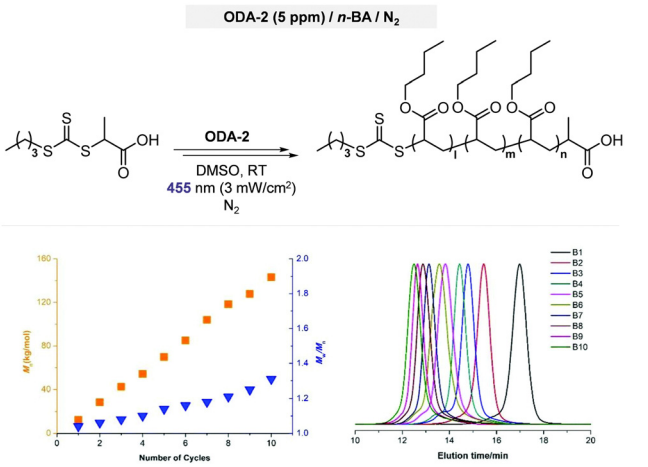

Fig. 11 Multiblock polymers of *n*-BA obtained by ODA-2-catalyzed PET-RAFT polymerization. Evolution of M_n, M_w/M_n, and MWDs *vs.* number of cycles of chain extensions. Adapted with permission from ref. 267 (Copyright 2022 The Royal Society of Chemistry).

First of all, the same dormant TTC can be activated to undergo either PET-RAFT or (photomediated) cationic RAFT polymerization. Fors and coworkers, for the first time, reported wavelength-dependent activation of Ir(ppy)$_3$ at 450 nm for PET-RAFT polymerization of MA and of pyrylium tetrafluoroborate salt at 520 nm for photomediated cationic RAFT polymerization of iBVE (Table 3, entry 1).[124] However, as the pyrylium salt also exhibited absorption at 450 nm, the catalyst loading had to be regulated to selectively activate PET-RAFT polymerization and avoid the synthesis of tapered block copolymers. On the other hand, cationic RAFT polymerization could be activated by (electro)chemical means which are completely orthogonal to light stimuli. The CTA was oxidized by adding ferrocenium tetrafluoroborate salt and deactivated by adding one equivalent of DTC anion into the reaction mixture to cap the propagating cations and reduce the ferrocenium salt (Table 3, entry 2).[119] In the electrochemical activation, the CTA was oxidized by anodic oxidation of ferrocene (as a redox mediator) to ferrocenium and deactivated by applying cathodic current, and the concentration of ferrocene should be kept low to prevent the quenching of the triplet excited-state of Ir(ppy)$_3$ and block the PET-RAFT polymerization (Table 3, entry 3).[116] Instead, Alaniz, Sepunaru, and coworkers utilized PTH as the redox mediator (Table 3, entry 4).[117] As PTH catalyzed the PET-RAFT polymerization of MA (380 nm, 3 mW cm^{-2}), switching between two polymerizations by toggling two corresponding external stimuli successfully generated block copolymers of vinyl ether and acrylate up to tetrablocks. Meanwhile, Satoh and coworkers reported that the change of irradiation wavelength could affect the ratio of the two monomers separately incorporated by two orthogonal processes and the number of interconversions (Table 3, entry 5).[121] Herein, cationic RAFT polymerization was kept constantly "on" by the presence of Lewis acid B(C$_6$F$_5$)$_3$ and only ZnTPP-catalyzed PET-RAFT polymerization could be reversibly activated. Under red light irradiation (630 nm, 45 mW), both MA and iBVE participated in polymerization. The diad sequence of iBVE in ^{13}C NMR

Table 3 Reported polymerization methods that can be combined with PET-RAFT polymerization for multiblock copolymer synthesis

	PET-RAFT polymerization			Combined polymerization			
Entry	PC (stimuli)	Monomer	Initiator	Mechanism	Reagents (stimuli)	Monomer	Ref.
1	$Ir(ppy)_3$ (on/off: light, 450 nm)	MA	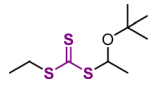	Cationic RAFT polymerization	Pyrylium salt (on/off: light, 520 nm)	iBVE	124
2	$Ir(ppy)_3$ (on/off: light, 450 nm)	MA	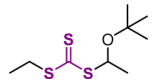	Cationic RAFT polymerization 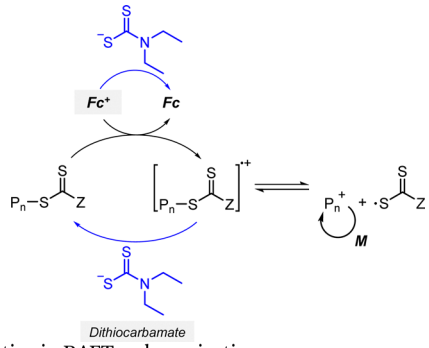	Ferrocenium tetrafluoroborate salt ($FcBF_4$)/ dithiocarbamate (on/off: chemical redox reaction)	iBVE	119
3	$Ir(ppy)_3$ (on/off: light, 455 nm)	MA	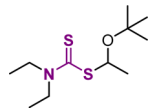	Cationic RAFT polymerization 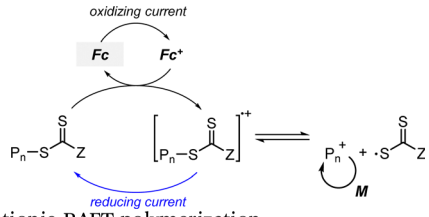	Ferrocene (Fc) (on/off: electrical redox reaction)	iBVE	116
4	10-phenyl phenothiazine (PTH) (on/off: light, 380 nm)	MA	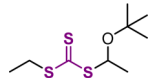	Cationic RAFT polymerization 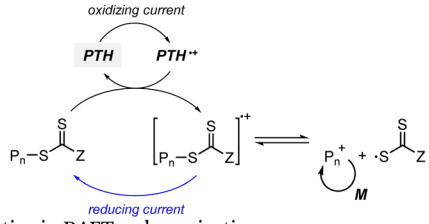	PTH (on/off: electrical redox reaction)	iBVE	117
5	ZnTPP (on/off: light, 630 nm)	MA	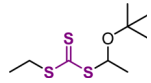	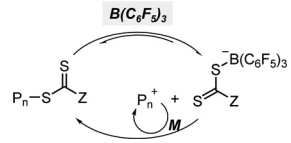	$B(C_6F_5)_3$ (only on)	iBVE	121

Table 3 (*continued*)

Entry	PET-RAFT polymerization: PC (stimuli)	Monomer	Initiator	Combined polymerization: Mechanism	Reagents (stimuli)	Monomer	Ref.
6	$Ir(ppy)_3$ (on/off: light, 460 nm)	MA	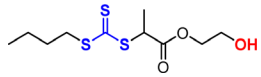	Cationic ring-opening polymerization	Diphenyl phosphate (on)	ε-Caprolactone	123
7	$Ir(ppy)_3$ (on/off: light, blue)	MA	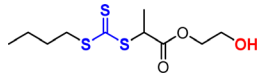	Cationic ring-opening polymerization	Diphenyliodinium triflate (DPITF) + $Ir(ppy)_3$ (on/off: light, blue) 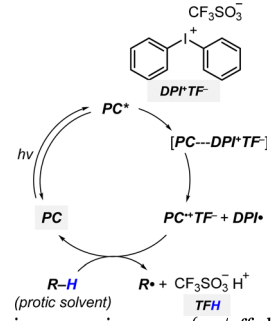	δ-Valerolactone	120
8	ZnTPP (on/off: light, 635 nm)	MA	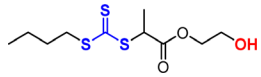	Cationic ring-opening polymerization	Merocyanine ↔ spiropyran (on/off: light, 460 nm) 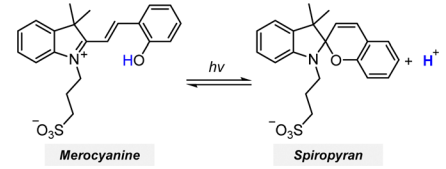	δ-Valerolactone	118
9	$Ir(ppy)_3$ (on/off: light, blue)	DMAm, NIPAm	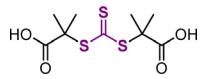	Anionic ring-opening polymerization 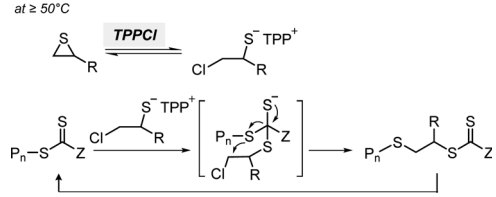	Tetraphenylphosphonium chloride (TPPCl) (on/off: heat, >50 °C)	Thiiranes	115

spectra, which was not observed in the PET-RAFT polymerization of MA and iBVE, confirmed that the Lewis acid-catalyzed cationic RAFT and ZnTPP-catalyzed PET-RAFT polymerization from the common CTA were interconvertible. Under green light irradiation (525 nm, 20 mW), the contribution of PET-RAFT polymerization was higher and the consumption of iBVE was lower than that under red light irradiation owing to more active generation of the TTC anion.

Other monomers including cyclic monomers (*e.g.*, cyclic esters and epoxides) can be incorporated into a single polymer chain using a bifunctional initiator prepared by the functionalization of the CTA with a hydroxyl group, for example, *via* the esterification of the carboxylic acid moiety in the R group. Boyer and coworkers firstly reported the one-pot synthesis of block copolymers by a combination of PET-RAFT polymerization and another polymerization method (Table 3, entry 6).[123] The block copolymer of ε-caprolactone and MA was synthesized using diphenyl phosphate and $Ir(ppy)_3$ and the ratio of the length of each block was simply controlled *via* the temporal control of PET-RAFT polymerization (460 nm, 0.7 mW cm^{-2}). You and coworkers employed diphenyliodonium triflate that only generated photoacid in the presence of $Ir(ppy)_3$ under blue light irradiation (10 W) and then catalyzed the cationic ROP of δ-valerolactone (Table 3, entry 7).[120] $Ir(ppy)_3$ could still catalyze PET-RAFT polymerization after the addition of MA to the reaction mixture. In this case, both processes required irradiation such that only diblock copolymers with defined orders could be obtained. Boyer and coworkers reported the generation of photoacid *via* intramolecular cyclization of merocyanine to spiropyran followed by dissociation of the proton under blue light irradiation (460 nm, 0.7 m cm^{-2}) (Table 3, entry 8).[118] ZnTPP that absorbs at 635 nm afforded orthogonality in wavelength and thus selective activation of two polymerizations. However, upon changing the light source from blue to red, the ROP of δ-valerolactone was not completely inactivated due to slow inactivation of the photoacid molecule. Effective switching between anionic ROP and PET-RAFT polymerization was realized using a combination of heat and light as two external stimuli (Table 3, entry 9).[115] Herein, the anionic ROP of the cyclic thiirane monomer using quaternary onium salts (tetraphenylphosphonium chloride) and TTC only proceeded at >50 °C due to the energy barrier to open the ring such that PET-RAFT polymerization of acrylamides under blue light irradiation (5 W) was orthogonally conducted at room temperature. As the reaction temperature and irradiation wavelength were easily switched in an orthogonal manner, interconversion of two polymerizations five times from symmetric TTC provided an undecablock copolymer (Fig. 12). Programmed heating and/or irradiation, such as intermittent irradiation during heating, enabled precise insertion of the DMA block at any position within the homopolymer of thiiranes, which would otherwise require careful consideration of the reactivities of monomers.

Lastly, in addition to ionic polymerization, radical-mediated O-ATRP was selectively activated with PET-RAFT polymerization. Boyer, Miyake, and coworkers reported that *N*,*N*-diaryl dihydrophenazine could catalyze not only O-ATRP but also PET-RAFT polymerization, based on the similarity between two reaction mechanisms and hence the required catalytic properties.[125] Interestingly, PET-RAFT polymerization required less amount of PC as compared to O-ATRP of MMA. Therefore, using alkyl bromide-functionalized CTA and by increasing the loading of PC from 50 to 500 ppm, diblock copolymers could be obtained *via* PET-RAFT polymerization of MA followed by O-ATRP of MMA.

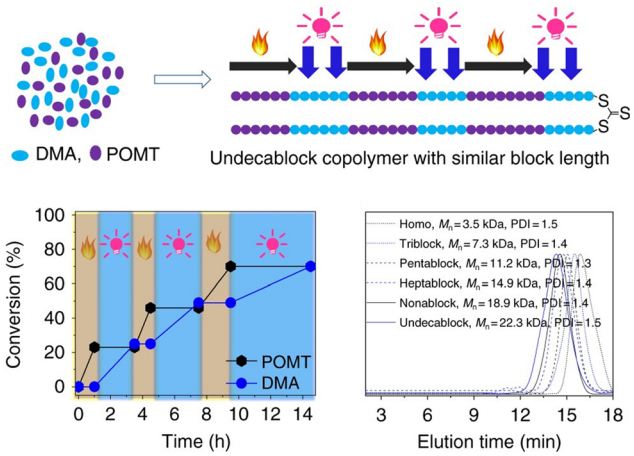

Fig. 12 Synthesis of an undecablock copolymer by multiple cycles of heating and irradiation. Under heating, 2-(phenoxymethyl) thiirane (POMT) was selectively consumed by TTC-mediated anionic ROP whereas under irradiation DMAm was consumed by PET-RAFT polymerization. Adapted with permission from ref. 115 (open access).

4.3.1.3. Single unit monomer insertion (SUMI). SUMI refers to selective insertion of a single unit monomer at a time.[268] As the stability of the C–S bond changes after the insertion of a certain monomer, carefully designed reaction conditions (the combination of CTA, monomer, and PC) can only activate the initial CTA to which the monomer is added.[109] The monoadduct can be isolated and its synthesis can be confirmed by NMR, mass spectrometry, and gel permeation chromatography. Sequential SUMI of a series of monomers leads to discrete oligomers with known monomer sequences, which would pave the way for synthetic polymer chemistry to reach DNA or proteins possessing a high precision in the monomer sequence and the resulting functionalities. For example, the well-defined oligomers can be the building blocks for higher-order polymers or can provide a hint at the stereochemical effect on the activation of the diastereomeric oligomeric CTA, which has been challenged by the difficulties in the preparation of appropriate materials.[269–271] Visible-light-driven RAFT polymerization under mild reaction conditions in the absence of exogenous radical initiators is advantageous to prepare polymers with high end-group fidelity and prevent the formation of initiator-derived byproducts, when compared to conventional thermally initiated polymerizations.

For successful SUMI (*i.e.*, to limit multiple additions of monomers), dissociation of the initial CTA should be preferred compared to that of the monoadduct *via* the increase in C–S bond dissociation energy along with the insertion of a monomer with a less stable R group (Scheme 20a). If the monoadduct

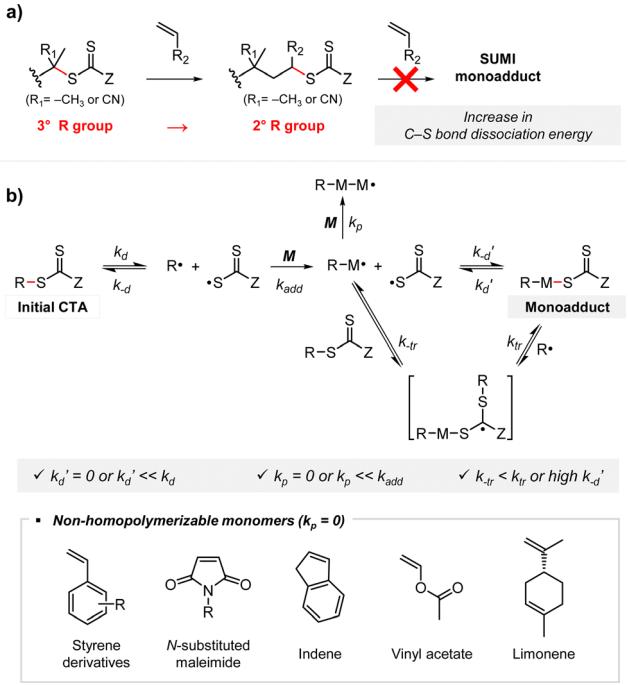

Scheme 20 (a) Mechanism and (b) requirements for SUMI, where k_d (k_{-d}) is the decomposition (recombination) rate constant of the initial CTA under irradiation, k_{add} is the addition rate constant of a monomer to the R group radical of the initial CTA, k_p is the propagation rate constant of the second monomer to the R group radical of the SUMI monoadduct, k_{tr} is the chain transfer rate constant of the R group radical of the initial CTA to the SUMI monoadduct, k_{-tr} is the chain transfer rate constant of the R group radical of the SUMI monoadduct to the initial CTA, and k_d' (k_{-d}') is the decomposition (recombination) rate constant of the SUMI monoadduct under irradiation.

decomposes, deactivation of the propagating radical instead of propagation by either recombination or chain transfer to the initial CTA is required (Scheme 20b). The use of non-homopolymerizable monomers, such as styrene, *N*-substituted maleimide, VAc, limonene, and indene, with low k_p is also helpful. The blue shift of the UV absorption band of the monoadduct to lower wavelengths as compared to that of the initial CTA enabled selective and efficient activation of the initial CTA by light.[272] However, in cases where the selected monomers were purposely inserted in desired sequences *via* success SUMI, PCs such as PheoA,[106] Ir(ppy)$_3$,[89] and/or ZnTPP[89,269,270,273,274] were necessary to achieve reasonably high reaction efficiencies under mild reaction conditions. Using ZnTPPS$_4^-$, a water-soluble analogue of ZnTPP, Moad and coworkers observed the significant enhancement of reaction kinetics in SUMI of DMAm as a model monomer in water.[199]

For example, in the first report of the synthesis of trimers by Boyer, Moad, Hawker, Xu, and coworkers, the insertion of the first monomer styrene into CDTPA under green light irradiation (530 nm, 0.6 m cm^{-2}) was followed by the Ir(ppy)$_3$-catalyzed PET-RAFT polymerization of the second monomer *N*-substituted maleimide under blue light irradiation (460 nm, 0.8 mW cm^{-2}) (Scheme 21a).[89] The combination of styrene and maleimides is well-known for alternative copolymerization due to the formation of donor–acceptor pairs. The last third monomer VAc or limonene was inserted using ZnTPP under red light irradiation (635 nm, 0.4 mW cm^{-2}) or Ir(ppy)$_3$, respectively, because Ir(ppy)$_3$ resulted in multiple addition of VAc. Further functionalization of the trimers provided a new methacrylate monomer possessing a precisely defined side chain of hexamer as a potential building block for periodic polymers. Later, Boyer and coworkers

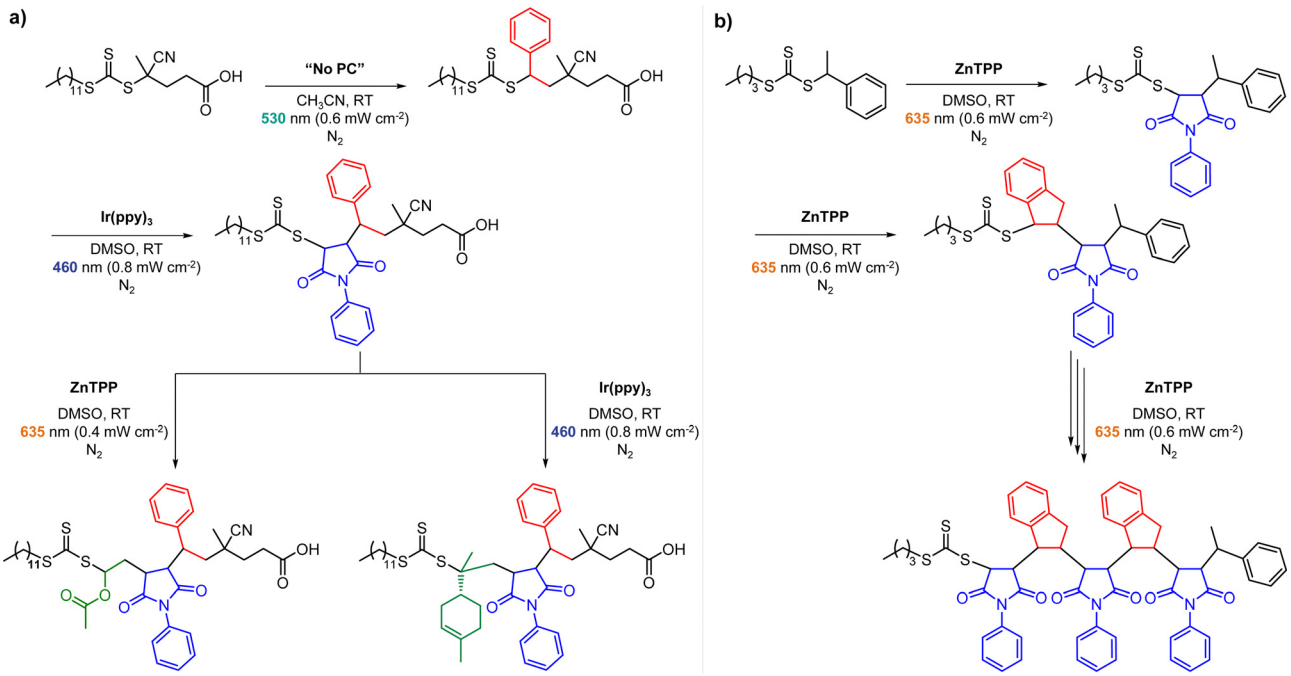

Scheme 21 Synthetic scheme for a discrete (a) trimer[89] and (b) pentamer.[273]

conducted sequential SUMI of up to five monomers in the gram scale while addressing scalability problems by the use of flow reactors for reaction and automated flash chromatography for purification.[273] ZnTPP in DMSO imparted oxygen tolerance and non-homopolymerizable electron-donating indene and electron-accepting *N*-substituted maleimide derivatives were alternatively polymerized (Scheme 21b).

Meanwhile, discrete oligomeric CTAs have aided the investigation of the stereochemical effect on photoactivation, copolymerization kinetics of a certain monomer in the RAFT process, and the influence of precisely designed sequences on polymeric properties. Into the pool of pairs of electron-donating (*e.g.*, indenes and (β-methyl)styrene derivatives) and electron-accepting monomers (*e.g.*, *N*-substituted maleimides), various functionalities can be introduced as their substituents. Initially, SUMI of various α,β-disubstituted vinyl monomers led to the synthesis of a stereospecific discrete oligomeric CTA.[269,270] Insertions of the examined cyclic *N*-substituted maleimides in trans-configurations were preferred owing to steric hindrances and restricted rotations of cyclic monomers, as combinedly evidenced by structural analysis by single-crystal X-ray diffraction and QC calculations.[269]

Xu and coworkers reported that for the successful SUMI of β-methylstyrene derivatives, careful selection of the CTA was required.[275] When β-methylstyrene derivatives were inserted next to maleimide into TTCs with different R groups using ZnTPP, the dimer was formed in 50% yield despite the complete conversion of the starting monoadduct of maleimide due to the degradation of the desired dimer after a certain reaction time. The proposed degradation mechanism was based on the β-methylstyrenenic carbon radical, which when fragmented abstracts hydrogen from an excess of β-methylstyrene derivatives and can no longer participate in the RAFT process (*i.e.*, chain transfer or recombination). Therefore, the authors postulated that to prevent the degradation of the product, (i) chain transfer of the fragmented β-methylstyrenenic carbon radical should occur faster than the hydrogen abstraction and (ii) the starting monoadduct should possess a better leaving R group than β-methylstyrenes. As expected, quantitative formation of the dimer was achieved when the first monomer was changed from maleimide to acrylonitrile (AN).

Xiao, Lai, and coworkers synthesized trimers consisting of two *N*-substituted maleimides and 5,6-benzo-2-mehtylene-1,3-dioxepane (BMDO) in between from *n*-butyl benzyl TTC (BBTC).[274] BMDO is a cyclic ketene acetal monomer whose radical ROP affords a polymer with a degradable ester bond in the backbone. Contrary to the successful insertion of *N*-substituted maleimide into BBTC using ZnTPP in DMSO under red light irradiation (620 nm), the use of thermal initiator lauroyl peroxide in toluene was required for the insertion of BMDO due to hydrolysis of BMDO in hygroscopic DMSO and poor solubility of ZnTPP in toluene (Scheme 22a). Two model trimers, BBTC-*N*-phenyl maleimide (PMI)-BMDO-*N*-methyl maleimide (MMI) and BBTC-PMI-BMDO-PMI, were degradable under basic conditions and cytocompatible with the human normal cell line (HUVEC) at up to 600 μmol L^{-1} concentration (Scheme 22b), but only BBTC-PMI-BMDO-MMI was cytotoxic to the human cancer cell line

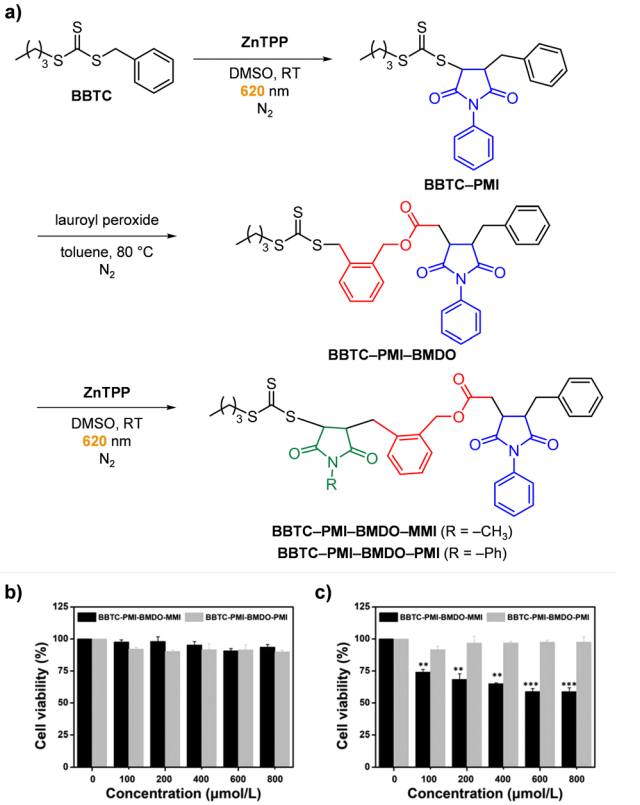

Scheme 22 (a) Synthetic scheme for the trimers BBTC-PMI-BMDO-MMI and BBTC-PMI-BMDO-PMI. Cell viability of the two trimers against (b) human normal cell line (HUVEC) and (c) human cancer cell line (MCF-7) after 24 hours of incubation. Adapted with permission from (b) and (c) ref. 274 (Copyright 2021 American Chemical Society).

(MCF-7) (Scheme 22c) implying the potential of sequence-defined oligomers for biological applications.

4.3.2. Architecture control

4.3.2.1. Design of the CTA. Designing an appropriate initiator is one of the simplest ways to obtain polymers with complex architectures (Scheme 23). For example, star or multi-arm polymers have been synthesized from multi-arm CTAs.[265,276–279] Multi-arm TTCs were prepared from thiols, carbon disulfide, and scaffold molecules with multiple bromines which underwent substitution reactions, whereas multi-arm xanthates were prepared using xanthogenate instead of thiol and carbon disulfide. Multi-arm polymers have been examined for various applications. Chapman, Boyer, and coworkers prepared a series of star polymers from two, three, or four-arm CTAs to investigate the relationship between the structures and binding affinities of polymers to protein.[265] Gormley, Chapman, and coworkers employed simple and oxygen-tolerant HTP polymerization to build a library of multivalent polymers possessing a strained alkyne at each arm end, which may be useful for conjugating biomolecules *via* strain-promoted azide-alkyne cycloaddition (SPAAC).[276] Boyer, Corrigan, Zhang, and coworkers controlled the mechanical properties of 3D printed objects in a broad range by optimizing the compositions (*i.e.*, the ratio and concentrations of multi-arm CTAs possessing different number of arms) of

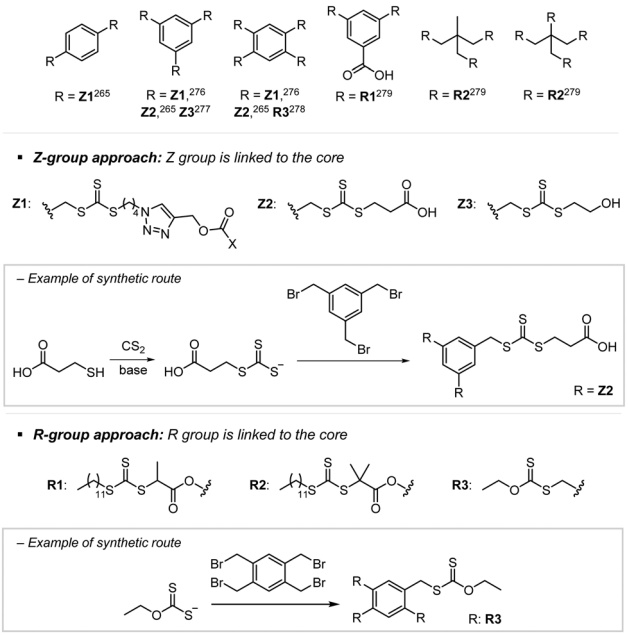

Scheme 23 Examples of multi-arm CTAs and the corresponding synthetic routes.

3D printable resins.[279] Finally, Chapman and coworkers analyzed the effects of the type of monomers (hydrophobic, hydrophilic, and charged) and their order of arrangements on the sizes and assemblies of multiblock star polymers in solution.[277]

It is noted that the core of star polymers can be linked to either the R or Z group of the CTA (Scheme 23). In the Z-group approach, the polymers grow from the fragmented R group liberated from the core, whereas in the R-group approach, the polymers grow from the core. For controlled polymerization, the Z-group approach is suitable to attach short arms at low grafting density because steric hindrance limits reattachment and chain transfer of propagating chains to the core Z group. The R-group approach suffers from biomolecular radical termination between either two star polymers (star–star coupling) or a star polymer and an exogenous macroradical rather than from the steric hindrance. Star–star coupling results in higher molecular weight byproducts, and reattachment of the exogenous macroradical instead of the Z group leads to the loss of CTA functionality and livingness, preventing further polymerization from dead chains to broaden the dispersity. Therefore, the synthesis of well-defined star polymers with (ultra)high molecular weights or multiple blocks with preserved end-group fidelity has particularly been challenging. Photocontrolled RAFT polymerization in the absence of exogenous initiating radicals thus emerged as a successful solution to the abovementioned problem as observed for photoiniferter polymerization by Qiao and coworkers[278] and PET-RAFT polymerization by Chapman and coworkers (Fig. 13).[277]

4.3.2.2. Design of the monomer. Other unique advantages of photocontrolled RAFT polymerization include spatiotemporal control, selectivity (which needs to be satisfied for the productive activation of the RAFT process), and orthogonality (to other polymerization methods). Carefully designed reaction conditions or systems along with properly functionalized monomers have enabled the preparation of complex polymeric architectures such as graft, comb-like, bottlebrush, and (hyper)branched polymers. For example, so-called "inimer" contains initiating moieties for two polymerizations, which can be activated selectively and in series (Scheme 24). Initially, as a mono"mer" for RAFT polymerization, the vinyl moiety comprises a polymer backbone while the other initiating moiety remains unreacted in the side chain. By changing the reaction conditions (*e.g.*, irradiation wavelength) or adding different types of monomers, the remaining "ini"tiator is then activated for another polymerization to transform the linear polymer into polymers with grafting chains or other high complexities.

Boyer, Xu, and coworkers synthesized graft copolymers *via* two selectively activated PET-RAFT polymerizations (Scheme 8 and 24a).[106] The reaction mixture contained two pairs of PC

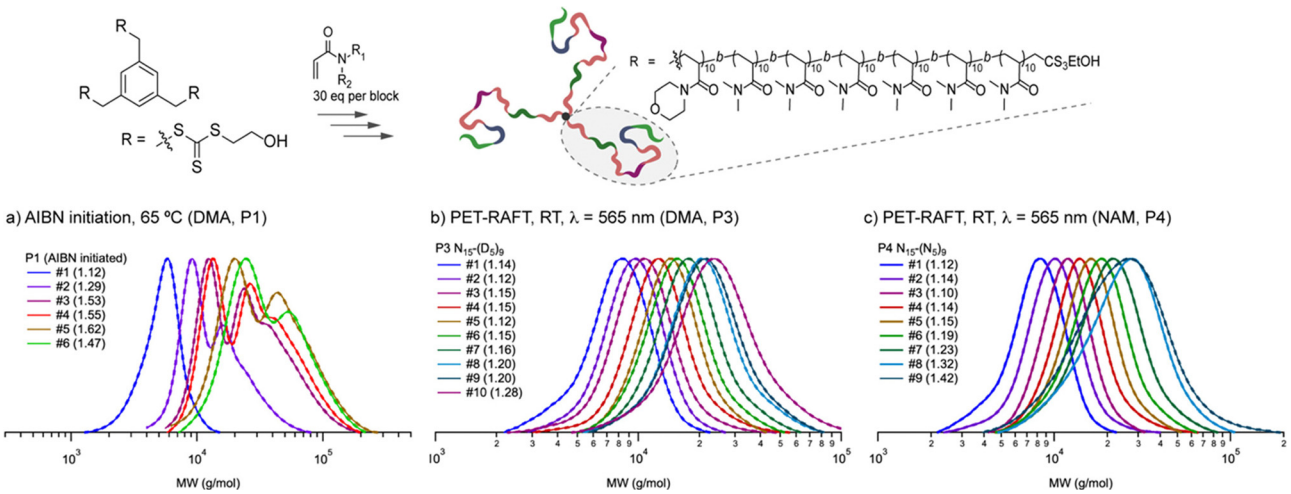

Fig. 13 Synthesis of multiblock star polymers by thermal and ZnhTPP-catalyzed PET-RAFT polymerization. MWDs after each chain extension are shown below. Adapted with permission from ref. 277 (Copyright 2022 American Chemical Society).

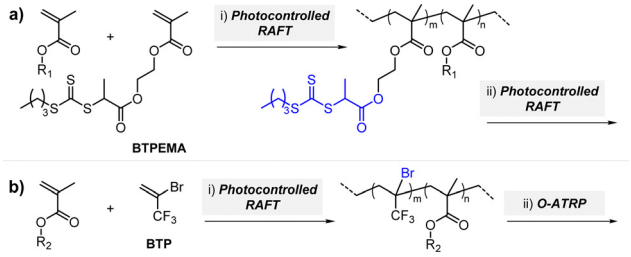

Scheme 24 Example of functionalized monomers and their stepwise activation to control polymer architectures.[106,211]

and CTA. The methacrylic polymer backbone was synthesized by the PheoA-catalyzed PET-RAFT polymerization of MMA and another methacrylate embedded with a TTC (BTPEMA) from CPADB under red light irradiation (690 nm, 2 mW cm^{-2}). Then, MA was added to the reaction mixture for the ZnTPP-catalyzed PET-RAFT polymerization from the TTCs under green light irradiation (530 nm, 0.6 mW cm^{-2}) to graft acrylic chains along the backbone. Herein, selective activation was possible as (i) the irradiation wavelengths were carefully set to avoid overlap in the absorption profiles of the two PCs PheoA and ZnTPP, and (ii) the pair of PheoA–CPADB and ZnTPP–TTC exhibited specific PC–CTA interaction. Selective excitation of one PC led to concomitant selective activation of one CTA within the reaction mixture. Switching the irradiation wavelength enabled sequential two-step polymerization in one-pot. However, it is noted that the second monomer MA should be added after the polymerization of MMA from CPADB because otherwise the insertion of MA into CPADB would block further propagation due to the change in C–S bond dissociation energy. Boyer, Hawker, Moad, and coworkers coupled PET-RAFT polymerization with photoiniferter polymerization (Fig. 14a).[280] At first, the methacrylic backbone of MMA and BTPEMA was prepared from CDTPA *via* green light-mediated photoiniferter polymerization (520 nm, 4.4 W m^{-2}) at 60 °C. Model polymerization of MMA confirmed that after the addition of MMA into CDTPA or BTPA, fragmentation of the RAFT intermediate was only favored for CDTPA owing to higher C–S bond dissociation energy. Subsequently, the unreacted BTPA moieties in the side chains were polymerized with DMAm. In this step, despite the increase in reaction temperature and/or irradiation at shorter wavelengths (*i.e.*, with higher energy), the rate of polymerization was not sufficiently high. Thus, PET-RAFT polymerization using ZnTPP was conducted instead. This one-pot approach could be operated even in one-pass using a flow reactor. In a one-pass reaction system, the solution of DMAm and ZnTPP for the second reaction was easily added before the reaction mixture flows to the second batch, and irradiation of each batch was separately turned on and off. Moreover, by simply varying the injection volume, concentration, flow rate, and/or irradiation time, the synthesis of diverse graft and branched copolymers possessing backbones and/or side chains with different lengths and backbones with different numbers of grafted chains was achieved. Matyjaszewski and coworkers utilized two sequential photoiniferter polymerizations for the synthesis of comb-like and bottlebrush polymers.[110] The polymerization of the methacrylic backbone from CDTPA under green light irradiation (520 nm, 4.25 mW cm^{-2}) was followed by the polymerization of MA or DMAm from pendant BTPA of polymerized BTPEMA under blue light irradiation (465 nm, 6.5 mW cm^{-2}). Depending on the MMA/BTPEMA ratio in the first polymerization, the grafting density of acrylic side chains in the resulting polymer was facilely controlled so that the homopolymer of "inimer" was transformed into a bottlebrush polymer.

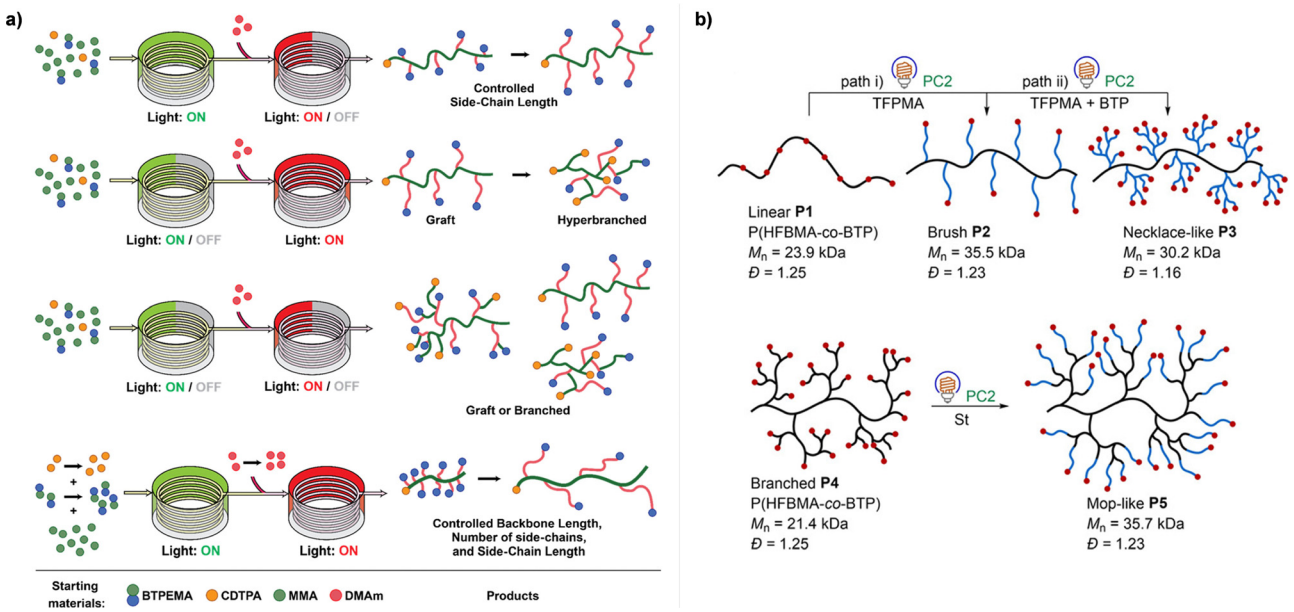

Fig. 14 Diverse polymer architectures obtained by (a) switching each reactor on and off or manipulating the parameters (*e.g.*, flow rate and injection volume) in flow chemistry and (b) combination of different photomediated RDRP processes. Adapted with permission from (a) ref. 280 (Copyright 2021 American Chemical Society) and (b) ref. 211 (Copyright 2020 John Wiley & Sons, Inc.).

The second polymerization from the initiating moiety of the inimer after the first polymerization of vinyl moieties need not be limited to visible-light-driven RAFT polymerization. The orthogonality of visible-light-driven RAFT polymerization to other polymerization methods and the accompanying ability to interconvert two orthogonal processes for the facile synthesis of multiblock copolymers possessing various (non)vinyl monomers has been discussed in Section 4.3.1.2. Chen and coworkers designed an inimer containing both vinyl and alkyl bromide functionalities for photocontrolled divergent synthesis of polymers with a wide variety of topologies (Scheme 24b).[211] The reaction system comprised two PCs (EY and a phenothiazine derivative), fluorinated-TTC, methacrylate monomers bearing different numbers of fluorine atoms, and 2-bromo-trifluoropropene (BTP) as an inimer (Fig. 14b). Owing to the different excited-state redox potentials, reduction of bromine for O-ATRP after the polymerization of BTP could only be achieved using the phenothiazine-derived PC, whereas TTC could be reduced by both PCs for PET-RAFT polymerization. Therefore, EY-catalyzed PET-RAFT polymerization of the linear copolymer of BTP and other monomers followed by phenothiazine derivative-catalyzed O-ATRP afforded branched polymers in which bromine at any location served as a branching point. Variation in the ratio of BTP and other monomers in copolymerization, target DP, and/or location of bromine led to various polymer topologies such as linear, brush, necklace-like, branched, and mop-like.

4.3.3. Stereochemistry control. Control over stereochemistry during polymerization or tacticity of polymers is known to critically affect the thermomechanical properties of polymeric materials. However, stereocontrolled polymerization of vinyl monomers has been challenged by the generation of a planar sp^2-hybridized propagating radical with no facial preference for the addition of monomer.[281] Selective addition of the monomer to one face can be achieved in the presence of auxiliary additives that confine the propagating radical. Boyer and coworkers added rare earth triflate $Y(OTf)_3$ into the stereocontrolled $Ir(ppy)_3$-catalyzed PET-RAFT polymerization of DMAm in a methanol/toluene mixture under blue light irradiation (460 nm, 0.7 mW cm^{-2}).[282] Coordination of the Lewis acid $Y(OTf)_3$ to the amide functionalities of the monomer during polymerization allowed good control over the tacticity of polymers (Scheme 25). Although the weaker yet possible coordination of $Y(OTf)_3$ to TTCs slightly increased the dispersity, control over the molecular weight or livingness was not influenced so that a stereoblock or stereogradient copolymer of atactic and isotactic blocks could be prepared. The authors modulated the tacticity of polymers by using DMSO which tightly complexes with $Y(OTf)_3$ to weaken the complexation between $Y(OTf)_3$ and DMAm and thereby offers stereochemistry control. Nevertheless, the reaction system could not be expanded to another PC (*i.e.*, $Ru(bpy)_3Cl_2$) presumably due to unfavorable interaction between the bipyridine ligand and $Y(OTf)_3$. Substitution of $Ir(ppy)_3$ for $Ru(bpy)_3Cl_2$ resulted in no or poorly controlled polymerization. On the other hand, for photoiniferter polymerization in the absence of a PC, Zhu, Boyer, and coworkers employed the fluoroalcohol 1,1,1,3,3,3-hexafluoro-2-propanol (HFIP) to control the stereochemistry of poly(VAc).[283] Interaction of fluoroalcohol with vinyl monomers introduced steric hindrance and improved stereospecificity during propagation. These interactions enhanced at low temperatures, so syndiotacticity of the polymer was controlled by temperature and the choice of solvent. The highest syndiotacticity diad (62%) for polymerization in HFIP as a solvent at −20 °C was decreased to 59 and 56% along with an increase in the polymerization temperature to 0 and 25 °C, respectively, whereas the change of solvent to isopropyl alcohol or bulk polymerization led to 52 or 53%. The dependencies of stereospecificity on the polymerization temperature and solvent were consistent with those reported by Kwark and coworkers for the preparation of syndiotactic-rich poly(VAc) using fluoroalcohols.[284] Herein, the polymerization was initiated by photoinitiator BAPO.

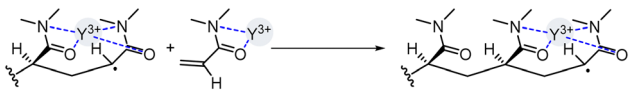

Scheme 25 Coordination of $Y(OTf)_3$ to the amide functionality to increase the isotacticity of poly(DMAm).[282]

4.3.4. Dispersity control. Apart from the main challenge and aim of RDRP to synthesize nearly monodisperse polymers, the usefulness to tailor the dispersity and shape (*e.g.*, breadth, skewness, and kurtosis) of MWD has been revealed to be important for controlling the physical, thermal, and rheological properties of polymers.[53,285,286] Synthetic strategies reported thus far include physical blending of polymers with a range of dispersities, temporally regulated initiation to prepare polymers with different lengths, and tailoring catalyst concentration.[287]

Boyer and coworkers introduced flow chemistry in combination with the use of ZnTPP as a PC.[288–290] In PET-RAFT polymerization of acrylamides in a continuous flow reactor, polymers of different molecular weights were generated by simply adjusting the flow rates, concentration of the CTA, and intensity or wavelength of the light source (blue, green, or red).[288] Blending of the prepared polymers resulted in the target MWD as per the calculated theoretical curves (Fig. 15a)[288] or the mathematically modelled fitting which is the so called computer-guided approach.[290] The polymer retained high end-group fidelity so that polymerization from the blended poly(DMAm) led to successful copolymerization with NAM or benzyl acrylate (BzA) and yielded a block copolymer with tailored compositional gradients (Fig. 15b).[289] The second monomer was easily added from a separated line (pump) in the flow setup. However, to fully utilize the aforementioned simplicity and robustness of the flow chemistry technique for dispersity control, fluid dynamics or profiles and parameters such as tube diameter, volume, flow rate, and reactant volume have to be carefully investigated and optimized.[290]

In the case of PET-RAFT polymerization in batch, Anastasaki and coworkers mixed two CTAs at varying ratio,[291] as previously applied for AIBN-initiated conventional RAFT polymerization by the same research group.[292] In EY-catalyzed PET-RAFT polymerization in DMSO under blue light irradiation (465 nm, 12 W), two CTAs possessing different transfer constants or reactivities

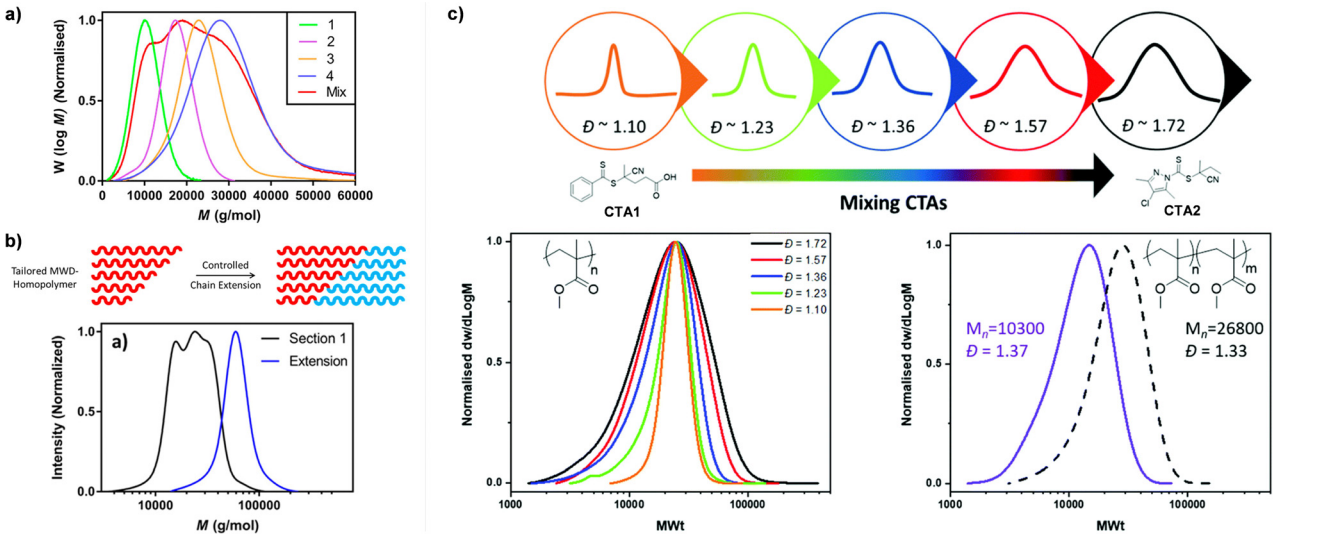

Fig. 15 (a) MWDs for monomodal poly(DMAm)s (1–4) and their blended mixture. (b) Narrowing the initially broad MWD through chain extensions. (c) The variation in dispersity as two CTAs were mixed in different ratios (aligned by the peak molecular weight value). Poly(MMA) prepared from 10 mol% CTA1 and 90 mol% CTA2 was successfully extended with MMA. Adapted with permission from (a) ref. 288 (Copyright 2017 American Chemical Society), (b) ref. 289 (Copyright 2018 American Chemical Society), and (c) ref. 292 (Copyright 2020 The Royal Society of Chemistry).

(dictated by R and mostly Z group) were mixed at varying ratios to obtain polymers with any intermediate targeted value of dispersity (Fig. 15c). One CTA with the higher transfer constant afforded polymers with low dispersity (as the lower limit), whereas another CTA with the lower transfer constant afforded polymers with high dispersity (as the higher limit). Apart from the discrepancy in reactivities, two CTAs should separately provide monomodal MWD, high end-group fidelity, and agreement between theoretical and experimental molecular weights for polymerization of a given monomer. The method was effective for MMA, MA, and DMAm in which dispersity was tunable across a wide range (1.08–1.82). Konkolewicz and coworkers expanded the abovementioned method to poly(vinyl ketone)s.[293] Herein, after the generation of initiating radicals through Norrish chemistry of vinyl ketone monomers under blue light irradiation (450 nm, 7.9 mW cm^{-2}), either homopolymers of phenyl or methyl vinyl ketone or copolymers of ethyl acrylate were synthesized from the mixture of TTC (higher activity) and xanthate (lower activity). Dispersity was increased with the ratio of xanthate and was able to be modulated further owing to the photodegradable nature of vinyl ketone under UV light irradiation.

Anastasaki and coworkers also utilized their strategy of mixing CTAs to prepare two homopolymers each possessing a wide range of dispersities and blended them to provide polymers with unrivalled precise control of both dispersity and MWD shape.[294] Moreover, the strategy was still valid for a single CTA with switchable reactivity, rather than the mixture of two CTAs.[295] Herein, the reactivity of the CTA (methyl 2-[methyl(4-pyridinyl)-carbamothioylthio]propionate) was *in situ* switched back and forth by the addition of acid and base to the reaction mixture. It was still only reported for VA-044 initiated thermal RAFT polymerization; nevertheless, it is notable that on-demand control over dispersity of the sequence-defined multiblock copolymer of acrylamides was accomplished by simply adjusting acidic and basic conditions along with the subsequent monomer addition.

4.3.5. Ultrahigh-molecular-weight (UHMW) polymer synthesis. Synthesis of UHMW polymers, with molecular weights over 10^6 g mol^{-1}, requires fast and efficient generation of propagating radicals and monomers with a high propagation rate, while minimizing the probability of side reactions (*i.e.*, chain transfer and termination).[296] As neither PET-RAFT nor photoiniferter polymerization uses external initiators, the reaction becomes free of the initiator-derived radicals and side reactions therefrom. Acrylamide monomers possessing high k_p in high polarity solvents (mostly water) coupled with efficiently photolyzable CTAs (mostly xanthate) thus has been extensively employed for UHMW polymer synthesis. Radical influx should be kept high enough for fast and efficient propagation but should be (re)generated in a controlled manner, which could be achieved under visible light irradiation exclusively by the use of a highly efficient PC in the case of PET-RAFT polymerization.

Supramolecular perylene diimide/cucurbit[7]uril complex/TEOA under green light irradiation (535 nm, 5 W) induced aqueous polymerization of DMAm from TTC with molecular weight up to 1.04×10^6 g mol^{-1} and a dispersity of 1.33 after 8 hours.[297] This photoinitiating system was so efficient that only 1 ppm was required, but the role of TEOA was claimed to be rather complex, including initiation of RAFT polymerization after its single-electron oxidation by excited-state perylene diimide. Photoenzymatic RAFT polymerization enabled the synthesis of UHMW polymers of unconjugated NVP, *N*-vinylcaprolactam with rather narrow dispersity ($Đ = \sim 1.39$)[164] and of monomers with low k_p (*e.g.*, OEGMA)[165] under violet light irradiation (405 nm, 11.5 W). These exceptional reactivities were attributed to the generation of stable radicals in low concentration by GOx/glucose as the PC, and the high reducing

power of excited-state $FADH^-$ to efficiently conduct the polymerization process.

On the other hand, Chen and coworkers reported a mechanically distinct strategy for the synthesis of UHMW fluoropolymers from TTCs (up to 3.05×10^6 g mol^{-1} and $D \leq 1.12$ after 2–8 hours) using $Ir(ppy)_3$ in DMSO under white light irradiation (33 mW cm^{-2}) (Fig. 16a).[190] Fluoropolymers from a polymer chemistry perspective have been appreciated due to their functionally diverse properties,[298] but here strong and selective fluorine–fluorine interaction also played a key role in excellent regulation over propagation (Fig. 16b). As depicted, at first, the CTA with a lipophilic DMAm block as the R group (denoted as R2) and an alkyl chain as the Z group (denoted as R1) stabilized the resulting emulsion with a fluorophilic interior where fluoromonomers were located. As some portions of the CTA (propagating group, PG) participated in polymerization, fluorine–fluorine interaction between the grown polymers and the monomers resulted in phase separation. The remaining intact CTA (supporting group, SG) residing in the outer solvent phase had no access to the monomer but to RAFT equilibrium, providing the polymerization of fluoromonomers from PG with the additional control and livingness. Replacing $Ir(ppy)_3$ with a PC possessing a fluoro-substituent significantly reduced monomer conversion, evidencing that single-electron transfer between the excited-state PC and CTA and subsequent polymerization occurred in the outer solvent phase. This distinctive spatial confinement strategy for the preparation of well-defined UHMW fluoropolymers was compatible with fluorinated (meth)acrylates and methacrylamides as well.

4.3.6. Photoinitiated polymerization-induced self-assembly (photo-PISA). Visible-light-driven RAFT polymerization has been applied to polymerization-induced self-assembly (PISA) to construct nano-sized assemblies with various morphologies including worms, vesicles, and micelles. These assemblies are used for nanocomposite fabrication or the encapsulation of hydrophobic drugs or proteins in vesicles. As the solvophobic block is extended from a macro-CTA with a solvophilic block, the resulting morphologies depend on the target DP or length of the solvophobic block, composition of the copolymer, and solid content. Compared to the case of the conventional thermally initiated RAFT polymerization, visible-light-driven RAFT polymerization has offered better control over particle size and expanded the available morphologies. In addition to the absence of exogenous radicals, the ability to maintain the reaction temperature throughout the entire process (from polymerization to phase separation-induced morphological transition) reduced the influence of high temperature on both the polymerization kinetics and morphology and allowed deriving an isothermal phase diagram. As not all thermal initiators require severe heating (typically above 70 °C), O'Reilly and coworkers could examine the influence of the initiation method on end-group fidelities of polymers and the resulting morphological transitions. In the case of photo-PISA under violet light irradiation (405 nm, 800 mW) based on the photoiniferter process, further irradiation of the synthesized polymer assemblies (post-synthetic irradiation) removed the end group of polymers and transformed their morphologies.[299] In contrast, *via* an identical process under lower irradiation power (160 mW) either in the presence or absence of VAZO-44 which decomposes at 37 °C, stable aggregates were formed irrespective of the initiation mechanism. Type I and II photoinitiators that produce free radicals under irradiation *via* homolytic cleavage or hydrogen abstraction have also been widely employed; however, in this section, we focus on the use of PCs. For the current status and future directions of RAFT-mediated PISA initiated by various means including visible light, please refer to the very recent review article reported by Thang, Fan, and coworkers.[300]

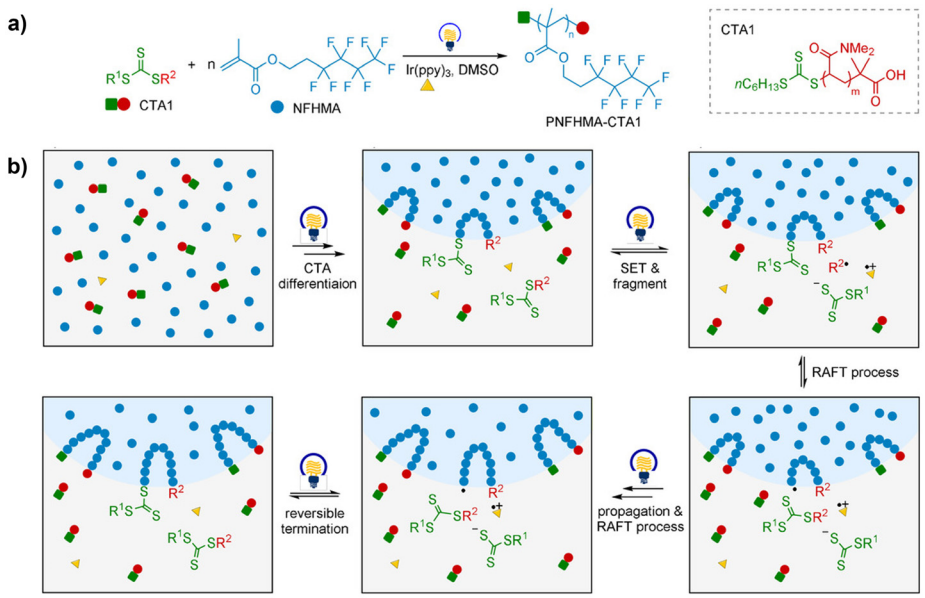

Fig. 16 (a) Synthetic scheme of UHMW fluoropolymers and (b) mechanistic concept for CTA differentiation for regulation over propagation. Adapted with permission from ref. 190 (Copyright 2020 John Wiley & Sons, Inc.).

Boyer and coworkers reported the first photo-PISA that was mediated by $Ru(bpy)_3Cl_2$ under blue light irradiation (460 nm, 0.7 mW cm^{-2}).[192] Up to 100 ppm of $Ru(bpy)_3Cl_2$ was loaded for the dispersion polymerization of solvophobic benzyl methacrylate (BzMA) from the solvophilic poly(OEGMA)-based macro-CTA. The dispersity of the polymer was maintained at lower than 1.3 despite the presence of unreacted or dead chains with lower molecular weight than the theoretical values and increase in the viscosity of the solution. ZnTPP was the very first PC for oxygen-tolerant photo-PISA and under red or yellow light irradiation at longer wavelength (635 and 560 nm, respectively).[301] Oxygen tolerance was achieved by the combination of ZnTPP as a singlet oxygen generator and ascorbic acid[301] or 9,10-dimethylanthracene[146] as a singlet oxygen quencher, so as to conduct the reaction in an open vessel at ultralow volumes (40 μL scale) without prior deoxygenation. However, only in the presence of 9,10-dimethylanthracene, perfect temporal control of polymerization was observed. Furthermore, ascorbic acid in larger amount seemed to affect self-assembly behavior. Very recently, Boyer and coworkers for the first time reported oxygen-tolerant photo-PISA under NIR irradiation (730 nm, 12 mW cm^{-2}) using $ZnPCS_4^-$ in combination with TEOA.[173]

Meanwhile, ZnTPP could still generate singlet oxygen after its encapsulation in the hydrophobic core of the vesicle *via* dialysis of the reaction mixture into water, implying the potential use of the resulting vesicle as a photodynamic therapeutic agent.[301] It was insolubility of ZnTPP in water that enabled the encapsulation. Similarly, doxorubicin, a hydrophobic antitumor drug, was encapsulated in spherical polymeric NPs.[302] Herein, doxorubicin was added into the reaction mixture from the beginning of the polymerization. While the polymerization process did not significantly affect the bioactivity of doxorubicin, the polymerization kinetics were improved, implying the potential photocatalytic capability of doxorubicin for photomediated polymerization.

ZnTMPyP, as a water-soluble analogue of ZnTPP, allowed aqueous dispersion polymerization,[147] and simplified photo-PISA by eliminating the preparation of solvophilic macro-CTAs which undergo chain extension with solvophobic monomers.[200,201] Instead, hydrophilic OEGMA and hydrophobic core-forming diacetone acrylamide (DAAm) were put together for gradient copolymerization based on preferential incorporation of OEGMA over DAAm owing to different reactivities of methacrylates and acrylamides for polymerization.[201] If both solvophilic and solvophobic blocks are prepared from the same monomer families, slow injection of solvophobic monomers into the reaction mixture gradually changed the ratio of the solvophobic- to solvophilic block length within a polymer chain, which led to PISA.[200] Lastly, Chen and coworkers controlled the size of raspberry-like NPs with a poly(pentafluorostyrene) core by light intensity.[303] At around 330 ppm of $Ir(ppy)_3$ and the same target DP, strong irradiation (33 W cm^{-2}) as compared to weak light irradiation (0.56 W cm^{-2}) activated more CTAs to decrease the polymer molecular weight at the same monomer conversion, and then to reduce the size of NPs. The effect of intensity and wavelength of light irradiated on polymerization control (*e.g.*, molecular weight and end group fidelity) and thus the morphologies of synthesized NPs has been reported for several cases.[301,303]

Organic PCs such as PTH,[304] EY,[135,170,305] Rose Bengal,[306] and Rhodamine 6G[307] have also been employed but mostly in combination of tertiary amines to achieve oxygen-tolerant reaction systems and enhance the reaction rate. Oxygen tolerance in photo-PISA particularly allows one to conduct the reaction in a continuous flow reactor with simple optimization of reaction parameters.[135,305,308]

4.3.7. Bioapplications. For the successful preparation of hybrid biomaterials composed of natural biomolecules (*e.g.*, DNA, cells, and proteins) and synthetic polymers, deoxygenation processes (*e.g.*, freeze–pump–thaw method and N_2 purging process) and harsh reaction conditions that would affect the integrity of biomolecules should be avoided. In this regard, PET-RAFT polymerization has been widely applied for bioapplications because it is rapid, oxygen-tolerant and can be conducted in biologically relevant media under mild reaction conditions without heating.[309,310]

Soh, Hawker and coworkers reported *in situ* grafting-to conjugation of poly(acrylamide)s onto several biomolecules (L-phenylalanine, 5-[(2-aminoethyl)amino]-naphthalene-1-sulfonic acid sodium salt (EDANS), and bovine serum albumin (BSA)) *via* $Ru(bpy)_3Cl_2$/sodium ascorbate-catalyzed PET-RAFT polymerization under blue light irradiation (470 nm, 80 mW cm^{-2}).[150] The copolymerization of NAM and *N*-acryoylsulfosuccinimide (NASS) with the target DP of 40 reached 95% conversion after 15 minutes even without prior deoxygenation. This short reaction time minimized the hydrolysis of succinimides and allowed *in situ* preparation of bioconjugates *via* the addition of biomolecules to the polymerization mixture.

To functionalize the surface of live cells, more rapid kinetics under milder reaction conditions are required to reduce the potential harm to the cells. Soh, Hawker and coworkers employed EY/TEA-catalyzed PET-RAFT polymerization under blue light irradiation (465 nm, 5.0 mW cm^{-2}) for grafting-from functionalization of live yeast and mammalian cells.[67] After 10 minutes of Ar purging and 5 minutes of irradiation, the cell surface was successfully functionalized with polyacrylamides bearing poly(ethylene glycol) (PEG) side chains while maintaining both high control over polymerization and high cell viability. Copolymerization with azido- or biotin-incorporated monomers allowed post-polymerization functionalization of the cells *via* copper-free SPAAC or streptavidin conjugation chemistry, respectively, which is promising to manipulate the cell surface and regulate cell–cell interactions. Although this early demonstration required Ar purging and the use of blue light, the recently reported examples with novel modified PCs have improved the reaction system toward a wide range of irradiation wavelengths. Qiao, Tang, Fu, and coworkers synthesized SA-TCPP for TEOA-cocatalyzed PET-RAFT polymerization of OEGMA (M_n = 480 g mol^{-1}) in the presence of mouse fibroblast cells (NIH 3T3) in a 96-well plate.[223] After 45 minutes of red light irradiation, the monomer conversion and cell viability were 11 and 46%, respectively. Subsequently, a ZnTPP-derived 2D nanosheet

reported by Cai, Li, and coworkers was employed for the ascorbic acid-cocatalyzed PET-RAFT polymerization of OEGA (M_n = 480 g mol^{-1}) in the presence of human embryonic kidney 293 cells.[149] The monomer conversion was 60.8–73.2% resulting in polymers with a rather broad dispersity (1.21–1.32) without negatively impacting the cell viability after two hours of irradiation under red light (635 nm, 3.6 mW cm^{-2}). Although the reaction conditions have to be further optimized, these preliminary studies suggested that PET-RAFT polymerization is suitable for cytocompatible *in vivo* polymerization in cellular applications.

Barner-Kowollik, Ng, Weil, and coworkers synthesized DNA–polymer conjugates from CTA-terminated single-stranded DNA (ssDNA) (Fig. 17a).[311] EY with the aid of ascorbic acid as a singlet oxygen quencher under blue light irradiation (470 nm, 4.0 mW cm^{-2}) was employed to avoid problematic deoxygenation at ultralow reaction volumes (20 μL). However, good control over dispersity could only be achieved after the freeze–pump–thaw process despite the use of ascorbic acid. The synthesized ssDNA–polymer conjugates could be hybridized with complementary ssDNA, and the size of the hybridized structure was increased with the size of the conjugated polymer. Lipid–polymer conjugates, prepared from CTA-terminated lipid using EY under blue light irradiation (465 nm, 5.0 mW cm^{-2}), could self-assemble and were used to mediate assemblies of gold NPs.[312]

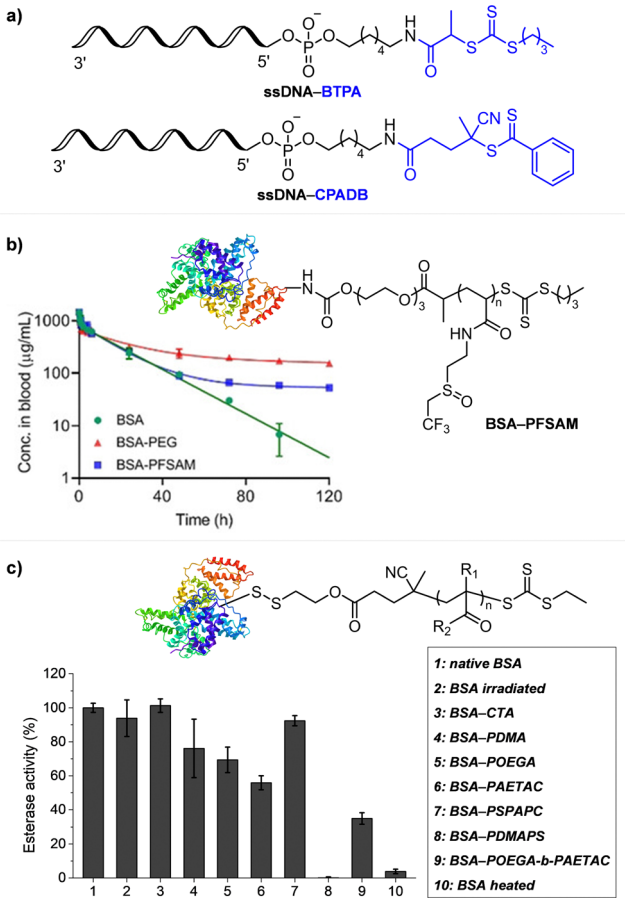

Fig. 17 (a) Schematic representation of ssDNA–CTA conjugates for synthesis of ssDNA–polymer conjugates.[311] (b) Pharmacokinetics and (c) enzymatic activities of BSA and various BSA–polymer conjugates. Adapted with permission from (b) ref. 70 (Copyright 2020 John Wiley & Sons, Inc.) and (c) ref. 176 (Copyright 2022 John Wiley & Sons, Inc.).

Lastly, proteins are also of great interest. Once a polymer is conjugated to a protein, the properties of the protein would be influenced as in the case of a protein attached to PEG, being widely used in the clinic worldwide.[313,314] PEG enhances the pharmacokinetic/dynamic properties while reducing the immunogenicity of therapeutic proteins.[315] Therefore, owing to the large diversity of polymers and the increasing desire to utilize proteins for the degradation of plastics,[316] for capture of heavy metal ions,[317,318] and as catalysts in organic chemical synthesis,[319] researchers are attracted to develop novel protein–polymer conjugates (PPCs). To reduce the potential harm to the structural integrity of proteins and preserve their enzymatic activities after polymerization, PET-RAFT polymerization that operates under mild reaction conditions and offers oxygen tolerance has been particularly recognized as a promising method.

Averick and coworkers studied the effects of the hydrophobicity and molecular weight of grafted acrylamide polymers on the enzymatic activities of two lipases (*Candida antarctica* lipase B and *Thermomyces lanuginosus* lipase).[141] EY/TEMED-catalyzed PET-RAFT polymerization from the grafted TTC in DMF was performed. Hydrophobic polyacrylamides led to a molecular weight-dependent increase in the activities and stability of lipases, so that the resulting hydrophobic hybrids could be immobilized on a glass slide while retaining the enzymatic activities. Whittaker and coworkers utilized EY with a tertiary amine to attach hydrophilic and low-fouling fluoropolymers to BSA as a model protein for *in vivo* quantitative tracking of polymer-conjugated therapeutics by ^{19}F magnetic resonance imaging (MRI) and extending the pharmacokinetics (*e.g.*, blood circulation time) (Fig. 17b).[70] Another hydrophilic sulfoxide-containing polymer improved the pharmacokinetics of lysozymes by reducing macrophage cellular uptake.[320] Although the listed applications of PPCs still have been mainly limited to therapeutics, many researchers focused on how to use PET-RAFT polymerization as a more efficient platform for preparation of PPCs, which would allow extension of the diversity of protein-based functional materials in the near future. For example, macromolecular and heterogeneous PCs for their facile purification after the reaction,[247,321,322] or PCs operating under irradiation at longer wavelength (*i.e.*, with lower energy) were developed.

Ever since Boyer and coworkers employed Ru(bpy)$_3$Cl$_2$ under blue light irradiation for PET-RAFT polymerization from BSA macroinitiator which was chemically modified to possess TTC moieties,[193] Ru(bpy)$_3$Cl$_2$,[323] EY and its derivatives,[68,70,141,247,249,320,321] ZnTPP derivative,[322] and a novel purely organic PC[176] have been discovered and utilized. Although EY is biocompatible and has facilitated the use of green LEDs as an irradiation source, tertiary amines[68,70,141,247,320] and/or ascorbic acid[247,321] need to be added to achieve oxygen tolerance. Photodegradation of EY is another issue.[141,247,324] Averick and coworkers observed photodegradation of EY in the presence of TEMED as an amine cocatalyst in DMF after up to 60 min of irradiation at

460 nm.[141] Sumerlin and coworkers observed photobleaching of EY under irradiation at 458 nm (0.6 mW cm^{-2}) and 515 nm (0.5 mW cm^{-2}), which was attributed to one of the possible side reactions caused by ascorbic acid at high concentration.[247] Due to the lack of singlet oxygen quenchers under aqueous conditions, the ZnTPP derivative where zinc porphyrin was integrated into a MOF (MOF-525-Zn) required purging with Ar, in contrast to the excellent oxygen tolerance of ZnTPP observed in the presence DMSO which acted as both a solvent and a singlet oxygen quencher.[322] Although these water-insoluble and heterogeneous PCs can be easily purified after the reaction and even reused, a water-soluble PC that enables oxygen-tolerant polymerization without additives is also beneficial; nevertheless, it has been limited to $Ru(bpy)_3Cl_2$. In this regard, Kwon and coworkers in collaboration with Gierschner and Koo developed a highly efficient water-soluble purely organic PC 3DPMSDP-IPN.[176] Efficient generation of triplet excited states, substantially negative E^*_{ox} (−1.56 V *vs.* Ag/AgCl), and highly stable radical cation of the PC synergetically afforded oxygen tolerance (or even acceleration of polymerization kinetics by oxygen present at limited concentration; for a detailed explanation, please see Section 3.4). Thus, polymerization was conducted using the BSA macroinitiator in ambient and aqueous environments without additives under green light irradiation (515 nm, 10 mW cm^{-2}). A variety of acrylamide/acrylate monomers, including hydrophilic and ionic (cationic, anionic, and zwitterionic) monomers, were polymerized from the protein macroinitiator to affect the enzymatic activities to varying degrees as compared to native BSA (Fig. 17c). However, the authors observed that the molecular weights of the polymers cleaved from the protein were smaller than the corresponding theoretical values and presumed that *via* reactions between the excited-state PC and disulfide bonds of BSA, thiyl radicals might be generated and became additional reaction sites for the propagating radical intermediates. Although the formation of thiyl radicals has not yet been detected, the selectivity issue for the PC, by PET, to selectively activate the CTA over other reactive groups within proteins (*e.g.*, TTCs over disulfide bonds) needs to be further investigated to design better photocatalytic systems for future bioapplications. Development of novel PCs and expansion of the available water-soluble and/or biocompatible PCs, rather than $Ru(bpy)_3Cl_2$ and EY, would stimulate related research and allow the synthesis of polymers comprising various monomers rather than acrylamide monomers which are extensively preferred because of their more rapid polymerization kinetics than those of other monomer families.

Meanwhile, without grafting and conjugation, polymers can also affect biomolecules. In polymer–protein hybrids, certain polymers could be hybridized with certain proteins, thereby helping to maintain the protein activities in non-native environments such as organic solvents[316,325,326] and thermal denaturing conditions.[266] Synthetic antimicrobial polymers that mimic the peptides with antimicrobial activities were discovered by investigating the structure–activity relationships of a large library of polymers composed of different categories of monomers (*e.g.*, hydrophobic, hydrophilic, and cationic) with varying compositions[263,327] and compositional drifts along the polymer backbone,[264] or by incorporating additional functional monomers into the polymers.[328] Wong, Boyer and coworkers synthesized a novel monomer (acrylated ZnTPP) that not only self-catalyzed the oxygen-tolerant PET-RAFT polymerization of monomers, but also enhanced the production of reactive oxygen species to promote antimicrobial activities.[328] Gianneschi and coworkers synthesized enzyme-responsive and pro-apoptotic peptide-modified vinyl monomers to prepare cytotoxic peptide brush polymers, which disrupted the mitochondrial membrane and triggered the death of cancer cells.[69] Later, copolymerization of these peptide-functionalized monomers with hydrophobic acrylamide monomers, and subsequent PISA resulted in synthesis of peptide brush polymer NPs, proposing their applications for peptide delivery systems.[329] Regardless of the applications, the discovery of high-performing synthetic polymers has been boosted by PET-RAFT polymerization (mostly catalyzed by ZnTPP in DMSO due to its excellent oxygen tolerance), specifically in combination with HTP synthesis (please see Section 4.4.4) and very recently with machine learning approaches and automated polymer chemistry,[266,330–332] which has enabled the facile preparation of a large number of polymers at a time.

4.4. Advanced techniques

4.4.1. Surface functionalization. Surface-initiated polymerization from the initiator-functionalized surface allows modulation of physical and chemical properties of material surfaces by the type of monomers and properties of tethered polymers (*e.g.*, composition and molecular weights). Various RDRPs have been employed for surface-initiated polymerization, but were challenged by their oxygen sensitivity.[333] Simple reaction conditions, scalability of the process, and oxygen tolerance are also beneficial for large-scale functionalization of surfaces. In addition, light-driven polymerization affords spatiotemporal control, where the thickness of the polymer film is controlled by irradiation time and patterning of polymer brushes is provided by spatially controlled irradiation using a photomask. Therefore, PET-RAFT polymerization that offers polymerization control over a wide range of monomers under mild and ambient reaction conditions (*i.e.*, in the presence of oxygen) is expected to be a promising method.

Surface-initiated PET-RAFT (SI-PET-RAFT) polymerization was firstly demonstrated by Pester, Boyer and coworkers (Fig. 18a).[334] Given the well-known oxygen tolerance of ZnTPP-catalyzed PET-RAFT polymerization in DMSO, the polymerization from a CTA-functionalized silicon oxide surface was successfully performed without prior deoxygenation. The polymerization mixture deposited on the surface was covered with a glass coverslip and irradiated at 405 or 590 nm (1.1 μm cm^{-2}). As expected, PET-RAFT polymerization provided polymer brushes with uniform thickness and high end-group fidelity, allowing the synthesis of diblock copolymers by chain extension of the prepared polymer brushes. Fabrication of a patterned surface *via* spatially controlled polymerization using a photomask was also demonstrated.

Since then, ZnTPP in combination with DMSO as a solvent has been widely utilized for oxygen-tolerant SI-PET-RAFT polymerization under violet,[335] green,[336–338] or yellow light

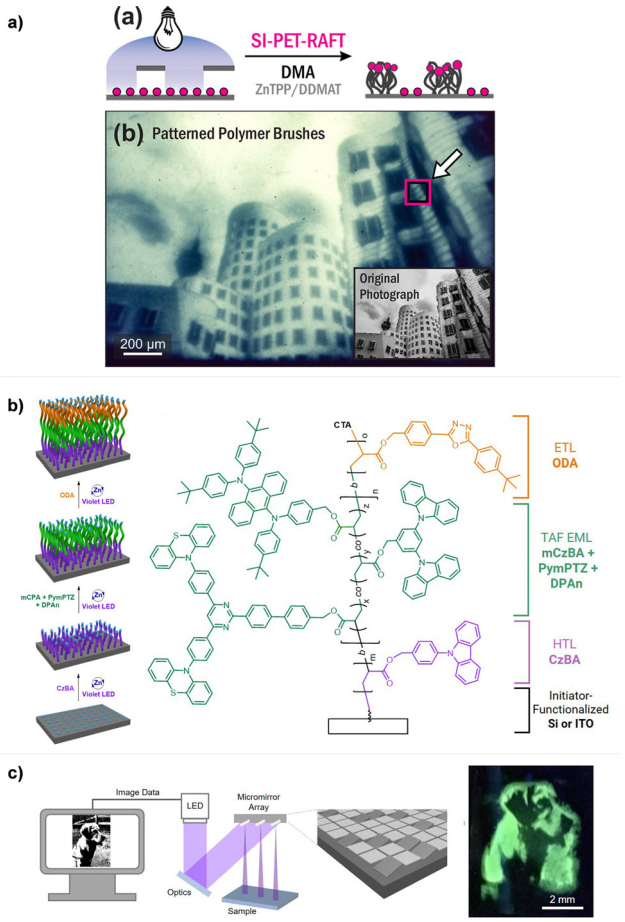

Fig. 18 Schematic representation of (a) spatially controlled SI-PET-RAFT polymerization using a photomask, (b) stepwise polymerization for fabrication of a multilayer architecture, and (c) spatially controlled SI-PET-RAFT polymerization of fluorescent monomers using a digital micromirror device (DMD). Adapted with permission from (a) ref. 334 (Copyright 2019 American Chemical Society), and (b) and (c) ref. 335 (Copyright 2021 John Wiley & Sons, Inc.).

irradiation.[338] A water-soluble $ZnTPPS_4^-$ under green light irradiation[339] or EY in the presence of TEOA under blue[140,340] or green light irradiation[138,341] expanded the polymerization media to aqueous systems. The lack of oxygen tolerance in the absence of TEOA required prior degassing[342] or enzymatic degassing strategy using GOx and glucose.[163] Using these various PCs, SI-PET-RAFT polymerization has been employed for fabrication of antifouling surfaces for biomedical and industrial applications,[138,140,336–338,340] polycarbonate surface with tuned hydrophilicity,[339] organic–inorganic hybrid materials,[235,341–344] and functional polymeric materials.[335]

Antifouling surfaces were prepared from hydrophilic, zwitterionic (*e.g.*, carboxybetaine methacrylamide (CBMAm)[140,340]), and low-fouling monomers (*e.g.*, sulfoxide-[336] or fluorine monomers[337]) to inhibit adsorption of biomolecules such as bacteria, proteins, and cells. Besides its role as a PC, ZnTPP that remained after the polymerization was effective as an antifouling agent through photodynamic inactivation of bacteria owing to its ability to generate singlet oxygen under irradiation.[337] The presence of residual ZnTPP was ascribed to covalent incorporation of ZnTPP into the polymer chain by radical-mediated polymerization of the reduced porphyrin macrocycle. This photodynamic activity of the residual ZnTPP, on the other hand, likely caused a significant cytotoxicity to mouse macrophage-like (RAW 264.7) cells, implying the need for the use of organic PCs in biomedical applications.[336]

Organic–inorganic hybrid materials were provided *via* grafting-from synthesis of polymers from mesoporous silica NPs,[342] mesoporous silica films,[343] gold-coated silicon wafers,[140] indium tin oxide (ITO)/gold-coated electrodes,[341] $NaYF_4$:Tm/Yb UCNPs,[344] and CdSe QDs.[235] On the ITO/gold-coated electrode surface, the CTA possessing an electrochemically active carbazole moiety was immobilized by an electrodeposition method.[341] $NaYF_4$:Tm/Yb UCNPs[344] and CdSe QDs[235] acted as both substrates and PCs for SI-PET-RAFT polymerization, where the synthesized polymers were tethered to the surfaces of nanocomposites *via* ligand exchange between the initial ligands of nanocomposites and TCT groups of the polymers. Encapsulation of gold NPs by the poly(dimethylaminoethyl acrylate (DMAEA))-tethered surface[341] and subsequent immobilization of antibodies onto the prepared polymer brushes[140] implied that SI-PET-RAFT polymerization would become a promising strategy for the development of organic–inorganic hybrid biosensors.

Very recently, Hudson, Pester, and coworkers employed ZnTPP-catalyzed SI-PET-RAFT polymerization under violet irradiation (405 or 415 nm) for fabrication of multilayer thin films for organic electrodes.[335] Using various acrylic monomers comprised of thermally activated delayed fluorescence (TADF) emitters, stepwise polymerization from CTA-functionalized ITO provided multilayer architectures of hole-transport layer (HTL), emissive layer (EML), and electron-transport layer (ETL), mimicking the structure of multilayer organic light-emitting diodes (OLEDs) (Fig. 18b). Moreover, combined with the recently emerged digital projection lithography technique using arrayed digital micromirror devices (DMDs), a spatial control over complex polymer architectures at high resolution was imparted (Fig. 18c)

A bare surface without prior functionalization with a CTA was also utilized for the preparation of a polyvinyl alcohol (PVA)-based hydrogel. The PVA-based hydrogel was immersed in the reaction mixture of PC (*i.e.*, $Ru(bpy)_3Cl_2$,[345,346] fluorescein,[347] EY,[348] and aluminum phthalocyanine chloride[349]), CTA, monomers, and TEA. It was proposed that alkoxyl radicals generated from PVA by a one-electron oxidized PC or by irradiation participated in PET-RAFT polymerization. Zwitterionic monomers such as CBMA were polymerized to provide antifouling properties to PVA-based materials for biomedical applications.[345–349] Thermoresponsive poly(NIPAm) brushes provided surface properties which were adjustable by temperature.[347]

4.4.2. 3D/4D printing – living additive manufacturing. 3D printing is an additive manufacturing technology which enables the fabrication of objects with complex structures using a layer-by-layer approach from digitally sliced computer-aided designs. Since the development of the first 3D printing process by Charles Hull in the early 1980s,[350,351] this technique has had scientific, technological, and economic impacts[352,353] by shifting from a

rapid prototyping technology to an advanced material manufacturing platform for diverse applications ranging from biomaterials[354] and soft robotics,[355] to construction.[356] More specifically, vat photopolymerization-based 3D printing techniques, including DLP[357,358] and stereolithography (SLA),[351] where light is used to activate polymerization and cure a liquid resin to form solid materials, have been widely applied.[359] Most of the photopolymerization-based 3D printing techniques employ uncontrolled polymerization methods, *i.e.*, photoinduced conventional free radical or cationic polymerization, to cure the polymers and form the object due to their fast polymerization rates and simplicity.[360] However, the polymers prepared during these photoinduced conventional free radical or cationic polymerizations cannot be reactivated, limiting the opportunity for the functionalization of 3D printed objects. To overcome these limitations, in recent years, PET-RAFT polymerization has been implemented in additive manufacturing to 3D print functional objects.[361] To achieve a reasonable polymerization rate and oxygen tolerance, polymerization *via* RQP was first implemented using xanthene dyes, such as erythrosin and EY, in the presence of a tertiary amine. For example, Boyer and coworkers reported an ultrafast DLP 3D printing system using EB and TEOA as the PC and cocatalyst, respectively, under green light irradiation (525 nm, 0.32 mW cm^{-2}).[142] In contrast to conventional free radical polymerization, the network growth was controlled by the RAFT equilibrium, *i.e.*, the degenerative chain transfer between active and dormant chains.[18] Careful optimization of the stoichiometry of reagents in the resin formulation (EB, TEOA, DMAm and PEG diacrylate (PEGDA) (M_n = 250 g mol^{-1})) resulted in a build speed of 1.2 cm h^{-1} allowing 3D printing of complex objects. A 4D printed object capable of swelling- and desolvation-induced actuation by differentiation of mechanical properties of two layers based on the control of light dose and curing time was also fabricated (Fig. 19a). The same research group then investigated the effect of various CTAs (TTCs, dithioesters, xanthates, and DTCs) under otherwise identical reaction conditions (Fig. 19b).[362] Interestingly, the structure of the CTA, such as Z and R groups, significantly affected the kinetics of network formation. This result is in alignment with the well-established design rules in conventional RAFT polymerization.[61,363,364] In parallel, Jin, Bagheri, and coworkers in collaboration with the research group of Boyer utilized EY and TEA under blue (483 nm, 4.16 mW cm^{-2}) or green light irradiation (532 nm, 0.48 mW cm^{-2}).[134] However, the fastest build speeds were 0.08 and 0.14 cm h^{-1} under blue or green light irradiation, respectively, which were lower than that achieved by EB.[142] This was attributed to more favorable photophysical and electrochemical properties of EB over EY.[204,214] The build speed still reached 0.23 cm h^{-1} after further optimization of the formulation of resin utilizing EY and TEOA under violet light irradiation (405 nm, 0.10 mW cm^{-2}).[139]

ZnTPP then extended the operation wavelength to red (635 nm, 0.5 mW cm^{-2}) although 3D printing was performed under a N_2 atmosphere to achieve a reasonable maximum build speed of 0.1 cm h^{-1} due to the long inhibition period in the presence of air.[365] Nevertheless, there is still a need to develop new PCs capable of achieving faster polymerization, which would enable 3D printing with a reasonable build speed. To overcome the slow printing speed achieved by PET-RAFT polymerization, Norrish type I photoinitiator diphenyl (2,4,6-trimethylbenzoyl) phosphine oxide (TPO) replaced the PC, which resulted in the fabrication of 3D printing objects at a faster printing rate (up to 9 cm h^{-1}).[366] The incorporation of the CTA conferred additional properties to the 3D printed objects, including capability for surface modification[366] and self-healing property.[367] More recently, the incorporation of macro-CTAs in the 3D printing resins enabled the preparation of 3D printed materials containing defined nanostructures *via* polymerization-induced microphase separation.[368–370] This technique would open opportunities for on-demand fabrication of nanostructured polymer materials with tunable mechanical properties and ion conductivity for energy storage applications.[371,372]

4.4.3. Flow chemistry. Flow chemistry has improved the practicality and scalability of photomediated synthesis of advanced functional materials including QDs, NPs, and dyes.[373] According to the Beer–Lambert law, it is difficult to perform the light-driven reactions on a large scale because the intensity of light significantly decreases with increasing optical path length. In a continuous flow reactor, the reaction mixtures flow inside a light-permeable tubing which is irradiated.[374] High surface area-to-volume ratio of the tubing ensures effective light penetration and a concomitant increase in the photon flux and reaction

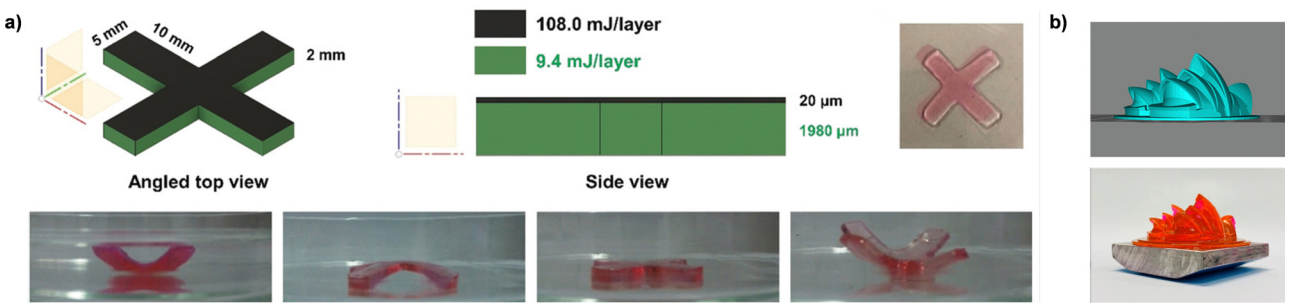

Fig. 19 (a) Synthesis of a 4D printed object capable of swelling- and desolvation-induced actuation owing to difference in mechanical properties of two layers by the spatially resolved light doses. (b) Original stl file image and 3D printed theater complex. Adapted with permission from (a) ref. 142 (Copyright 2019 John Wiley & Sons, Inc.) and (b) ref. 362 (Copyright 2021 American Chemical Society).

efficiency. Therefore, flow chemistry is expected to expand the versatility of photomediated polymerization.[375–378]

Among visible-light-driven RAFT polymerizations, PET-RAFT polymerization was the first to be performed in a continuous flow reactor, owing to its superior oxygen tolerance.[145] In contrast, there were a few reports employing flow chemistry techniques to (UV light-induced) photoiniferter[379–381] and photomediated cationic RAFT polymerizations, owing to their sensitivity to oxygen.[382] Oxygen tolerance is not a prerequisite for flow chemistry techniques; nevertheless, the high surface-area-to-volume of tubing reactors may facilitate the diffusion of oxygen into the reaction mixtures, causing a negative impact on oxygen-sensitive reactions.[264] In this regard, the more rapid polymerization kinetics of PET-RAFT polymerization compared to other polymerizations is also beneficial for operationally reasonable reaction conditions.[380]

Flow chemistry has been applied to rapid syntheses of homopolymers[209] or multiblock copolymers,[136,204] photo-PISA[135,305] and gram-scale synthesis of discrete pentamers *via* sequential SUMI.[273] Theoretically, the synthesis of polymers within minutes could enable their large-scale production (*e.g.*, multi-gram within a day). In addition to enhanced polymerization kinetics, the molecular weights and monomer compositions can be controlled by simply adjusting the compositions of the reaction mixtures, flow rates (*i.e.*, residence time), and irradiation times. In the case of block copolymer synthesis, different monomers can be sequentially added in order at defined times through separate channels (Fig. 20). Furthermore, in a one-pass reaction system, each batch can be irradiated at a different wavelength and separately turned on and off, such that multiple polymerization reactions are sequentially and selectively activated during the reaction in one pass. This approach was then employed to the synthesis of diverse polymers with complex architectures.[280] At last, dispersity control was achieved *via* temporally regulated initiation and/or adjustment of the reaction parameters (*e.g.*, flow rate and wavelength and intensity of irradiation).[288–290]

Nevertheless, to fully realize the potential of flow chemistry for expanding the current lab-scale polymerization system into the industrial scale, the influences of fluid dynamics and reactor parameters (such as tubing diameter and operation method) on polymerization control must be thoroughly investigated.[204,290] For example, in the synthesis of high-molecular-weight polymers, the polymer properties were inconsistent because the polymers caused reactor fouling and affected the fluidic profiles of the reaction mixture due to low Reynolds number.[204] Homogeneity of the reaction mixture within flow could be improved by applying a plug packed of low-cost and easily accessible silicon oxide beads.[383]

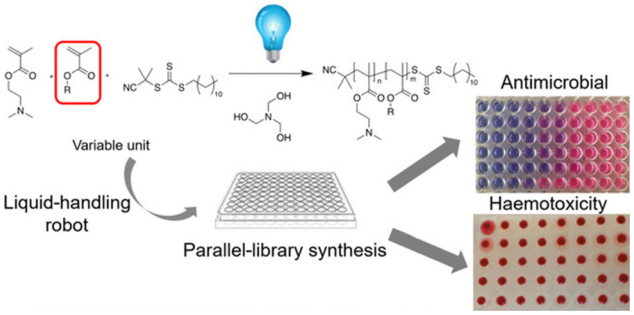

Fig. 21 Combinatorial approach for the discovery of antimicrobial polymers prepared by high-throughput PET-RAFT polymerization. Adapted with permission from ref. 386 (Copyright 2018 John Wiley & Sons, Inc.).

4.4.4. High-throughput (HTP) synthesis. HTP synthesis allows facile preparation of a large library of polymers in small volumes, which enables the identification of structure–property relationship. By distributing a stock solution of the reaction mixture into each well, and placing the well plate under a LED, polymerization is performed in each well at the μL scale (at most 200 μL in the case of a 96-well plate). As deoxygenation is difficult at the μL scale, PET-RAFT polymerization with intrinsic oxygen tolerance has exclusively been utilized for HTP synthesis,[384] although in some cases, oxygen-tolerant visible-light-driven RAFT polymerization in the absence of a PC was utilized, where $Zn_{0.64}Fe_{2.36}O_4$[155] and the tertiary amine,[152,385,386] added instead of the PC, facilitated photomediated deoxygenation and/or photolysis of the excited-state CTA. Polymerization at a low volume scale is also considered to be beneficial for potential bioapplications where it is difficult to prepare reaction substrates (*e.g.*, proteins and DNA) in large quantities.[170] Moreover, new polymers with desired biological activities can be efficiently discovered *via* a combinatorial approach (Fig. 21).[386]

Among PCs, ZnTPP dissolved in DMSO demonstrating extreme oxygen tolerance without additives was extensively employed. ZnTPP-catalyzed HTP polymerization has enabled the simple and efficient construction of a library of polymers without prior deoxygenation.[262–266,276,387–390] *Via* preparation

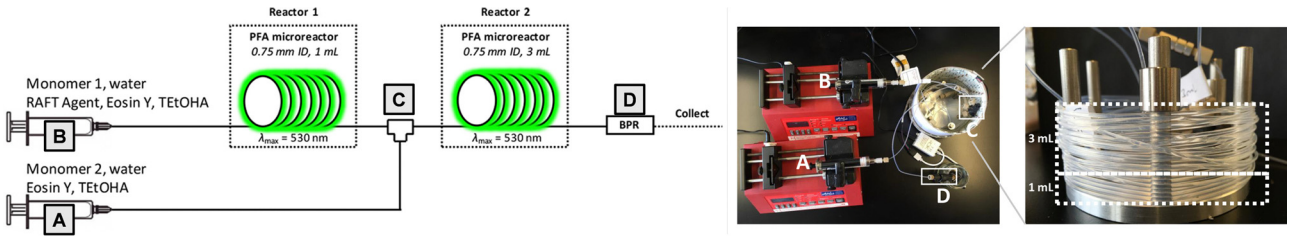

Fig. 20 Schematic representation and photographs of a continuous flow reactor for the block copolymer synthesis. The reactor system is composed of two separated syringe pumps for two tubing reactors, a micromixer tee, and a back-pressure regulator (BPR). Adapted with permission from ref. 136 (Copyright 2019 American Chemical Society).

and investigation of a large combinatorial library of polymers, researchers efficiently optimized polymerization conditions[262,389] and screened structure–activity relationships of polymers synthesized for antimicrobial applications,[155,263,264] polymer–protein binding interactions,[265,266] conjugation of biomolecules,[276] preparation of a glycopolymer library,[390] and design of single-chain polymer NPs.[388] Other than ZnTPP, EY was also employed for photo-PISA in a 96-well plate, but ascorbic acid was necessary to achieve oxygen tolerance.[170]

Apart from its outstanding oxygen tolerance in DMSO, ZnTPP also showed promise in characterization of polymerization at low volumes.[387] Boyer and coworkers noticed that fluorescence emission bands of ZnTPP changed owing to incorporation of ZnTPP into the polymer chain during polymerization. The linear relationship between fluorescence emission and monomer conversion allowed online monitoring of polymerization within a few minutes using plate readers, which was consistent with the results provided by NMR analysis. Herein, polymerization and direct characterization were conducted at below 40 μL scale in a 382-well plate. This ultralow volume is typically difficult to sample for NMR analysis that is carried out to determine monomer conversion in polymerization in batch. Therefore, the merge of HTP synthesis in well-plates and simple online monitoring of polymerization, combined with machine learning approaches and automated polymer chemistry,[266,330,331,391] is expected to accelerate the discovery of novel functional polymers.[392,393]

5. Photoiniferter polymerization

In the absence of additives and/or PCs, simplicity and efficiency of the reaction system would be further increased. Moreover, the negative impacts of remaining additives on polymer properties will no longer become a concern. Nevertheless, since the first application of DTCs by Otsu and coworkers,[40] the operating wavelength has been limited to the UV region. Because UV light can lead to undesired decomposition of the CTA and loss of controllability of polymerization, CTAs that can be cleaved by milder visible light have been extensively explored, and the relevant applications have recently emerged. Accordingly, the very recent review article reported by Hartlieb covered the concept, history, and various applications of photoiniferter polymerization irrespective of the irradiation wavelength.[56] In this section, particular emphasis is placed on the examples harnessing visible light rather than UV light.

5.1. CTAs for polymerization

Theoretically, visible-light-induced photocleavage of the C–S bond is possible for xanthates or TTCs and DTBs owing to their n → π* electronic transitions. The n → π* electronic transition of TTCs and DTBs occurs under blue and green light irradiation, respectively (Fig. 22).[394] The red-shift effect for DTBs is due to a resonance in the Z group. In contrast, both n → π* and π → π* electronic transitions of xanthates[395] and DTCs occur under UV light irradiation because of electron-rich

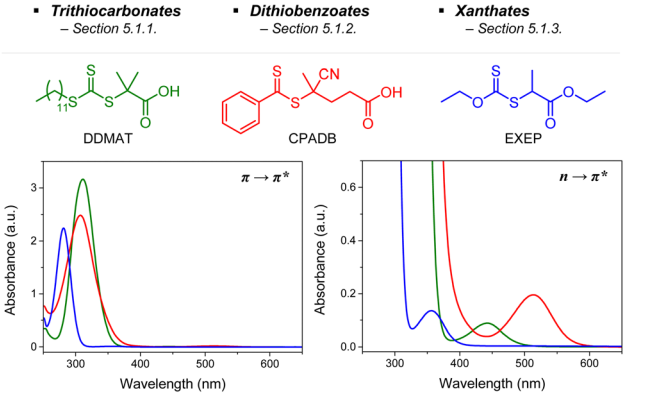

Fig. 22 UV/Vis absorption spectra of DDMAT (green), CPADB (red), and EXEP (blue) in DMSO at 0.2 and 2.0 mM concentration to present π → π* and n → π* electronic transitions, respectively.

oxygen and nitrogen in the Z group, respectively. Although n → π* electronic transitions at longer wavelengths are beneficial due to lower energies, their spin-forbidden nature and consequently small molar extinction coefficient make it challenging to achieve visible-light-driven photoiniferter polymerization at a reasonable polymerization rate. Therefore, the recently reported photoiniferter polymerization from TTCs still mostly harnesses UV light to target π → π* electronic transition-derived homolysis of the C–S bond regardless of the type of monomers (methacrylates,[396] acrylates,[33,379] acrylamides,[33,58,397] and other monomers[380,397]). The use of a continuous flow reactor and/or high reaction temperature helped to improve the practicality and polymerization kinetics. Johnson and coworkers adapted a flow reactor for UV light irradiation (352 nm)-induced polymerization of acrylates and acrylamides.[379] Junker, Abetz, and coworkers increased the reaction temperature to 120 °C for polymerization of isoprene and styrene in a flow reactor.[380] On the other hand, in this section, we focus on the visible-light-driven photoiniferter polymerization using TTCs, DTBs, xanthates, and others. Scheme 26 depicts the monomers employed thus far.

5.1.1. Trithiocarbonates. In 2015, Boyer and coworkers reported the first visible-light-driven photoiniferter polymerization of methacrylates in the presence of a CTA and monomer without the addition of a PC.[32] Among CDTPA, DDMAT, BTPA (TTCs) and CPADB (a DTB), only CDPTA under green light irradiation (530 nm, 5 W) led to controlled polymerization of MMA. The loss of polymerization control under blue light irradiation (461 nm, 5 W) implied that the irradiation wavelength should overlap with the absorption profile of the CTA; however, too high energy would cause partial degradation of the CTA. For other TTCs, the controllability of polymerization was likely affected by the stability of the R group during the fragmentation of the C–S bond. For example, in contrast to CDTPA, BTPA possessing an R group with a secondary carbon led to poorly controlled polymerization of MMA under blue light irradiation because the propagating radical with tertiary carbon was more stable, not favoring the RAFT process. The study of the effect of the R group on blue light (460 nm, 1.5 mW cm^{-2})-induced photolysis of the CTA by UV/Vis spectroscopy, by Qiao

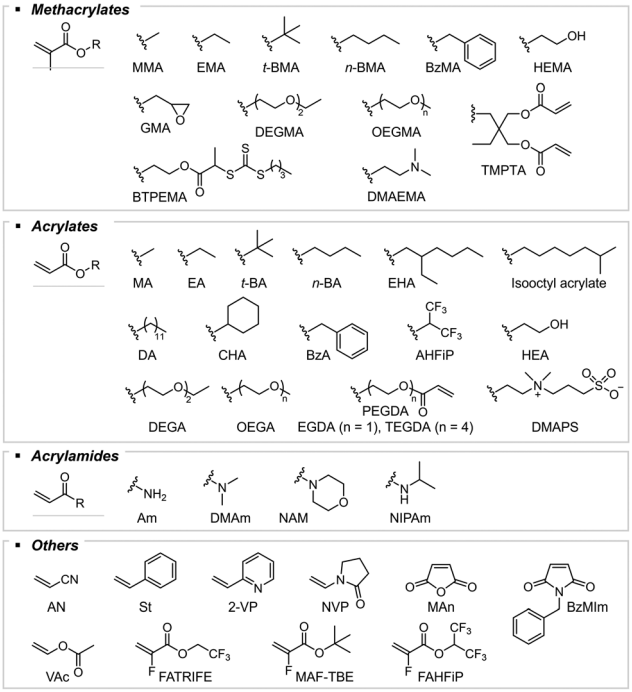

Scheme 26 Chemical structures and abbreviations of monomers employed for visible-light-driven photoiniferter polymerization.

and coworkers, indicated that as the thiyl radical generated after photolysis could be irreversibly degraded into carbon disulfide and thiol, polymerization from a CTA with a more stable R group that efficiently generated fragments with extended lifetimes was more prone to lose its living character.[398] The efficient fragmentation, on the other hand, decreased the induction period implying that controlled polymerization of a given monomer with a reasonable induction period would be achieved *via* careful selection of the CTA and light source.

The monomer scope was expanded to methacrylates,[110,157,280,381,399,400] acrylates,[33,88,110,134,157,401–408] acrylamides,[33,110,157,404,407,409] AN,[410] 2-vinylpyridine (2-VP),[411] styrene,[404,406] and fluoro(meth)acrylates[412] (Table 4). Compared to UV light, the use of milder visible light (460 nm, 4.8 W) prohibited the self-initiation of MA although the induction period was increased by four times.[33] The authors ascribed the increase in the induction period to the prolonged time of addition of the first monomer to the CTA. Then, the same authors reported that the induction period was rather related to the R-group stability or inactivation of residual oxygen or trace impurities within the reaction mixture before the polymerization.[398] TTCs with better fragmenting R groups demonstrated significantly reduced induction periods for initiation, whereas during propagation the R-group effect became less important owing to the similar acrylate-inserted R groups of all TTCs. Junker and coworkers also discovered that in the polymerization of MMA under blue light irradiation (450 nm, 14.4 W), the adduct of CTA with one, two, or three MMAs resulted in polymers with lower dispersity.[381] However, to eliminate the need for the preparation of SUMI adducts, the authors suggested to render the initiation process effective by increasing photon flux in a continuous flow reactor. To achieve fast reaction kinetics, the reaction temperature was also increased to 90 °C, which was sufficiently low not to cause the autoinitiation of MMA or degradation of TTC. As reported by Cameron, Saito, and coworkers, temperature control is particularly important at high irradiation powers.[409] In the aqueous polymerization of acrylamides such as DMAm under irradiation (402 or 451 nm, and 6, 26, 104, or 208 W), high irradiation powers increased not only photon flux and photolysis, but also the reaction temperature, which considerably reduced the polymerization time from 12 hours to 11 minutes, while broadening the dispersity of polymers. Dispersity was narrowed by controlling the temperature to prevent hydrolytic degradation of the CTA and concomitant formation of low molecular weight dead chains.

Very recently, Sumerlin and coworkers reported that irradiation with visible light to target $n \rightarrow \pi^*$ electronic transitions led to more efficient and well-controlled polymerization than irradiation with UV light to target $\pi \rightarrow \pi^*$ electronic transitions, if the light intensity was identical (0.6 mW cm^{-2}).[407] Due to the spin-forbidden nature, $n \rightarrow \pi^*$ electronic transitions show a much smaller molar extinction coefficient than $\pi \rightarrow \pi^*$ electronic transitions. Nevertheless, the polymerization results and the radical-trapping experiment using 2,2,6,6-tetramethylpiperidine-1-oxyl (TEMPO) confirmed that $n \rightarrow \pi^*$ electronic transitions led to the higher quantum yield of photolysis of the C–S bond, higher radical concentration, and more rapid polymerization. This result was consistent with xanthates.

5.1.2. Dithiobenzoates. In the first study of visible-light-driven photoiniferter polymerization of MMA and MA by Boyer and coworkers, CPADB was inactive for both monomers under blue light irradiation (461 nm, 5 W) in contrast to CDTPA (a TTC) (Table 5).[32] This was ascribed to the maximum $n \rightarrow \pi^*$ absorption of CPADB at 513 nm corresponding to green light rather than blue light, although polymerization data under green light irradiation were not shown here. The seminal report demonstrated that green light irradiation (530 nm) was also inefficient for photoiniferter polymerization of MMA in DMSO due to a poor quantum yield of the photochemical relaxation of excited-state CPADB.[398] In DES, on the other hand, MMA was polymerized under green light irradiation (525 nm, 1.2 mW cm^{-2}) even in a completely open vial.[158] The effect of DES needs to be investigated.

Meanwhile, Sumerlin and coworkers prepared a UHMW polymer *via* alternative copolymerization of styrene and benzyl maleimide or maleic anhydride under 450 nm irradiation.[413] 2-(dimethylamino)ethyl methacrylate (DMAEMA) also underwent polymerization under irradiation with a household lamp (14 W, 2.4 mW cm^{-2}), but here the acceleration effect of the amine incorporated in DMAEMA on the polymerization mechanism needs to be considered. Electron transfer from the amine to excited-state CPADB generated the CPADB anion and facilitated the polymerization as in the case of amine-catalyzed polymerization using TTCs[71,151,152] and DTB.[72] By the addition of TEA, polymerization of MMA from CPDB even under green (520 nm, 5.9 mW cm^{-2}) or sunlight irradiation was realized.[72] Recently, Konkolewicz and coworkers reported that an electron-donating substituent at the para position of the benzyl Z group of CPDB

Table 4 Chemical structures of TTCs employed for visible-light-driven photoiniferter polymerization

CTA (common name)	Irradiation wavelength	Monomer			
		Methacrylates	Acrylates	Acrylamides	Others
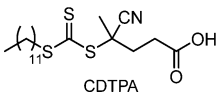 CDTPA	Violet (405 nm) Blue (455–472 nm)	BzMA	PEGDA *n*-Bu, *t*-Bu, BzA, CHA, DA, EA, EHA, HEA, MA, AHFiP		St
	Green (520, 530 nm)	*n*-BMA, BzMA, BTPEMA, DMAEMA, GMA, HEMA, MMA			
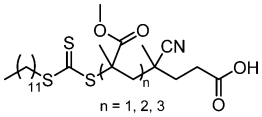 n = 1, 2, 3	Blue (450 nm)[a]	*t*-BMA, DEGMA, EMA, HEMA, MMA			
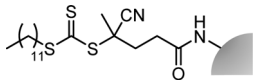	Blue (460 nm) Green (530 nm)	GMA, HEMA, OEGMA			
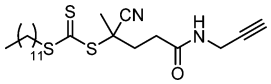	Blue (460 nm)		OEGA		
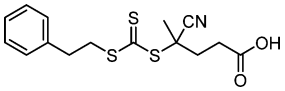	White				FATRIFE, FAHFiP, MAF-TBE
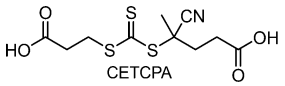 CETCPA	Blue (455 nm)		DMAPS, HEA, OEGA		
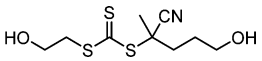	Blue (455 nm)		*n*-BA, MA		
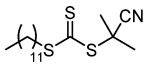	Blue (460, 470 nm)		MA		AN
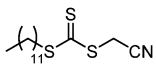	Blue (472 nm)		*n*-BA		
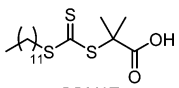 DDMAT	Violet (420 nm) Blue (450–460 nm)		*n*-BA, MA	NAM	2-VP St
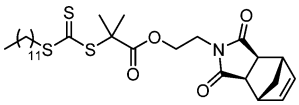	Blue (450 nm)		*n*-BA		
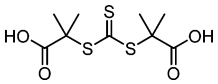	Violet (402 nm) Blue (450, 451 nm)		MA	Am, DMAm Am	
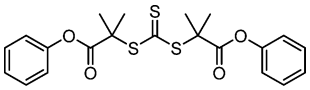	Blue (450 nm)	MMA	*n*-BA, *t*-BA, DEGA, MA	Am, DMAm, NIPAm	
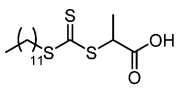 DTPA	Blue (460 nm)		MA		
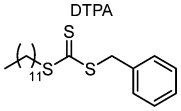	Blue (460, 480 nm)		MA		
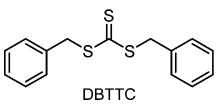 DBTTC	White Violet (405 nm) Blue (460 nm)		OEGA, TEGDA *n*-BA, OEGA, TEGDA		FATRIFE
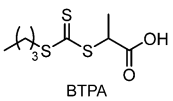 BTPA	Blue (460 nm)		MA, *t*-BA, EGDA	NIPAm	

Table 4 (*continued*)

CTA (common name)	Irradiation wavelength	Monomer: Methacrylates	Acrylates	Acrylamides	Others
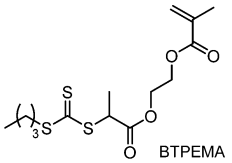 BTPEMA	Green (520 nm)		MA	DMAm	
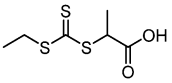	Blue (453 nm)			DMAm	

[a] Performed in a continuous flow reactor, at 90 °C.

Table 5 Chemical structures of DTBs employed for visible-light-driven photoiniferter polymerization

CTA (common name)	Irradiation wavelength	Monomer: Methacrylates	Acrylates	Acrylamides	Others
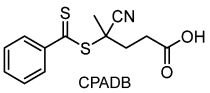 CPADB	Blue (440 nm) Green (510 nm) Household lamp	MMA MMA DMAEMA			St and BzMIm, St and MAn
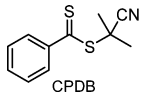 CPDB	Blue (460 nm)[a] Green (520 nm)[a]	MMA			
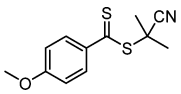	Blue (440 nm)	MMA			

[a] Performed in the presence of TEA.

dramatically accelerated the polymerization of MMA under blue light irradiation (440 nm, 11.6 mW cm^{-2}) in the absence of an amine additive.[87] The monomer conversion (85%) was comparable to the conversion in polymerization using 1 ppm of $Ir(ppy)_3$ (*i.e.*, PET-RAFT polymerization). The polymerization rate (k_p^{app} = 0.2 h^{-1}) was much faster than that using CPDB (k_p^{app} = 0.017 h^{-1}) despite the slight deviation in molecular weight control ($Đ$ = 1.28) and end-group fidelity. The investigation of five CPDB derivatives confirmed the similar molar extinction coefficient at irradiation wavelength, but their Hammett Sigma parameters (σ_p) and E^0_{red}s were decreased by the presence of electron-donating substituents. The linear relationship between logarithm of k_p^{app} and σ_p or E^0_{red} and σ_p proposed that homolysis of the C–S bond (i) could be enhanced by electronics, (ii) might involve the formation of partial positive charge on the DTB group in the transition state, and thus (iii) the polymerization was accelerated by the electron-donating para methoxy substituent.

5.1.3. Xanthates. Photolysis of EXEP under blue light (460–470 nm) or sunlight irradiation was reported by Zhu, Zhang, and coworkers for the first time (Table 6).[162,394] Introduction of carboxylic acid or triisopropylsilyl-protected alkyne into the R group of EXEP did not interfere in the photoiniferter polymerization of VAc in the bulk. By the way, substitution of the ethyl Z-group of EXEP with a phenyl group (PXEP) led to a blue-shifted n → π* electronic transition.[159] Under violet light irradiation (390 nm), more-activated monomers such as *n*-butyl and *t*-butyl acrylates (*n*- and *t*-BA) and NIPAm were polymerized in the bulk within an hour, whereas the polymerization of VAc took a far longer time. When fluorine was inserted in the para position of the phenyl Z-group of PXEP (FPXEP), even homopolymerization of VAc and block copolymerization of MA as the first block with VAc as the second block were realized under violet light irradiation (390 nm, 0.72 W).[414] The compatibility of FPXEP with both less- and more-activated monomers was ascribed to the well-balanced addition and fragmentation during the RAFT process, which was induced by the introduction of fluorine. The molecular geometry optimized by DFT implied that fluorine weakened the conjugation between benzene and the C–S double bond and lowered the lowest unoccupied molecular orbital (LUMO) of FPXEP to facilitate the addition of free radicals. PXPE, where the R group of PXEP was further modified to the 1-(phenyl-ethyl) group, was also suitable for more-activated monomers.[415] Similar to FPXEP, only after the polymerization of more-activated monomers (*i.e.*, MA, *n*-BA, or styrene) under blue (465 nm, 1.8 mW cm^{-2}) or violet light irradiation (391 nm, 0.6 mW cm^{-2}), chain extension with VAc or NVP was possible. Although the wavelength was extended to visible light (blue or violet), still UV light showed the highest

Table 6 Chemical structures of xanthates employed for visible-light-driven photoiniferter polymerization

CTA (common name)	Irradiation wavelengths	Monomer			
		Methacrylates	Acrylates	Acrylamides	Others
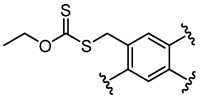	Violet (401 nm)			DMAm	
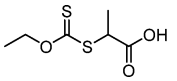	Blue (460–470 nm)				VAc
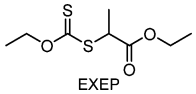 EXEP	Blue (460–470 nm)				VAc
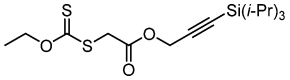	Blue (460–470 nm)				VAc
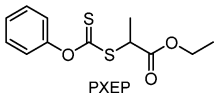 PXEP	Violet (390 nm)		*n*-BA, *t*-BA	NIPAm	
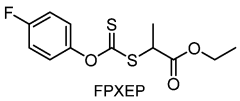 FPXEP	Violet (390 nm)		*n*-BA, MA	NIPAm	VAc
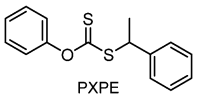 PXPE	Violet (391 nm) Blue (465 nm) Violet (391 nm)		*n*-BA MA		 St
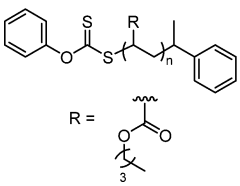	Violet (391 nm) Blue (465 nm)				VAc NVP
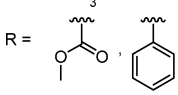	Violet (391 nm)				NVP, VAc

k_p^{app} albeit with higher dispersity due to the generation of dead chains.

5.1.4. Others. In 1982, Otsu and coworkers demonstrated the living polymerization using DTCs as an iniferter under UV light irradiation.[39] In order to extend the absorption of DTCs from UV to longer wavelength, Poly and coworkers conjugated carbazole in the Z group. Therefore, photoiniferter polymerization of *n*-BA was realized even under blue (472 nm, 96 mW cm^{-2}) or green (525 nm, 26.5 mW cm^{-2}) light irradiation (Table 7).[401] An *N*-heterocyclic DTC-based CTA possessing tetraphenylethylene (TPE) as the R group showed absorption at 400–500 nm.[416] Not only acrylates, MMA, and styrene were polymerized under blue light irradiation (460 nm, 4.8 W), but also the polymerization could be monitored *in situ* by naked eyes *via* aggregation-induced emission of TPE. As the polymerization proceeded, the viscosity of the solution increased, and photoluminescence intensity quantitatively increased to reflect monomer conversion during polymerization. When TPE was physically blended within the reaction mixture, the PL intensity increased in an irregular manner due to the indirect interaction between TPE and the growing polymer network.

5.2. Recent developments and applications

Visible-light-driven photoiniferter polymerization has recently been employed in numerous applications; nevertheless, the range of applications is still narrower than those reported for PET-RAFT polymerization owing to the lack of oxygen tolerance of the reaction system and the decreased polymerization rate caused by the absence of a PC. For example, photomediated expansion of the polymer network through incorporation of additional monomers was significantly efficient in the presence of PTH in terms of reaction rate and controllability of polymerization.[208] Moreover, direct photolysis of TTC under visible-light irradiation, which was less efficient than EY/TEA-catalyzed PET-RAFT polymerization, was impractical for 3D printing application where a sufficiently fast photocuring (*i.e.*, a high build speed) is required.[134] In this section, the reported examples of applications that were realized solely by visible-light-driven photoiniferter polymerization are described. The other examples which were aided by PET-RAFT polymerization are mentioned in the relevant subsections throughout Sections 4.3 and 4.4. Herein, the applications driven by UV light are basically excluded, whereas several noteworthy examples which show implications for their expansion to visible-light-driven

Table 7 Chemical structures of other CTAs employed for visible-light-driven photoiniferter polymerization

CTA (common name)	Irradiation wavelengths	Monomer			
		Methacrylates	Acrylates	Acrylamides	Others
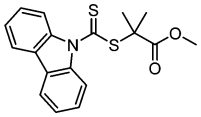	Blue (472 nm) Green (525 nm)		*n*-BA	DMAm	
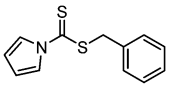	Blue (460 nm)		MA		
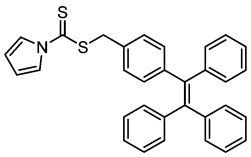	Blue (460 nm)	MMA	*n*-BA, MA, OEGA, isooctyl acrylate		St

reaction systems are mentioned. For the applications under UV light irradiation, please refer to the review article by Hartlieb.[56]

5.2.1. Multiblock copolymer synthesis. Hartlieb and coworkers successfully synthesized an acrylamide-based multiblock copolymer with up to 20 blocks and relatively low dispersity ($Đ$ = 1.29) from a xanthate under UV light irradiation (365 nm, 2 W).[417] The high livingness of the polymerization was ascribed to reduction in the feeding rate of monomers. The authors postulated that the slow monomer addition increased the number of reversible deactivations per monomer addition owing to the low chain transfer coefficient of acrylamide monomers for xanthate, and suppressed irreversible termination; however, too slow feeding rate would cause the degradation of the CTA and broad dispersity. Therefore, to prepare polymers with narrow dispersity, a series of chain extensions rather than one polymerization reaction was recommended. Although oxygen had to be removed before each addition of monomers, and molecular weights of the obtained polymers were consistently lower than the theoretical values in every step, this work demonstrated the promise of photoiniferter polymerization for the synthesis of multiblock copolymers.

If different types of monomers have to be involved in each block, the monomer that would become a better leaving group needs to be polymerized first to favor fragmentation and chain extension with the second monomer during addition–fragmentation in the RAFT process. If the order is inverted, the second monomer with a better leaving group, instead of the first block, is likely to favor fragmentation and propagation, and will be homo-polymerized in the presence of an exogenous radical derived from external initiators. As a result, a mixture of homopolymers rather than the desired uniform block copolymers comprising two types of monomers is provided. Sumerlin and coworkers surmised that this restriction regarding the order of blocks in a copolymer would be resolved *via* photoiniferter polymerization.[418] Photoiniferter polymerization that is mediated by (i) direct photolysis of the C–S bond, which does not require an exogenous radical initiator, and (ii) reversible termination rather than degenerative chain transfer is thus expected not to restrict the sequence of blocks in copolymers based on the difference in leaving group abilities. Initially, DMAm was polymerized as the first block from TTC by conventional RAFT polymerization or from xanthate by photoiniferter polymerization. As expected, subsequent photoiniferter polymerization of poly(DMAm)-xanthate under UV light irradiation (365 nm, 5.0 mW cm^{-2}) successfully extended poly(DMAm)-xanthate with MMA, whereas thermally initiated polymerization provided a mixture of homopolymers of DMAm and MMA. Poly(DMAm)-TTC was also extended with MMA under blue light irradiation, but the rate of photolysis was slower. Using xanthate that was efficiently cleaved under UV light irradiation as a CTA, not only DMAm but also MA and *N*-vinylcarbazole were used as the first blocks and were extended by MMA.

Diblock copolymers of poly(acrylamide)s and polyethers were synthesized by combined photoiniferter polymerization under UV light irradiation (365 nm, 3.5 mW cm^{-2}) and *t*-Bu-P$_2$/triethylborane-catalyzed ROP at room temperature.[122] As TTCs remained intact under the reaction conditions of ROP, either sequentially or simultaneously performed photoiniferter polymerization and ROP from the mono-hydroxyl-functionalized TTC provided the diblock copolymers. α,ω-Di-hydroxyl-functionalized TTC provided the α,ω-di-hydroxyl-functionalized polyacrylates that could serve as building blocks for polyurethane (PU).[88] After the preparation of poly(*n*-BA) ($M_{n,GPC}$ = 3100 g mol^{-1} and $Đ$ = 1.03) under blue light irradiation (455 nm, 5 mW cm^{-2}), thermoplastic PU elastomer was synthesized from the mixture of 5 mol% poly(*n*-BA) and 95 mol% poly(tetramethylene ether glycol) as a soft segment, isophorone diisocyanate as a hard segment, and ethylene glycol as a chain extender. The prepared elastomer surprisingly overcame the strength-elongation and robustness-self-healing ability trade-off relationships typically observed in elastomers. As various monomers can be incorporated as a part of soft segments to influence phase separation behavior and chain mobility within the polymer network, the development of thermoplastic PU elastomers with unprecedented properties was expected. In addition, *via* copper-catalyzed azide–alkyne reaction, polymers prepared from α-alkyne-functionalized TTC under blue light irradiation (460 nm, 4 mW cm^{-2}) could be linked to bioactive peptides possessing the *N*-terminal azide functionality.[408] Thus, high end-group fidelity

under mild reaction conditions of visible-light-driven photoiniferter polymerization was highlighted.

5.2.2. Single unit monomer insertion (SUMI). Photoiniferter polymerization has only been applied in the first step (*i.e.*, the preparation of monoadducts) of sequential SUMI, as discussed in Section 4.3.1.2. For the synthesis of trimers and pentamers, a styrene and indene were inserted into CDTPA *via* direct photolysis under green light irradiation (530 nm, 0.6 mW cm^{-2})[89] and blue light irradiation (460 nm, 0.8 mW cm^{-2}),[269] respectively. Postma, Moad, and coworkers investigated the potential for sequential SUMI by successive photoiniferter polymerizations.[272] Using DMAm as a monomer and CETCPA as a CTA under irradiation with various light sources (402, 451, 512, and 633 nm), red light (633 nm, 8 W m^{-2}) provided the most selective formation of the monoadduct with almost no byproduct formation but at the slowest reaction rate. Nevertheless, red light was not appropriate for the second SUMI owing to significantly less overlap between the emission of the LED and the absorption profile of the resulting monoadduct as the absorption band for the n → π* transition was changed from 442.9 to 427.0 nm. Instead, irradiation at lower wavelengths (402, 451, and 512 nm with 20, 8, and 14 W m^{-2}, respectively) with diminished yet sufficient overlap led to the formation of not only the desired diadducts but also byproducts *via* multiple insertions of monomers and photodecomposition of the TTC moiety.

In the absence of a PC, sequence-defined oligomers could be prepared *via* an iterative method rather than sequential SUMI (Fig. 23).[419] Boyer and coworkers in collaboration with Moad and Hawker confirmed the high end-group fidelity of the monoadduct of MA and CDTPA and functionalized the TTC moiety. Aminolysis of TTC into thiol was followed by a thiol–ene reaction with a second monomer containing a hydroxy group (2-hydroxyethyl acrylate (2-HEA)). Thereafter, the hydroxy group underwent esterification with CDTPA to introduce a new CDTPA for another SUMI using DMAm as a third monomer. Finally, aminolysis, thiol–ene reaction with a fourth monomer (2-hydroxy butyl acrylate), and esterification with CDTPA were repeated to insert BzA as the last monomer to provide a sequence-defined pentamer. Although the monomer scope was expanded to acrylates and acrylamides, pre-functionalization of the carboxylic acid group of the starting CDTPA with a 3-trimethylsiyl protecting group to block its esterification with the lately introduced monomers with hydroxy groups and isolation of each intermediate can be cumbersome in this strategy.

5.2.3. Ultrahigh-molecular-weight (UHMW) polymer synthesis. Successful synthesis of UHMW polymers requires fast photolysis of the CTA, high radical concentration, and high k_p of monomers, while keeping the probability of termination low. Thus, photoiniferter polymerization in the absence of an initiator and initiator-derived radicals is advantageous. Owing to the weaker C–S bond in xanthates compared to that in TTCs and accordingly more efficient generation of initiating radicals through photolysis, xanthates have been extensively employed for synthesis of UHMW polymers.[278,395,420] With regard to the fast polymerization kinetics, acrylamides with high k_p were selected as monomers. Sumerlin and coworkers synthesized UHMW poly(DMAm)s in water under UV light irradiation.[395] Moreover, a highly viscous reaction mixture prevented termination reactions between propagating radicals. Both xanthate and TTC underwent photolysis, but the reaction time was significantly lowered for xanthate (30 minutes) as compared to TTC (10 hours) because the n → π* transition of xanthate led to more efficient photolytic cleavage compared to the π → π* transition of TTC at 365 nm. To facilitate the n → π* transition of TTC, Cameron, Saito, and coworkers used visible light (402 or 451 nm, 6 W), but higher intensity (208 W) was required to achieve a reasonably short reaction time (12 hours *vs.* 11 minutes).[409] However, higher intensity of irradiation also

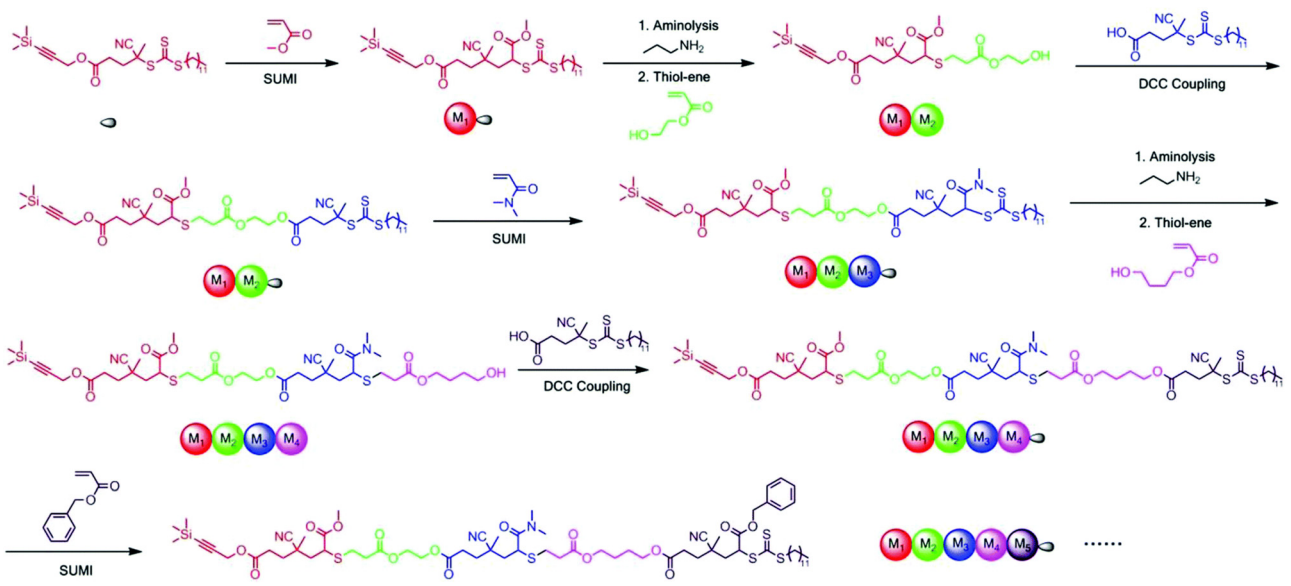

Fig. 23 Schematic representation of the synthesis of a sequence-defined pentamer *via* iterative SUMI, aminolysis, thiol–ene, and esterification reactions. Adapted with permission from ref. 419 (Copyright 2017 The Royal Society of Chemistry).

caused heating of the reaction mixture and subsequent hydrolysis of the CTA resulted in the loss of polymerization control. Qiao and coworkers synthesized UHMW star polymers from 4- and 21-arm xanthates in DMSO.[278] UV light irradiation was more efficient than violet light to reach 96% monomer conversion after 6 and 102 hours, respectively, although UV light could lead to unselective activation of the monomer and loss of polymerization control. UHMW linear and branched block copolymers of acrylic acid and various acrylamides for application as microgel viscosifiers for water-based drilling fluids were synthesized in water under UV light irradiation (350 nm, 7.2 mW cm^{-2}).[420]

Sumerlin and coworkers expanded the monomer scope to monomers with relatively low k_p such as (meth)acrylates and styrene in DMSO.[413] In DMSO, monomer concentrations should be higher than those in water to achieve sufficiently high polymerization kinetics. In particular, synthesis of UHMW poly(MMA) from TTC under UV light irradiation (365 nm, 7.0 mW cm^{-2}) required the addition of tertiary amine PMDETA. It was presumed that in the absence of PMDETA, the TTC sulfanyl radical abstracted the hydrogen atom from the propagating methacryloyl chain end, thereby affording a dead chain *via* disproportionation. The lower k_p of styrene needed to be compensated by alternatively copolymerizing styrene with maleic anhydride or maleimide *via* charge-transfer complex formation. However, because of absorption and background initiation from the charge-transfer complex in the UV region, TTC was replaced with DTB to shift the irradiation wavelength from 365 nm to 450 nm.

5.2.4. Photo-PISA. Boyer and coworkers, for the first time, demonstrated the potential of photo-PISA in the absence of a PC to encapsulate hydrophobic drug molecules into polymer micelles.[421] A poly(OEGMA)-based macro-CTA was initially synthesized from CDTPA by thermally initiated RAFT polymerization. Photoiniferter polymerization of BzMAs from the macro-CTA in acetonitrile/ethanol cosolvent under blue (460 nm, 0.7 mW cm^{-2}) or green light irradiation (530 nm, 0.7 mw cm^{-2}) led to the formation of worm-like micelles. When Nile Red, a model hydrophobic drug, was introduced into the reaction mixture, Nile Red was *in situ* encapsulated in the worm-like micelles, suggesting the potential application of photo-PISA for delivery of hydrophobic drugs. Blue light degraded the end group of CTAs and broadened the dispersity of polymers, but was appropriate for the polymerization in the presence of Nile Red as the polymerization under green light irradiation was significantly inhibited by the absorption of green light by Nile Red. This encapsulation methodology *via* photo-PISA was successfully expanded to another hydrophobic drug doxorubicin using a continuous flow reactor equipped with a 460 nm LED strip.[422] The continuous flow reactor not only enabled the scalable synthesis of polymeric NPs, but also the facile control of NP morphologies by simply adjusting the flow rate and residence time to modulate the length of a solvophobic block. Besides the drug encapsulation, spherical NPs prepared from photo-PISA served as a template to synthesize 3D mesoporous carbon materials.[406]

5.2.5. Surface functionalization. Photoiniferter polymerization from CDTPA grafted on UCNPs led to the grafting-from

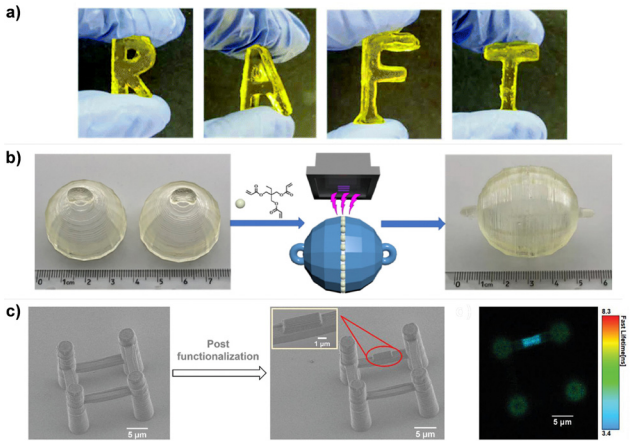

Fig. 24 (a) 3D printed objects. (b) Welding two 3D printed balls by adding fresh TMPTA on the interface and subsequent irradiation. (c) SEM images of the 3D printed bridge before and after post-modification with fluorescein-conjugated TMPTA. The fluorescein-embedded layer was visualized by fluorescence lifetime imaging microscopy (FLIM). Adapted with permission from (a) ref. 403 (Copyright 2020 The Royal Society of Chemistry), (b) ref. 161 (Copyright 2022 American Chemical Society), and (c) ref. 424 (Copyright 2021 John Wiley & Sons, Inc.).

surface functionalization with polymers comprised of glycidyl methacrylate (GMA), OEGMA, and hydroxyethyl methacrylate (HEMA) under blue (460 nm, 0.7 mW cm^{-2}) or green light irradiation (530 nm, 0.7 mW cm^{-2}).[400] The absence of a PC was advantageous because the remaining PC would interfere with the optical or upconversion properties of the resulting particles.

5.2.6. 3D printing. Jin, Bagheri, and coworkers in collaboration with the research group of Boyer applied photoiniferter polymerization of TTCs under violet light irradiation (405 nm, 1.8 mW cm^{-2}) to 3D printing (Fig. 24a).[403] The build speed was limited by the slow and inefficient photolysis of TTC. Nevertheless, reactivation of TTC units after 3D printing allowed transformation of the 3D printed object. Soaking the 3D printed object in *n*-BA dissolved in DMSO followed by blue light irradiation (460 nm, 0.7 mW cm^{-2}) facilitated insertion of hydrophobic *n*-BA into outer layers of the object and modified surface hydrophilicity. This report was the first to present implementation of photoiniferter polymerization in 3D printing, but 3D printing was performed under a N_2 atmosphere with degassed reaction solutions.

Open-to-air 3D printing by the DLP technique under violet light irradiation (405 nm, 2.0 mW cm^{-2}) was performed using EXEP.[161] DFT calculations and ESR spin-trapping experiments confirmed that photolysis of EXEP under irradiation at 325–480 nm was more efficient than that of structurally similar TTC due to the lower bond dissociation energy of EXEP (38.06 kcal mol^{-1} *vs.* 41.5 kcal mol^{-1}). Although oxidation-induced loss of end-group fidelity of polymers was previously observed for photoiniferter polymerization using EXEP under blue light irradiation (460–470 nm),[162] the end-group fidelity of polymers within 3D printed objects seemed to be preserved allowing post-functionalization with the freshly added PEGDA and trimethyloylpropane triacrylate (TMPTA) or welding,

without an additional introduction of the photoinitiator or PC (Fig. 24b). When this photoiniferter polymerization was combined with cationic RAFT polymerization using diphenyliodonium hexafluorophosphate onium salt, welding of 3D printed objects was realized by either photoiniferter polymerization under violet light irradiation (405 nm, 60 mW cm^{-2}) or $ZnCl_2$-mediated conventional cationic RAFT polymerization without irradiation.[423] Herein, polymerization (*i.e.*, 3D printing) was initiated by photolysis of two types of CTAs which were expected to orthogonally proceed radical and cationic RAFT polymerization, which would allow tailoring of the mechanical properties of polymeric materials by adjusting the ratio of radically and cationically polymerizable monomers.

DTC bearing conjugated carbazole in the Z group was also applied to prepare 3D microstructures by the direct laser writing technique in the presence of air.[424] Photoiniferter polymerization of *n*-BA under blue light irradiation (480 nm) followed by subsequent photoiniferter polymerization with TMPTA under green light irradiation (532 nm) provided mechanically stable 3D microstructures. Owing to the preserved DTC units, fabrication of multilayered microstructures comprised of multiple polymeric materials *via* repeated polymerization was successfully realized. Post-modification by polymerization with thermoresponsive NIPAm provided the printed object capable of heating-induced shrinkage and cooling-induced swelling, whereas polymerization with fluorescein-conjugated TMPTA allowed the visualization of the modified layer by fluorescence lifetime imaging microscopy (FLIM) (Fig. 24c).

6. Photomediated cationic RAFT polymerization

6.1. PCs for polymerization

A strongly oxidizing pyrylium salt was first employed for the photomediated cationic RAFT polymerization of vinyl ethers under blue light irradiation (450 nm) (Scheme 27).[43] The excited-state pyrylium salt oxidized the vinyl ether-derived CTA to generate a carbocation intermediate and reversible generation of the carbocations enabled the regulation of cationic RAFT polymerization by light. iBVE and other vinyl ethers (*i.e.*, ethyl, 2-chloroethyl, *n*-propyl, and *n*-butyl-vinyl ethers) were polymerized from DTC and TTC, respectively. In contrast to PET-RAFT polymerization, photomediated cationic RAFT polymerization required CTAs possessing vinyl ether as the R group. However, imperfect temporal control and monomer conversion in the absence of irradiation were observed in further studies, which was ascribed to the decomposition of the PC. Moreover, the experimental molecular weights of polymers were significantly lower than the theoretical value when the authors targeted to synthesize polymers with molecular weight above 20 kg mol^{-1}.

Other oxidizing PCs including the Ru complex and acridinium salt, however, were unsuccessful for the polymerization of iBVE from DTCs.[90] Thereafter, Kamigaito, Ohkubo, and coworkers discovered that acridinium salts at doubled catalyst loadings to that of the previous study[90] could catalyze the polymerization from TTC at −40 °C despite imperfect temporal control,[91] where the polymerization rate was somehow affected by the type of counter-anions of acridinium salts which possessed the same structure and similar redox potentials. Although the polymerization of the chloroethyl vinyl monomer from DTC was uncontrolled because the high E^*_{ox} (2.06–2.25 V *vs.* SCE) oxidized the chloroethyl substituent of the monomer or the amino substituent of the CTA, acridinium salts extended the polymerization wavelength from blue to white and green.

The imperfect temporal control (*i.e.*, monomer conversion in the dark), observed particularly at high monomer conversion, that was noticed for both pyrylium and acridinium salts was ascribed to low stability of the PC or high E^*_{ox}. Instead, Ir complexes with enhanced stability demonstrated no monomer conversion in the dark.[425] Moreover, appropriate redox potentials of Ir complexes enabled the synthesis of high-molecular-weight polymers owing to the well-balanced rates of activation and deactivation steps, and the preferential oxidation of the CTA over that of vinyl ether monomers. Owing to more reducing E^0_{red}, Ir complex in contrast to pyrylium salt efficiently generated the thiolate anion that recaps the propagating cation intermediates and completely prevented the polymerization in the dark.[426] Herein, a thioacetal instead of a dithioester was used as a CTA, but the mechanism was technically identical except that the sulfonium intermediate participated in degenerative chain transfer. The importance of an appropriate redox potential was also verified by Liao and coworkers in the case of bisphosphonium salt (E^*_{ox} = 2.01–2.06 V *vs.* SCE).[427] The bisphosphonium salt allowed the polymerization of a variety of vinyl ethers from TTC with excellent temporal control at low catalyst loadings (in the ppm range) under sunlight irradiation. Similarly, the monophosphonium salt synthesized by the same research group exhibited excellent temporal control.[428] The relationship between the structure of the PC and polymerization activity was explored based on high modularity of the structure of the PC and the concomitantly widened redox window. The controllability of

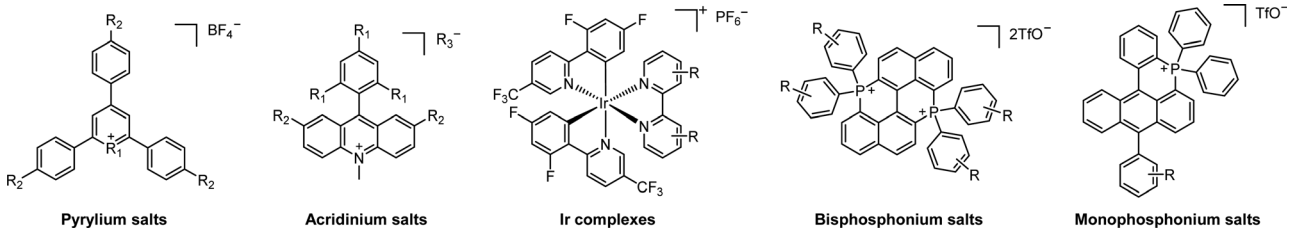

Scheme 27 Chemical structures of PCs employed for photomediated cationic RAFT polymerization.

polymerization was dependent on the successful oxidation of the CTA by the excited-state PC, which was influenced by the redox potential, lifetime, and Φ_{FL} of the excited-state PC.

On the other hand, cationic RAFT polymerization under NIR light irradiation (788 nm, 14 mW cm^{-2}) was induced by $Fe_2(Cp)_2(CO)_4$ in combination with alkyl bromide as an initiating system,[429] where *in situ*-generated $FeCp(CO_2)Br$ upon irradiation oxidizes a carbon-centered radical to provide an initiating cation *via* a mechanic process similar to photoinduced radical oxidation/addition/deactivation (PROAD) that was previously reported by Yagci and coworkers.[430] Zhu, Perrier, and coworkers employed $Mn(CO)_{10}$/alkyl bromide[431] or $Mn(CO)_5Br$ alone under blue light irradiation (440 nm, 10 mWcm^{-2}).[432] $Mn(CO)_5Br$, a bench-stable PC with reduced sensitivity to oxygen compared to the $Mn(CO)_{10}$/alkyl bromide system, for the first time facilitated the polymerization of iBVE without prior deoxygenation either in a batch or continuous flow reactor.

6.2. Applications

Selective activation of $Ir(ppy)_3$-catalyzed PET-RAFT and pyrylium salt-catalyzed photomediated cationic RAFT polymerization of MA and iBVE, respectively, by simply changing the irradiation wavelength was applied in one-pot synthesis of a multiblock copolymer (Table 2, entry 1).[124] According to the absorption profile of PCs, absorption of $Ir(ppy)_3$ and subsequent PET-RAFT polymerization of MA under blue light (450 nm), and absorption of the pyrylium salt and subsequent photomediated cationic RAFT polymerization of iBVE under green light (520 nm) were expected. However, partially overlapping absorption profiles of two PCs also resulted in photomediated cationic RAFT polymerization at 450 nm and the problematic synthesis of tapered block copolymers. Fors and coworkers took advantage of the simultaneous PET-RAFT and photomediated cationic RAFT polymerizations to modulate the mechanical properties of thermoset polymers.[126] Cross-linking of 1,4-butanediol divinyl ethers under green light irradiation (525 nm, 142 mW cm^{-2}) generated the polymer network, whereas by switching to blue light (456 nm, 108 mW cm^{-2}), butanediol diacrylates were also incorporated into the network and increased the cross-linking density and Young's modulus. Thus, the mechanical properties of the polymer network became easily adjustable by the amount of diacrylates, irradiation time and light intensity, and *via* spatially controlled PET-RAFT polymerization by applying a photomask. Nevertheless, photomediated cationic RAFT polymerization is still at an early stage for numerous applications owing to the narrow scope of monomers, PCs, and solvents and lack of oxygen tolerance in the reaction system. The recent development of PCs[92] or use of continuous flow reactors[382] combined with further studies would expand the utility of the polymerization.

7. Summary and outlook

Among photocontrolled RAFT polymerization reactions, visible-light-driven RAFT polymerization which harnesses visible light or even sunlight has drawn attention in various fields including polymer chemistry, materials science, and bioengineering to name a few. As visible light is an environmentally benign and easily accessible energy source and visible-light photocatalysis provides oxygen tolerance that simplifies the reaction design by eliminating laborious deoxygenation, visible-light-driven RAFT polymerization is expected to be soon utilized at an industrial scale and face the new era in the near future. In particular, PET-RAFT polymerization with highly efficient oxygen tolerance has been successfully adapted for bioapplications, surface functionalization, 3D/4D printing, and HTP synthesis in readily accessible reactor system designs without prior degassing.

In addition, polymers synthesized by RAFT polymerization have recently been subjected to depolymerization, drawing attention to a sustainable future of polymer chemistry. Anastasaki and coworkers reported radical-mediated, catalyst-free, and near-quantitative depolymerization of various methacrylic polymers.[433] Thermally induced homolytic cleavage of the C–S bond at 120 °C generated chain-end radicals and released monomers from the end of the polymer. Depolymerization of the polymer became favored over re-insertion of the released monomers under highly dilute conditions (5 mM relative to the monomer; 200 times lower than that of typical polymerization conditions). Again, *via* visible-light-driven photocatalysis both in the presence[434] and absence of a PC,[435] faster rates and higher conversions of depolymerization were achieved despite the temperature being lowered to 100 °C. The improved reaction efficiencies were attributed to more efficient generation of chain-end radicals *via* the combined thermally and photo-induced homolytic cleavage of the C–S bond. In all cases, high end-group fidelity of polymers provided by RAFT polymerization was essential for efficient depolymerization. These initial demonstrations of depolymerization are expected to be applied for a wider scope of polymers (*i.e.*, prepared from non-methacrylic monomers and various CTAs) under milder reaction conditions. Combined with the synthesis of degradable vinyl polymers *via* copolymerization with macrocyclic allylic sulfones,[100,185] radical-mediated depolymerization would provide further opportunities for polymer chemistry.

However, there is still room for improvement. First, although the interest in comprehensively elucidating mechanistic backgrounds using computational chemistry and kinetic modeling has increased, it is currently limited to only a few types of PCs and/or CTAs. Only when the discrepancy in each combination of PC and/or CTA is considered, a fully optimized reaction system for the intended applications may be designed.[436] Second, compared to PET-RAFT polymerization, the applications of photoiniferter and photomediated cationic RAFT polymerizations are still limited by the lack of oxygen tolerance and a rather narrow range of operational irradiation wavelengths and solvents for the polymerization reactions. Regardless of the polymerization method, a fundamental understanding of the mechanisms of the photomediated process (*e.g.*, the involvement of singlet or triplet excited states, the transfer of electron or energy, and the fate of the reaction intermediates) would improve the reaction system. Third, although the introduction of flow chemistry has enhanced the scalability of visible-light-driven RAFT polymerizations, the design of a reactor that could provide an accurate control over the light

intensity (*i.e.*, photon flux) and reaction temperature is necessary for consistency of polymer properties. This influence of the reactor geometry and volume on PET-RAFT polymerization was also reported for a cylindrical batch system.[437]

In summary, we have provided herein a brief history, progress, and future challenges of photocontrolled RAFT polymerization. Recent studies on degradation and thermally or photo-induced depolymerization of polymers synthesized *via* RAFT polymerization, which potentially provide closed-loop recycling of the polymers synthesized by RAFT polymerization, have also been mentioned. Therefore, photocontrolled RAFT polymerization holds significant promise in polymer chemistry ranging from an environmentally friendly synthesis to a green future of polymers such as commercial vinyl polymers including plastics.[438] We anticipate that this review will provide guidance on how and to what extent the photocontrolled RAFT polymerization could be utilized, and attract researchers from various fields to achieve the full potential of the method, which pose a greater impact on our society in line with the ever-growing need for environmental compatibility.

Conflicts of interest

There are no conflicts to declare.

Acknowledgements

This work at SNU was supported by the National Research Foundation of Korea (NRF) funded by the Korean government (MSIT) (2022R1A2C2011627 and 2021R1A5A1030054) and the Challengeable Future Defense Technology Research and Development Program (No. 912909601) of Agency for Defense Development in 2022. Professor Cyrille Boyer (or C.B.) is the recipient of an Australian Research Council Australian Laureate Fellowship (FL220100016) funded by the Australian government.

References

1 L. J. Malone and T. Dolter, *Basic Concepts of Chemistry*, John Wiley & Sons, Inc., 2008.
2 G. Ciamician, *Science*, 1912, **36**, 385–394.
3 B. König, *Eur. J. Org. Chem.*, 2017, 1979–1981.
4 D. A. Nicewicz and D. W. C. MacMillan, *Science*, 2008, **322**, 77–80.
5 M. A. Ischay, M. E. Anzovino, J. Du and T. P. Yoon, *J. Am. Chem. Soc.*, 2008, **130**, 12886–12887.
6 J. M. R. Narayanam, J. W. Tucker and C. R. J. Stephenson, *J. Am. Chem. Soc.*, 2009, **131**, 8756–8757.
7 T. P. Yoon, M. A. Ischay and J. Du, *Nat. Chem.*, 2010, **2**, 527–532.
8 J. M. R. Narayanam and C. R. J. Stephenson, *Chem. Soc. Rev.*, 2011, **40**, 102–113.
9 C. K. Prier, D. A. Rankic and D. W. C. MacMillan, *Chem. Rev.*, 2013, **113**, 5322–5363.
10 L. Marzo, S. K. Pagire, O. Reiser and B. König, *Angew. Chem., Int. Ed.*, 2018, **57**, 10034–10072.
11 N. A. Romero and D. A. Nicewicz, *Chem. Rev.*, 2016, **116**, 10075–10166.
12 T. Rigotti and J. Alemán, *Chem. Commun.*, 2020, **56**, 11169–11190.
13 V. Srivastava, P. K. Singh and P. P. Singh, *J. Photochem. Photobiol., C*, 2022, **50**, 100488.
14 J.-F. Lutz, J.-M. Lehn, E. W. Meijer and K. Matyjaszewski, *Nat. Rev. Mater.*, 2016, **1**, 16024.
15 W. A. Braunecker and K. Matyjaszewski, *Prog. Polym. Sci.*, 2007, **32**, 93–146.
16 K. Matyjaszewski, *Adv. Mater.*, 2018, **30**, 1706441.
17 J.-S. Wang and K. Matyjaszewski, *Macromolecules*, 1995, **28**, 7901–7910.
18 J. Chiefari, Y. K. (Bill) Chong, F. Ercole, J. Krstina, J. Jeffery, T. P. T. Le, R. T. A. Mayadunne, G. F. Meijs, C. L. Moad, G. Moad, E. Rizzardo and S. H. Thang, *Macromolecules*, 1998, **31**, 5559–5562.
19 M. Chen, M. Zhong and J. A. Johnson, *Chem. Rev.*, 2016, **116**, 10167–10211.
20 N. Corrigan, S. Shanmugam, J. Xu and C. Boyer, *Chem. Soc. Rev.*, 2016, **45**, 6165–6212.
21 S. Dadashi-Silab, M. Atilla Tasdelen and Y. Yagci, *J. Polym. Sci., Part A: Polym. Chem.*, 2014, **52**, 2878–2888.
22 Y. Yagci, S. Jockusch and N. J. Turro, *Macromolecules*, 2010, **43**, 6245–6260.
23 M. A. Tasdelen, M. Uygun and Y. Yagci, *Macromol. Rapid Commun.*, 2011, **32**, 58–62.
24 A. Anastasaki, V. Nikolaou, Q. Zhang, J. Burns, S. R. Samanta, C. Waldron, A. J. Haddleton, R. McHale, D. Fox, V. Percec, P. Wilson and D. M. Haddleton, *J. Am. Chem. Soc.*, 2014, **136**, 1141–1149.
25 R. Ran, Y. Yu and T. Wan, *J. Appl. Polym. Sci.*, 2007, **105**, 398–404.
26 H. Wang, Q. Li, J. Dai, F. Du, H. Zheng and R. Bai, *Macromolecules*, 2013, **46**, 2576–2582.
27 Y. Kwak and K. Matyjaszewski, *Macromolecules*, 2010, **43**, 5180–5183.
28 B. P. Fors and C. J. Hawker, *Angew. Chem., Int. Ed.*, 2012, **51**, 8850–8853.
29 D. Konkolewicz, K. Schröder, J. Buback, S. Bernhard and K. Matyjaszewski, *ACS Macro Lett.*, 2012, **1**, 1219–1223.
30 M. A. Tasdelen, M. Ciftci and Y. Yagci, *Macromol. Chem. Phys.*, 2012, **213**, 1391–1396.
31 J. Xu, K. Jung, A. Atme, S. Shanmugam and C. Boyer, *J. Am. Chem. Soc.*, 2014, **136**, 5508–5519.
32 J. Xu, S. Shanmugam, N. A. Corrigan and C. Boyer, *Controlled Radical Polymerization: Mechanisms*, American Chemical Society, Washington, DC, 2015, vol. 1187, pp. 247–267.
33 T. G. McKenzie, Q. Fu, E. H. H. Wong, D. E. Dunstan and G. G. Qiao, *Macromolecules*, 2015, **48**, 3864–3872.
34 N. Corrigan, K. Jung, G. Moad, C. J. Hawker, K. Matyjaszewski and C. Boyer, *Prog. Polym. Sci.*, 2020, **111**, 101311.
35 C. Aydogan, G. Yilmaz, A. Shegiwal, D. M. Haddleton and Y. Yagci, *Angew. Chem., Int. Ed.*, 2022, **61**, e202117377.

36 D. A. Corbin and G. M. Miyake, *Chem. Rev.*, 2022, **122**, 1830–1874.
37 S. Perrier, *Macromolecules*, 2017, **50**, 7433–7447.
38 J. F. Quinn, L. Barner, C. Barner-Kowollik, E. Rizzardo and T. P. Davis, *Macromolecules*, 2002, **35**, 7620–7627.
39 T. Otsu and M. Yoshida, *Macromol. Rapid Commun.*, 1982, **3**, 127–132.
40 T. Otsu, M. Yoshida and T. Tazaki, *Macromol. Rapid Commun.*, 1982, **3**, 133–140.
41 M. Uchiyama, K. Satoh and M. Kamigaito, *Angew. Chem., Int. Ed.*, 2015, **54**, 1924–1928.
42 S. Sugihara, N. Konegawa and Y. Maeda, *Macromolecules*, 2015, **48**, 5120–5131.
43 V. Kottisch, Q. Michaudel and B. P. Fors, *J. Am. Chem. Soc.*, 2016, **138**, 15535–15538.
44 J. Phommalysack-Lovan, Y. Chu, C. Boyer and J. Xu, *Chem. Commun.*, 2018, **54**, 6591–6606.
45 S. Dadashi-Silab, S. Doran and Y. Yagci, *Chem. Rev.*, 2016, **116**, 10212–10275.
46 S. Shanmugam, J. Xu and C. Boyer, *Macromol. Rapid Commun.*, 2017, **38**, 1700143.
47 X. Pan, M. A. Tasdelen, J. Laun, T. Junkers, Y. Yagci and K. Matyjaszewski, *Prog. Polym. Sci.*, 2016, **62**, 73–125.
48 M. L. Allegrezza and D. Konkolewicz, *ACS Macro Lett.*, 2021, **10**, 433–446.
49 J. Yeow, R. Chapman, A. J. Gormley and C. Boyer, *Chem. Soc. Rev.*, 2018, **47**, 4357–4387.
50 N. Corrigan, J. Yeow, P. Judzewitsch, J. Xu and C. Boyer, *Angew. Chem., Int. Ed.*, 2019, **58**, 5170–5189.
51 S. Li, G. Han and W. Zhang, *Polym. Chem.*, 2020, **11**, 1830–1844.
52 V. Bellotti and R. Simonutti, *Polymers*, 2021, **13**, 1119.
53 K. Parkatzidis, H. S. Wang, N. P. Truong and A. Anastasaki, *Chem*, 2020, **6**, 1575–1588.
54 T. G. McKenzie, Q. Fu, M. Uchiyama, K. Satoh, J. Xu, C. Boyer, M. Kamigaito and G. G. Qiao, *Adv. Sci.*, 2016, **3**, 1500394.
55 M. D. Nothling, Q. Fu, A. Reyhani, S. Allison-Logan, K. Jung, J. Zhu, M. Kamigaito, C. Boyer and G. G. Qiao, *Adv. Sci.*, 2020, **7**, 2001656.
56 M. Hartlieb, *Macromol. Rapid Commun.*, 2022, **43**, 2100514.
57 C. A. Figg, J. D. Hickman, G. M. Scheutz, S. Shanmugam, R. N. Carmean, B. S. Tucker, C. Boyer and B. S. Sumerlin, *Macromolecules*, 2018, **51**, 1370–1376.
58 H. Zhou and J. A. Johnson, *Angew. Chem., Int. Ed.*, 2013, **52**, 2235–2238.
59 Q. Wang, F.-Y. Bai, Y. Wang, F. Niu, Y. Zhang, Q. Mi, K. Hu and X. Pan, *J. Am. Chem. Soc.*, 2022, **144**, 19942–19952.
60 E. E. Stache, V. Kottisch and B. P. Fors, *J. Am. Chem. Soc.*, 2020, **142**, 4581–4585.
61 G. Moad, E. Rizzardo and S. H. Thang, *Aust. J. Chem.*, 2012, **65**, 985–1076.
62 L. T. Strover, A. Cantalice, J. Y. L. Lam, A. Postma, O. E. Hutt, M. D. Horne and G. Moad, *ACS Macro Lett.*, 2019, **8**, 1316–1322.
63 F. Izadi, E. Arthur-Baidoo, L. T. Strover, L.-J. Yu, M. L. Coote, G. Moad and S. Denifl, *Angew. Chem., Int. Ed.*, 2021, **60**, 19128–19132.
64 Z. Wu, K. Jung, C. Wu, G. Ng, L. Wang, J. Liu and C. Boyer, *J. Am. Chem. Soc.*, 2022, **144**, 995–1005.
65 C. Yu, J. Song, T. I. Kim, Y. Lee, Y. Kwon, J. Kim, J. Park, J. Choi, J. Doh, S. K. Min, S. Cho and M. S. Kwon, *ACS Catal.*, 2023, **13**, 665–680.
66 J. Xu, S. Shanmugam, H. T. Duong and C. Boyer, *Polym. Chem.*, 2015, **6**, 5615–5624.
67 J. Niu, D. J. Lunn, A. Pusuluri, J. I. Yoo, M. A. O'Malley, S. Mitragotri, H. T. Soh and C. J. Hawker, *Nat. Chem.*, 2017, **9**, 537–545.
68 B. S. Tucker, M. L. Coughlin, C. A. Figg and B. S. Sumerlin, *ACS Macro Lett.*, 2017, **6**, 452–457.
69 H. Sun, W. Choi, N. Zang, C. Battistella, M. P. Thompson, W. Cao, X. Zhou, C. Forman and N. C. Gianneschi, *Angew. Chem., Int. Ed.*, 2019, **58**, 17359–17364.
70 C. Fu, B. Demir, S. Alcantara, V. Kumar, F. Han, H. G. Kelly, X. Tan, Y. Yu, W. Xu, J. Zhao, C. Zhang, H. Peng, C. Boyer, T. M. Woodruff, S. J. Kent, D. J. Searles and A. K. Whittaker, *Angew. Chem., Int. Ed.*, 2020, **59**, 4729–4735.
71 Q. Fu, T. G. McKenzie, S. Tan, E. Nam and G. G. Qiao, *Polym. Chem.*, 2015, **6**, 5362–5368.
72 M. L. Allegrezza, Z. M. DeMartini, A. J. Kloster, Z. A. Digby and D. Konkolewicz, *Polym. Chem.*, 2016, **7**, 6626–6636.
73 B. Nomeir, O. Fabre and K. Ferji, *Macromolecules*, 2019, **52**, 6898–6903.
74 J. W. Beatty and C. R. J. Stephenson, *Acc. Chem. Res.*, 2015, **48**, 1474–1484.
75 J.-H. Back, Y. Kwon, H. Cho, H. Lee, D. Ahn, H.-J. Kim, Y. Yu, Y. Kim, W. Lee and M. S. Kwon, *Adv. Mater.*, 2022, 2204776.
76 F. Strieth-Kalthoff, M. J. James, M. Teders, L. Pitzer and F. Glorius, *Chem. Soc. Rev.*, 2018, **47**, 7190–7202.
77 F. Strieth-Kalthoff and F. Glorius, *Chem*, 2020, **6**, 1888–1903.
78 D. L. Dexter, *J. Chem. Phys.*, 1953, **21**, 836–850.
79 S. S. Skourtis, C. Liu, P. Antoniou, A. M. Virshup and D. N. Beratan, *Proc. Natl. Acad. Sci. U. S. A.*, 2016, **113**, 8115–8120.
80 R. A. Marcus, *Rev. Mod. Phys.*, 1993, **65**, 599–610.
81 P. Seal, J. Xu, S. Luca, C. Boyer, S. C. Smith, S. De Luca, C. Boyer and S. C. Smith, *Adv. Theory Simulations*, 2019, **2**, 1900038.
82 M. D. Thum, S. Wolf and D. E. Falvey, *J. Phys. Chem. A*, 2020, **124**, 4211–4222.
83 J. Christmann, A. Ibrahim, V. Charlot, C. Croutxé-Barghorn, C. Ley and X. Allonas, *ChemPhysChem.*, 2016, **17**, 2309–2314.
84 N. Corrigan, J. Xu, C. Boyer and X. Allonas, *ChemPhotoChem*, 2019, **3**, 1193–1199.
85 L. R. Kuhn, M. L. Allegrezza, N. J. Dougher and D. Konkolewicz, *J. Polym. Sci.*, 2020, **58**, 139–144.
86 T. Otsu, *J. Polym. Sci., Part A: Polym. Chem.*, 2000, **38**, 2121–2136.
87 M. L. Allegrezza, N. De Alwis Watuthanthrige, Y. Wang, G. A. Garcia, H. Ren and D. Konkolewicz, *Polym. Chem.*, 2020, **11**, 6129–6133.
88 C. Yu, J.-K. Ha, J. Ahn, J. Lee, J. Choi, T. Chang, S. K. Min and M. S. Kwon, *Chemrxiv*, 2023, DOI: **10.26434/chemrxiv-2023-dl842**.

89 J. Xu, C. Fu, S. Shanmugam, C. J. Hawker, G. Moad and C. Boyer, *Angew. Chem., Int. Ed.*, 2017, **56**, 8376–8383.
90 Q. Michaudel, T. Chauviré, V. Kottisch, M. J. Supej, K. J. Stawiasz, L. Shen, W. R. Zipfel, H. D. Abruña, J. H. Freed and B. P. Fors, *J. Am. Chem. Soc.*, 2017, **139**, 15530–15538.
91 M. Matsuda, M. Uchiyama, Y. Itabashi, K. Ohkubo and M. Kamigaito, *Polym. Chem.*, 2022, **13**, 1031–1039.
92 R. J. Sifri, Y. Ma and B. P. Fors, *Acc. Chem. Res.*, 2022, **55**, 1960–1971.
93 S. Shanmugam, J. Xu and C. Boyer, *Macromolecules*, 2017, **50**, 1832–1846.
94 M. Chen, S. Deng, Y. Gu, J. Lin, M. J. MacLeod and J. A. Johnson, *J. Am. Chem. Soc.*, 2017, **139**, 2257–2266.
95 Y. Huang, X. R. Zhang, S. Ye, J. Le Li, X. Li and T. Cai, *Nanoscale*, 2019, **11**, 13502–13510.
96 C. Wu, H. Chen, N. Corrigan, K. Jung, X. Kan, Z. Li, W. Liu, J. Xu and C. Boyer, *J. Am. Chem. Soc.*, 2019, **141**, 8207–8220.
97 X. Li, Y. C. Zhang, Y. Zhao, H. P. Zhao, B. Zhang and T. Cai, *Macromolecules*, 2020, **53**, 1550–1556.
98 S. Shanmugam, J. Xu and C. Boyer, *Polym. Chem.*, 2016, **7**, 6437–6449.
99 L. Zhang, C. Wu, K. Jung, Y. H. Ng and C. Boyer, *Angew. Chem., Int. Ed.*, 2019, **58**, 16811–16814.
100 W. Wang, Z. Zhou, D. Sathe, X. Tang, S. Moran, J. Jin, F. Haeffner, J. Wang and J. Niu, *Angew. Chem., Int. Ed.*, 2022, **61**, e202113302.
101 X. Li, S. Ye, Y. C. Zhang, H. P. Zhao, Y. Huang, B. Zhang and T. Cai, *Nanoscale*, 2020, **12**, 7595–7603.
102 X. Li, J. Le Li, W. G. Huang, X.-Z. Zhang, B. Zhang and T. Cai, *Nanoscale*, 2018, **10**, 19254–19261.
103 L. Hu, Q. Wang, X. Zhang, H. Zhao, Z. Cui, P. Fu, M. Liu, N. Liu, S. He, X. Pang and X. Qiao, *RSC Adv.*, 2020, **10**, 6850–6857.
104 C. A. Cox, A. N. Ogorek, J. P. Habumugisha and J. D. Martell, *J. Am. Chem. Soc.*, 2023, **145**, 1818–1825.
105 S. Shanmugam, J. Xu and C. Boyer, *J. Am. Chem. Soc.*, 2015, **137**, 9174–9185.
106 J. Xu, S. Shanmugam, C. Fu, K. F. Aguey-Zinsou and C. Boyer, *J. Am. Chem. Soc.*, 2016, **138**, 3094–3106.
107 S. Houshyar, D. J. Keddie, G. Moad, R. J. Mulder, S. Saubern and J. Tsanaktsidis, *Polym. Chem.*, 2012, **3**, 1879–1889.
108 J. Vandenbergh, G. Reekmans, P. Adriaensens and T. Junkers, *Chem. Commun.*, 2013, **49**, 10358–10360.
109 J. Xu, *Macromolecules*, 2019, **52**, 9068–9093.
110 S. Shanmugam, J. Cuthbert, T. Kowalewski, C. Boyer and K. Matyjaszewski, *Macromolecules*, 2018, **51**, 7776–7784.
111 C. Wu, K. Jung, Y. Ma, W. Liu and C. Boyer, *Nat. Commun.*, 2021, **12**, 478.
112 N. Corrigan, M. Ciftci, K. Jung and C. Boyer, *Angew. Chem., Int. Ed.*, 2021, **60**, 1748–1781.
113 P. Lu, D. Ahn, R. Yunis, L. Delafresnaye, N. Corrigan, C. Boyer, C. Barner-Kowollik and Z. A. Page, *Matter*, 2021, **4**, 2172–2229.
114 N. Corrigan and C. Boyer, *ACS Macro Lett.*, 2019, **8**, 812–818.
115 Z. Zhang, T.-Y. Zeng, L. Xia, C.-Y. Hong, D.-C. Wu and Y.-Z. You, *Nat. Commun.*, 2018, **9**, 2577.
116 M. J. Supej, B. M. Peterson and B. P. Fors, *Chem*, 2020, **6**, 1794–1803.
117 A. Nikolaev, Z. Lu, A. Chakraborty, L. Sepunaru and J. Read de Alaniz, *J. Am. Chem. Soc.*, 2021, **143**, 12278–12285.
118 C. Fu, J. Xu and C. Boyer, *Chem. Commun.*, 2016, **52**, 7126–7129.
119 B. M. Peterson, V. Kottisch, M. J. Supej and B. P. Fors, *ACS Cent. Sci.*, 2018, **4**, 1228–1234.
120 L. Xia, Z. Zhang and Y.-Z. You, *Polym. J.*, 2020, **52**, 1323–1331.
121 K. Satoh, Z. Sun, M. Uchiyama, M. Kamigaito, J. Xu and C. Boyer, *Polym. J.*, 2020, **52**, 65–73.
122 Y. Xia, G. M. Scheutz, C. P. Easterling, J. Zhao and B. S. Sumerlin, *Angew. Chem., Int. Ed.*, 2021, **60**, 18537–18541.
123 C. Fu, J. Xu, M. Kokotovic and C. Boyer, *ACS Macro Lett.*, 2016, **5**, 444–449.
124 V. Kottisch, Q. Michaudel and B. P. Fors, *J. Am. Chem. Soc.*, 2017, **139**, 10665–10668.
125 J. C. Theriot, G. M. Miyake and C. A. Boyer, *ACS Macro Lett.*, 2018, **7**, 662–666.
126 Y. Ma, V. Kottisch, E. A. McLoughlin, Z. W. Rouse, M. J. Supej, S. P. Baker and B. P. Fors, *J. Am. Chem. Soc.*, 2021, **143**, 21200–21205.
127 M. Fromel, E. M. Benetti and C. W. Pester, *ACS Macro Lett.*, 2022, 415–421.
128 P. Xiao, J. Zhang, F. Dumur, M. A. Tehfe, F. Morlet-Savary, B. Graff, D. Gigmes, J. P. Fouassier and J. Lalevée, *Prog. Polym. Sci.*, 2015, **41**, 32–66.
129 J. Xu, K. Jung and C. Boyer, *Macromolecules*, 2014, **47**, 4217–4229.
130 I.-H. Lee, E. H. Discekici, A. Anastasaki, J. R. de Alaniz and C. J. Hawker, *Polym. Chem.*, 2017, **8**, 3351–3356.
131 S. Shanmugam, J. Xu and C. Boyer, *Macromolecules*, 2016, **49**, 9345–9357.
132 H. Lu, Y. Huang, E. Zhang, Y. Liu, F. Lv, L. Liu, Y. Ma and S. Wang, *ACS Macro Lett.*, 2021, **10**, 996–1001.
133 M. Fromel, D. M. Sweeder, S. Jang, T. A. Williams, S. H. Kim and C. W. Pester, *ACS Appl. Polym. Mater.*, 2021, **3**, 5291–5301.
134 A. Bagheri, C. W. A. Bainbridge, K. E. Engel, G. G. Qiao, J. Xu, C. Boyer and J. Jin, *ACS Appl. Polym. Mater.*, 2020, **2**, 782–790.
135 N. Zaquen, W. A. A. W. Azizi, J. Yeow, R. P. Kuchel, T. Junkers, P. B. Zetterlund and C. Boyer, *Polym. Chem.*, 2019, **10**, 2406–2414.
136 N. Zaquen, A. M. N. B. P. H. A. Kadir, A. Iasa, N. Corrigan, T. Junkers, P. B. Zetterlund and C. Boyer, *Macromolecules*, 2019, **52**, 1609–1619.
137 E. Roeven, A. R. Kuzmyn, L. Scheres, J. Baggerman, M. M. J. Smulders and H. Zuilhof, *Langmuir*, 2020, **36**, 10187–10199.
138 A. R. Kuzmyn, A. T. Nguyen, L. W. Teunissen, H. Zuilhof and J. Baggerman, *Langmuir*, 2020, **36**, 4439–4446.
139 C. W. A. Bainbridge, K. E. Engel and J. Jin, *Polym. Chem.*, 2020, **11**, 4084–4093.
140 A. R. Kuzmyn, L. W. Teunissen, P. Fritz, B. van Lagen, M. M. J. Smulders and H. Zuilhof, *Adv. Mater. Interfaces*, 2022, **9**, 2101784.

141 M. Kovaliov, M. L. Allegrezza, B. Richter, D. Konkolewicz and S. Averick, *Polymer*, 2018, **137**, 338–345.
142 Z. Zhang, N. Corrigan, A. Bagheri, J. Jin and C. Boyer, *Angew. Chem., Int. Ed.*, 2019, **58**, 17954–17963.
143 Q. Fu, Q. Ruan, T. G. McKenzie, A. Reyhani, J. Tang and G. G. Qiao, *Macromolecules*, 2017, **50**, 7509–7516.
144 E. Paola Fonseca Parra, B. Chouchene, J.-L. Six, R. Schneider and K. Ferji, *ACS Appl. Polym. Mater.*, 2021, **3**, 3649–3658.
145 N. Corrigan, D. Rosli, J. W. J. Jones, J. Xu and C. Boyer, *Macromolecules*, 2016, **49**, 6779–6789.
146 G. Ng, J. Yeow, J. Xu and C. Boyer, *Polym. Chem.*, 2017, **8**, 2841–2851.
147 S. Xu, J. Yeow and C. Boyer, *ACS Macro Lett.*, 2018, **7**, 1376–1382.
148 S. Xu, G. Ng, J. Xu, R. P. Kuchel, J. Yeow and C. Boyer, *ACS Macro Lett.*, 2017, **6**, 1237–1244.
149 Y. Huang, W. L. Guo, J. C. He, X. Li and T. Cai, *Macromol. Rapid Commun.*, 2022, **43**, 2200020.
150 J. Niu, Z. A. Page, N. D. Dolinski, A. Anastasaki, A. T. Hsueh, H. T. Soh and C. J. Hawker, *ACS Macro Lett.*, 2017, **6**, 1109–1113.
151 Q. Fu, K. Xie, T. G. McKenzie and G. G. Qiao, *Polym. Chem.*, 2017, **8**, 1519–1526.
152 C. Stubbs, T. Congdon, J. Davis, D. Lester, S.-J. Richards and M. I. Gibson, *Macromolecules*, 2019, **52**, 7603–7612.
153 Y. Huang, Y. Sun, Y. Weng and W. Zhang, *ChemistrySelect*, 2022, **7**, e202201583.
154 J. Wang, M. Rivero, A. Muñoz Bonilla, J. Sanchez-Marcos, W. Xue, G. Chen, W. Zhang and X. Zhu, *ACS Macro Lett.*, 2016, **5**, 1278–1282.
155 Y. Zheng, Y. Luo, K. Feng, W. Zhang and G. Chen, *ACS Macro Lett.*, 2019, **8**, 326–330.
156 Y. Zhou, C. Gu, L. Zheng, F. Shan and G. Chen, *Polym. Chem.*, 2022, **13**, 989–996.
157 J. R. Lamb, K. P. Qin and J. A. Johnson, *Polym. Chem.*, 2019, **10**, 1585–1590.
158 C.-Y. Li and S.-S. Yu, *Macromolecules*, 2021, **54**, 9825–9836.
159 J. Li, C. Ding, Z. Zhang, X. Pan, N. Li, J. Zhu and X. Zhu, *Macromol. Rapid Commun.*, 2017, **38**, 1600482.
160 K. M. Burridge, N. De Alwis Watuthanthrige, C. Payne, R. C. Page and D. Konkolewicz, *J. Polym. Sci.*, 2021, **59**, 2530–2536.
161 B. Zhao, J. Li, Y. Xiu, X. Pan, Z. Zhang and J. Zhu, *Macromolecules*, 2022, **55**, 1620–1628.
162 C. Ding, C. Fan, G. Jiang, X. Pan, Z. Zhang, J. Zhu and X. Zhu, *Macromol. Rapid Commun.*, 2015, **36**, 2181–2185.
163 S. E. Seo, E. H. Discekici, Y. Zhang, C. M. Bates and C. J. Hawker, *J. Polym. Sci.*, 2020, **58**, 70–76.
164 R. Li and Z. An, *Angew. Chem., Int. Ed.*, 2020, **59**, 22258–22264.
165 F. Zhou, R. Li, X. Wang, S. Du and Z. An, *Angew. Chem., Int. Ed.*, 2019, **58**, 9479–9484.
166 J. Lalevée, A. Dirani, M. El-Roz, X. Allonas and J. P. Fouassier, *Macromolecules*, 2008, **41**, 2003–2010.
167 S. C. Ligon, B. Husár, H. Wutzel, R. Holman and R. Liska, *Chem. Rev.*, 2014, **114**, 557–589.
168 D. Ahn, L. M. Stevens, K. Zhou and Z. A. Page, *ACS Cent. Sci.*, 2020, **6**, 1555–1563.
169 D. Ahn, L. M. Stevens, K. Zhou and Z. A. Page, *Adv. Mater.*, 2021, **33**, 2104906.
170 J. Yeow, R. Chapman, J. Xu and C. Boyer, *Polym. Chem.*, 2017, **8**, 5012–5022.
171 L. Yu, Y. Wei, Y. Tu, S. Lin, Z. Huang, J. Hu, Y. Chen, H. Qiao and W. Zou, *J. Polym. Sci., Part A: Polym. Chem.*, 2018, **56**, 2437–2444.
172 H. Yang, Z. Lu, X. Fu, Q. Li, Y. Zhao, L. Xiao and L. Hou, *Polym. Chem.*, 2022, **13**, 4776–4781.
173 Z. Wu, W. Fang, C. Wu, N. Corrigan, T. Zhang, S. Xu and C. Boyer, *Chem. Sci.*, 2022, **13**, 11519–11532.
174 J. Sun, S. Ren, H. Zhao, S. Zhang, X. Xu, L. Zhang and Z. Cheng, *ACS Macro Lett.*, 2023, **12**, 165–171.
175 H. Yang, Z. Lu, X. Fu, Q. Li, L. Xiao, R. Zhao, Y. Zhao and L. Hou, *Polym. Chem.*, 2021, **12**, 6998–7004.
176 Y. Lee, Y. Kwon, Y. Kim, C. Yu, S. Feng, J. Park, J. Doh, R. Wannemacher, B. Koo, J. Gierschner and M. S. Kwon, *Adv. Mater.*, 2022, **34**, 2108446.
177 C. Lv, C. He and X. Pan, *Angew. Chem., Int. Ed.*, 2018, **57**, 9430–9433.
178 O. R. Wilson and A. J. D. Magenau, *ACS Macro Lett.*, 2018, **7**, 370–375.
179 Y. Peng, S. Liu, L. Wang, Y. Xu, Z. Wu and H. Chen, *Macromol. Rapid Commun.*, 2022, **43**, 2100920.
180 S. Shanmugam and C. Boyer, *Science*, 2016, **352**, 1053–1054.
181 J. T. Trotta and B. P. Fors, *Synlett*, 2016, 702–713.
182 V. K. Singh, C. Yu, S. Badgujar, Y. Kim, Y. Kwon, D. Kim, J. Lee, T. Akhter, G. Thangavel, L. S. Park, J. Lee, P. C. Nandajan, R. Wannemacher, B. Milián-Medina, L. Lüer, K. S. Kim, J. Gierschner and M. S. Kwon, *Nat. Catal.*, 2018, **1**, 794–804.
183 C. Wu, N. Corrigan, C.-H. Lim, W. Liu, G. Miyake and C. Boyer, *Chem. Rev.*, 2022, **122**, 5476–5518.
184 Y. Lee and M. S. Kwon, *Eur. J. Org. Chem.*, 2020, 6028–6043.
185 W. Wang, B. Rondon, Z. Wang, J. Wang and J. Niu, *Macromolecules*, 2023, **56**, 2052–2061.
186 S. Shanmugam, J. Xu and C. Boyer, *Macromolecules*, 2014, **47**, 4930–4942.
187 J. A. Reeves, N. De Alwis Watuthanthrige, C. Boyer and D. Konkolewicz, *ChemPhotoChem*, 2019, **3**, 1171–1179.
188 P. Yang, P. Pageni, M. P. Kabir, T. Zhu and C. Tang, *ACS Macro Lett.*, 2016, **5**, 1293–1300.
189 G. Li, W. Feng, N. Corrigan, C. Boyer, X. Wang and J. Xu, *Polym. Chem.*, 2018, **9**, 2733–2745.
190 H. Gong, Y. Gu, Y. Zhao, Q. Quan, S. Han and M. Chen, *Angew. Chem., Int. Ed.*, 2020, **59**, 919–927.
191 Q. Yang, V. Ladmiral and B. Améduri, *ChemPhotoChem*, 2019, **3**, 1095–1099.
192 J. Yeow, J. Xu and C. Boyer, *ACS Macro Lett.*, 2015, **4**, 984–990.
193 J. Xu, K. Jung, N. A. Corrigan and C. Boyer, *Chem. Sci.*, 2014, **5**, 3568–3575.

194 S. Shanmugam, J. Xu and C. Boyer, *Chem. Sci.*, 2015, **6**, 1341–1349.
195 C. Wu, S. Shanmugam, J. Xu, J. Zhu and C. Boyer, *Chem. Commun.*, 2017, **53**, 12560–12563.
196 S. Shanmugam, J. Xu and C. Boyer, *Angew. Chem., Int. Ed.*, 2016, **55**, 1036–1040.
197 Z. Yajun, Z. Shuaishuai, L. Xiaojing, Z. Xiaoyu, X. Jing, X. Bijin, W. Yong, Z. Xingping and X. Xiaolin, *CCS Chem.*, 2021, **4**, 122–131.
198 J. Xu, S. Shanmugam and C. Boyer, *ACS Macro Lett.*, 2015, **4**, 926–932.
199 Y. Zhou, Z. Zhang, C. M. Reese, D. L. Patton, J. Xu, C. Boyer, A. Postma and G. Moad, *Macromol. Rapid Commun.*, 2020, **41**, 1900478.
200 S. Xu, N. Corrigan and C. Boyer, *Polym. Chem.*, 2021, **12**, 57–68.
201 S. Xu, T. Zhang, R. P. Kuchel, J. Yeow and C. Boyer, *Macromol. Rapid Commun.*, 2020, **41**, 1900493.
202 L. Shen, Q. Lu, A. Zhu, X. Lv and Z. An, *ACS Macro Lett.*, 2017, **6**, 625–631.
203 W. Wang, S. Zhong, G. Wang, H. Cao, Y. Gao and W. Zhang, *Polym. Chem.*, 2020, **11**, 3188–3194.
204 N. Corrigan, L. Zhernakov, M. H. Hashim, J. Xu and C. Boyer, *React. Chem. Eng.*, 2019, **4**, 1216–1228.
205 D. P. Hari and B. König, *Chem. Commun.*, 2014, **50**, 6688–6699.
206 N. J. Treat, H. Sprafke, J. W. Kramer, P. G. Clark, B. E. Barton, J. Read De Alaniz, B. P. Fors and C. J. Hawker, *J. Am. Chem. Soc.*, 2014, **136**, 16096–16101.
207 M. Chen, M. J. MacLeod and J. A. Johnson, *ACS Macro Lett.*, 2015, **4**, 566–569.
208 M. W. Lampley and E. Harth, *ACS Macro Lett.*, 2018, **7**, 745–750.
209 H. Gong, Y. Zhao, X. Shen, J. Lin and M. Chen, *Angew. Chem., Int. Ed.*, 2018, **57**, 333–337.
210 Q. Quan, H. Wen, S. Han, Z. Wang, Z. Shao and M. Chen, *ACS Appl. Mater. Interfaces*, 2020, **12**, 24319–24327.
211 Y. Zhao, M. Ma, X. Lin and M. Chen, *Angew. Chem., Int. Ed.*, 2020, **59**, 21470–21474.
212 K. Jiang, S. Han, M. Ma, L. Zhang, Y. Zhao and M. Chen, *J. Am. Chem. Soc.*, 2020, **142**, 7108–7115.
213 Q. Quan, Y. Zhao, K. Chen, H. Zhou, C. Zhou and M. Chen, *ACS Catal.*, 2022, **12**, 7269–7277.
214 C. Wu, N. Corrigan, C.-H. Lim, K. Jung, J. Zhu, G. Miyake, J. Xu and C. Boyer, *Macromolecules*, 2019, **52**, 236–248.
215 Y. Song, Y. Kim, Y. Noh, V. K. Singh, S. K. Behera, A. Abudulimu, K. Chung, R. Wannemacher, J. Gierschner, L. Lüer and M. S. Kwon, *Macromolecules*, 2019, **52**, 5538–5545.
216 B.-H. He, M. Lu, C.-X. Yang, Y. Liu, E. Liang and G.-X. Wang, *J. Macromol. Sci., Part A: Pure Appl.Chem.*, 2018, **55**, 583–587.
217 W. Zhang, X. Zhang, Y. Ma, D. Chen and W. Yang, *Macromol. Chem. Phys.*, 2019, **220**, 1900022.
218 Q. Yang, X. Zhang, Y. Ma, D. Chen and W. Yang, *J. Polym. Sci., Part A: Polym. Chem.*, 2018, **56**, 2072–2079.
219 Q. Yang, X. Zhang, W. Ma, Y. Ma, D. Chen, L. Wang, C. Zhao and W. Yang, *J. Polym. Sci., Part A: Polym. Chem.*, 2018, **56**, 229–236.
220 H. Tao, L. Xia, G. Chen, T. Zeng, X. Nie, Z. Zhang and Y. You, *Polymers*, 2019, **11**, 892.
221 H. Cao, G. Wang, Y. Xue, G. Yang, J. Tian, F. Liu and W. Zhang, *ACS Macro Lett.*, 2019, **8**, 616–622.
222 Q. Ma, W. Wang, L. Zhang and H. Cao, *Macromol. Rapid Commun.*, 2022, **43**, 2200122.
223 S. Allison-Logan, Q. Fu, Y. Sun, M. Liu, J. Xie, J. Tang and G. G. Qiao, *Angew. Chem., Int. Ed.*, 2020, **59**, 21392–21396.
224 L. Zhang, G. Ye, X. Huo, S. Xu, J. Chen and K. Matyjaszewski, *ACS Omega*, 2019, **4**, 16247–16255.
225 S. Han, T. Qiu, C. Xiong, X. Li and L. Guo, *Macromolecules*, 2022, **55**, 5314–5325.
226 L. Xia, B.-F. Cheng, T.-Y. Zeng, X. Nie, G. Chen, Z. Zhang, W.-J. Zhang, C.-Y. Hong and Y.-Z. You, *Adv. Sci.*, 2020, **7**, 1902451.
227 Z. Lu, H. Yang, X. Fu, Y. Zhao, L. Xiao, Z. Zhang and L. Hou, *Macromol. Rapid Commun.*, 2021, **42**, 2100384.
228 J. Jiang, G. Ye, Z. Wang, Y. Lu, J. Chen and K. Matyjaszewski, *Angew. Chem., Int. Ed.*, 2018, **57**, 12037–12042.
229 T. Zhang, J. Yeow and C. Boyer, *Polym. Chem.*, 2019, **10**, 4643–4654.
230 J. Jiang, G. Ye, F. Lorandi, Z. Liu, Y. Liu, T. Hu, J. Chen, Y. Lu and K. Matyjaszewski, *Angew. Chem., Int. Ed.*, 2019, **58**, 12096–12101.
231 E. Liang, M. Liu, B. He and G.-X. Wang, *Adv. Polym. Technol.*, 2018, **37**, 2879–2884.
232 K. Hakobyan, T. Gegenhuber, C. S. P. McErlean and M. Müllner, *Angew. Chem., Int. Ed.*, 2019, **58**, 1828–1832.
233 K. P. McClelland, T. D. Clemons, S. I. Stupp and E. A. Weiss, *ACS Macro Lett.*, 2020, **9**, 7–13.
234 Y. Liang, H. Ma, W. Zhang, Z. Cui, P. Fu, M. Liu, X. Qiao and X. Pang, *Polym. Chem.*, 2020, **11**, 4961–4967.
235 Y. Zhu and E. Egap, *Polym. Chem.*, 2020, **11**, 1018–1024.
236 Q. Wang, L. Hu, Z. Cui, P. Fu, M. Liu, X. Qiao and X. Pang, *ACS Appl. Mater. Interfaces*, 2020, **12**, 42161–42168.
237 Y. Zhu, Y. Liu, K. A. Miller, H. Zhu and E. Egap, *ACS Macro Lett.*, 2020, **9**, 725–730.
238 C. Ding, J. Wang, W. Zhang, X. Pan, Z. Zhang, W. Zhang, J. Zhu and X. Zhu, *Polym. Chem.*, 2016, **7**, 7370–7374.
239 Y. Zhu and E. Egap, *ACS Polym. Au*, 2021, **1**, 76–99.
240 Y. Chu, N. Corrigan, C. Wu, C. Boyer and J. Xu, *ACS Sustainable Chem. Eng.*, 2018, **6**, 15245–15253.
241 Y. Chu, Z. Huang, K. Liang, J. Guo, C. Boyer and J. Xu, *Polym. Chem.*, 2018, **9**, 1666–1673.
242 Y. Huang, X. Li, J. Le Li, B. Zhang and T. Cai, *Macromolecules*, 2018, **51**, 7974–7982.
243 Y. Chu, Z. Huang, R. Liu, C. Boyer and J. Xu, *ChemPhotoChem*, 2020, **4**, 5201–5208.
244 S. Shanmugam, S. Xu, N. N. M. Adnan and C. Boyer, *Macromolecules*, 2018, **51**, 779–790.
245 K. Bell, S. Freeburne, A. Wolford and C. W. Pester, *Polym. Chem.*, 2022, **13**, 6120–6126.
246 K. Bell, S. Freeburne, M. Fromel, H. J. Oh and C. W. Pester, *J. Polym. Sci.*, 2021, **59**, 2844–2853.
247 R. A. Olson, J. S. Levi, G. M. Scheutz, J. J. Lessard, C. A. Figg, M. N. Kamat, K. B. Basso and B. S. Sumerlin, *Macromolecules*, 2021, **54**, 4880–4888.

248 J. J. Lessard, G. M. Scheutz, A. B. Korpusik, R. A. Olson, C. A. Figg and B. S. Sumerlin, *Polym. Chem.*, 2021, **12**, 2205–2209.
249 X. Li, Y. C. Zhang, S. Ye, X. R. Zhang and T. Cai, *J. Mater. Chem. A*, 2020, **8**, 25363–25370.
250 Y. Zhao, S. Shao, J. Xia, Y. Huang, Y. C. Zhang, X. Li and T. Cai, *J. Mater. Chem. A*, 2020, **8**, 9825–9831.
251 C. Chen, G. A. Zhou, H. R. Zhang, X. Tang, J. N. Cheng, Y. H. Zhao, X. Li and T. Cai, *Chem. Eng. J.*, 2021, **424**, 130395.
252 M. Zhao, S. Zhu, X. Yang, Y. Wang, X. Zhou and X. Xie, *Macromol. Rapid Commun.*, 2022, **43**, 2200173.
253 F. Li, Y. Yu, H. Lv, G. Cai and Y. Zhang, *Polym. Chem.*, 2021, **12**, 2258–2270.
254 F. Li, Y. Yu, H. Lv, Y. Wan, X. Gao, Y. Li and Y. Zhang, *Eur. Polym. J.*, 2022, **178**, 111519.
255 Y. Zhu, D. Zhu, Y. Chen, Q. Yan, C.-Y. Liu, K. Ling, Y. Liu, D. Lee, X. Wu, T. P. Senftle and R. Verduzco, *Chem. Sci.*, 2021, **12**, 16092–16099.
256 H. Yang, Z. Lu, X. Fu, Q. Li, L. Xiao, Y. Zhao and L. Hou, *Eur. Polym. J.*, 2022, **173**, 111306.
257 L. Zhang, X. Shi, Z. Zhang, R. P. Kuchel, R. Namivandi-Zangeneh, N. Corrigan, K. Jung, K. Liang and C. Boyer, *Angew. Chem., Int. Ed.*, 2021, **60**, 5489–5496.
258 L. Zhang, G. Ng, N. Kapoor-Kaushik, X. Shi, N. Corrigan, R. Webster, K. Jung and C. Boyer, *Angew. Chem., Int. Ed.*, 2021, **60**, 22664–22671.
259 X. Li, Y. Huang, W. F. Wei, W. L. Guo, Z. Luo, J. Xu and T. Cai, *Chem. Eng. J.*, 2022, **434**, 134692.
260 V. P. Beyer, J. Kim and C. R. Becer, *Polym. Chem.*, 2020, **11**, 1271–1291.
261 C. Fu, J. Xu, L. Tao and C. Boyer, *ACS Macro Lett.*, 2014, **3**, 633–638.
262 G. Ng, J. Yeow, R. Chapman, N. Isahak, E. Wolvetang, J. J. Cooper-White and C. Boyer, *Macromolecules*, 2018, **51**, 7600–7607.
263 P. R. Judzewitsch, L. Zhao, E. H. H. Wong and C. Boyer, *Macromolecules*, 2019, **52**, 3975–3986.
264 P. R. Judzewitsch, N. Corrigan, F. Trujillo, J. Xu, G. Moad, C. J. Hawker, E. H. H. Wong and C. Boyer, *Macromolecules*, 2020, **53**, 631–639.
265 A. J. Gormley, J. Yeow, G. Ng, Ó. Conway, C. Boyer and R. Chapman, *Angew. Chem., Int. Ed.*, 2018, **57**, 1557–1562.
266 M. J. Tamasi, R. A. Patel, C. H. Borca, S. Kosuri, H. Mugnier, R. Upadhya, N. S. Murthy, M. A. Webb and A. J. Gormley, *Adv. Mater.*, 2022, **34**, 2201809.
267 Q. Ma, X. Zhang, Y. Jiang, J. Lin, B. Graff, S. Hu, J. Lalevée and S. Liao, *Polym. Chem.*, 2022, **13**, 209–219.
268 C. Boyer, M. Kamigaito, K. Satoh and G. Moad, *Prog. Polym. Sci.*, 2023, **138**, 101648.
269 Z. Huang, B. B. Noble, N. Corrigan, Y. Chu, K. Satoh, D. S. Thomas, C. J. Hawker, G. Moad, M. Kamigaito, M. L. Coote, C. Boyer and J. Xu, *J. Am. Chem. Soc.*, 2018, **140**, 13392–13406.
270 S. Lin, L. Zhang, Z. Huang, P. V. Kumar and J. Xu, *Macromolecules*, 2019, **52**, 7157–7166.
271 L. Zhang, S. Lin and J. Xu, *Macromolecules*, 2022, **55**, 2463–2474.
272 A. Aerts, R. W. Lewis, Y. Zhou, N. Malic, G. Moad and A. Postma, *Macromol. Rapid Commun.*, 2018, **39**, 1800240.
273 Z. Huang, N. Corrigan, S. Lin, C. Boyer and J. Xu, *J. Polym. Sci., Part A: Polym. Chem.*, 2019, **57**, 1947–1955.
274 Y. Yang, K. Yu, S. Liu, J. Yan, H. Lai, F. Xing and P. Xiao, *Macromolecules*, 2021, **54**, 10923–10930.
275 L. Zhang, R. Liu, S. Lin and J. Xu, *Chem. Commun.*, 2021, **57**, 10759–10762.
276 Z. Li, S. Kosuri, H. Foster, J. Cohen, C. Jumeaux, M. M. Stevens, R. Chapman and A. J. Gormley, *J. Am. Chem. Soc.*, 2019, **141**, 19823–19830.
277 H. Foster, M. H. Stenzel and R. Chapman, *Macromolecules*, 2022, **55**, 5938–5945.
278 S. Allison-logan, F. Karimi, Y. Sun, T. G. McKenzie, M. D. Nothling, G. Bryant and G. G. Qiao, *ACS Macro Lett.*, 2019, **8**, 1291–1295.
279 X. Shi, J. Zhang, N. Corrigan and C. Boyer, *Mater. Chem. Front.*, 2021, **5**, 2271–2282.
280 N. Corrigan, F. J. Trujillo, J. Xu, G. Moad, C. J. Hawker and C. Boyer, *Macromolecules*, 2021, **54**, 3430–3446.
281 A. J. Teator, T. P. Varner, P. C. Knutson, C. C. Sorensen and F. A. Leibfarth, *ACS Macro Lett.*, 2020, **9**, 1638–1654.
282 S. Shanmugam and C. Boyer, *J. Am. Chem. Soc.*, 2015, **137**, 9988–9999.
283 N. Li, D. Ding, X. Pan, Z. Zhang, J. Zhu, C. Boyer and X. Zhu, *Polym. Chem.*, 2017, **8**, 6024–6027.
284 S.-H. Shim, M. Ham, J. Huh, Y.-K. Kwon and Y.-J. Kwark, *Polym. Chem.*, 2013, **4**, 5449–5455.
285 D. T. Gentekos, R. J. Sifri and B. P. Fors, *Nat. Rev. Mater.*, 2019, **4**, 761–774.
286 S. Xu, F. J. Trujillo, J. Xu, C. Boyer and N. Corrigan, *Macromol. Rapid Commun.*, 2021, **42**, 2100212.
287 R. Whitfield, N. P. Truong, D. Messmer, K. Parkatzidis, M. Rolland and A. Anastasaki, *Chem. Sci.*, 2019, **10**, 8724–8734.
288 N. Corrigan, A. Almasri, W. Taillades, J. Xu and C. Boyer, *Macromolecules*, 2017, **50**, 8438–8448.
289 N. Corrigan, R. Manahan, Z. T. Lew, J. Yeow, J. Xu and C. Boyer, *Macromolecules*, 2018, **51**, 4553–4563.
290 K. Liu, N. Corrigan, A. Postma, G. Moad and C. Boyer, *Macromolecules*, 2020, **53**, 8867–8882.
291 K. Parkatzidis, N. P. Truong, M. N. Antonopoulou, R. Whitfield, D. Konkolewicz and A. Anastasaki, *Polym. Chem.*, 2020, **11**, 4968–4972.
292 R. Whitfield, K. Parkatzidis, N. P. Truong, T. Junkers and A. Anastasaki, *Chem*, 2020, **6**, 1340–1352.
293 T. Nwoko, N. De Alwis Watuthanthrige, B. Parnitzke, K. Yehl and D. Konkolewicz, *Polym. Chem.*, 2021, **12**, 6761–6770.
294 R. Whitfield, N. P. Truong and A. Anastasaki, *Angew. Chem., Int. Ed.*, 2021, **60**, 19383–19388.
295 M.-N. Antonopoulou, R. Whitfield, N. P. Truong, D. Wyers, S. Harrisson, T. Junkers and A. Anastasaki, *Nat. Chem.*, 2022, **14**, 304–312.

296 Z. An, *ACS Macro Lett.*, 2020, **9**, 350–357.
297 Y. Yang and Z. An, *Polym. Chem.*, 2019, **10**, 2801–2811.
298 B. Ameduri, *Chem. – Eur. J.*, 2018, **24**, 18830–18841.
299 L. D. Blackman, K. E. B. Doncom, M. I. Gibson and R. K. O'Reilly, *Polym. Chem.*, 2017, **8**, 2860–2871.
300 J. Wan, B. Fan and S. H. Thang, *Chem. Sci.*, 2022, **13**, 4192–4224.
301 J. Yeow, S. Shanmugam, N. Corrigan, R. P. Kuchel, J. Xu and C. Boyer, *Macromolecules*, 2016, **49**, 7277–7285.
302 L. Zhang, L. Xie, S. Xu, R. P. Kuchel, Y. Dai, K. Jung and C. Boyer, *Biomacromolecules*, 2020, **21**, 3887–3897.
303 S. Han, Y. Gu, M. Ma and M. Chen, *Chem. Sci.*, 2020, **11**, 10431–10436.
304 J. Zhou, C. Hong and C. Pan, *Mater. Chem. Front.*, 2017, **1**, 1200–1206.
305 N. Zaquen, H. Zu, A. M. N. B. P. H. A. Kadir, T. Junkers, P. B. Zetterlund and C. Boyer, *ACS Appl. Polym. Mater.*, 2019, **1**, 1251–1256.
306 A. B. Korpusik, Y. Tan, J. B. Garrison, W. Tan and B. S. Sumerlin, *Macromolecules*, 2021, **54**, 7354–7363.
307 C. Lin, S. K. Katla and J. Perez-Mercader, *J. Photochem. Photobiol., A*, 2021, **406**, 112992.
308 J. Wang, X. Hu, N. Zhu and K. Guo, *Chem. Eng. J.*, 2021, **420**, 127663.
309 R. A. Olson, A. B. Korpusik and B. S. Sumerlin, *Chem. Sci.*, 2020, **11**, 5142–5156.
310 M. S. Messina, K. M. M. Messina, A. Bhattacharya, H. R. Montgomery and H. D. Maynard, *Prog. Polym. Sci.*, 2020, **100**, 101186.
311 T. Lueckerath, T. Strauch, K. Koynov, C. Barner-Kowollik, D. Y. W. Ng and T. Weil, *Biomacromolecules*, 2019, **20**, 212–221.
312 A. Watanabe, J. Niu, D. J. Lunn, J. Lawrence, A. S. Knight, M. Zhang and C. J. Hawker, *J. Polym. Sci., Part A: Polym. Chem.*, 2018, **56**, 1259–1268.
313 J. M. Harris and R. B. Chess, *Nat. Rev. Drug Discovery*, 2003, **2**, 214–221.
314 E. M. Pelegri-O'Day, E.-W. Lin and H. D. Maynard, *J. Am. Chem. Soc.*, 2014, **136**, 14323–14332.
315 A. Abuchowski, T. van Es, N. C. Palczuk and F. F. Davis, *J. Biol. Chem.*, 1977, **252**, 3578–3581.
316 C. DelRe, Y. Jiang, P. Kang, J. Kwon, A. Hall, I. Jayapurna, Z. Ruan, L. Ma, K. Zolkin, T. Li, C. D. Scown, R. O. Ritchie, T. P. Russell and T. Xu, *Nature*, 2021, **592**, 558–563.
317 W.-H. Leung, P.-K. So, W.-T. Wong, W.-H. Lo and P.-H. Chan, *RSC Adv.*, 2016, **6**, 106837–106846.
318 M. Liu, L. Jia, Z. Zhao, Y. Han, Y. Li, Q. Peng and Q. Zhang, *Chem. Eng. J.*, 2020, **390**, 124667.
319 A. J. Russell, S. L. Baker, C. M. Colina, C. A. Figg, J. L. Kaar, K. Matyjaszewski, A. Simakova and B. S. Sumerlin, *AIChE J.*, 2018, **64**, 3230–3245.
320 Y. Yu, W. Xu, X. Huang, X. Xu, R. Qiao, Y. Li, F. Han, H. Peng, T. P. Davis, C. Fu and A. K. Whittaker, *ACS Macro Lett.*, 2020, **9**, 799–805.
321 W. L. Guo, Y. Zhou, B. Duan, W. F. Wei, C. Chen, X. Li and T. Cai, *Chem. Eng. J.*, 2022, **429**, 132120.
322 Y. Huang, X. Li, Y. C. Zhang, Z. Shi, L. Zeng, J. Xie, Y. Du, D. Lu, Z. Hu, T. Cai and Z. Luo, *ACS Appl. Mater. Interfaces*, 2021, **13**, 44488–44496.
323 C. Ma, X. Liu, G. Wu, P. Zhou, Y. Zhou, L. Wang and X. Huang, *ACS Macro Lett.*, 2017, **6**, 689–694.
324 G. Szczepaniak, J. Jeong, K. Kapil, S. Dadashi-Silab, S. S. Yerneni, P. Ratajczyk, S. Lathwal, D. J. Schild, S. R. Das and K. Matyjaszewski, *Chem. Sci.*, 2022, **13**, 11540–11550.
325 B. Panganiban, B. Qiao, T. Jiang, C. DelRe, M. M. Obadia, T. D. Nguyen, A. A. Smith, A. Hall, I. Sit, M. G. Crosby and P. B. Dennis, *Science*, 2018, **359**, 1239–1243.
326 C. DelRe, B. Chang, I. Jayapurna, A. Hall, A. Wang, K. Zolkin and T. Xu, *Adv. Mater.*, 2021, **33**, 2105707.
327 P. R. Judzewitsch, T.-K. Nguyen, S. Shanmugam, E. H. H. Wong and C. Boyer, *Angew. Chem., Int. Ed.*, 2018, **57**, 4559–4564.
328 P. R. Judzewitsch, N. Corrigan, E. H. H. Wong and C. Boyer, *Angew. Chem., Int. Ed.*, 2021, **60**, 24248–24256.
329 H. Sun, W. Cao, N. Zang, T. D. Clemons, G. M. Scheutz, Z. Hu, M. P. Thompson, Y. Liang, M. Vratsanos, X. Zhou, W. Choi, B. S. Sumerlin, S. I. Stupp and N. C. Gianneschi, *Angew. Chem., Int. Ed.*, 2020, **59**, 19136–19142.
330 A. J. Gormley and M. A. Webb, *Nat. Rev. Mater.*, 2021, **6**, 642–644.
331 M. Tamasi, S. Kosuri, J. DiStefano, R. Chapman and A. J. Gormley, *Adv. Intell. Syst.*, 2020, **2**, 1900126.
332 R. Upadhya, A. Punia, M. J. Kanagala, L. Liu, M. Lamm, T. A. Rhodes and A. J. Gormley, *ACS Appl. Polym. Mater.*, 2021, **3**, 1525–1536.
333 J. O. Zoppe, N. C. Ataman, P. Mocny, J. Wang, J. Moraes and H.-A. Klok, *Chem. Rev.*, 2017, **117**, 1105–1318.
334 M. Li, M. Fromel, D. Ranaweera, S. Rocha, C. Boyer and C. W. Pester, *ACS Macro Lett.*, 2019, **8**, 374–380.
335 J. Poisson, A. M. Polgar, M. Fromel, C. W. Pester and Z. M. Hudson, *Angew. Chem., Int. Ed.*, 2021, **60**, 19988–19996.
336 X. Xu, X. Huang, Y. Chang, Y. Yu, J. Zhao, N. Isahak, J. Teng, R. Qiao, H. Peng, C.-X. Zhao, T. P. Davis, C. Fu and A. K. Whittaker, *Biomacromolecules*, 2021, **22**, 330–339.
337 G. Ng, P. Judzewitsch, M. Li, C. W. Pester, K. Jung and C. Boyer, *Macromol. Rapid Commun.*, 2021, **42**, 2100106.
338 G. Ng, M. Li, J. Yeow, K. Jung, C. W. Pester and C. Boyer, *ACS Appl. Mater. Interfaces*, 2020, **12**, 55243–55254.
339 M. Fromel and C. W. Pester, *Macromolecules*, 2022, **55**, 4907–4915.
340 A. R. Kuzmyn, L. W. Teunissen, M. V. Kroese, J. Kant, S. Venema and H. Zuilhof, *ACS Omega*, 2022, **7**, 38371–38379.
341 L.-H. Rong, X. Cheng, J. Ge, O. K. Krebs, J. R. Capadona, E. B. Caldona and R. C. Advincula, *ACS Appl. Polym. Mater.*, 2022, **4**, 6449–6457.
342 T. Joshi and L. Nebhani, *Surf. Interfaces*, 2022, **29**, 101764.
343 C. Förster, L. Veith and A. Andrieu-Brunsen, *RSC Adv.*, 2022, **12**, 27109–27113.
344 L. Hu, Q. Hao, L. Wang, Z. Cui, P. Fu, M. Liu, X. Qiao and X. Pang, *Polym. Chem.*, 2021, **12**, 545–553.

345 J. Zhou, L. Ye, Y. Lin, L. Wang, L. Zhou, H. Hu, Q. Zhang, H. Yang and Z. Luo, *J. Appl. Polym. Sci.*, 2019, **136**, 47653.
346 J. Zhou, Y. Lin, L. Ye, L. Wang, L. Zhou, H. Hu, Q. Zhang, H. Yang and Z. Luo, *Macromol. Res.*, 2019, **27**, 1144–1154.
347 J. Zhou, Y. Sun, Z. Huang, Z. Luo and H. Hu, *J. Appl. Polym. Sci.*, 2021, **138**, 51395.
348 Y. Lin, L. Wang, J. Zhou, L. Ye, H. Hu, Z. Luo and L. Zhou, *Polymer*, 2019, **162**, 80–90.
349 J. Zhou, Y. Lin, L. Wang, L. Zhou, B. Yu, X. Zou, Z. Luo and H. Hu, *Colloids Surf., A*, 2021, **617**, 126369.
350 H. Kodama, *Rev. Sci. Instrum.*, 1981, **52**, 1770–1773.
351 C. W. Hull, *US Pat.*, **4575330**, 1986.
352 S. C. Ligon, R. Liska, J. Stampfl, M. Gurr and R. Mülhaupt, *Chem. Rev.*, 2017, **117**, 10212–10290.
353 T. T. Wohlers, W. A. (Firm), R. I. Campbell, O. Diegel, J. Kowen, R. Huff, N. Mostow, I. Fidan, D. L. Bourell, J. Van Rensburg and others, *Wohlers Report 2022: 3D Printing and Additive Manufacturing Global State of the Industry*, Wohlers Associates, 2022.
354 H. N. Chia and B. M. Wu, *J. Biol. Eng.*, 2015, **9**, 4.
355 T. J. Wallin, J. Pikul and R. F. Shepherd, *Nat. Rev. Mater.*, 2018, **3**, 84–100.
356 A. Paolini, S. Kollmannsberger and E. Rank, *Addit. Manuf.*, 2019, **30**, 100894.
357 C. Sun, N. Fang, D. M. Wu and X. Zhang, *Sens. Actuators, A*, 2005, **121**, 113–120.
358 X. Zheng, J. Deotte, M. P. Alonso, G. R. Farquar, T. H. Weisgraber, S. Gemberling, H. Lee, N. Fang and C. M. Spadaccini, *Rev. Sci. Instrum.*, 2012, **83**, 125001.
359 K. Jung, N. Corrigan, M. Ciftci, J. Xu, S. E. Seo, C. J. Hawker and C. Boyer, *Adv. Mater.*, 2020, **32**, 1903850.
360 A. Bagheri and J. Jin, *ACS Appl. Polym. Mater.*, 2019, **1**, 593–611.
361 V. A. Bobrin, J. Zhang, N. Corrigan and C. Boyer, *Adv. Mater. Technol.*, 2022, 2201054.
362 Z. Zhang, N. Corrigan and C. Boyer, *Macromolecules*, 2021, **54**, 1170–1182.
363 G. Moad, E. Rizzardo and S. H. Thang, *Polymer*, 2008, **49**, 1079–1131.
364 G. Moad, E. Rizzardo and S. H. Thang, *Acc. Chem. Res.*, 2008, **41**, 1133–1142.
365 A. Bagheri, H. Ling, C. William Anderson Bainbridge and J. Jin, *ACS Appl. Polym. Mater.*, 2021, **3**, 2921–2930.
366 K. Lee, N. Corrigan and C. Boyer, *Angew. Chem., Int. Ed.*, 2021, **60**, 8839–8850.
367 Z. Zhang, N. Corrigan and C. Boyer, *Angew. Chem., Int. Ed.*, 2022, **61**, e202114111.
368 V. A. Bobrin, K. Lee, J. Zhang, N. Corrigan and C. Boyer, *Adv. Mater.*, 2022, **34**, 2107643.
369 X. Shi, V. A. Bobrin, Y. Yao, J. Zhang, N. Corrigan and C. Boyer, *Angew. Chem., Int. Ed.*, 2022, **61**, e202206272.
370 V. A. Bobrin, Y. Yao, X. Shi, Y. Xiu, J. Zhang, N. Corrigan and C. Boyer, *Nat. Commun.*, 2022, **13**, 3577.
371 D. Melodia, A. Bhadra, K. Lee, R. Kuchel, D. Kundu, N. Corrigan and C. Boyer, *Small*, 2023, 2206639.
372 K. Lee, Y. Shang, V. A. Bobrin, R. Kuchel, D. Kundu, N. Corrigan and C. Boyer, *Adv. Mater.*, 2022, **34**, 2204816.
373 R. M. Myers, D. E. Fitzpatrick, R. M. Turner and S. V. Ley, *Chem. – A Eur. J.*, 2014, **20**, 12348–12366.
374 M. B. Plutschack, B. Pieber, K. Gilmore and P. H. Seeberger, *Chem. Rev.*, 2017, **117**, 11796–11893.
375 T. Junkers and B. Wenn, *React. Chem. Eng.*, 2016, **1**, 60–64.
376 N. Zhu, X. Hu, Z. Fang and K. Guo, *ChemPhotoChem*, 2018, **2**, 831–838.
377 B. L. Buss and G. M. Miyake, *Chem. Mater.*, 2018, **30**, 3931–3942.
378 M. H. Reis, F. A. Leibfarth and L. M. Pitet, *ACS Macro Lett.*, 2020, **9**, 123–133.
379 M. Chen and J. A. Johnson, *Chem. Commun.*, 2015, **51**, 6742–6745.
380 F. Lauterbach, M. Rubens, V. Abetz and T. Junkers, *Angew. Chem., Int. Ed.*, 2018, **57**, 14260–14264.
381 M. Rubens, P. Latsrisaeng and T. Junkers, *Polym. Chem.*, 2017, **8**, 6496–6505.
382 C. Sambiagio, M. Ferrari, K. van Beurden, N. della Ca', J. Van Schijndel and T. Noël, *Org. Lett.*, 2021, **23**, 2042–2047.
383 F. Zhong, Y. Zhou and M. Chen, *Polym. Chem.*, 2019, **10**, 4879–4886.
384 S. Oliver, L. Zhao, A. J. Gormley, R. Chapman and C. Boyer, *Macromolecules*, 2019, **52**, 3–23.
385 C. Stubbs, K. A. Murray, T. Ishibe, R. T. Mathers and M. I. Gibson, *ACS Macro Lett.*, 2020, **9**, 290–294.
386 S.-J. Richards, A. Jones, R. M. F. Tomás and M. I. Gibson, *Chem. – A Eur. J.*, 2018, **24**, 13758–13761.
387 J. Yeow, S. Joshi, R. Chapman and C. Boyer, *Angew. Chem., Int. Ed.*, 2018, **57**, 10102–10106.
388 R. Upadhya, N. S. Murthy, C. L. Hoop, S. Kosuri, V. Nanda, J. Kohn, J. Baum and A. J. Gormley, *Macromolecules*, 2019, **52**, 8295–8304.
389 G. Ng, K. Jung, J. Li, C. Wu, L. Zhang and C. Boyer, *Polym. Chem.*, 2021, **12**, 6548–6560.
390 M. Nagao, Y. Kimoto, Y. Hoshino and Y. Miura, *ACS Omega*, 2022, **7**, 13254–13259.
391 S. Kosuri, C. H. Borca, H. Mugnier, M. Tamasi, R. A. Patel, I. Perez, S. Kumar, Z. Finkel, R. Schloss, L. Cai, M. L. Yarmush, M. A. Webb and A. J. Gormley, *Adv. Healthcare Mater.*, 2022, **11**, 2102101.
392 R. Upadhya, S. Kosuri, M. Tamasi, T. A. Meyer, S. Atta, M. A. Webb and A. J. Gormley, *Adv. Drug Delivery Rev.*, 2021, **171**, 1–28.
393 F. Soheilmoghaddam, M. Rumble and J. Cooper-White, *Chem. Rev.*, 2021, **121**, 10792–10864.
394 J. Li, M. Zhang, J. Zhu and X. Zhu, *Polymers*, 2019, **11**, 1722.
395 R. N. Carmean, T. E. Becker, M. B. Sims and B. S. Sumerlin, *Chem*, 2017, **2**, 93–101.
396 K. Ferji, P. Venturini, F. Cleymand, C. Chassenieux and J.-L. Six, *Polym. Chem.*, 2018, **9**, 2868–2872.
397 P. Lertturongchai, M. I. A. Ibrahim, A. Durand, P. Sunintaboon and K. Ferji, *Macromol. Rapid Commun.*, 2020, **41**, 2000058.
398 T. G. McKenzie, L. P. da, M. Costa, Q. Fu, D. E. Dunstan and G. G. Qiao, *Polym. Chem.*, 2016, **7**, 4246–4253.

399 K. Jung, C. Boyer and P. B. Zetterlund, *Polym. Chem.*, 2017, **8**, 3965–3970.
400 A. Bagheri, Z. Sadrearhami, N. N. M. Adnan, C. Boyer and M. Lim, *Polymer*, 2018, **151**, 6–14.
401 B. Cabannes-Boué, Q. Yang, J. Lalevée, F. Morlet-Savary and J. Poly, *Polym. Chem.*, 2017, **8**, 1760–1770.
402 A. Bagheri, C. Bainbridge and J. Jin, *ACS Appl. Polym. Mater.*, 2019, **1**, 1896–1904.
403 A. Bagheri, K. E. Engel, C. W. A. Bainbridge, J. Xu, C. Boyer and J. Jin, *Polym. Chem.*, 2020, **11**, 641–647.
404 K. J. Arrington and J. B. Matson, *Polym. Chem.*, 2017, **8**, 7452–7456.
405 T. G. McKenzie, E. H. H. Wong, Q. Fu, A. Sulistio, D. E. Dunstan and G. G. Qiao, *ACS Macro Lett.*, 2015, **4**, 1012–1016.
406 V. Tkachenko, C. Matei Ghimbeu, C. Vaulot, L. Vidal, J. Poly and A. Chemtob, *Polym. Chem.*, 2019, **10**, 2316–2326.
407 R. W. Hughes, M. E. Lott, J. I. Bowman and B. S. Sumerlin, *ACS Macro Lett.*, 2023, **12**, 14–19.
408 A. Rasines Mazo, T. N. Tran, W. Zhang, Y. Meng, A. Reyhani, S. Pascual, L. Fontaine, G. G. Qiao and S. Piogé, *Polym. Chem.*, 2020, **11**, 5238–5248.
409 R. W. Lewis, R. A. Evans, N. Malic, K. Saito and N. R. Cameron, *Polym. Chem.*, 2018, **9**, 60–68.
410 J. Li, C. Ding, Z. Zhang, J. Zhu and X. Zhu, *React. Funct. Polym.*, 2017, **113**, 1–5.
411 J. Luo, M. Li, M. Xin, W. Sun and W. Xiao, *Macromol. Chem. Phys.*, 2016, **217**, 1777–1784.
412 Q. Yang, M. Guerre, V. Ladmiral and B. Ameduri, *Polym. Chem.*, 2018, **9**, 3388–3397.
413 R. N. Carmean, M. B. Sims, C. A. Figg, P. J. Hurst, J. P. Patterson and B. S. Sumerlin, *ACS Macro Lett.*, 2020, **9**, 613–618.
414 J. Li, X. Pan, N. Li, J. Zhu and X. Zhu, *Polym. Chem.*, 2018, **9**, 2897–2904.
415 Y. Wang, M. Wang, L. Bai, L. Zhang, Z. Cheng and X. Zhu, *Polym. Chem.*, 2020, **11**, 2080–2088.
416 S. Liu, Y. Cheng, H. Zhang, Z. Qiu, R. T. K. Kwok, J. W. Y. Lam and B. Z. Tang, *Angew. Chem., Int. Ed.*, 2018, **57**, 6274–6278.
417 A.-C. Lehnen, J. A. M. Kurki and M. Hartlieb, *Polym. Chem.*, 2022, **13**, 1537–1546.
418 C. P. Easterling, Y. Xia, J. Zhao, G. E. Fanucci and B. S. Sumerlin, *ACS Macro Lett.*, 2019, **8**, 1461–1466.
419 C. Fu, Z. Huang, C. J. Hawker, G. Moad, J. Xu and C. Boyer, *Polym. Chem.*, 2017, **8**, 4637–4643.
420 S. Shanmugam, G. Ross, C. Y. Mbuncha and A. Santra, *Polym. Chem.*, 2021, **12**, 6705–6713.
421 J. Yeow, O. R. Sugita and C. Boyer, *ACS Macro Lett.*, 2016, **5**, 558–564.
422 N. Zaquen, J. Yeow, T. Junkers, C. Boyer and P. B. Zetterlund, *Macromolecules*, 2018, **51**, 5165–5172.
423 B. Zhao, J. Li, Z. Li, X. Lin, X. Pan, Z. Zhang and J. Zhu, *Macromolecules*, 2022, **55**, 7181–7192.
424 X. Wu, B. Gross, B. Leuschel, K. Mougin, S. Dominici, S. Gree, M. Belqat, V. Tkachenko, B. Cabannes-Boué, A. Chemtob, J. Poly and A. Spangenberg, *Adv. Funct. Mater.*, 2022, **32**, 2109446.
425 V. Kottisch, M. J. Supej and B. P. Fors, *Angew. Chem., Int. Ed.*, 2018, **57**, 8260–8264.
426 R. J. Sifri, A. J. Kennedy and B. P. Fors, *Polym. Chem.*, 2020, **11**, 6499–6504.
427 X. Zhang, Y. Jiang, Q. Ma, S. Hu and S. Liao, *J. Am. Chem. Soc.*, 2021, **143**, 6357–6362.
428 Z. Yang, J. Chen and S. Liao, *ACS Macro Lett.*, 2022, **11**, 1073–1078.
429 J. Li, M. Chen, X. Lin, Q. Li, W. Zhang, G. Jin, X. Pan, J. Zhu and X. Zhu, *ACS Macro Lett.*, 2020, **9**, 1799–1805.
430 M. Ciftci, Y. Yoshikawa and Y. Yagci, *Angew. Chem., Int. Ed.*, 2017, **56**, 519–523.
431 J. Li, A. Kerr, S. Häkkinen, T. Floyd, M. Zhang, X. Pan, X. Zhu, S. Perrier and J. Zhu, *Polym. Chem.*, 2020, **11**, 2724–2731.
432 J. Li, A. Kerr, Q. Song, J. Yang, S. Häkkinen, X. Pan, Z. Zhang, J. Zhu and S. Perrier, *ACS Macro Lett.*, 2021, **10**, 570–575.
433 H. Suk Wang, N. P. Truong, Z. Pei, M. L. Coote, A. Anastasaki, H. S. Wang, N. P. Truong, Z. Pei, M. L. Coote and A. Anastasaki, *J. Am. Chem. Soc.*, 2022, **144**, 4678–4684.
434 V. Bellotti, K. Parkatzidis, H. S. Wang, N. De Alwis Watuthanthrige, M. Orfano, A. Monguzzi, N. P. Truong, R. Simonutti and A. Anastasaki, *Polym. Chem.*, 2023, **14**, 253–258.
435 J. B. Young, J. I. Bowman, C. B. Eades, A. J. Wong and B. S. Sumerlin, *ACS Macro Lett.*, 2022, **11**, 1390–1395.
436 S. V. Wanasinghe, M. Sun, K. Yehl, J. Cuthbert, K. Matyjaszewski and D. Konkolewicz, *ACS Macro Lett.*, 2022, **11**, 1156–1161.
437 P. N. Kurek, A. J. Kloster, K. A. Weaver, R. Manahan, M. L. Allegrezza, N. De Alwis Watuthanthrige, C. Boyer, J. A. Reeves and D. Konkolewicz, *Ind. Eng. Chem. Res.*, 2018, **57**, 4203–4213.
438 Y. Lee, C. Boyer and M. S. Kwon, *Nat. Rev. Mater.*, 2022, **7**, 74–75.

EurJOC
European Journal of Organic Chemistry

Minireview
doi.org/10.1002/ejoc.202000720

Chemistry Europe
European Chemical Societies Publishing

Organic Photoredox Catalysts

Emerging Organic Photoredox Catalysts for Organic Transformations

Yungyeong Lee[b] and Min Sang Kwon*[a]

Abstract: A lot of efforts have been made for the development of novel organic photoredox catalysts (PCs) due to their gratifying replacement for conventional transition metal-based PCs in photoredox catalysis. In this minireview, we summarized and classified the recently reported organic PCs into several categories based on functional groups (e.g. cyanoarene, phenazine, xanthene, and others) with their applications to various organic transformations including polymerization reactions. The strategies used to design organic PCs then also introduced. The emerging trends for the discovery of organic PCs are systematic approaches which include computer-aided and mechanism-based design. We anticipate that this minireview will provide not only the characteristics of the recently reported organic PCs, but also an insight into the design and discovery of organic PCs for desired applications.

1. Introduction

Photoredox catalysis has been of tremendous interest as a green and mild alternative to conventional syntheses.[1] Photoredox refers to harnessing light energy, instead of thermal energy commonly used in chemical syntheses, to excite reactant species and proceed a redox-mediated reaction. Pioneering works have utilized organometallic photoredox catalysts (PCs), embedded rare-earth metals such as iridium[2] or ruthenium,[3,4] but their cost and potential toxicity still raised the need for the preparation of purely organic PCs. Since the recent successful replacement of organometallic PCs with previously well-known organic dyes,[5–14] the development of organic PCs has mostly relied on the structural modification of these organic dyes based on a "trial-and-error" approach and/or the "serendipitous finding" of a new core structure. More recently, systematic approaches have emerged toward the more straightforward and efficient design and discovery of organic PCs including computer-aided design[15,16] and mechanism-based design in which consecutive photoinduced electron transfer (con-PET)[17,18] and triplet-triplet annihilation (TTA) up-conversion are employed.[19,20]

There already exist excellent review articles on the overview of organic photoredox catalysis,[1,5,21] the photophysics of organic photoredox catalysis,[22] mechanistic studies on (organic)

[a] *Prof. Dr. M. S. Kwon*
Department of Materials Science and Engineering, Seoul National University,
Seoul 08826, South Korea
E-mail: minsang@snu.ac.kr
http://kwonlab.snu.ac.kr/
[b] *Y. Lee*
Department of Materials Science and Engineering, Ulsan National Institute of Science and Technology (UNIST),
Ulsan 44919, South Korea
Supporting information and ORCID(s) from the author(s) for this article are available on the WWW under https://doi.org/10.1002/ejoc.202000720.

Yungyeong Lee received her B.S. and M.S. degrees in Chemistry at the Ulsan National Institute of Science and Technology (UNIST) in 2017 and 2019, respectively. She is currently pursuing a Ph.D. in Materials Science and Engineering at UNIST under the supervision of Prof. Min Sang Kwon. Her recent research interest focuses on the development of organic photocatalysts, investigation of their photophysical and electrochemical properties, and application to visible-light-mediated polymerization reaction.

Min Sang Kwon received his B.S. degrees in Chemistry and Materials Science and Engineering from the Seoul National University (SNU). Then, he completed his Ph.D. in Chemistry at SNU in 2011 under the guidance of Prof. Eun Lee. After finishing his postdoctoral studies at SNU with Prof. Soo Young Park, he moved to the University of Michigan to work with Prof. Jinsang Kim. Upon completing his postdoctoral studies in 2016, he began his independent career at UNIST as an Assistant Professor of Materials Science and Engineering. In 2020, he moved back to his alma mater, SNU where he is currently an Assistant Professor of Materials Science and Engineering. He has a broad interest in organic chemistry, photochemistry, and polymer chemistry.

photoredox catalysis,[23] the use of organic electronic semiconductors for new PCs,[24] and the use of (organic) PCs in a variety of organic[5,6,25,26] and polymer syntheses.[6,7,27] Several recent reviews also focused on purely organic PCs utilized for photoredox-mediated controlled radical polymerizations[8–10,28,29] where a reduction in the catalyst loading or the complete removal of the metal are necessary for the synthesized polymers to be applied in electronic and/or biomedical fields. However, recent advances in the development of organic PCs still remain unaddressed, especially the recent emergence of new organic PCs and the reactions catalyzed thereby, based on conceptually new approaches.

Herein, we aim to update the list of organic molecules newly designed or applied as organic PCs with an emphasis on the underlying principles of their design. After a brief review of the key aspects of PC design, we summarize and classify the recently reported organic PCs into several categories based on functional groups with their applications in various organic transformations. In addition, the strategies used to design and discover these organic PCs are introduced. This review will primarily cover the literature on the development of organic PCs that has appeared since the publication of the review published by Nicewicz and co-workers in 2016;[5] In fact, the review by Nicewicz and co-workers covers almost all of the organic PCs developed before 2016. We also introduce several earlier papers that were not included in the previous review articles mentioned beforehand. The work cited in the previous reviews is only mentioned again when necessary to reflect the context of the latest work in this minireview.

2. General Considerations for the Design of Organic PCs

To efficiently catalyze a given photo-mediated redox reaction, in brief, the PC strongly absorbs light to be excited and possesses proper ground and excited state of oxidation or reduction potentials to facilitate two important electron-transfer (ET) processes within the catalytic cycle via either an oxidative or reductive quenching pathway, i.e. a photo-induced ET to quench the excited state (opening the catalytic cycle) and a subsequent ET to regenerate the ground-state catalyst (closing the catalytic cycle) (Scheme 1). A variety of light sources (e.g. halogen lamp, fluorescent bulb, LED, and others) can be employed for irradiations, of which, visible-light LED is advantageous in terms of mild reaction conditions, eco-friendliness, and sustainability.[26] In addition to strong absorption and appropriate redox potentials, the population of the lowest triplet excited state (T_1) plays a critical role since the PC in the excited state has to diffuse to the substrate of interest before returning to its ground state. Here, the involvement of the lowest singlet excited state (S_1) has been recently claimed by Orr-Ewing and co-workers from the investigation of photochemical dynamics of organocatalyzed atom transfer radical polymerization (O-ATRP).[30,31] However, because of the longer lifetime of T_1, the efficient generation of T_1 has been mainly considered for the development of highly efficient organic PCs. The stability of radical ion intermediates is also an important factor. For successful photoredox catalysis, radical ion intermediates should be quenched by ET and regenerate the ground-state PC. Unstable radical ions can promote undesirable side reactions before the ET process and, consequently, limit the deactivation process in the catalyst cycle; In contrast, interestingly, König and co-workers recently reported that a side reaction can produce a substrate with higher catalytic activity and stability, which subsequently promotes the reaction (Section 3.1, Scheme 5 and Scheme 6).[32,33] Finally, high (photo)stability of the PC under the reaction conditions is highly required. For further details on the photophysical, electrochemical, and mechanistic aspects of photoredox catalysis, the review articles by Nicewicz and co-workers,[5,34] Wangelin and co-workers,[35] Melchiorre and co-workers,[23] and McCusker and co-workers[22] are highly recommended.

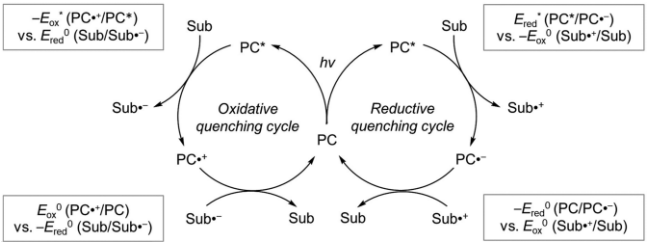

Scheme 1. Oxidative and reductive quenching cycles of PCs (Sub: substrate).

3. Recently Reported Organic Photocatalysts

In photoredox catalysis, organic dyes have been employed as an organic PC since the early 2010s[36,37] thanks to their well-known light-absorbing characteristics. Several organic dyes turned out to be good alternatives to organometallic counterparts with comparable (or even better) photocatalytic performance albeit in lower catalyst loading in a variety of organic transformations and polymerization reactions.[11,38] Then, structural modification of well-known organic dyes has been intensively investigated to discover new organic PCs with tuned catalytic parameters, which thereby enable the design and development of new photoredox-mediated reactions. More recently, systematic approaches such as computer-aided and mechanism-based catalysts design have been proposed to discover organic PCs. In this section, newly reported organic PCs being classified by a core scaffold are introduced (Scheme 2, Table S1, Supporting Information). Again, for the organic PCs reported before 2016, please refer to the review written by Nicewicz and co-workers which provided their photophysical and electrochemical characteristics and synthetic applications thereof.[5,34]

3.1. Cyanoarenes

1,4-Dicyanobenzene (DCB), 1,4-dicyanonaphthalene (DCN), and 9,10-dicyanoanthracene (DCA) are commonly employed cyanoarene-based organic PCs, which display a wide range of ground-state reduction potential (E_{red}^{0}) from –0.7 to 1.7 V (vs. SCE). However, concerns regarding the possible degradation of catalyst put a limitation on reducing their loading.[5] Here, E_{red}

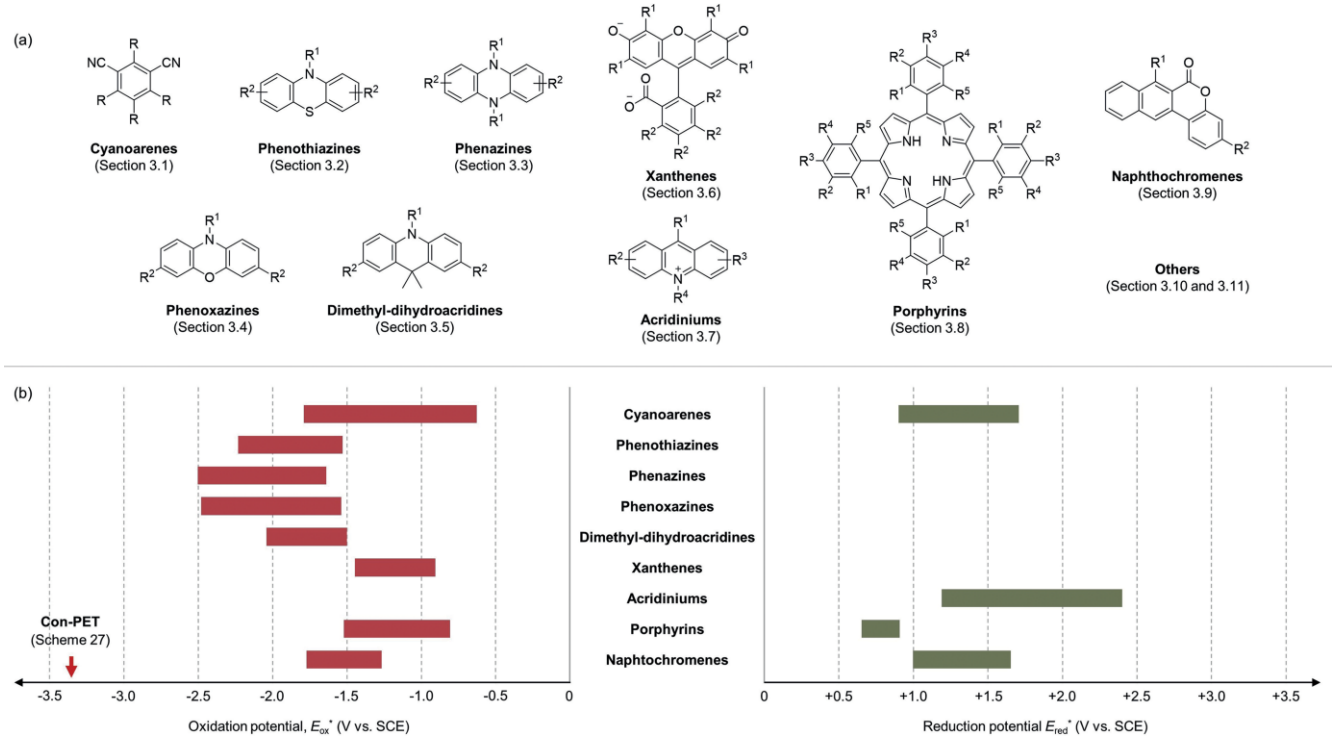

Scheme 2. Organic PCs introduced in this paper. (a) Representative scaffold structures and (b) oxidation or reduction potential values at excited state defined as $E_{ox}^*(PC^{\bullet+}/PC^*)$ or $E_{red}^*(PC^*/PC^{\bullet-})$, respectively. Except for xanthenes, the values at singlet excited state ($E_{ox}^*(S_1)$ or $E_{red}^*(S_1)$) were depicted. Please note that potential values were obtained under different conditions. The exact values are listed in Table S1 (Supporting Information).

(E_{ox}) is defined by the half-reaction $A + e^- \rightarrow A^{\bullet-}$ ($D^{\bullet+} + e^- \rightarrow D$) and is referred to as the "reduction (oxidation) potential of A (D)". All potential values are written against SCE throughout this review.

In 2016, Zhang and co-workers prepared carbazolyl dicyanobenzene (CDCB) derivatives as PCs, which are based on a donor–acceptor (D–A) molecular dyad with the carbazole moiety as an electron donor and the dicyanoarene as an acceptor.[39] The acceptor's lowest unoccupied molecular orbital (LUMO) (donor's highest occupied molecular orbital (HOMO)) determines E_{red}^0 and E_{ox}^* (E_{ox}^0 and E_{red}^*) in the D–A dyad in principle and therefore, expected to provide PCs with a wide range of redox potentials. Six molecules with different numbers and positions of carbazolyl and cyano groups on the benzene core were synthesized from commercially available precursors using a rather simple procedure (Scheme 3, **1**–**6**). The resulting PCs exhibited decent oxidizing and reducing powers and efficiently catalyzed the photoredox/Ni dual-catalyzed cross-coupling of *N*-Boc-proline with methyl 4-iodobenzoate, which requires a highly oxidative PC. Among them, **1** (as reported **4CzIPN**) showed the best catalytic activity although all of the developed PCs have similar redox potentials. Further examination revealed that the difference in the catalytic activity can be attributed to the relatively higher photostability of **1** in DMF. **1** was also successfully applied for more challenging reactions such as the photoredox/Ni dual-catalyzed cross-coupling of α-amino acids/alkyltrifluoroborates with aryl halides (Scheme 4). Since the first report of **1** by Zhang and co-workers, it has been widely utilized in a variety of challenging photocatalytic transformations with

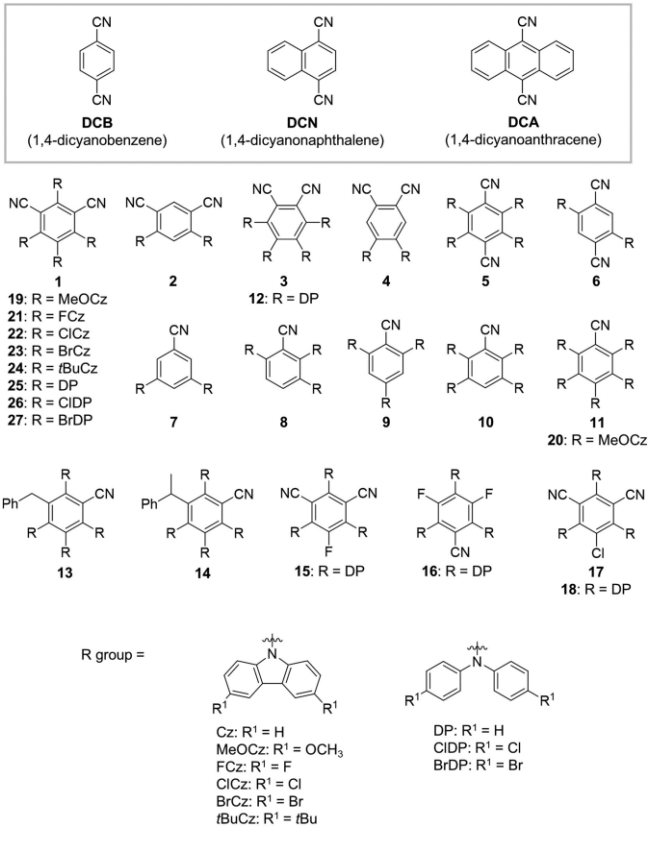

Scheme 3. Cyanoarene-based organic PCs. R group depicts carbazole (Cz) otherwise noted.

or without metal catalysts. Examples including the selective hydrocarboxylation of styrenes with CO_2 and the selective activation of bonds albeit with similar bond dissociation energies are well-summarized by He, Yu, and co-workers.[40] Very recent work includes the benzylation of aliphatic aldehydes[32] (Scheme 5) and the photocarboxylation of benzylic C–H bonds with CO_2 via carbanion generation by König and co-workers[33] (Scheme 6). Interestingly, the degradation products, **13**[32] and **14**,[33] where one cyano group of **1** was eliminated under the reaction condition were isolated and found to be more photostable and thus to proceed the reaction well.

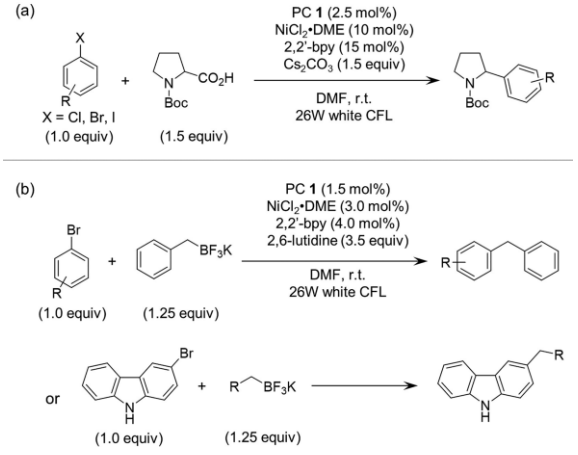

Scheme 4. Photoredox/Ni dual-catalyzed cross-coupling of (a) α-amino acids and (b) alkyltrifluoroborates with aryl halides.

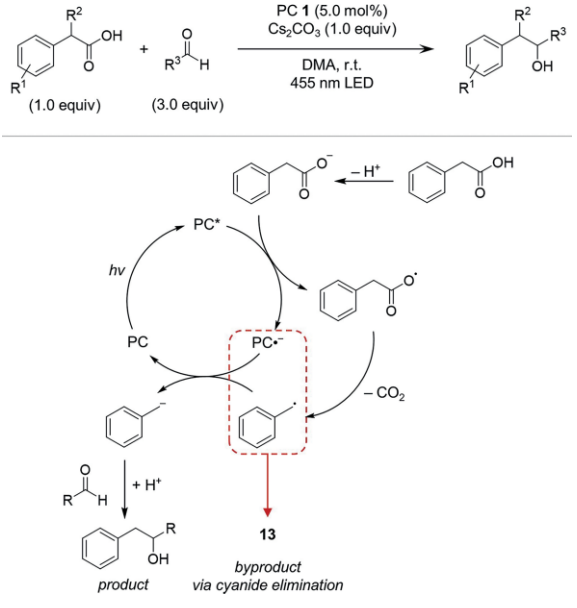

Scheme 5. Benzylation of aliphatic aldehydes.

Li, Huang, Zhang, and co-workers reported that CDCB derivatives are also effective for energy transfer (EnT)-based photocatalytic reaction.[41] Five additional organic PCs (**7**–**11**) with varying numbers and positions of carbazole moieties on the benzonitrile core were prepared and underwent the *Z*/*E* isomerization of stilbene analogs where the higher *Z*/*E* ratio or the promoted isomerization from the *E*- to *Z*-isomer originates from the EnT

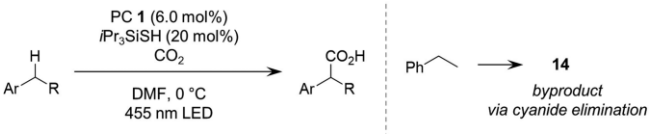

Scheme 6. Photocarboxylation of benzylic C–H bonds with CO_2 via carbanion generation.

process from T_1 of the PC to the *E*-isomer if T_1 lies in between of energy levels of the *Z*- and *E*-isomers. The triplet excited energy can be divided into locally excited (^{3}LE) with a fixed energy level or charge transfer triplet state (^{3}CT) with a tunable energy level. Femto- and nanosecond transient absorption spectroscopic analysis on two representative PCs (**1** and **4**) in the presence of *E*-stilbene revealed that both states participated, but their relative contributions were different. The authors found that changing the solvent to a less polar one or increasing the CT character of the D–A dyad decreases the ^{1}CT energy and increases the ^{3}CT population. As the mechanistic origin of the EnT state was provided, PCs with an appropriate triplet excited-state energy together with E_{red}^* (**1** and **12**) afforded the desired EnT-product in the cross-coupling of carboxylic acids and aryl halides, where the EnT competes with the ET.

4DPAIPN where diphenylamine substituted for the carbazole of **4CzIPN** (**1**) was synthesized in the aforementioned publications by Zhang and co-workers, but later it turned out to be **3DPAFIPN** (**15**). Therefore, the photophysical properties and catalytic performance of **3DPAFIPN** (**15**[42]) and **4DPAIPN** (**25**, appeared after then[15,43,44]) are not mentioned here for clarity.

In fact, **1** was originally proposed as thermally activated delayed fluorescence (TADF) emitter for highly efficient organic light-emitting diodes (OLEDs).[45] Strongly distorted D–A structure exemplified in **1** leads to the strong localization of the HOMO and LUMO on the spatially separated D and A moieties respectively, resulting in a small singlet-triplet energy gap (ΔE_{ST}), thereby promoting the intersystem crossing (ISC) even without a heavy-metal atom. The efficient generation of long-lived triplet excited state is thus realized in a given molecule so that the structurally distorted D–A dyad has served as a molecular platform to unveil a new class of organic PC.[15,42]

In 2018, Zeitler and co-workers provided a systematic approach to develop tailored cyanoarene-based PCs with either strongly oxidizing or reducing powers in a predictable manner.[42] Inspired by the successful employment of the TADF strategy and outstanding catalytic performance of **1**, it became the starting point to prepare eight molecules (**1**, **11**, and **15**–**20**) through a combination of three donors and five acceptors consisting of a halogen atom (F and Cl) and cyano group incorporated on the electron-accepting core. The type and number of donors (electron-withdrawing substituents on the acceptor) were considered to affect and thus finely tune the reducing (oxidizing) power of the PC. In particular, halogen substituents have both inductive electron-withdrawing and mesomeric electron-donating abilities. The measured ground-state redox potentials were well-tuned although the reduction potential was rather difficult to predict than the oxidation potential. The prepared catalysts processed model reactions which require a

strongly reducing or oxidizing catalyst effectively on a par with $Ir(ppy)_3$ or Fukuzumi's catalyst, respectively.

Likewise, the fine-tuning of the E_{red}^* of **1** was attempted by Waser and co-workers using substituted carbazole[46] or diphenylamine.[43] In the case of halogenation, the computed E_{red}^0 or E_{red}^* values increased in the order of H, F, Cl, Br (**1** and **21**–**23**), whereas the values could not be determined experimentally due to the poor quality of the CV measurements.[46] The latter work was aimed to impart selectivity to the carboxylic acids on the C-terminus over those on aspartic acid or glutamic acid based on their different oxidation potential during decarboxylative alkynylation of peptides.[43] Halogenation on the diphenylamine of **25** (**24**, **26**, and **27**) increased the E_{red}^* and a methoxy group on the carbazole of **1** (**24**) decreased E_{red}^*, but how effectively the finely tuned E_{red}^* deals with the selectivity issue was not demonstrated.

3.2. Phenothiazines

Among the various photomediated controlled radical polymerizations (photo-CRP), a metal-free method was first suggested in photoredox-mediated atom transfer radical polymerization (ATRP) by Fors, Hawker, and co-workers by replacing an Ir-based catalyst with a phenothiazine-based organic PC.[47] ATRP has been widely used to synthesize polymers with precisely defined structures, but concerns on metal residues, which could hamper the use of the polymers in biological or microelectronic applications, have led to the development of metal-free system.[29] In O-ATRP, the PC has to be highly reducing in its excited state to activate carbon–halogen (C–X) bond (initially from the initiator and subsequently from the dormant polymer chain). The resulting radical cation should be sufficiently stable and appropriately oxidative to close the catalytic cycle (Scheme 7a). The authors adopted phenothiazine as the core structure in terms of its desirable radical stability, but commercially available 10-methylphenothiazine (Scheme 8, **28**) gave poor control over the molecular weight distribution (or dispersity) possibly due to catalyst decomposition. Eosin Y or methylene blue with the oxidizing excited state was not able to promote the polymerization at all. Instead, **29** with a phenyl group as the nitrogen substituent allowed the controlled polymerization of vinyl monomers including methyl methacrylate (MMA). Notably, the less oxidizing ground state of **29** than that of $Ir(ppy)_3$ prevented the oxidation of amine, which was thought to broaden the dispersity of poly (2-(diethylamino)ethyl methacrylate). Therefore, the necessity to purposely build up a new class of organic PCs with proper redox potentials in both the ground and excited states was again highlighted.

As Matyjaszewski and co-workers reported, **29** also achieved O-ATRP of acrylonitrile.[48] Two more phenothiazine derivatives with different nitrogen substituents were investigated under the same polymerization condition. **31** with a methoxy group showed a similar catalytic performance to **29**, whereas the polymerization took longer after an induction period for **32** with a 1-naphthyl group. However, the reason for the catalyst design and a detailed study on their different performance was not provided. The effect of *N*-arylation was explained later by the same research group in the work which elucidated the mechanism through cyclic voltammetry measurements, laser flash photolysis, and density functional theory (DFT) calculations.[49] Several classes of catalysts including phenothiazine-based organic PCs (**28**, **29**, and **31**–**35**) were tested in the model reaction to prepare poly(methyl methacrylate) (PMMA) under different conditions (varying the solvent system, light intensity, initiator, and catalyst). Only *N*-arylated phenothiazines which were stable over a longer polymerization time without decomposition of corresponding radical cations provided well-defined polymers. Others that underwent decomposition showed limited control despite their similar redox potentials.

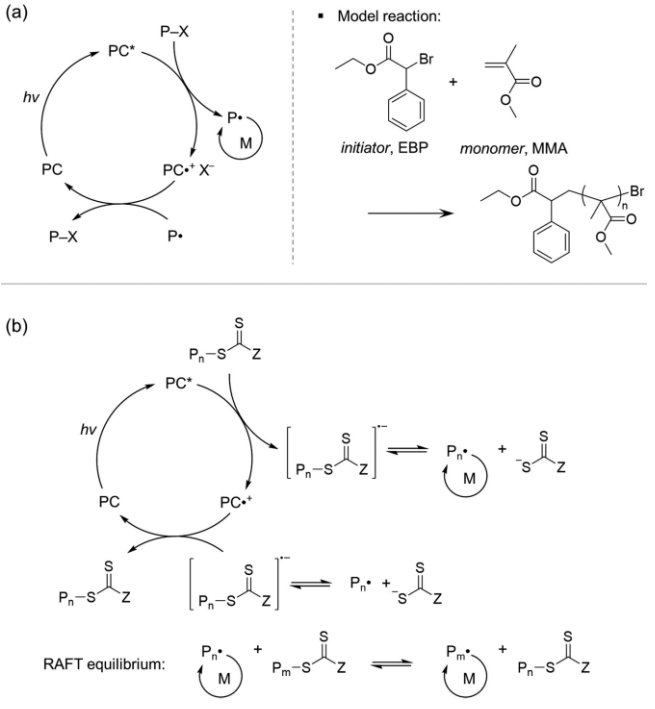

Scheme 7. Reaction mechanism for the (a) O-ATRP and (b) PET-RAFT polymerization (P–X: dormant polymer chain, P•: propagating polymer chain, M: monomer, EBP: ethyl α-bromophenylacetate, MMA; methyl methacrylate).

29 promoted the photomediated reversible addition-fragmentation chain transfer (RAFT) polymerization of a variety of acrylate and acrylamide in a controlled manner in the presence of a chain transfer agent (CTA) with a trithiocarbonate (TTC) moiety.[50] **36**, a model compound functionalized with an acrylamide group, was shown to retain the electrochemical property of **29** so that even the gel formed via the copolymerization of **37** with *N*-isopropylacrylamide (NIPAAM) served as a heterogeneous and recyclable PC for photomediated RAFT polymerization and O-ATRP.[51] In particular, the resulting gel displayed a lower critical solution temperature (LCST) behavior in water owing to poly(NIPAAM). The photo-CRP only became possible at temperatures below the LCST where the reagents are allowed to diffuse into the swollen and transparent gel and thus participate in PET.

Modification of the core of **29** with 4-*n*-butylphenyl groups led to the development of **38**, which exhibited a red-shifted absorption profile by 30 nm and increased molar absorptivity

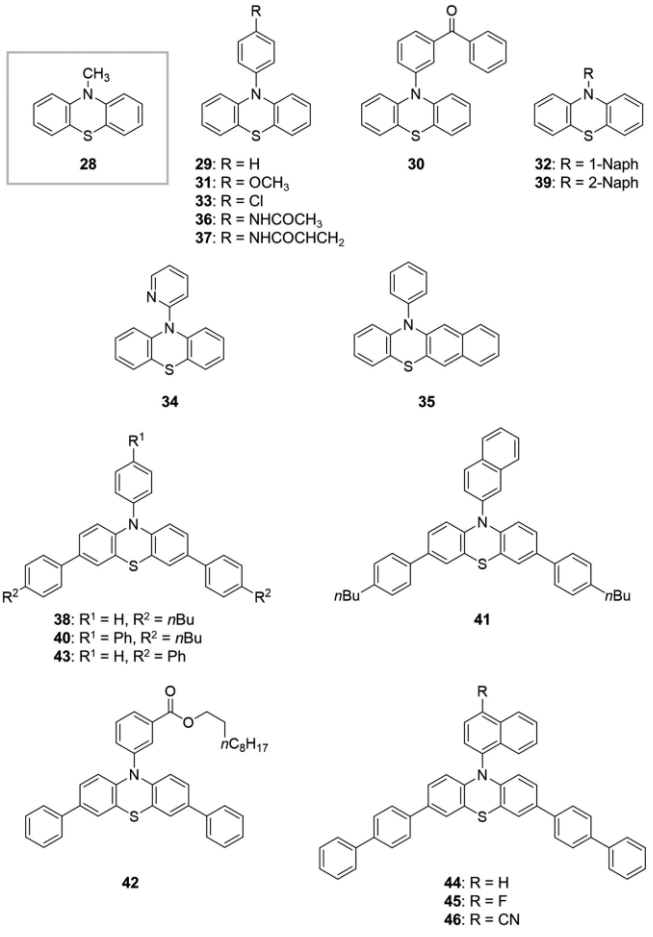

Scheme 8. Phenothiazine-based organic PCs.

by around 4 times.[52] The E_{ox}^* of **38** was similar to **29**, but only **38** provided well-controlled semifluorinated (meth)acrylate polymers in the presence of TTC upon visible-light irradiation due to the low visible-light absorption of **29**. However, simply improving the absorption profile in the visible-region of **29** and **39** was insufficient for the preparation of poly(meth)acrylates and poly(meth)acrylamides possessing (hetero)aryl chain ends.[53] The proposed mechanism was similar to that of O-ATRP except for using an arylsulfonyl halide instead of an alkyl halide as the initiator. Despite their similar light absorption profile, E_{ox}^* and fluorescence lifetime of the excited states of **38**, **40**, and **41**, **41** afforded the best result given the distinct value of fluorescence quantum yield (Φ_{FL}) (30, 15, and 61 %, respectively). Very recently, Chen and co-workers reported the PET-RAFT copolymerization of chlorotrifluoroethylene, which suffered from the low boiling point, and vinyl ethers at ambient temperature and pressure.[54] Although the electron-withdrawing substituent on **28** decreased the E_{ox}^* of the fluorinated PC (**42**), **42** imparted better control due to the fluorine-fluorine interaction with the copolymers which were observed to self-assemble during the polymerization process.

The highly reducing nature of **29** in its excited state enabled the dehalogenation of unactivated alkyl and aryl halides (Cl, Br, and I)[55] which further improved the same reaction using perylene diimides (PDI)[17] or $Ir(ppy)_3$.[56] By **29**, iodobenzene underwent the reduction even in air, whereas, **30** which was exclusively led to form a triplet excited state due to benzophenone moiety, resulted in no reaction under the same conditions. Based on these results, the authors suggested that only the singlet excited state of **29** contributes to catalyze the reaction thus rendering the accessibility to challenging substrates and oxygen tolerance.

Recently Damrauer and co-workers provided insight on how to promote Φ_{ISC},[57] in line with their research interest on the design principles of structurally similar phenoxazines although the difference between sulfur and oxygen has to be accounted for. Four molecules with the same 4-biphenyl substituents on the core and *N*-aryl substituents bearing increasing electron-withdrawing character (**43**–**46**) were prepared and the electronic character of their excited states was assigned by transient absorption spectroscopy and DFT calculations. As the accessibility to singlet charge transfer state from the phenothiazine core to naphthyl group ($S_{CT\text{-}Naph}$) increases by lowering its energy level along with increasing electron-withdrawing character of naphthyl group, radiative decay is slowed to promote ISC to triplet charge transfer state from the core to biphenyl group. However, if too much lowered as in the case of **46**, Φ_{ISC} became too low due to more favored nonradiative decay from $S_{CT\text{-}Naph}$.

3.3. Phenazines

In 2016, Miyake and co-workers developed a series of organic PCs for O-ATRP based on a 5,10-diphenyl-5,10-dihydrophenazine core (Scheme 9)[16] in line with their discovery to use perylene.[58] Here, computational chemistry played a notable role. First of all, the core was unbiasedly screened out of a variety of different cores based on their theoretically calculated value of E_{ox}^*. The calculated redox potentials showed good agreement with the experimental values obtained throughout the paper. The presence of electron-donating (**47**), -withdrawing (**49**, **50**), or neutral (**48**) *N*-phenyl substituents gave a rather wide range of E_{ox}^* from –2.06 to –2.36 V which were sufficiently high to reduce ethyl α-bromophenylacetate (EBP) (E_{red}^0 = –0.74 V) which was employed as an initiator. $PC^{\bullet+}$ was oxidizing enough (E_{ox}^0 = ca. –0.1 V) to deactivate the propagating radical and thus close the catalytic cycle. Therefore, the O-ATRP of MMA under white LEDs or even sunlight was achieved in a controlled manner. Interestingly, **49** outperformed the other catalysts in spite of them all exhibiting the appropriate redox potentials. DFT calculation on the frontier molecular orbitals contributing to the T_1 revealed that the higher-lying SOMOs in **49** and **50** were localized on the phenyl moiety to which the electron-withdrawing substituents were attached, in contrast to that observed for **47** and **48** localized on the phenazine core along with their lower-lying SOMOs. Observations on the effect of electron-withdrawing *N*-phenyl substituents to cause the spatial separation of the electrons in T_1 led the authors to suggest the 2-naphthyl (**51**) and 1-naphthyl (**52**) derivatives based on quantum chemical calculations. As expected, both catalysts possessing not only proper redox potentials but also spatially separated SOMOs worked well in the polymerization reaction.

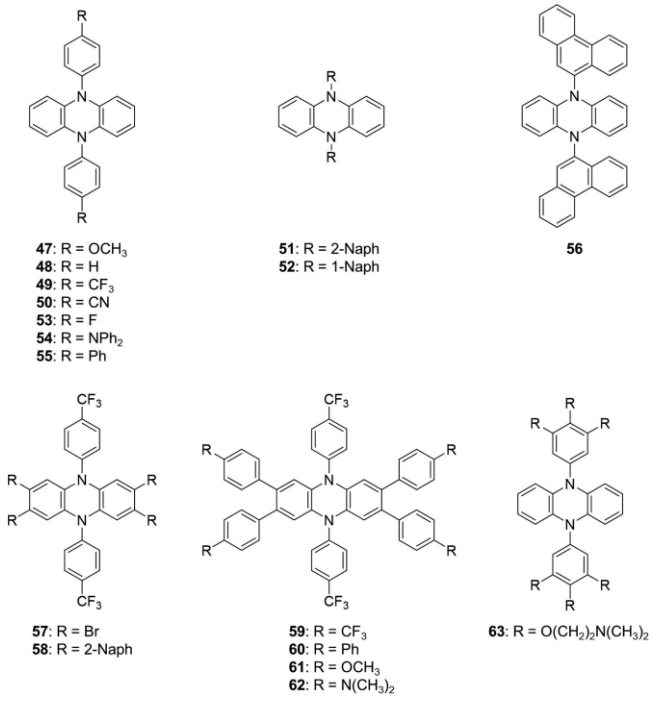

Scheme 9. Phenazine-based organic PCs.

It was later confirmed that the intramolecular charge transfer (CT) character, which can be accessed by (the choice of the *N*-aryl substituent and thereby) the spatially separated SOMOs in the lowest excited state, is important for the controlled O-ATRP of MMA.[59,60] TD-DFT calculation combined with UV/Vis spectroscopy predicted the excitation character of the local excitation (LE) in **48** and of CT in **51** and **52**.[60] Since the HOMO was localized on the dihydrophenazine core for both cases, the location of the LUMO defined the character: LE if localized on the core with an unfunctionalized phenyl moiety as the *N*-aryl substituent (**48**) or CT if localized on the *N*-aryl substituent with phenyl moiety functionalized with an electron-withdrawing group or extended conjugation (**51** and **52**). The nature of the CT was further supported computationally by the change in the dipole moment from the ^{1}PC to ^{3}PC* state in the electrostatic potential (ESP) map and experimentally by the large Stokes shift and solvatochromic shift in the emission behavior. As expected, PCs which do possess CT character (**49**, **51**, **52**, **55**, and **56** with an electron-withdrawing *N*-aryl group) outperformed those PCs without CT character (**47**, **48**, **53**, and **54** with an electron-donating *N*-aryl group) albeit with similar redox properties.[59] Given the similar role of the PC in PET-RAFT polymerization as in O-ATRP, the former reaction with a variety of monomers using **47** and **49** was also dependent on the accessibility of the PC to CT character.[61] Of note, **49** was the first organic PC to catalyze the PET-RAFT polymerization of vinyl acetate. **51** and **55** also allowed the PET-RAFT polymerization of methyl acrylate (MA) at a much faster rate than non-CT PCs (**47**, **53**, and **54**) potentially because of the more efficient activation of the RAFT agent.

Subsequently, the effect of the modification of the dihydrophenazine core was studied.[62] PCs with electron-withdrawing (**59**), conjugation-extending (**58**, **60**), and electron-donating (**61**, **62**) substituents were prepared from **57**. The absorption profile was red-shifted with increased molar absorptivity in all the PCs when compared to **49**. Similar to the *N*-aryl substituent modification, only PCs with electron-withdrawing or conjugation-extending groups were computationally predicted to have spatially separated SOMOs. However, the higher-lying SOMO was found to reside on the core-substituent instead of the *N*-aryl substituent, whereas the lower-lying SOMO was consistently located on the core. With the resulting CT character and high molar absorptivity, **58**–**60** outperformed **49** in the O-ATRP of MMA at the significantly decreased catalyst loadings (e.g. from 1000 ppm to even 5 ppm relative to MMA in the case of **58**). At 50 ppm, **58** and **59** showed oxygen tolerance.

The introduction of CO_2-responsive tertiary amine moieties in **48** facilitated the almost complete removal of the catalyst after the polymerization.[63] **63** is hydrophobic in absence of CO_2, whereas it becomes hydrophilic under CO_2. The difference in solubility allowed the controlled O-ATRP to be conducted in a hydrophobic organic solvent and catalyst removal via extraction with a CO_2-saturated aqueous solution after the reaction (and vice versa). The recovered catalyst could be reused in subsequent reactions.

Meanwhile, Miyake and co-workers utilized a strongly reducing power of **51** to directly reduce CF_3I or C_2F_5I in trifluoromethylation of unsaturated indoles, pyrroles, arenes, and alkenes and photoredox/Ni dual-catalyzed C–N cross-coupling reactions of primary and secondary amines with aryl bromides.[64] Glorius and co-workers employed **49** for photoredox/Cu dual-catalyzed decarboxylative olefination of various activated aliphatic acids.[65] Alkyl radicals were formed from aliphatic acids ($E_{1/2}^{red} < -1.28$ V), followed by Cu^{II} catalyst-mediated oxidation to the alkene. A series of PCs (**48**, **50**, **53**, and **55**) were ineffective despite appropriate E_{ox}^* and the superior performance of **49** was ascribed to the faster reaction rate in the reaction.

3.4. Phenoxazines

In 2016, Miyake and co-workers reported that *N*-aryl phenoxazines can mediate O-ATRP.[66] The catalysts were designed to have the spatially separated SOMOs in their T_1s to extend the validity of this design principle to different classes of PCs over phenazine. PCs with different *N*-phenyl substituents all possessed strongly reducing excited states (E_{ox}^* = ca. –2 V) and oxidizing radical ions (E_{ox}^0 = ca. 0.5 V), but only naphthyl substituents yielded spatially separated SOMOs (Scheme 10, **64**–**67**). Thus, successful control of the O-ATRP of MMA was achieved using **66** and **67** under irradiation at 365 nm and 2-bromo-2-methylmalonate (DBM) as an initiator. Furthermore, 4-biphenyl substituents on the core of **66**, as directed by computational studies, brought about the preparation of a more useful catalyst **68** which can absorb visible-light while retaining superior control over the polymerization. **68** showed air tolerance as well when the volume of the vial headspace was reduced in the later work albeit with a lower I*.[67] A series of structurally modified PCs (**70**, **75**, **77**, **78**, and **81**) were prepared to understand the mechanism, but all resulted in the consist-

ently low I*. I* is defined by dividing the theoretical number average molecular weight (M_n) by experimental M_n, so the low value of I* suggested that a side reaction likely occurred by the presence of air.

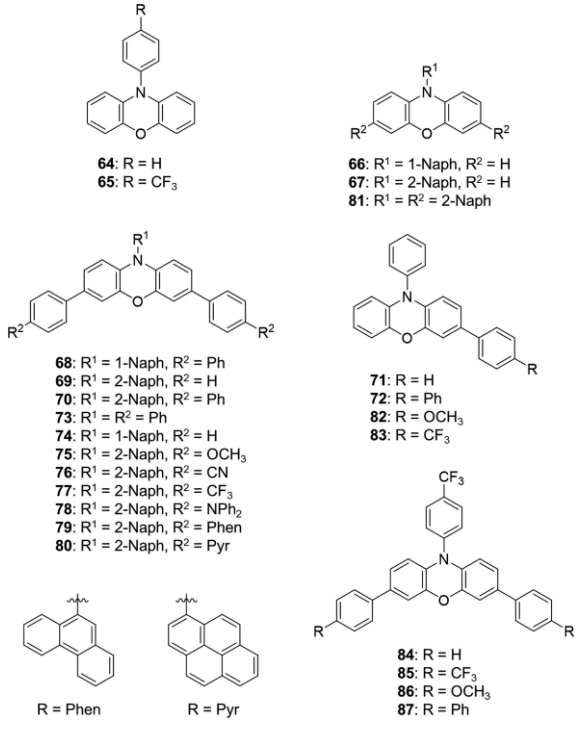

Scheme 10. Phenoxazine-based organic PCs.

In addition, **32** as an *S*-analog of **66** was studied to investigate the effect of different atoms on its physical properties and thus their catalytic performance in O-ATRP.[66] **32** with a phenothiazine core produced a less controlled PMMA with broad dispersity. The X-ray crystal structure of **32** and electrostatic potential mapped electron density of its T_1 were compared to those obtained for **66** and **48** (as an *N*-analog), which indicated that the bent boat conformation of the phenothiazine moiety due to the larger sulfur atom limited the intramolecular CT process. The larger dispersity was also attributed to the higher structural reorganization energy of phenothiazines in the transition from the boat ground state to the planar radical cation and then to the boat at T_1, as inferred from the computation on **29**, **48**, and **64**. Meanwhile, the similar smaller size of the oxygen and nitrogen atoms when compared to sulfur resulted in the consistently planar structures of the phenoxazine and phenazine moieties throughout their transitions and the lower structural reorganization energy, which favors kinetically fast ET processes.

The requirements of the PC to successfully carry out O-ATRP (efficient visible-light absorption, proper redox properties at its ground and excited states, and spatially separated SOMOs) were validated through a study of the structure–property relationships of a series of phenoxazine derivatives (**64** and **66**–**83**).[68] It was previously shown that core modification enhances the visible-light absorption (**66** vs. **68**) and a naphthyl moiety as the *N*-aryl substituent generates intramolecular CT character in the triplet excited state (**64** vs. **66**, **67**), but an investigation on a larger number of PCs enabled a more detailed catalytic design principle to be established.[66] For example, a core-extended 10-phenylphenoxazine (**73**) without an *N*-aryl substituent was also able to access the CT states albeit to a lesser extent because their SOMOs were separately localized on the core and core substituent. **70** with a 2-naphthyl substituent on **73** was expected to induce CT character from the core to 2-naphthyl substituent but was similar to **73** in terms of the nature of CT character and catalytic performance implying that the core substitution influenced the catalytic properties more than *N*-aryl substitution. The core substituent also affected the light absorption profile and redox properties. Similar trends were also seen in the novel phenoxazine-based PCs (**83**–**87**) developed by Lee, Son, and co-workers[69] with the aid of DFT calculations. **87** showed the best performance in the O-ATRP of MMA in the presence of DBM.

Besides O-ATRP, **68** possessing photophysical characteristics (e.g. E_{ox}^*, E_{ox}^0, energy level of T_1, and triplet quantum yield) which are comparable to those of $Ir(ppy)_3$, as well as remarkably longer-living T_1 (480 ± 50 μs vs. 1.9 μs) catalyzed the organic transformation of small molecules such as photoredox/Ni dual-catalyzed C–N cross-coupling reactions of amines and C–S cross-coupling reactions of thiols with aryl bromides.[64] König and co-workers reported **68**-catalyzed photocatalytic Barbier-type reaction of allyl or benzyl bromides with aromatic aldehydes or ketones to generate allylic or benzylic alcohols via a reductive radical-radical cross-coupling.[70] Aldehydes underwent single-electron reduction by **68** in the excited state in the presence of *N*,*N*-diisopropylethylamine (DIPEA) and $LiBF_4$, followed by coupling with allyl or benzyl radical produced by DIPEA and light irradiation. Although the homocoupling by-products were inevitably formed, the photocatalytic reaction eliminated the need for various metals in the conventional Barbier-type reaction.

Given the recent publications by Damrauer and co-workers describing the detailed analysis of photophysics regarding the ISC yield, (non)radiative rate constants, and relevant photophysical parameters,[71,72] it is expected to disclose the intentional design of phenoxazine-based PCs and broaden their application to organic transformations.[21]

3.5. Dimethyl-Dihydroacridines

Very recently Miyake and co-workers presented dimethyl-dihydroacridines, which have been applied in the field of OLED, as a new scaffold.[73] Inspired by their structural similarity to dihydrophenazines and phenoxazines (see Section 3.3 and 3.4, respectively) introduced in their previous works, seven PCs (Scheme 11, **88**–**94**) were synthesized in an analogous fashion guided by DFT calculations to tune the light absorption profile, intramolecular CT character in the excited state, Φ_{FL}, and redox properties and compare their catalytic performance in the O-ATRP of acrylic monomers, which necessitates a highly negative E_{ox}^*. Likewise, the accessibility to CT character was corroborated with the reduced Φ_{FL} and thereby relatively more controlled polymerization of *n*-butyl acrylate (BA) in the presence of DBM

under irradiation at 365 nm. However, the lower dispersity (1.35) of the resulting polymer could only be accompanied by uniform irradiation in a continuous-flow reactor and the addition of bromide salts to promote the deactivation of the propagating polymer ends due to the significant autopolymerization of BA.

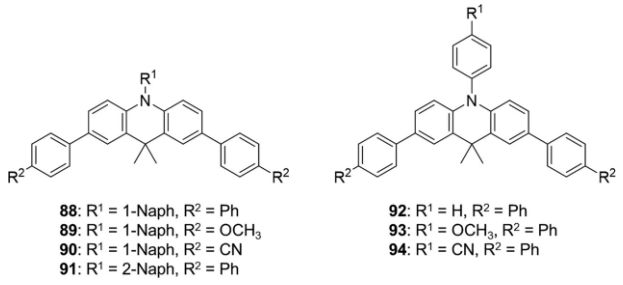

Scheme 11. Dimethyl-dihydroacridine-based organic PCs.

3.6. Xanthenes

Xanthenes are in either neutral or ionized state and have different absorption properties depending on the pH. Eosin Y, erythrosine B, phloxine B, and Rose Bengal (RB) are examples sharing a common halogenated xanthene dye scaffold, but each with different halogen atoms (Scheme 12). Owing to their photoredox potential comparable to that of transition metal complexes, numerous reactions have been successfully catalyzed by eosin Y[13,14] and the other xanthene dyes.[5]

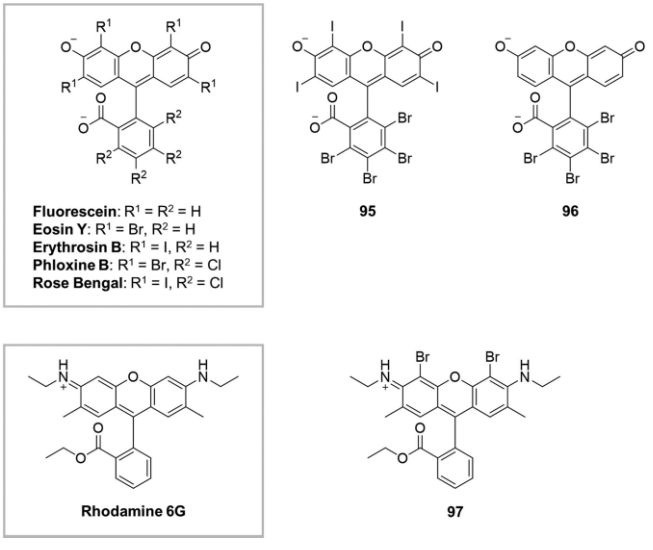

Scheme 12. Xanthene-based organic PCs.

In 2015, it was demonstrated that for the PET-RAFT polymerization organic dyes can replace $Ir(ppy)_3$[74] or $Ru(bpy)_3Cl_2$[75] by Xu, Boyer, and co-workers for the first time.[12] Five dyes (eosin Y, fluorescein, rhodamine 6G, Nile red, and methylene blue) commonly employed as organic PCs in organic synthesis, were screened, but only the first two dyes were effective thanks to proper E_{ox}^* and Φ_{FL}; the E_{ox}^* should be lower than the E_{red}^0 of CTA in the absence of oxygen via an oxidative quenching cycle, while efficient PET was reflected by the low Φ_{FL}. In the presence of oxygen, another mechanism via a reductive quenching cycle was proposed using an amine as a sacrificial reducing agent. In fluorescein-catalyzed O-ATRP of MMA in the presence of triethylamine as an electron donor,[76] the basicity of amine also helped fluorescein to maintain its structure in fluorescent ring-opened form and the corresponding photophysical properties. The polymerization was completely out of control under acidic conditions.

Meanwhile, a comprehensive investigation of the structure-performance relationship of conventional molecules guided the design of a new organic PC as is the case of **95** reported by Boyer and co-workers.[77] In PET-RAFT polymerization, a higher $k_{p.app}$ (apparent polymerization rate) or catalytic efficiency can be achieved by the efficient generation of $^3PC^*$ (high Φ_T) for PET and more negative E_{red}^* to reduce the RAFT agent. The structure–property relationship of four commercial fluorescein derivatives was investigated by DFT calculation, and the polymerization results were compared. Then structure–property-performance relationship suggested that the introduction of a heavier atom on the R^1 position (I > Br > Cl > H) enhanced Φ_T. Electron-donating substituents on the xanthene core, which are involved in the higher-lying SOMO, increase the electron-donating ability and thus lower the E_{red}^*. Therefore, **95** was newly designed by substituting the Cl in RB for Br. Not only was the PET-RAFT polymerization of *N*,*N*-dimethylacrylamide (DMA) as the monomer and 2-(*n*-butyltrithiocarbonate)propionic acid (BTPA) as the CTA successfully carried out, but with oxygen tolerance arising from the sufficiently high Φ_T.

Xanthene scaffold, however, was excluded when constructing broadly applicable organic PCs due to their lack of stability upon pH change.[42] For instance, phloxine B becomes colorless thus catalytically inactive below pH 2.0 because of the structural transition from its salt to acid state. Liu, Xu, Boyer, and co-workers made use of this pH-responsiveness to discover an organic PC for PET-RAFT polymerization which is sensitive to both light and pH.[78] Advanced from their previous work developing **95**, triplet quantum yield calculations were used to successfully predict photophysical properties and led to the first example of a fully computer-guided discovery. The critical pH under which a given dye loses its color and photoactivity depends on the molecule itself. The authors postulated that the pH can be ideally controlled by altering the substituents on the benzoic acid group (R^1) and xanthene core (R^2) from an intensive study of the structure–property relationship of eosin Y and phloxine B. Further computational considerations on the E_{ox}^*, Φ_T, and photophysical properties, such as the rate constant of fluorescence (k_f) or internal conversion (k_{ic}), proposed **96** as the most applicable PC with a transition pH around 5. **96** was then synthesized, and its characterization results agreed well with the predictions. PET-RAFT polymerization was successful irrespective of the monomer, CTA, solvent, and monomer-to-CTA ratio used. The introduction of gaseous HCl/N_2 or CO_2 lowered the pH of the system to "off" the polymerization, whereas the introduction of $NaHCO_3$ powder turned "on" the reaction.

Recently, the heavy atom effect on the ISC efficiency of xanthene dyes for visible-light mediated photopolymerization

in xanthene/trialkylamine system was studied by Lee, Lee, and co-workers.[79] A high catalyst loading ensures rapid reaction but hampers biological application at the same time. The incorporation of a heavy atom into dyes can reduce the catalyst loading by decreasing the Φ_{FL}, whilst increasing the triplet excited-state population, ISC efficiency, and PET rate. Four fluorescein-based dyes (fluorescein, 4′,5′-dibromofluorescein, 2′,4′,5′,7′-tetrabromofluorescein, and 2′,4′,5′,7′-tetraiodofluorescein) and two rhodamine 6G-based dyes (rhodamine 6G and 4′,5′-dibromorhodamine 6G (**97**)) were chosen to compare the performance in relation to the number and type of halogen atoms (Br and I). The type of halogen atom affected the photocatalytic activity much more than the number of atoms. 2′,4′,5′,7′-tetraiodofluorescein out of fluorescein-based dyes and **97** out of rhodamine 6G-based dyes dramatically enhanced the degree of photopolymerization presumably due to high Φ_{ISC}.

3.7. Acridiniums

Fukuzumi's catalyst **98** (Scheme 13)[80] has been shown to be effective in most reactions where a strong oxidant is required.[81] The alkene anti-Markovnikov hydro-functionalization reactions (e.g. etherification and amination) mediated by an alkene cation radical can be an example as proposed by Nicewicz and co-workers,[82] and the research group have contributed to the derivatization of acridinium PCs to broaden the scope of chemical transformation. For example, in the regioselective anti-Markovnikov hydrofluorination of styrenes, **98** was degraded via nucleophilic demethylation by cesium fluoride acting as a fluoride source.[83] Neither newly synthesized *N*-phenyl

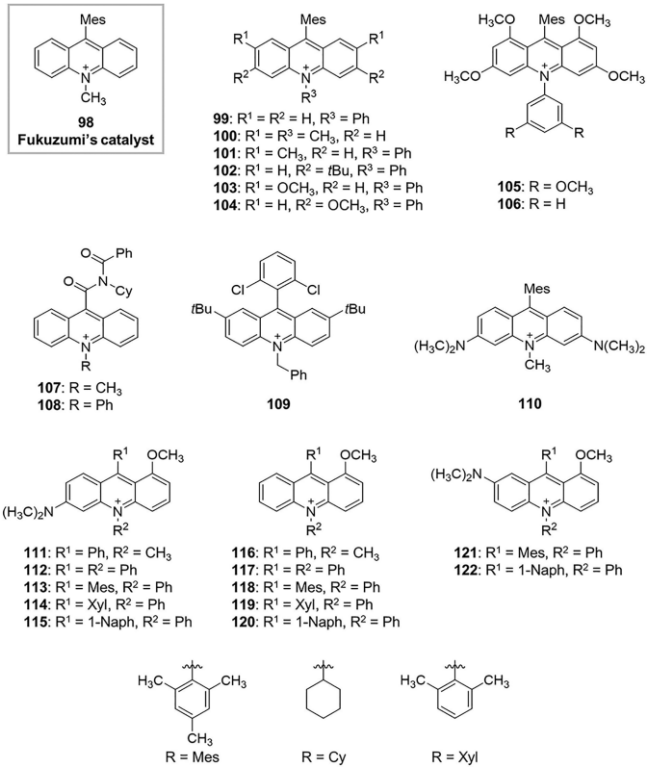

Scheme 13. Acridinium-based organic PCs.

analog (**99**) nor previously reported **100** were quite successful, which led to the synthesis of sterically hindered and thus stable PC (**101**). The yields were improved under the optimized condition using milder fluoride source and **101** (Scheme 14). However, site-selective arene C–H amination necessitated the preparation of an even more stable **102** than **99** and **101** which were subjected to degradation in the presence of oxygen-centered radicals formed during the reaction.[84]

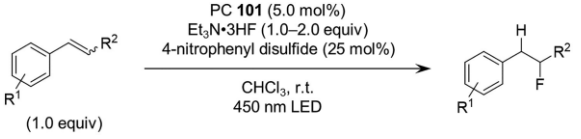

Scheme 14. Regioselective anti-Markovnikov hydrofluorination of styrenes.

An electron-donating methoxy-substituted core (**103**–**106**) resulted in a longer excited-state lifetime of fluorescence and similar (**106**) or more negative (**104**–**106**) E_{red}^0 compared to **102**, as reported by DiRocco and co-workers.[85] **105** with a tetra-substituted core outperformed **98** in the decarboxylative conjugate addition of Cbz-proline to dimethyl maleate (86 % vs. 5 % yield) due to enhanced stability of **105** in contrast of **98** which underwent complete degradation during the reaction (Scheme 15).

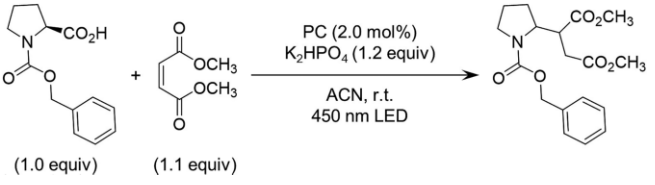

Scheme 15. Decarboxylative conjugate addition of Cbz-proline to dimethyl maleate.

Novel imide-acridinium-based PCs bearing an imide group as the C9-substituent were synthesized by Alemán, Mancheño, and co-workers through oxidative Ugi-type reaction of C9-unsubstituted acridanes with isocyanide and benzoyl peroxide, followed by aromatization (Scheme 16a).[86] Compared to **98**, the optimized **107** and **108** turned out to be both more powerful oxidant and reductant in their excited state, so outperformed **98** in dehydrogenative lactonization of 2-phenylbenzoic acid and reduction of bromo-ketone derivatives, respectively.

Acridiniums can also be synthesized through direct conversion of the corresponding xanthylium salt, as reported by Nicewicz and co-workers.[87] Xanthylium salt was prepared from double directed ortho-metalation (D*o*M) with lithium of biaryl ether, followed by the coupling of esters (Scheme 16b), which therefore rendered a facile and scalable method to separately modulate the acridinium core, C9- and *N*-substituents. Investigation of photophysical properties of 15 molecules suggested the authors inhibit the formation of the CT state and suppress C–C or C–N bond rotation and thus nonradiative decay for extension of the excited-state lifetime. The optimized **109** exhibited fluorescence lifetime exceeding 25 ns.

Wenger, Sparr, and co-workers reported novel amino- and methoxyacridinium-based PCs (**111**–**122**),[88] guided by **110**

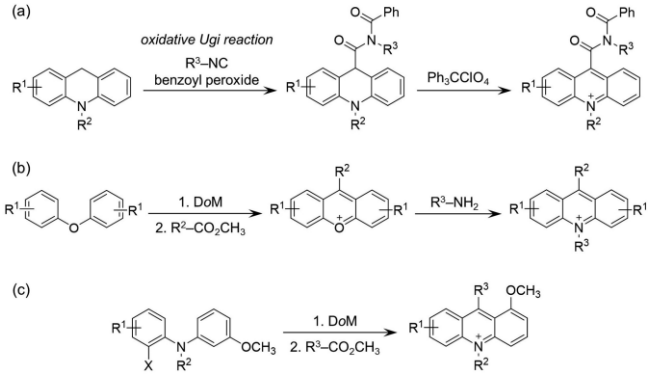

Scheme 16. Schematic representation of approaches for modular synthesis of acridinium-based organic PCs.

which do not possess CT character in the excited state due to the introduction of dimethylamino group in contrast to common acridinium PCs. X-M (halogen-metal) exchange combined with DoM from di- or triarylamines and esters as readily accessible starting materials was proposed for the modular synthesis of PCs in moderate-to-high yield (Scheme 16c). Photophysical and electrochemical properties were in a broad range that was influenced by the presence and location of dimethylamino or methoxy substituents.

Likewise, divergent synthesis of acridinium-based organic PCs has been achieved regarding various ways of disconnection. Given the synthetic ease and functional group tolerance, it is expected to easily expand the PC library which would be beneficial for understanding the photophysical characteristics. The recent development in modular synthesis of aminoacridiniums with their applications and catalytic parameters are well summarized by Sparr and co-workers.[89]

3.8. Porphyrins

Zawada, Kadish, Gryko, and co-workers pioneered the use of the free base tetraphenylporphyrin **123** (Scheme 17) as an organic PC in the α-alkylation of aldehydes with diazo esters in the presence of a secondary amine through a reductive quenching mechanism (Scheme 18).[90] The substituents on the macrocycle (**123**–**132**) affected the electronic nature thus the redox potentials, but a direct correlation with the reaction yield could not be determined because of their different solubility in the media.

123 was able to catalyze the direct C–H arylation of heteroarenes through an oxidative quenching mechanism.[91] A model reaction of furan and diazonium salt with various porphyrins (**123**–**125**, **128**, **132**, and **133**) as well as Stern-Volmer experiments showed that **124,** whose excited state was quenched by the diazonium salt with an optimal quenching rate and E_{ox}^*, was the best catalyst. At 1 mol% loading of **124**, the arylation of furan with an electron-acceptor-substituted diazonium salts or the arylation of thiophene and coumarin was also effective (Scheme 19). However, pyrrole derivatives were not suitable substrates likely because of the reduction of **124** by them competing with the oxidation of **124** by the diazonium salts to enter the catalytic cycle.

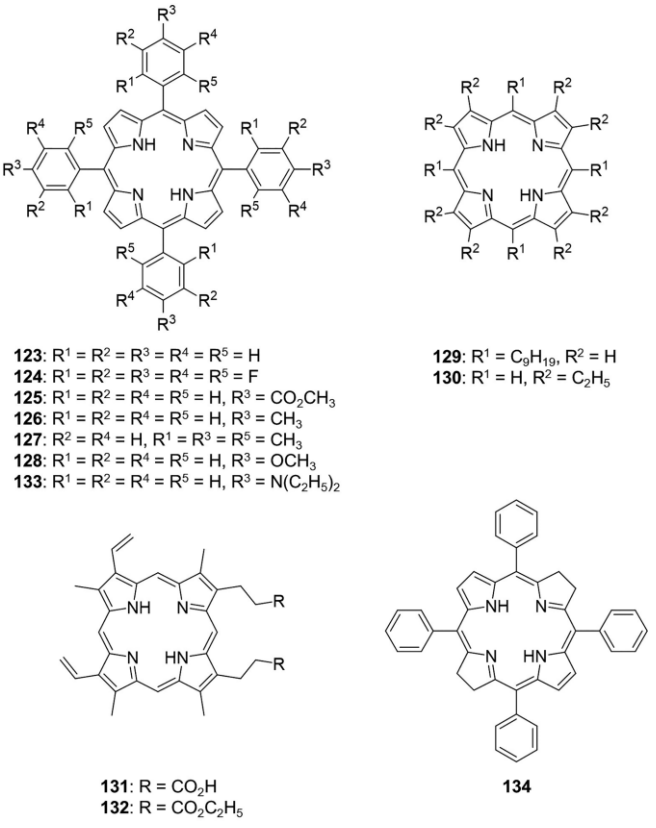

Scheme 17. Porphyrin-based organic PCs.

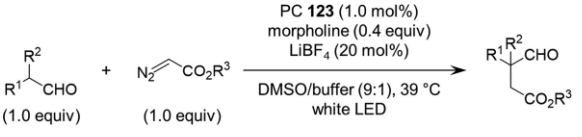

Scheme 18. α-Alkylation of aldehydes with diazo esters.

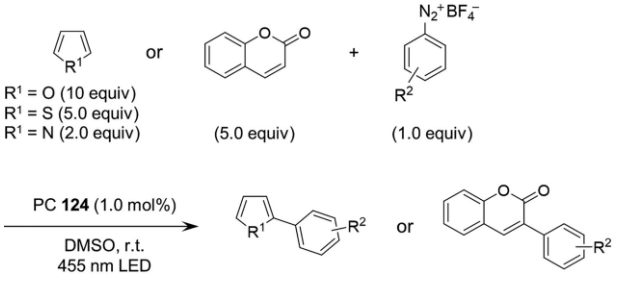

Scheme 19. Direct C–H arylation of heteroarenes.

Meanwhile, strong absorption in the far-red light region (700–765 nm) arose in **134** through the reduction of **123** and thus allowed the controlled PET-RAFT polymerization of MMA, glycidyl methacrylate, and BA under irradiation at 740 nm.[92] The reaction was not hindered when either the reaction vessel or the surface of the light source was covered by animal skin with a thickness up to 7 mm. Such a unique absorption profile scarcely seen for organic PCs may facilitate biomedical applications since far-red and near-infrared light can penetrate soft tissue while eliminating safety concerns.

3.9. Naphthochromenes

In the very recent work by Dell'Amico and co-workers, naphthochromenones was represented as a new class of organic PCs.[93] The scaffold was derived from the light-driven [4+2] cycloaddition reaction between benzophenone and coumarin and post-functionalization provided 12 candidates (Scheme 20, **135**–**146**). An extremely wide redox window up to 3.22 eV, but well-distributed potentials allowed them to engage in both oxidative and reductive quenching pathways. The developed PCs successfully catalyzed a variety of challenging reactions which have been furnished by only specific PCs or previously inaccessible at all: for reductive quenching: (i) Povarov-type addition of *N*,*N*-dimethylaniline bearing electron-withdrawing group (E_{ox}^0 = 1.05–1.33 V) to phenylmaleimide (Scheme 21), (ii) decarboxylative Giese-type addition between proline and dimethyl maleate, and (iii) light-driven acylation reaction of methyl crotonate, which involves the oxidation of acylsilane (E_{ox}^0 = 1.46 V), for oxidative quenching: (i) dehalogenation reactions of diverse benzyl halides and (ii) dehalogenation of methyl 4-iodobenzoate (E_{red}^0 = –1.96 V).

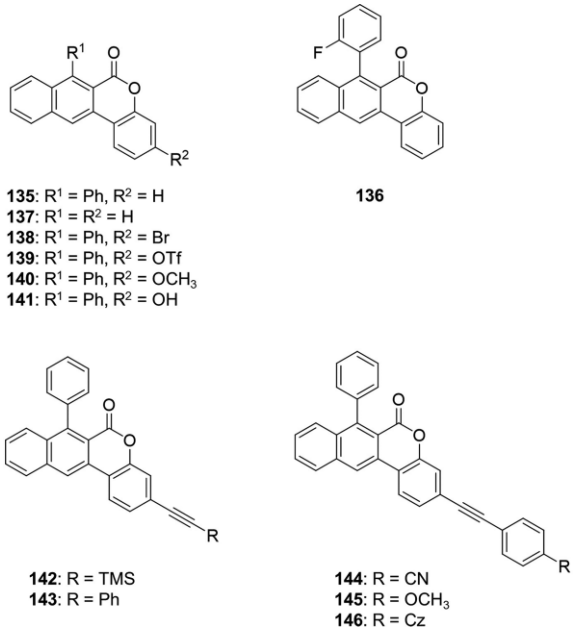

Scheme 20. Naphthochromene-based organic PCs.

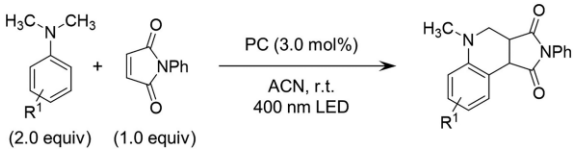

Scheme 21. Povarov-type addition of *N*,*N*-dimethylaniline to phenylmaleimide.

3.10. Others

3.10.1. Borane-Based

You, Cho, and co-workers utilized tri(9-anthryl)borane (Scheme 22, **147**) for the trifluoromethylation of unactivated alkenes through an oxidative quenching pathway.[94] **147** originally developed for OLEDs[95] was exploited as an organic PC for the first time. 0.5 mol% of **147** relative to 1-dodecene in the presence of an amine base yielded the *E*-selective product using CF_3I as a trifluoromethylating agent. Substrates with a variety of functional groups from ester, aryl halide (Br, Cl), amide, unprotected alcohol, lactam, silyl ether, sulfonates, to *N*-heterocycle (pyrrole and indole) were tolerated under mild reaction conditions (no heating, irradiation at 480 nm). Perfluoroalkylation with C_3F_7I or C_4F_9I was also possible. The successful employment of **147** suggested the potential of borane-based organic PCs in other photocatalytic transformations.

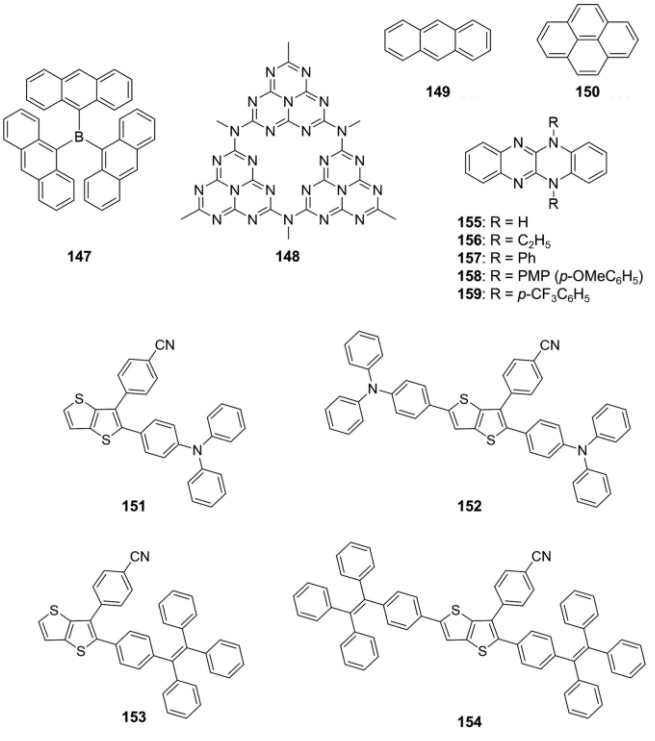

Scheme 22. Miscellaneous organic PCs.

3.10.2. Graphitic Carbon Nitride

(Mesoporous) Graphitic carbon nitride ((mpg) g-C_3N_4) (**148**) is a metal-free, heterogeneous polymeric semiconductor, which has been widely used in solar energy conversion or water splitting. Recently, it has also gained interest as a PC to be applied to free radical polymerization (visible-light photoinitiator),[96] PET-RAFT polymerization of acrylate and acrylamide[97] or MMA,[98] and the bifunctionalization of (hetero)arenes.[99] g-C_3N_4 is heterogeneous in bulk so can be easily separated via simple centrifugation or filtration and reused. It can be transformed into nanosized sheet to afford a homogeneous system as well. There is still much room for development on structure-performance relationship (e.g. morphology and pore volume/size).

3.10.3. Polynuclear Aromatic Hydrocarbons

Yagci and co-workers demonstrated the metal-free ATRP of (meth)acrylates and vinyl monomers using anthracene (**149**)

and pyrene (**150**).[100] Anthracene, in any concentration, resulted in PMMA in low yields and with dispersities around 1.5 in multimodal nature. Especially at high concentrations, the singlet excited state of anthracene underwent [4+4] cycloaddition with another molecule in the ground state rather than activating the alkyl halide initiator. Anthracene radicals were considered to be not as stable so that some polymers were grafted through the anthracene rings. On the other hand, pyrene formed excimers in the same way as anthracene, which are still prone to electron transfer with alkyl halides thus allowing the controlled polymerization.

3.10.4. Thienothiophenes

The same research group reported that metal-free ATRP could also be successfully catalyzed by electron-rich thienothiophenes (**151**–**154**).[101]

3.10.5. Others

A series of highly reducing PCs with strong visible-light absorption was developed by Xu and co-workers, starting from the modification of 10-phenylphenothiazine.[102] Subsequent structural modifications (e.g. extension of the conjugation, changing the scaffold from phenothiazine to phenazine or changing the *N*-substituent) finally resulted in both strongly reductive and (lower energy) visible-light-absorbing organic PCs (**155**–**159**). As expected, the developed PCs effectively catalyzed the challenging reactions including the activation of C–Br and C–Cl bonds at room temperature (by **155**), 1,5-H transfer reaction of aryl iodide (by **157**) (Scheme 23), the generation of acyl radical precursors from aroryl chlorides, and phosphorus radical-mediated cascade cyclization reaction of 1,6-diyne used to construct organophosphorus fluorene derivatives (by **158**) (Scheme 24).

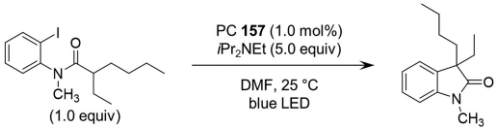

Scheme 23. 1,5-H transfer reaction of aryl iodide.

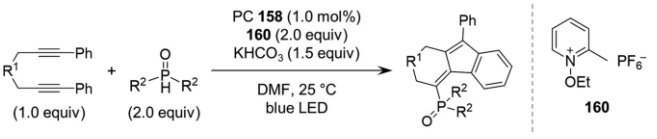

Scheme 24. Phosphorus radical-mediated cascade cyclization reaction of 1,6-diyne.

3.11. Design Strategy to Discover New Organic PCs: toward General Guidelines

In the previous sections, the molecules newly developed or applied as organic PCs in recent years were described according to their core scaffold. Herein, a rather systematic approach to prepare a series of PCs or strategies to enhance photocatalytic reactivity is introduced.

Our group recently proposed a general strategy or systematic platform for the design of organic PCs in collaborative work with Kim, Gierschner, and co-workers.[15] Strongly twisted D–A structures were introduced as a general scaffold, which in theory is capable of affording a large number of candidates through a combination of different donors and acceptors. The CT characteristics of the lowest excited states promote the generation of long-lived T_1 and allow the systematic control of the

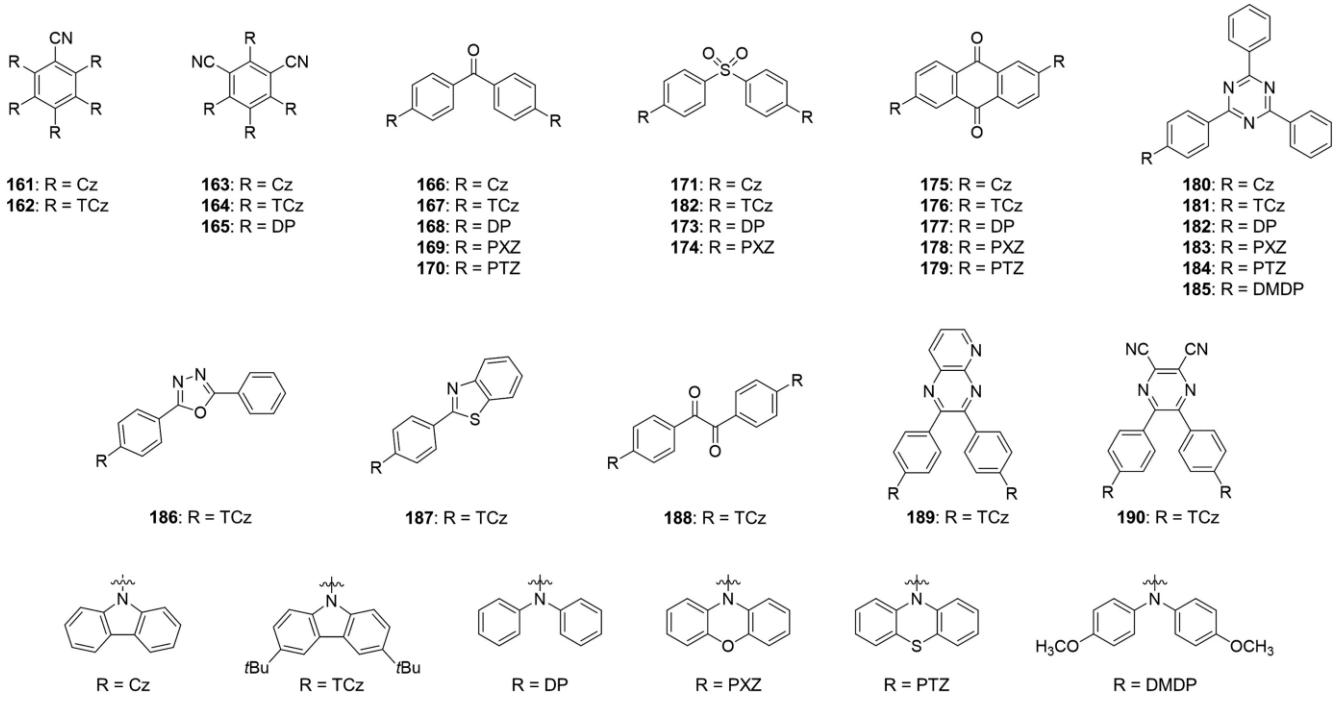

Scheme 25. Organic PCs developed via molecular platform of strongly twisted D–A group.

essential catalyst parameters over a broad range. Out of 30 molecules constructed from six donors and eleven acceptors (Scheme 25, **161**–**190**), nine molecules were excluded due to no absorption overlap with irradiation source (**166**, **171**–**173**, **186**, and **187**) or insolubility to reaction media (**175**, **176**, and **179**) and the rest molecules were employed for O-ATRP. Not all candidates showed good performance due to limited visible-light absorption (**170**, **180**, and **184**), inefficient triplet generation (**169**, **177**, **178**, and **183**), and insufficient reducing power (**177**, **178**, and **188**–**190**), but PCs with high reducing power in the excited state, in particular, were discovered for the successful O-ATRP of MMA at ultra-low catalyst loadings (**165**) and of non-acrylic monomers, such as styrene, under very mild condition. It should be noted that other known PCs were also proposed, implying the versatility of our strategy.

Some of the developed PCs (**161**, **165**, **168**, and **185**) were selected based on ground-/excited-state redox potentials and triplet excited-state energy and used for the PET-RAFT polymerization of MMA in our work.[44] **165** (**4DP-IPN**) outperformed other PCs, i.e. excellent control over the polymerizations at a ca. 5–50 times lower catalyst loading. In-depth experimental and computational investigations of **165** revealed that the outstanding performance over the other PCs was attributed to (i) strong visible-light absorption and (ii) the efficient generation of long-lived triplet excited states due to the strong intramolecular CT character of S_1. The Φ_{ISC} was measured to be 0.82 and 0.77 by time-resolved photoluminescence and transient absorption measurements, respectively.

Increasing the intramolecular CT character or Φ_{ISC} has been served as the strategy to broaden the redox window of organic PCs, but harnessing visible-light (ca. 1.8–3.1 eV) intrinsically has a limited window and it is difficult to fully utilize the absorbed light energy without any loss for chemical transformation. Instead, the recently proposed consecutive PET (con-PET) or multiphoton strategy can be a solution. Con-PET or consecutive excitation of the reaction intermediate, which is generated in situ following the first excitation of the PC, accumulates the energy of two photons. Firstly inspired by biological photosynthesis and proposed by König and co-workers, con-PET of perylene diimides (PDI) **191** enabled the reduction of aryl halides (Scheme 26).[17] Nicewicz and co-workers reported the con-PET of acridinium salt **102** for the reduction of aryl halides (Scheme 27) and the reductive detosylation of amines.[18] The strong reducing power was attributed to the twisted intramolecular CT (TICT) state of the neutral acridine radical **192**, which underwent a second excitation. Therefore, con-PET is a useful strategy, but the need for sacrificial electron donors to quench the firstly excited PC and that the resulting intermediate species have to be colored and sufficiently stable to be re-excited make it difficult to be widely applied. Synthetic photoelectrochemistry, e.g. which was very recently summarized by König and co-workers, works in a similar manner while electrical energy provides any additional energy.[103–106] There is no need of sacrificial electron donors and the energy level can be adjusted by that of the applied potential in the reaction system. Lastly, a multi-photon strategy reported by Wenger and co-workers including multi (two or more)-photon processes such as the aforementioned con-PET or triplet-triplet annihilation (TTA) up-conversion has also emerged recently.[20]

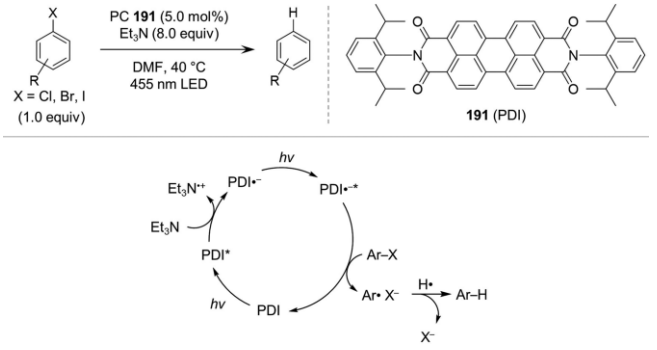

Scheme 26. Reduction of aryl halides using con-PET of **191**.

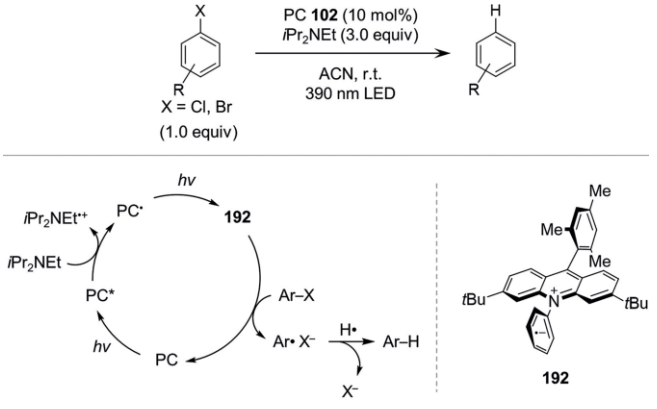

Scheme 27. Reduction of aryl halides using con-PET of **102**.

4. Summary and Outlook

It has been more than 10 years since the advent of photocatalysis for a variety of organic reactions.[107–110] Concerns on the expense and toxicity of classic rare earth metal-based PCs led current interest to seek purely organic alternatives. Traditional organic dyes were initially adopted as itself, or structurally modified to tune the catalytic parameters to achieve better performance although the outcome was not always straightforward. Instead, it has been proposed that (i) a comprehensive investigation on structure–property/performance relationship or (ii) strongly twisted D–A scaffold can be utilized for the design of many new organic PCs via general and systematic approaches. Not only are the structures diversified away from the common scaffolds, but also their properties can be adjusted in a predictable manner. Computational chemistry approaches reduce the time and effort by estimating some of the essential catalytic parameters prior to synthesis, yet are not perfect given unexpected inferior performance due to practical issues (solubility or photostability of molecules in the reaction system) or unspecified factors in some cases. The latter mostly arise from an unclear understanding of the reaction mechanism. In fact, there still remain unresolved questions regarding the overall picture of organic photoredox catalysis, although the detailed mechanisms have been revealed for several specific systems:[30,31,111]

Which excited state, singlet or triplet, is in charge during photophysical processes? What is transferred from the excited-state catalyst to the substrate, i.e. energy or electron?

However, now given the feasibility to generate a myriad of organic PC candidates bearing well-predicted catalytic parameters, it has become possible to gain a deeper understanding of reaction mechanisms through an intensive analysis of the outcomes from different PCs. In particular, an in-depth photophysical exploration of the electronic state or molecular system on rather promising and widely applicable organic PCs such as **1**/**161** or **25**/**165** will be beneficial to revealing the underlying fundamentals. Again, an improved understanding of the mechanism can help design a better photocatalytic system.

Various applications, e.g. in the field of biology, have become realizable as well: Eosin Y-catalyzed PET-RAFT polymerization on cell surface[112] or switchable catalysts that can be manipulated by external stimuli more than light through the introduction of pH- or CO_2-responsive moieties.[78] These trends reflect the need to mimic complex and dynamic living systems to improve synthetic chemical processes or even to intervene in nature. For upcoming relevant applications, it is worth further reducing the potential toxicity of organic PCs by imparting biodegradability/biocompatibility or improving their catalytic performance to minimize the catalyst loading as low as possible to avoid any damage. The light absorption range also needs to be expanded because irradiation at a longer wavelength (i.e. far-red and near-infrared light) can penetrate tissue deeper and cause lower photocytotoxicity.[92,113]

In summary, the library of organic PCs has been widened along with the establishment of the design strategies. We expect this minireview on the design and application of organic PCs to serve a viewpoint for researchers intending to develop new organic PCs or utilize them for new photoredox-mediated reactions.

Acknowledgments

The work at SNU was supported by the Technology Innovation Program (20010768, Development of Fast Curing Structural Adhesive with High Performance for Dissimilar Materials on High Speed Process) funded by the Ministry of Trade, Industry & Energy and by the Ministry of Education (NRF-2019R1I1A2A01059288).

Keywords: Catalyst design · Organic photocatalysts · Photochemistry · Photoredox catalysis

[1] M. H. Shaw, J. Twilton, D. W. C. MacMillan, *J. Org. Chem.* **2016**, *81*, 6898–6926.
[2] A. G. Condie, J. C. González-Gómez, C. R. J. Stephenson, *J. Am. Chem. Soc.* **2010**, *132*, 1464–1465.
[3] D. A. Nicewicz, D. W. C. MacMillan, *Science* **2008**, *322*, 77–80.
[4] M. A. Ischay, M. E. Anzovino, J. Du, T. P. Yoon, *J. Am. Chem. Soc.* **2008**, *130*, 12886–12887.
[5] N. A. Romero, D. A. Nicewicz, *Chem. Rev.* **2016**, *116*, 10075–10166.
[6] N. Corrigan, S. Shanmugam, J. Xu, C. Boyer, *Chem. Soc. Rev.* **2016**, *45*, 6165–6212.
[7] P. Xiao, J. Zhang, F. Dumur, M. A. Tehfe, F. Morlet-Savary, B. Graff, D. Gigmes, J. P. Fouassier, J. Lalevée, *Prog. Polym. Sci.* **2015**, *41*, 32–66.
[8] J. T. Trotta, B. P. Fors, *Synlett* **2016**, *27*, 702–713.
[9] J. C. Theriot, B. G. McCarthy, C.-H. Lim, G. M. Miyake, *Macromol. Rapid Commun.* **2017**, *38*, 1700040.
[10] G. Yilmaz, Y. Yagci, *Polym. Chem.* **2018**, *9*, 1757–1762.
[11] D. A. Nicewicz, T. M. Nguyen, *ACS Catal.* **2014**, *4*, 355–360.
[12] J. Xu, S. Shanmugam, H. T. Duong, C. Boyer, *Polym. Chem.* **2015**, *6*, 5615–5624.
[13] D. P. Hari, B. König, *Chem. Commun.* **2014**, *50*, 6688–6699.
[14] V. Srivastava, P. P. Singh, *RSC Adv.* **2017**, *7*, 31377–31392.
[15] V. K. Singh, C. Yu, S. Badgujar, Y. Kim, Y. Kwon, D. Kim, J. Lee, T. Akhter, G. Thangavel, L. S. Park, J. Lee, P. C. Nandajan, R. Wannemacher, B. Milián-Medina, L. Lüer, K. S. Kim, J. Gierschner, M. S. Kwon, *Nat. Catal.* **2018**, *1*, 794–804.
[16] J. C. Theriot, C.-H. Lim, H. Yang, M. D. Ryan, C. B. Musgrave, G. M. Miyake, *Science* **2016**, *352*, 1082–1086.
[17] I. Ghosh, T. Ghosh, J. I. Bardagi, B. König, *Science* **2014**, *346*, 725–728.
[18] I. A. MacKenzie, L. Wang, N. P. R. Onuska, O. F. Williams, K. Begam, A. M. Moran, B. D. Dunietz, D. A. Nicewicz, *Nature* **2020**, *580*, 76–80.
[19] B. D. Ravetz, A. B. Pun, E. M. Churchill, D. N. Congreve, T. Rovis, L. M. Campos, *Nature* **2019**, *565*, 343–346.
[20] F. Glaser, C. Kerzig, O. S. Wenger, *Angew. Chem. Int. Ed.* **2020**, *59*, 10266–10284; *Angew. Chem.* **2020**, *132*, 10350.
[21] B. König, *Eur. J. Org. Chem.* **2017**, *2017*, 1979–1981.
[22] D. M. Arias-Rotondo, J. K. McCusker, *Chem. Soc. Rev.* **2016**, *45*, 5803–5820.
[23] L. Buzzetti, G. E. M. Crisenza, P. Melchiorre, *Angew. Chem. Int. Ed.* **2019**, *58*, 3730–3747; *Angew. Chem.* **2019**, *131*, 3768.
[24] F. Dumur, D. Gigmes, J.-P. Fouassier, J. Lalevée, *Acc. Chem. Res.* **2016**, *49*, 1980–1989.
[25] L. Marzo, S. K. Pagire, O. Reiser, B. König, *Angew. Chem. Int. Ed.* **2018**, *57*, 10034–10072; *Angew. Chem.* **2018**, *130*, 10188.
[26] T. P. Yoon, M. A. Ischay, J. Du, *Nat. Chem.* **2010**, *2*, 527–532.
[27] N. Zivic, M. Bouzrati-Zerelli, A. Kermagoret, F. Dumur, J.-P. Fouassier, D. Gigmes, J. Lalevée, *ChemCatChem* **2016**, *8*, 1617–1631.
[28] J. Kreutzer, Y. Yagci, *Polymer* **2018**, *10*, 35.
[29] E. H. Discekici, A. Anastasaki, J. Read de Alaniz, C. J. Hawker, *Macromolecules* **2018**, *51*, 7421–7434.
[30] D. Koyama, H. J. A. Dale, A. J. Orr-Ewing, *J. Am. Chem. Soc.* **2018**, *140*, 1285–1293.
[31] L. Lewis-Borrell, M. Sneha, A. Bhattacherjee, I. P. Clark, A. J. Orr-Ewing, *Chem. Sci.* **2020**, *11*, 4475–4481.
[32] K. Donabauer, M. Maity, A. L. Berger, G. S. Huff, S. Crespi, B. König, *Chem. Sci.* **2019**, *10*, 5162–5166.
[33] Q.-Y. Meng, T. E. Schirmer, A. L. Berger, K. Donabauer, B. König, *J. Am. Chem. Soc.* **2019**, *141*, 11393–11397.
[34] H. G. Roth, N. A. Romero, D. A. Nicewicz, *Synlett* **2016**, *27*, 714–723.
[35] M. Majek, A. J. von Wangelin, *Acc. Chem. Res.* **2016**, *49*, 2316–2327.
[36] M. Neumann, S. Füldner, B. König, K. Zeitler, *Angew. Chem. Int. Ed.* **2011**, *50*, 951–954; *Angew. Chem.* **2011**, *123*, 981.
[37] S. P. Pitre, C. D. McTiernan, H. Ismaili, J. C. Scaiano, *J. Am. Chem. Soc.* **2013**, *135*, 13286–13289.
[38] D. Ravelli, M. Fagnoni, *ChemCatChem* **2012**, *4*, 169–171.
[39] J. Luo, J. Zhang, *ACS Catal.* **2016**, *6*, 873–877.
[40] T.-Y. Shang, L.-H. Lu, Z. Cao, Y. Liu, W.-M. He, B. Yu, *Chem. Commun.* **2019**, *55*, 5408–5419.
[41] J. Lu, B. Pattengale, Q. Liu, S. Yang, W. Shi, S. Li, J. Huang, J. Zhang, *J. Am. Chem. Soc.* **2018**, *140*, 13719–13725.
[42] E. Speckmeier, T. G. Fischer, K. Zeitler, *J. Am. Chem. Soc.* **2018**, *140*, 15353–15365.
[43] M. Garreau, F. Le Vaillant, J. Waser, *Angew. Chem. Int. Ed.* **2019**, *58*, 8182–8186; *Angew. Chem.* **2019**, *131*, 8266.
[44] Y. Song, Y. Kim, Y. Noh, V. K. Singh, S. K. Behera, A. Abudulimu, K. Chung, R. Wannemacher, J. Gierschner, L. Lüer, M. S. Kwon, *Macromolecules* **2019**, *52*, 5538–5545.
[45] H. Uoyama, K. Goushi, K. Shizu, H. Nomura, C. Adachi, *Nature* **2012**, *492*, 234–238.
[46] F. Le Vaillant, M. Garreau, S. Nicolai, G. Gryn'ova, C. Corminboeuf, J. Waser, *Chem. Sci.* **2018**, *9*, 5883–5889.
[47] N. J. Treat, H. Sprafke, J. W. Kramer, P. G. Clark, B. E. Barton, J. Read de Alaniz, B. P. Fors, C. J. Hawker, *J. Am. Chem. Soc.* **2014**, *136*, 16096–16101.

[48] X. Pan, M. Lamson, J. Yan, K. Matyjaszewski, *ACS Macro Lett.* **2015**, *4*, 192–196.
[49] X. Pan, C. Fang, M. Fantin, N. Malhotra, W. Y. So, L. A. Peteanu, A. A. Isse, A. Gennaro, P. Liu, K. Matyjaszewski, *J. Am. Chem. Soc.* **2016**, *138*, 2411–2425.
[50] M. Chen, M. J. MacLeod, J. A. Johnson, *ACS Macro Lett.* **2015**, *4*, 566–569.
[51] M. Chen, S. Deng, Y. Gu, J. Lin, M. J. MacLeod, J. A. Johnson, *J. Am. Chem. Soc.* **2017**, *139*, 2257–2266.
[52] H. Gong, Y. Zhao, X. Shen, J. Lin, M. Chen, *Angew. Chem. Int. Ed.* **2018**, *57*, 333–337; *Angew. Chem.* **2018**, *130*, 339.
[53] Y. Zhao, H. Gong, K. Jiang, S. Yan, J. Lin, M. Chen, *Macromolecules* **2018**, *51*, 938–946.
[54] K. Jiang, S. Han, M. Ma, L. Zhang, Y. Zhao, M. Chen, *J. Am. Chem. Soc.* **2020**, *142*, 7108–7115.
[55] E. H. Discekici, N. J. Treat, S. O. Poelma, K. M. Mattson, Z. M. Hudson, Y. Luo, C. J. Hawker, J. Read de Alaniz, *Chem. Commun.* **2015**, *51*, 11705–11708.
[56] J. D. Nguyen, E. M. D'Amato, J. M. R. Narayanam, C. R. J. Stephenson, *Nat. Chem.* **2012**, *4*, 854–859.
[57] S. M. Sartor, C. H. Chrisman, R. M. Pearson, G. M. Miyake, N. H. Damrauer, *J. Phys. Chem. A* **2020**, *124*, 817–823.
[58] G. M. Miyake, J. C. Theriot, *Macromolecules* **2014**, *47*, 8255–8261.
[59] M. D. Ryan, J. C. Theriot, C.-H. Lim, H. Yang, A. G. Lockwood, N. G. Garrison, S. R. Lincoln, C. B. Musgrave, G. M. Miyake, *J. Polym. Sci., Part A* **2017**, *55*, 3017–3027.
[60] C.-H. Lim, M. D. Ryan, B. G. McCarthy, J. C. Theriot, S. M. Sartor, N. H. Damrauer, C. B. Musgrave, G. M. Miyake, *J. Am. Chem. Soc.* **2017**, *139*, 348–355.
[61] J. C. Theriot, G. M. Miyake, C. A. Boyer, *ACS Macro Lett.* **2018**, *7*, 662–666.
[62] J. P. Cole, C. R. Federico, C.-H. Lim, G. M. Miyake, *Macromolecules* **2019**, *52*, 747–754.
[63] X. Su, P. G. Jessop, M. F. Cunningham, *Macromolecules* **2019**, *52*, 6725–6733.
[64] Y. Du, R. M. Pearson, C.-H. Lim, S. M. Sartor, M. D. Ryan, H. Yang, N. H. Damrauer, G. M. Miyake, *Chem. Eur. J.* **2017**, *23*, 10962–10968.
[65] A. Tlahuext-Aca, L. Candish, R. A. Garza-Sanchez, F. Glorius, *ACS Catal.* **2018**, *8*, 1715–1719.
[66] R. M. Pearson, C.-H. Lim, B. G. McCarthy, C. B. Musgrave, G. M. Miyake, *J. Am. Chem. Soc.* **2016**, *138*, 11399–11407.
[67] B. McCarthy, G. M. Miyake, *ACS Macro Lett.* **2018**, *7*, 1016–1021.
[68] B. G. McCarthy, R. M. Pearson, C.-H. Lim, S. M. Sartor, N. H. Damrauer, G. M. Miyake, *J. Am. Chem. Soc.* **2018**, *140*, 5088–5101.
[69] G. S. Park, J. Back, E. M. Choi, E. Lee, K. Son, *Eur. Polym. J.* **2019**, *117*, 347–352.
[70] A. L. Berger, K. Donabauer, B. König, *Chem. Sci.* **2018**, *9*, 7230–7235.
[71] S. M. Sartor, B. G. McCarthy, R. M. Pearson, G. M. Miyake, N. H. Damrauer, *J. Am. Chem. Soc.* **2018**, *140*, 4778–4781.
[72] S. M. Sartor, Y. M. Lattke, B. G. McCarthy, G. M. Miyake, N. H. Damrauer, *J. Phys. Chem. A* **2019**, *123*, 4727–4736.
[73] B. L. Buss, C.-H. Lim, G. M. Miyake, *Angew. Chem. Int. Ed.* **2020**, *59*, 3209–3217; *Angew. Chem.* **2020**, *132*, 3235–3243.
[74] J. Xu, K. Jung, A. Atme, S. Shanmugam, C. Boyer, *J. Am. Chem. Soc.* **2014**, *136*, 5508–5519.
[75] J. Xu, K. Jung, N. A. Corrigan, C. Boyer, *Chem. Sci.* **2014**, *5*, 3568–3575.
[76] X. Liu, L. Zhang, Z. Cheng, X. Zhu, *Polym. Chem.* **2016**, *7*, 689–700.
[77] C. Wu, N. Corrigan, C.-H. Lim, K. Jung, J. Zhu, G. Miyake, J. Xu, C. Boyer, *Macromolecules* **2019**, *52*, 236–248.
[78] C. Wu, H. Chen, N. Corrigan, K. Jung, X. Kan, Z. Li, W. Liu, J. Xu, C. Boyer, *J. Am. Chem. Soc.* **2019**, *141*, 8207–8220.
[79] J. Yoon, Y. J. Jung, J. B. Yoon, K. Damodar, H. Kim, M. Shin, M. Seo, D. W. Cho, J. T. Lee, J. K. Lee, *Polym. Chem.* **2019**, *10*, 5737–5742.
[80] S. Fukuzumi, H. Kotani, K. Ohkubo, S. Ogo, N. V. Tkachenko, H. Lemmetyinen, *J. Am. Chem. Soc.* **2004**, *126*, 1600–1601.
[81] S. Fukuzumi, K. Ohkubo, *Org. Biomol. Chem.* **2014**, *12*, 6059–6071.
[82] K. A. Margrey, D. A. Nicewicz, *Acc. Chem. Res.* **2016**, *49*, 1997–2006.
[83] D. J. Wilger, J.-M. M. Grandjean, T. R. Lammert, D. A. Nicewicz, *Nat. Chem.* **2014**, *6*, 720–726.
[84] N. A. Romero, K. A. Margrey, N. E. Tay, D. A. Nicewicz, *Science* **2015**, *349*, 1326–1330.
[85] A. Joshi-Pangu, F. Lévesque, H. G. Roth, S. F. Oliver, L.-C. Campeau, D. Nicewicz, D. A. DiRocco, *J. Org. Chem.* **2016**, *81*, 7244–7249.
[86] A. Gini, M. Uygur, T. Rigotti, J. Alemán, O. Garcia Mancheño, *Chem. Eur. J.* **2018**, *24*, 12509–12514.
[87] A. R. White, L. Wang, D. A. Nicewicz, *Synlett* **2019**, *30*, 827–832.
[88] C. Fischer, C. Kerzig, B. Zilate, O. S. Wenger, C. Sparr, *ACS Catal.* **2020**, *10*, 210–215.
[89] B. Zilate, C. Fischer, C. Sparr, *Chem. Commun.* **2020**, *56*, 1767–1775.
[90] K. Rybicka-Jasińska, W. Shan, K. Zawada, K. M. Kadish, D. Gryko, *J. Am. Chem. Soc.* **2016**, *138*, 15451–15458.
[91] K. Rybicka-Jasińska, B. König, D. Gryko, *Eur. J. Org. Chem.* **2017**, *2017*, 2104–2107.
[92] H. Cao, G. Wang, Y. Xue, G. Yang, J. Tian, F. Liu, W. Zhang, *ACS Macro Lett.* **2019**, *8*, 616–622.
[93] J. Mateos, F. Rigodanza, A. Vega-Peñaloza, A. Sartorel, M. Natali, T. Bortolato, G. Pelosi, X. Companyó, M. Bonchio, L. Dell'Amico, *Angew. Chem. Int. Ed.* **2020**, *59*, 1302–1312; *Angew. Chem.* **2020**, *132*, 1318–1328.
[94] J. Moon, Y. K. Moon, D. D. Park, S. Choi, Y. You, E. J. Cho, *J. Org. Chem.* **2019**, *84*, 12925–12932.
[95] S. Yamaguchi, S. Akiyama, K. Tamao, *J. Am. Chem. Soc.* **2000**, *122*, 6335–6336.
[96] B. Kiskan, J. Zhang, X. Wang, M. Antonietti, Y. Yagci, *ACS Macro Lett.* **2012**, *1*, 546–549.
[97] Q. Fu, Q. Ruan, T. G. McKenzie, A. Reyhani, J. Tang, G. G. Qiao, *Macromolecules* **2017**, *50*, 7509–7516.
[98] L. Zhang, G. Ye, X. Huo, S. Xu, J. Chen, K. Matyjaszewski, *ACS Omega* **2019**, *4*, 16247–16255.
[99] I. Ghosh, J. Khamrai, A. Savateev, N. Shlapakov, M. Antonietti, B. König, *Science* **2019**, *365*, 360–366.
[100] A. Allushi, S. Jockusch, G. Yilmaz, Y. Yagci, *Macromolecules* **2016**, *49*, 7785–7792.
[101] C. Kutahya, A. Allushi, R. Isci, J. Kreutzer, T. Ozturk, G. Yilmaz, Y. Yagci, *Macromolecules* **2017**, *50*, 6903–6910.
[102] D. Liu, M.-J. Jiao, Z.-T. Feng, X.-Z. Wang, G.-Q. Xu, P.-F. Xu, *Org. Lett.* **2018**, *20*, 5700–5704.
[103] J. P. Barham, B. König, *Angew. Chem. Int. Ed.* **2020**, *59*, 11732–11747; *Angew. Chem.* **2020**, *132*, 11828–11844.
[104] H. Huang, Z. M. Strater, M. Rauch, J. Shee, T. J. Sisto, C. Nuckolls, T. H. Lambert, *Angew. Chem. Int. Ed.* **2019**, *58*, 13318–13322; *Angew. Chem.* **2019**, *131*, 2367.
[105] W. Zhang, K. L. Carpenter, S. Lin, *Angew. Chem. Int. Ed.* **2020**, *59*, 409–417; *Angew. Chem.* **2020**, *132*, 417–425.
[106] H. Kim, H. Kim, T. H. Lambert, S. Lin, *J. Am. Chem. Soc.* **2020**, *142*, 2087–2092.
[107] G. Ciamician, *Science* **1912**, *36*, 385–394.
[108] G. Pandey, S. Hajra, M. K. Ghorai, K. R. Kumar, *J. Am. Chem. Soc.* **1997**, *119*, 8777–8787.
[109] S. Fukuzumi, K. Ohkubo, T. Suenobu, K. Kato, M. Fujitsuka, O. Ito, *J. Am. Chem. Soc.* **2001**, *123*, 8459–8467.
[110] A. Bauer, F. Westkämper, S. Grimme, T. Bach, *Nature* **2005**, *436*, 1139–1140.
[111] P. Seal, J. Xu, S. De Luca, C. Boyer, S. C. Smith, *Adv. Theory Simul.* **2019**, *2*, 1900038.
[112] J. Niu, D. J. Lunn, A. Pusuluri, J. I. Yoo, M. A. O'Malley, S. Mitragotri, H. T. Soh, C. J. Hawker, *Nat. Chem.* **2017**, *9*, 537–545
[113] S. Allison-Logan, Q. Fu, Y. Sun, M. Liu, J. Xie, J. Tang, G. G. Qiao, *Angew. Chem. Int. Ed.* 10.1002/anie.202007196

Received: May 21, 2020

ACS Catalysis

pubs.acs.org/acscatalysis Research Article

Silver Sulfide Nanocrystals as a Biocompatible and Full-Spectrum Photocatalyst for Efficient Light-Driven Polymerization under Aqueous and Ambient Conditions

Changhoon Yu,[‖] Jaejung Song,[‖] Tae In Kim,[‖] Yungyeong Lee, Yonghwan Kwon, Jongkyoung Kim, Jeehun Park, Jinho Choi, Junsang Doh, Seung Kyu Min,* Seungho Cho,* and Min Sang Kwon*

Cite This: *ACS Catal.* 2023, 13, 665−680 Read Online

ACCESS | Metrics & More | Article Recommendations | Supporting Information

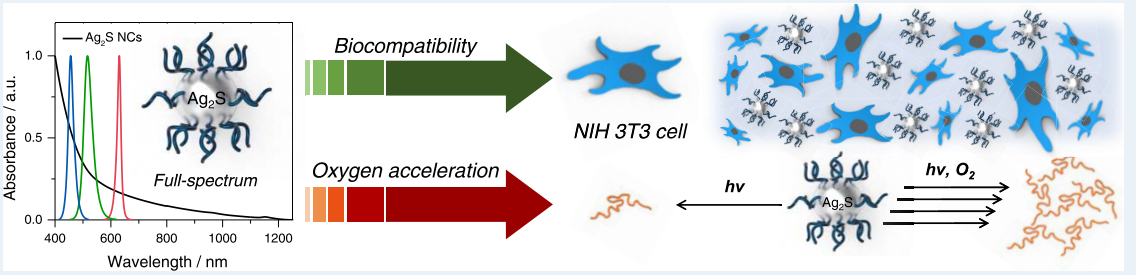

ABSTRACT: Owing to current global environmental concerns, polymers must be prepared under eco-friendly reaction conditions based on sustainable chemistry. In this context, highly efficient photoinduced energy/electron transfer reversible addition−fragmentation chain-transfer (PET-RAFT) polymerization under ambient/aqueous conditions without additives and/or with the aid of sunlight is the optimal approach for producing polymers with well-defined structures. This can be accomplished with a photocatalyst (PC) that utilizes the full spectrum of sunlight for maximum efficiency and has excellent water solubility or dispersibility, oxygen tolerance, and biocompatibility. However, a PC with all of these features has not yet been developed. In this study, we confirmed that this could be achieved using Ag_2S nanocrystals (NCs) as photocatalysts. The sufficient reducing power of Ag_2S NCs enabled the successful aqueous PET-RAFT polymerization of numerous acrylic monomers under ambient natural sunlight illumination without any additives. Under illumination, the small band gap of Ag_2S NCs suppressed the generation of singlet oxygen, resulting in low cytotoxicity toward three different cell lines. Finally, we demonstrated that PET-RAFT polymerization with Ag_2S NCs can be accomplished in biologically relevant media under natural sunlight illumination, indicating adequate biocompatibility and efficacy of the system.

KEYWORDS: *light-driven polymerization, controlled radical polymerization, photocatalysis, PET-RAFT, oxygen acceleration*

INTRODUCTION

The incorporation of photochemistry into controlled radical polymerization (CRP) enables the synthesis of polymers with well-defined structures under mild reaction conditions and spatiotemporal control.[1−4] In the past few years, numerous photomediated CRP (photo-CRP) methods have been proposed and studied.[5−9] Due to its mild reaction conditions, oxygen tolerance, and compatibility with other polymerization techniques, photoinduced energy/electron transfer reversible addition−fragmentation chain-transfer (PET-RAFT), which was first reported by Boyer et al.,[10] has emerged as a promising tool.[11−14] In contrast to conventional CRP techniques, the current approach allows the incorporation of photo-CRP into applications such as biological systems[6,15] and living additive manufacturing.[16−19]

From a fundamental standpoint, the PET-RAFT method can be regarded as an extension of the conventional RAFT procedure. Because PET-RAFT uses a photocatalyst (PC) as an energy and/or electron transfer source for radical generation, it does not require an external initiator and heat as an energy source to drive polymerization.[2,10−13,20,21] In contrast to conventional radical initiators, PCs exhibit great diversity in their materials and structures, making it possible to tailor their properties to a wide variety of conditions.[2,13,20,22,23] This implies that the successful polymerization of a variety of monomers under the desired reaction conditions could be achieved using the proper PC.

Received: September 22, 2022
Revised: December 12, 2022
Published: December 22, 2022

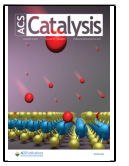

https://doi.org/10.1021/acscatal.2c04684
ACS Catal. 2023, 13, 665−680

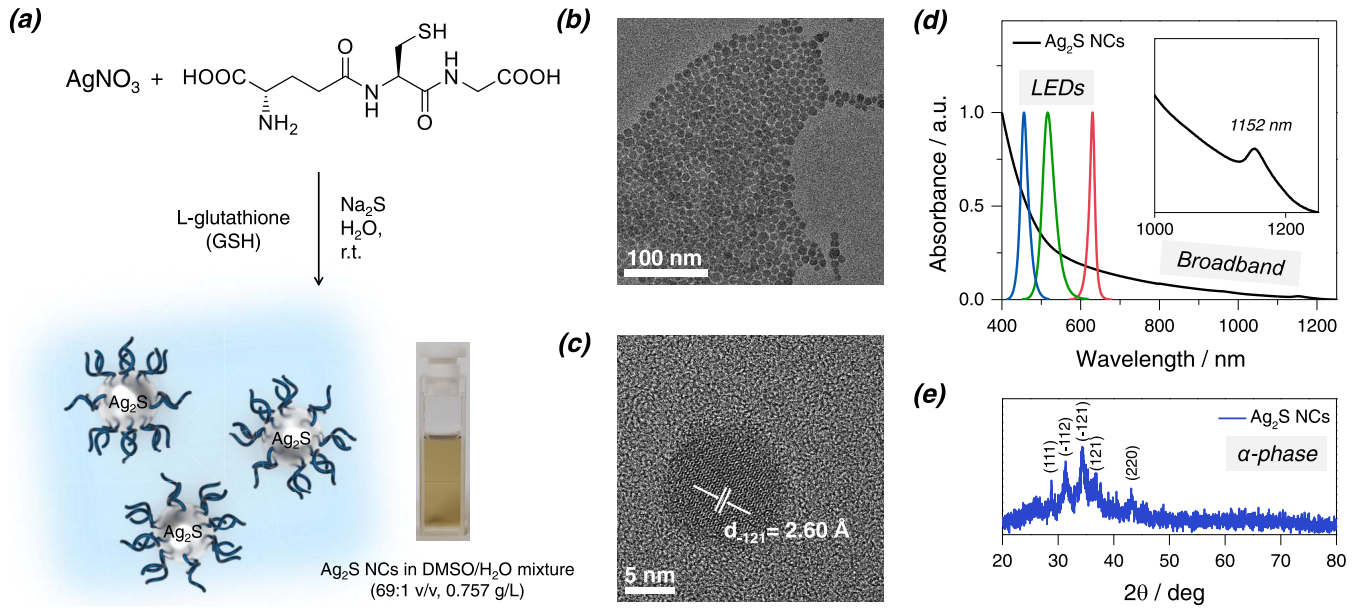

Figure 1. (a) Synthesis of Ag_2S NCs. (b) TEM image of Ag_2S NCs. (c) HRTEM image of a single Ag_2S NC. (d) UV−vis−NIR absorption spectrum of Ag_2S NCs (black line) and normalized emission spectrum of the excitation light sources (blue, green, and red lines). (e) Powder XRD patterns of the as-prepared Ag_2S NCs.

Table 1. Chemical Structures and Photochemical and Electrochemical Properties of (Single-Monomer-Inserted) RAFT Agents and Ag_2S NCs

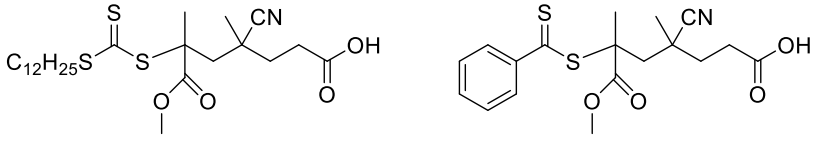

CDTPA−MMA ***CPADB−MMA***

entry	E^0_{red} (exp., onset), V	E^0_{red} (calc.), V	λ_{abs} (exp., onset), nm	$E_{00}(S_1)$ (exp., onset), eV	$E_{adia}(S_1)$ (calc.), eV	$E_{adia}(T_1)$ (calc.), eV
CDTPA	−0.78	−0.98	524	2.37	2.13	1.85
CDTPA−MMA		−1.00	519	2.39	2.11	1.82
CPADB	−0.65	−0.75	597	2.08	2.21	1.66
CPADB−MMA		−0.73	588	2.11	2.23	1.59

entry	IP (eV)	EA (eV)	E^0_{ox} (V)	E^*_{ox} (V)	λ_{abs} (nm) (onset)	E_g (eV)
Ag_2S nanocrystal (α-phase)	4.66	3.60	0.28	−0.78	1198	0.97

Recently, concerns regarding the life cycle of polymers, including raw materials for polymer production, energy sources, and end-of-life treatment, have been growing as a result of current global environmental issues.[24] Ideally, polymerization, which comprises the first step in the polymer life cycle, should be based on green chemistry and conducted under environmentally friendly reaction conditions. In accordance with the principles of green chemistry,[25−27] the ideal polymerization process would be a catalytic reaction for the quantitative conversion of monomers into polymers with maximum atom economy and minimum waste. Furthermore, these reactions should be conducted in an aqueous environment using a sustainable energy source. In this regard, highly efficient PET-RAFT polymerization performed under ambient and aqueous conditions without additives and driven by natural sunlight is an ideal approach to prepare polymers with well-defined structures.

PET-RAFT polymerization satisfying the aforementioned criteria can be accomplished by utilizing a PC that (i) covers the entire visible-light spectrum for high efficiency, (ii) has adequate water solubility or dispersibility, (iii) imparts oxygen tolerance without the use of additives, and (iv) demonstrates excellent biocompatibility under illumination. However, developing such a PC is technically difficult, and no such catalyst has been reported. Qiao et al., for instance, described a microsized rod-like PC prepared by the self-assembly of carboxy-phenol porphyrins (i.e., SA-TCPP) for aqueous PET-RAFT polymerization.[28] Although SA-TCPP exhibited full-spectrum absorption, water dispersity, and oxygen tolerance, it required a large amount of a sacrificial reducing agent (triethanolamine). Additionally, the biocompatibility of the catalyst was not adequately tested. Several xanthene-based dyes (e.g., Eosin Y) have also been reported as a PC for aqueous PET-RAFT polymerization. In an aqueous environment, they exhibited adequate catalytic activity for a variety of monomers.[29] For oxygen tolerance, however, they required significant amounts of sacrificial reducing agents, such as tertiary amines and ascorbic acid, and did not exhibit full-spectrum absorption. More examples of previously reported

https://doi.org/10.1021/acscatal.2c04684
ACS Catal. 2023, 13, 665−680

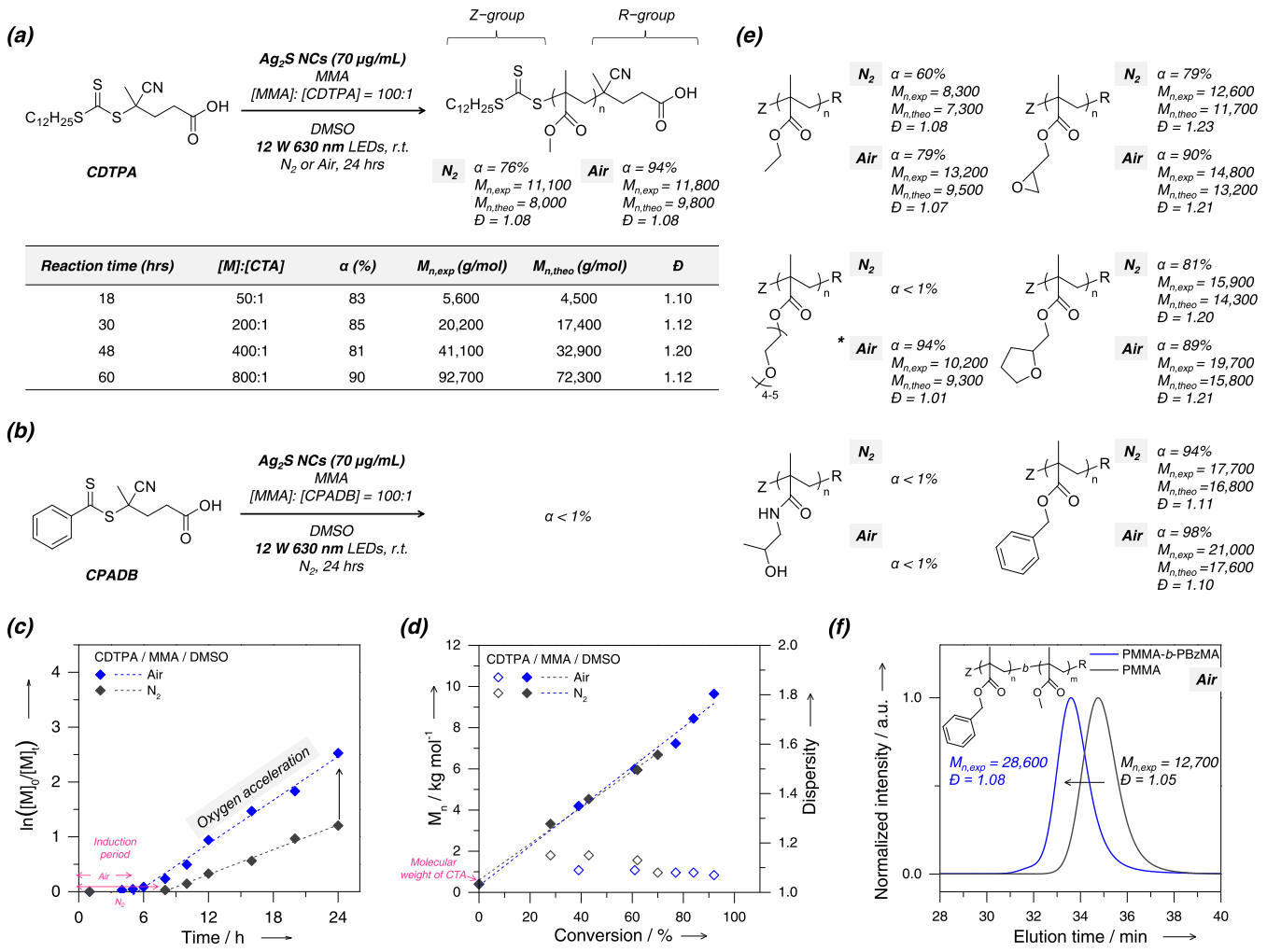

Reaction time (hrs)	[M]:[CTA]	α (%)	$M_{n,exp}$ (g/mol)	$M_{n,theo}$ (g/mol)	Đ
18	50:1	83	5,600	4,500	1.10
30	200:1	85	20,200	17,400	1.12
48	400:1	81	41,100	32,900	1.20
60	800:1	90	92,700	72,300	1.12

Figure 2. Results of PET-RAFT polymerizations of MMA using Ag_2S NCs in the presence of (a) CDTPA and (b) CPADB in DMSO under 12 W 630 nm irradiations (ca. 20 mW/cm^2). Kinetic plots for PET-RAFT polymerizations of MMA using Ag_2S NCs (70 μg/mL) under N_2 and air with 12 W 630 nm LED illuminations: (c) $\ln([M]_0/[M]_t)$ versus reaction time, (d) M_n (filled) and dispersity (empty) versus conversion. (e) Results of PET-RAFT polymerizations of various methacrylic monomers. (f) GPC traces of PMMA (black) and PMMA-b-PBzMA (blue). *Targeted degree of polymerization is 30.

Scheme 1. Multiple Mechanistic Pathways under PET-RAFT Conditions[a]

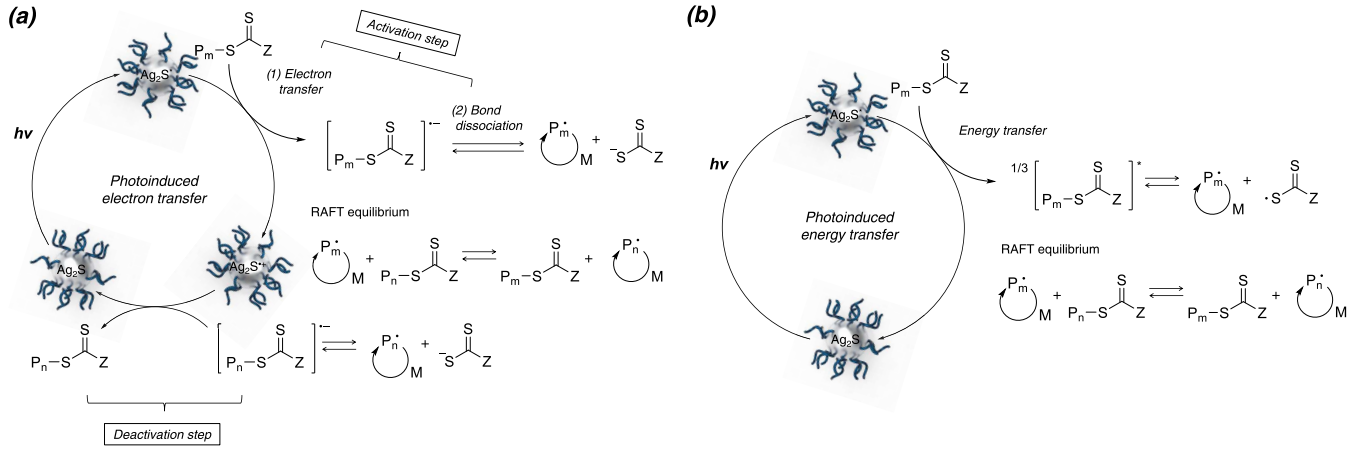

[a]Pathway for (a) photoinduced electron transfer and (b) photoinduced energy transfer.

PC systems for PET-RAFT polymerizations that satisfy either of those requirements are summarized in Figure S1.[18,30−52]

Herein, we present Ag_2S nanocrystals (NCs) as full-spectrum biocompatible PCs for efficient PET-RAFT polymerization in ambient and aqueous environments. The full-

https://doi.org/10.1021/acscatal.2c04684
ACS Catal. 2023, 13, 665−680

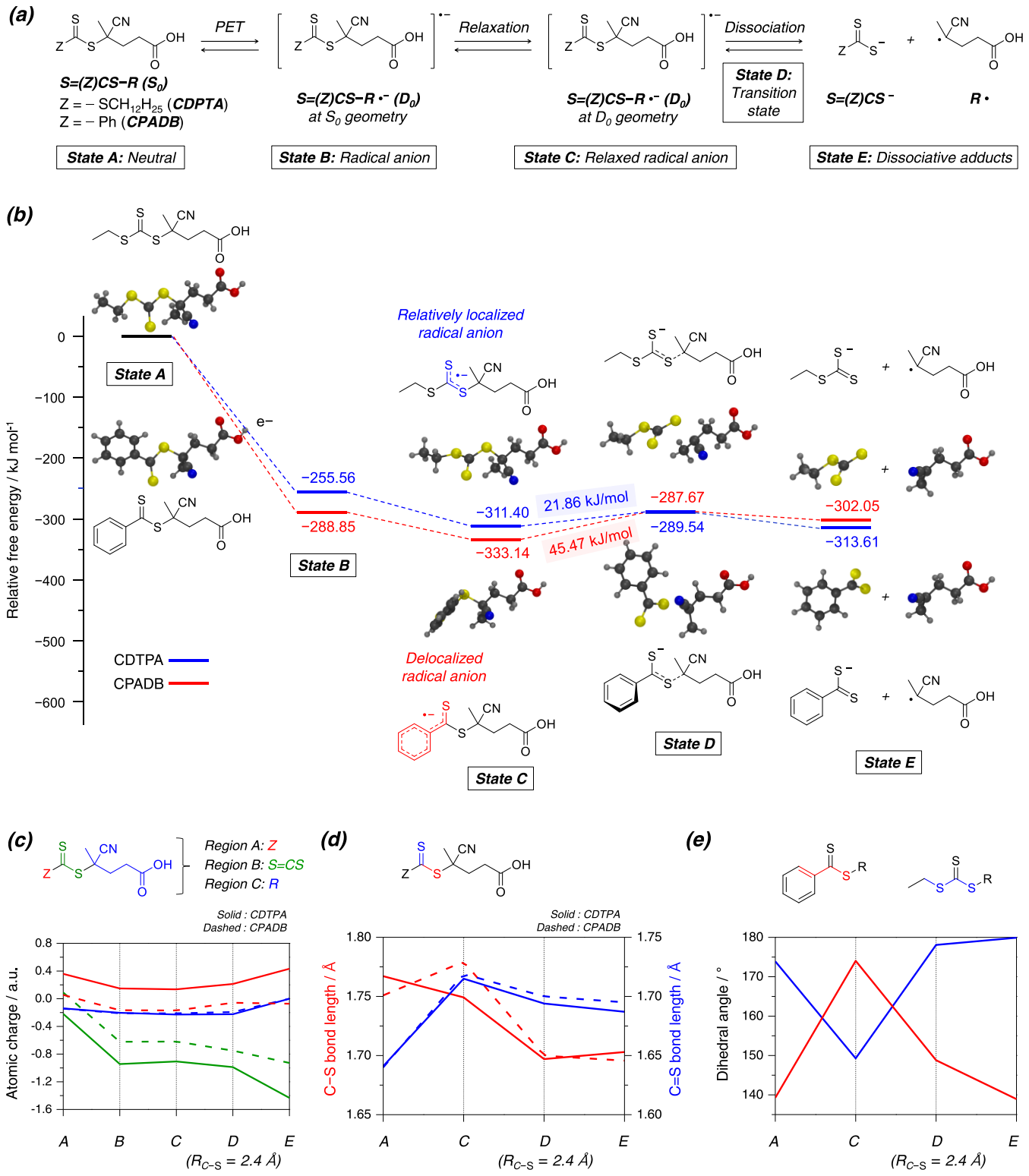

Figure 3. (a) Stepwise DET pathway with four consecutive steps. (b) Calculated free-energy profiles for the stepwise DET of CDTPA (blue) and CPADB (red). (c) Atomic charges for three different regions (Z, S═C−S, and R; indicated with red, green, and blue, respectively) in CDTPA and its intermediates (solid lines) and for CPADB and its intermediates (dashed lines). (d) C−S (red) and C═S (blue) bond lengths of CDTPA and its intermediates (solid lines) and of CPADB and its intermediates (dashed lines). (e) Dihedral angles of CDTPA and its intermediates (blue line) and of CPADB and its intermediates (red line).

spectrum absorption and sufficient reducing power of Ag_2S NCs enabled the additive-free aqueous PET-RAFT polymerization of a variety of acrylic monomers under blue, green, red, and natural sunlight. Even under illumination, the small band gap of Ag_2S NCs prevented the formation of singlet oxygen, resulting in low cytotoxicity to human cells. Confirming the biocompatibility and efficacy of the system, we demonstrated that PET-RAFT polymerization using Ag_2S NCs could be

https://doi.org/10.1021/acscatal.2c04684
ACS Catal. 2023, 13, 665−680

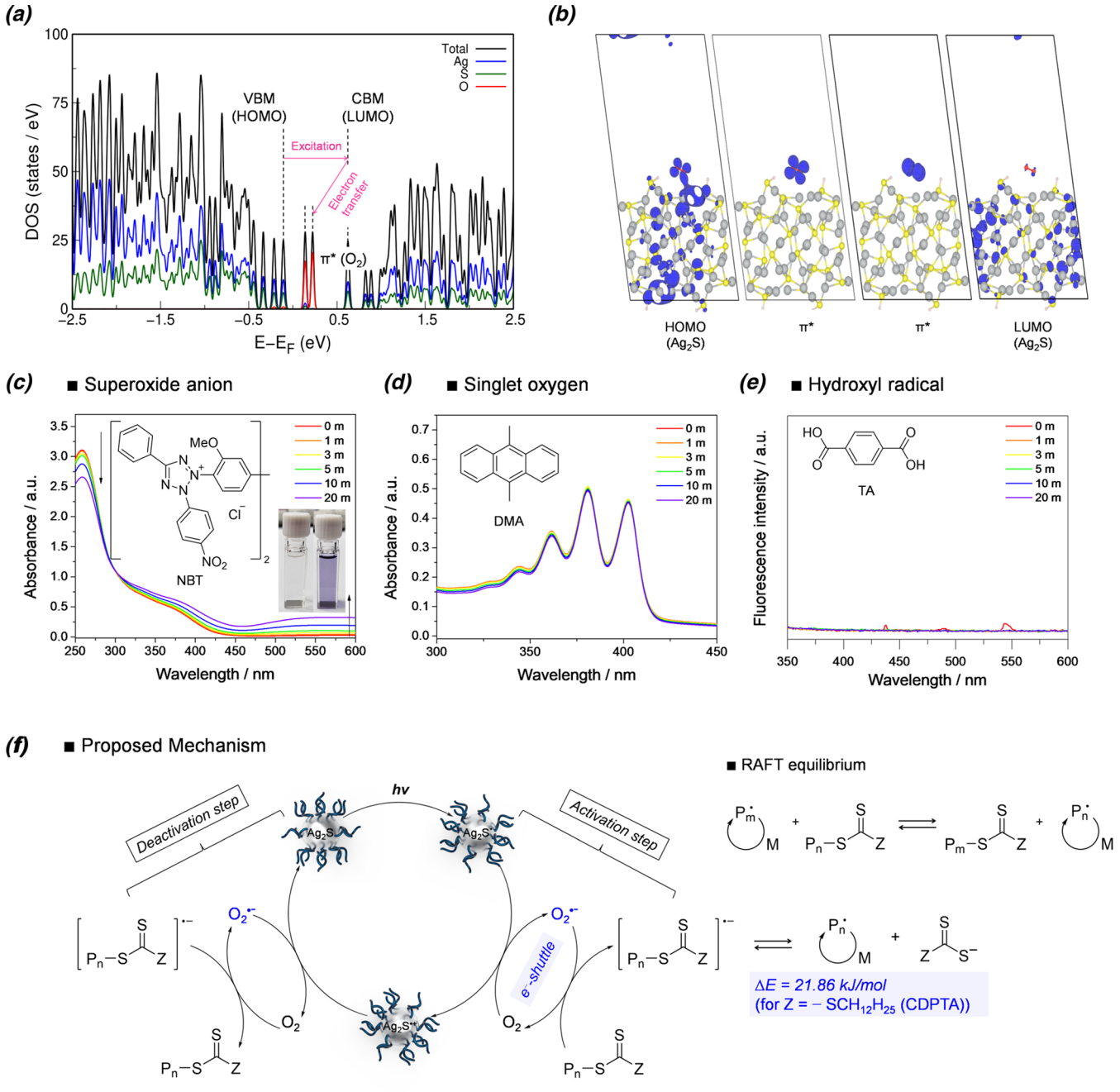

Figure 4. (a) Density of states for down spin, (b) squared Kohn–Sham orbitals, (c) UV–vis spectrum for superoxide anion detection using NBT (50 μM) and Ag_2S NCs (350 μg/mL) under 515 nm irradiation (ca. 5 mw/cm^2) at water. (d) UV–vis spectrum for singlet oxygen detection using DMA (50 μM) and Ag_2S NCs (350 μg/mL) under 515 nm irradiation (ca. 5 mw/cm^2) at DMSO. (e) PL spectrum for hydroxyl radical detection using TA (50 μM) and Ag_2S NCs (350 μg/mL) under 515 nm irradiation (ca. 5 mw/cm^2) at DMSO/water (75/1: v/v). (f) Proposed mechanism of oxygen-mediated PET-RAFT polymerization.

accomplished in biologically relevant media under natural sunlight illumination. In addition, we discovered that the Ag_2S NC-mediated PET-RAFT polymerization was driven solely by an electron transfer process due to its unusual electronic structure; this resulted in unanticipated reaction patterns based on the combination of the excitation light wavelength, monomer, and RAFT agent and accompanied by unorthodox "oxygen-acceleration" behavior. Experiments and quantum chemical (QC) calculations suggested that radical anion intermediates produced by photoinduced electron transfer play a crucial role in the observed unusual reaction patterns and oxygen-acceleration behavior. These findings contribute to a better understanding of the electron transfer pathway of PET-RAFT.

■ RESULTS AND DISCUSSION

Design Strategy. Due to their small band gap, the majority of PCs that absorb light in the low-energy region of the visible spectrum exhibit low reducing power and low triplet energy, resulting in slow electron/energy transfer between the PC and RAFT agent and, consequently, low efficiency for PET-RAFT. Such PCs typically have insufficient triplet energy (ΔE > 1.5

https://doi.org/10.1021/acscatal.2c04684
ACS Catal. 2023, 13, 665–680

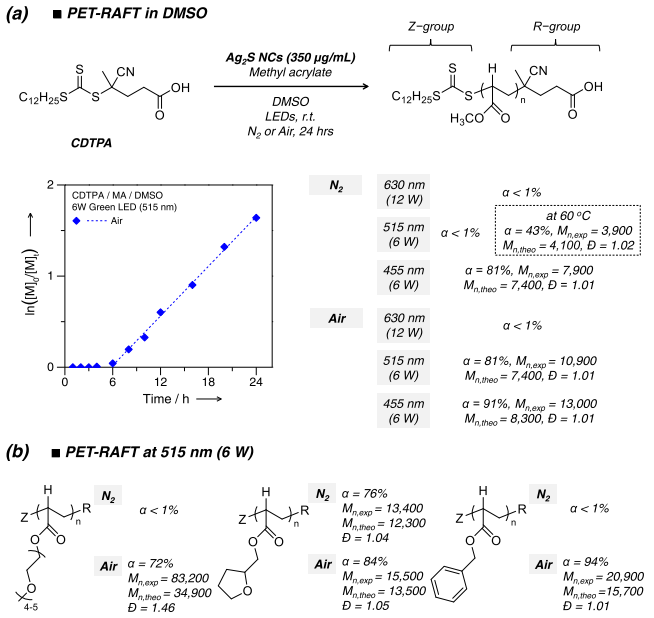

Figure 5. (a) PET-RAFT polymerizations of MA using Ag_2S NCs (350 μg/mL) in the presence of CDTPA in DMSO at r.t. and elevated temperature. Kinetic plots for the PET-RAFT polymerization of MA under air using Ag_2S NCs: $\ln([M]_0/[M]_t)$ versus reaction time (left) and summary of the PET-RAFT polymerizations of MA under various excitation lights (ca. 20 mW/cm^2 at 12 W 630 nm, ca. 5 mW/cm^2 at 6 W 515 and 455 nm) and atmospheres (right). (b) Results of the PET-RAFT polymerizations of various acrylic monomers using Ag_2S NCs (350 μg/mL) in DMSO under 515 nm irradiation conditions.

eV) to activate RAFT agents; however, they have sufficient energy to generate singlet oxygen ($^1O_2$) with extremely high cytotoxicity, which could significantly reduce biocompatibility under light illumination. To achieve sufficient reactivity and biocompatibility under illumination, a PC should have both sufficiently high reducing power to activate the RAFT agent by electron transfer [E_{ox}* (PC) < −0.8 V versus saturated calomel electrode (SCE)] and extremely low triplet energy (ΔE < 1.0 eV) to prevent the production of $^1O_2$.

Due to their near-infrared (NIR) photoluminescence (PL) in the NIR-II spectral range (in the region of 1000−1700 nm) and adequate biocompatibility, silver sulfide nanocrystals (Ag_2S NCs) have recently attracted considerable interest as bioimaging probes. According to recent reports, Ag_2S NCs have remarkable potential as PCs for hydrogen production and contaminant treatment owing to their broadband light-harvesting properties.[53−55] Particularly, Ag_2S NCs are known to have high reducing power despite their very small band gap,[56,57] which could facilitate electron transfer between the PC and RAFT agents without the need for a sacrificial reducing agent and suppress $^1O_2$ generation, allowing for sufficient reactivity and adequate biocompatibility. Thus, we hypothesized that the narrow band gap, negligible toxicity, and high water dispersibility of Ag_2S NCs would make them an ideal full-spectrum PC for efficient and environmentally friendly PET-RAFT polymerization.

Preparation and Characterization of Ag_2S NCs. We prepared Ag_2S NCs by modifying a previously reported eco-friendly procedure (Figure 1a).[58−60] As depicted in Figures 1b and S2, the as-prepared Ag_2S NCs were predominately monodispersed and 8.74 ± 0.92 nm in size. In the high-resolution transmission electron microscopy (TEM) image of Figure 1c, lattice fringes corresponding to an interplanar distance of 2.60 Å [$(\bar{1}21)$ d-spacing of the monoclinic acanthite structure, space group $P21/c$] can be observed, indicating a high degree of crystallinity of the synthesized NCs. X-ray diffraction was used to further investigate the crystalline nature of the NCs (XRD). Consistent with the observed lattice fringes, the Ag_2S structure was identified as monoclinic acanthite (α-phase) based on the XRD pattern (Figure 1e). The broadening of the XRD peaks suggests that the samples have a nanocrystalline morphology. The well-dispersed and well-ordered two-dimensional arrangement of the Ag_2S NCs indicated that the capping ligands (i.e., glutathione) remained predominantly on the surface of the crystals (Figure 1a). The ultraviolet−visible−near-infrared (UV−vis−NIR) spectroscopy confirmed the colloidal stability of the Ag_2S NCs and the absence of aggregates even after 1 week in ambient aqueous conditions. The negligible change in UV−vis−NIR spectra after exposure to 630 nm light illuminations for an hour also supported the high photostability of Ag_2S NCs (Figure S3). The successful synthesis of Ag_2S NCs with a Ag/S atomic ratio of 1.81:1 was also confirmed by energy-dispersive X-ray spectroscopy (Figure S4).

The UV−vis−NIR absorption spectrum of a colloidal solution of Ag_2S NCs in dimethyl sulfoxide (DMSO) revealed a broad, continuous absorption band throughout the entire visible spectrum and in the NIR region (Figure 1d). The absorption spectrum of Ag_2S NC allowed us to estimate an optical band gap of ∼0.97 eV through a Tauc plot (Figure S5), which is consistent with the previously reported optical band gap of similarly sized Ag_2S NCs.[53] The presence of indirect electronic transition in Ag_2S NCs can suppress radiative recombination within the direct band gap.[61−63] Based on the estimated band gap and reported electron affinity of the Ag_2S NCs (∼3.60 eV),[64] we have summarized the key parameters of the Ag_2S PC in Table 1, including the ionization potential and ground-/excited-state oxidation potential. As anticipated, Ag_2S NCs exhibited adequate reducing power (E_{ox}* = −0.78 V versus SCE) and a small band gap (∼0.97 eV), ensuring adequate reactivity and biocompatibility.

Ag_2S NC-Mediated PET-RAFT Polymerization of Methyl Methacrylate in DMSO under Red-Light Illumination. The broad-spectrum light absorption of Ag_2S allowed us to examine its catalytic performance during PET-RAFT polymerization under blue-, green-, and red-light illumination. We investigated Ag_2S NC-mediated PET-RAFT polymerization under red-light illumination because most previously reported PCs exhibited the lowest activity under red-light illumination. To compare the catalytic activity of Ag_2S NCs with those of previously reported systems, we selected the most commonly used monomers and solvents for PET-RAFT polymerization: methyl methacrylate (MMA) and dimethyl sulfoxide (DMSO). Without agglomeration, the Ag_2S NCs were uniformly dispersed under polymerization conditions. As a negative control, MMA polymerization was conducted in the absence of a PC under the illumination of 12 W light-emitting diodes (LEDs) emitting at 630 nm (irradiance of ∼20 mW/cm^2) in a nitrogen (N_2) atmosphere. There was no polymerization even after 48 h of continuous illumination in the absence of Ag_2S NCs. This indicates that, under the selected reaction conditions, the RAFT agents did not produce radicals (i.e., CDTPA and CPADB, see Figure 2a,b for the structure of the RAFT agents). In actuality, CDTPA and

https://doi.org/10.1021/acscatal.2c04684
ACS Catal. 2023, 13, 665−680

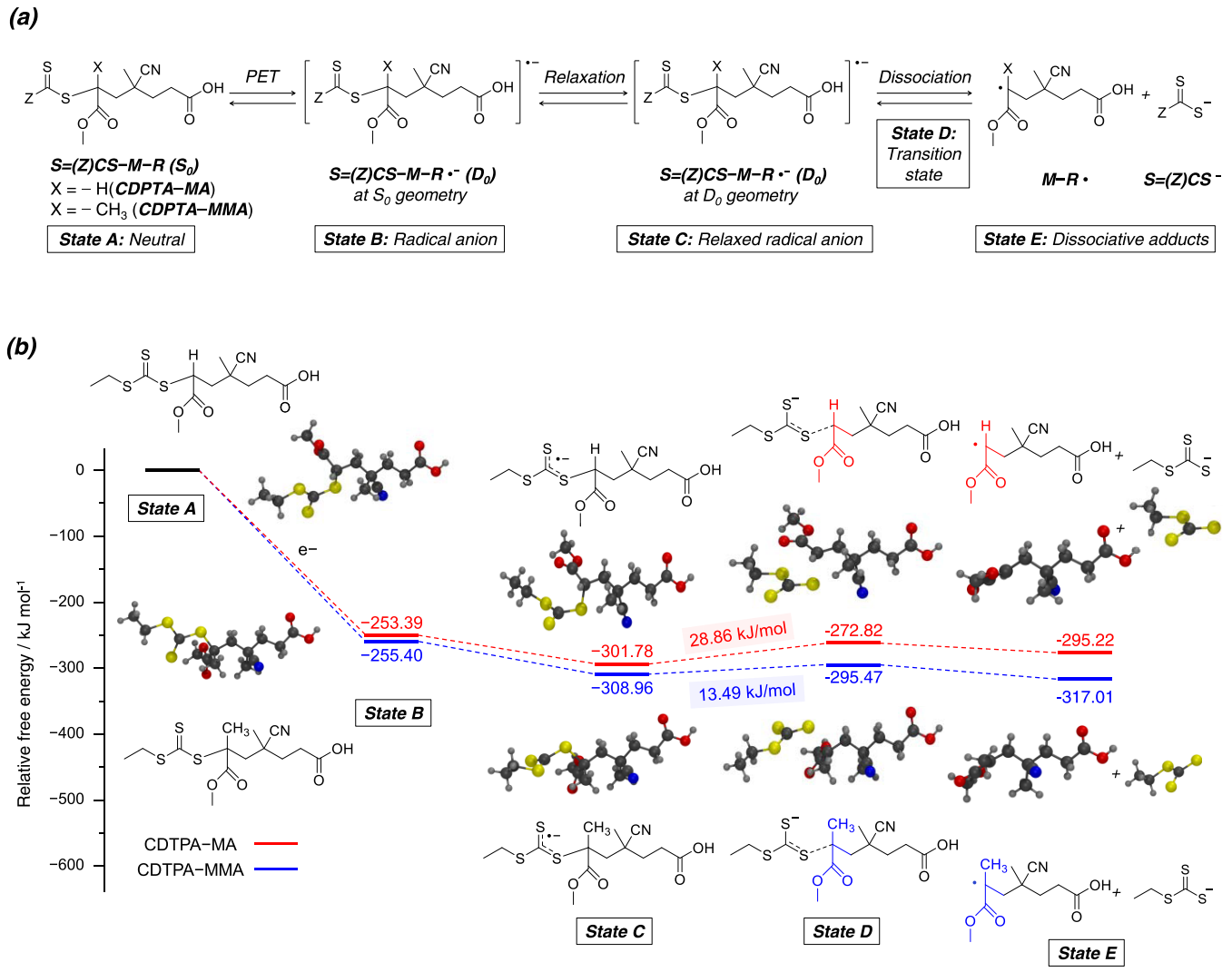

Figure 6. (a) Stepwise DET pathway with four consecutive steps. (b) Calculated free-energy profiles for the stepwise DET of CDTPA−MMA (blue) and CDTPA−MA (red).

CPADB do not absorb light at wavelengths > 600 nm (Figure S6) and therefore cannot function as iniferters under such illumination. Previous research has demonstrated the successful light-driven polymerization of various (meth)acrylic monomers under UV, blue, and green LED illumination even in the absence of a PC.[65−67]

Figure 2a summarize the outcomes of PET-RAFT of MMA performed with Ag_2S NCs as the PC and CDTPA as the RAFT agent. MMA polymerization in the presence of CDTPA under degassed conditions led to excellent control over the polymerization reaction evidenced by a narrow dispersity ($Đ$ = 1.08) and high conversion (α) of 76%; this result was highly reproducible and reliable (Table S1). The number average molecular weight (M_n) of poly(methyl methacrylate) (PMMA) was also well-controlled between 5.6 and 93 kg/mol, with narrow molecular weight distribution ($Đ$ < 1.20) and favorable conversion. Polymerization kinetics was monitored by ^{1}H NMR and gel-permeation chromatography (GPC) under 12 W 630 nm illumination conditions (black squares in Figure 2c,d). The living nature of the polymerization process is supported by the linear relationship between the monomer conversion and exposure time and between M_n and conversion. In addition, after 30 h of polymerization, the distinct chemical shifts of the trithiocarbonate functional group observed by ^{1}H NMR at 3.20−3.30 ppm and the absence of byproducts or side products confirm the high end-group fidelities of the polymers (Figure S7). Matrix-assisted laser desorption ionization time-of-flight (MALDI-TOF) analysis of the purified PMMA product confirmed the high end-group retention, and GPC recorded by refractive index (RI), light scattering (LS), and UV at 235 and 310 nm were precisely superimposed (Figure S8b−d). To confirm that Ag_2S NCs retained their catalytic performance following polymerization, *in situ* one-pot chain extension was conducted by sequentially adding a new MMA monomer. As depicted in Figure S8e, the successful chain extension experiment resulted in the production of a block copolymer in a single pot, indicating that the catalytic activity of Ag_2S NCs was maintained even after polymerization was complete. In addition, "ON/OFF" light experiments confirmed that the polymerization reaction can be controlled temporally (Figure S9). Polymerizations of a variety of methacrylic and methacrylamide monomers were also successful, confirming the excellent catalytic performance of Ag_2S NCs under low-energy light illumination (Figure 2e). Using CPADB, we also performed PET-RAFT polymerization of MMA (Figure 2b). Even after 24 h of continuous illumination, polymerization did

https://doi.org/10.1021/acscatal.2c04684
ACS Catal. 2023, 13, 665−680

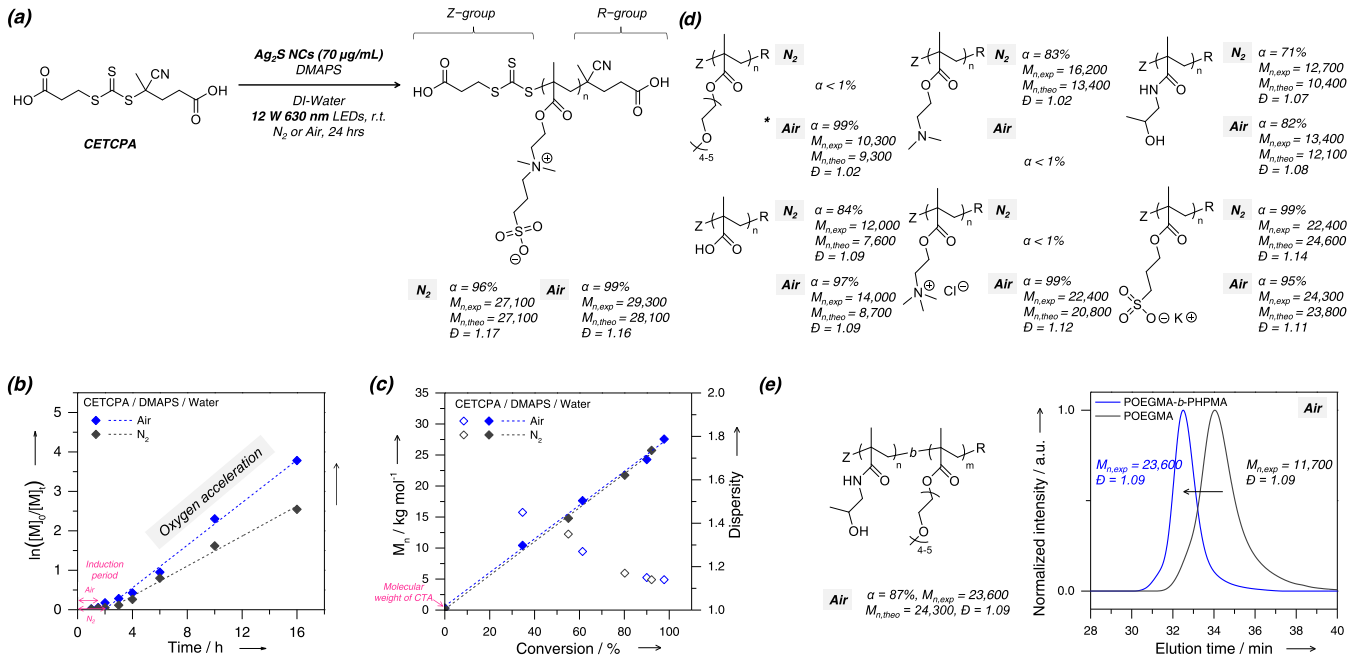

Figure 7. (a) Results of PET-RAFT polymerizations of MMA using Ag_2S NCs (70 μg/mL) in the presence of CETCPA in DI water under 12 W 630 nm irradiations (ca. 20 mW/cm^2). (b, c) Kinetic plots for PET-RAFT polymerizations of MMA using Ag_2S NCs (70 μg/mL) under N_2 and air with 12 W 630 nm LED illuminations. $\ln([M]_0/[M]_t)$ versus reaction time (b), M_n (filled) and dispersity (empty) versus conversion (c). (d) Results of aqueous PET-RAFT polymerizations of various methacrylic monomers. (e) GPC traces of POEGMA (black) and POEGMA-b-PHPMA (blue). *Targeted degree of polymerization is 30.

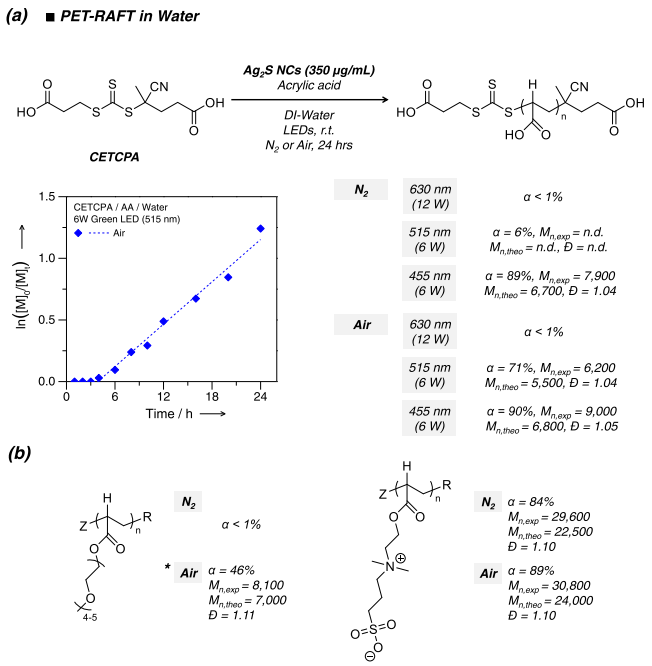

Figure 8. (a) PET-RAFT polymerizations of AA using Ag_2S NCs (350 μg/mL) in the presence of CETCPA in DI-water. Kinetic plots for PET-RAFT polymerization of AA under air using Ag_2S NCs under 6 W 515 nm LED irradiation conditions: $\ln([M]_0/[M]_t)$ versus the reaction time (left) and summary of the PET-RAFT polymerizations of MA under various excitation lights and atmospheres (right). (b) Results of the PET-RAFT polymerizations of various acrylic monomers using Ag_2S NCs (350 μg/mL) in DI-water under 515 nm irradiation conditions.

not occur, as confirmed by the lack of changes in the ^{1}H NMR spectra after polymerization (Figure S10). This result was unexpected because, as shown in Table 1, CPADB is predicted to be more oxidizing than CDTPA based on their ground-state reduction potentials.

To investigate the oxygen tolerance of the system, MMA polymerization was conducted under optimized conditions without degassing (Figure 2a). Unexpectedly, the polymerization resulted in a higher conversion of 94% with excellent control ($Đ$ = 1.08) compared to the conversion attained under inert conditions (α = 76%). This result differs from the generally observed oxygen tolerance behavior during PET-RAFT polymerization.[68] Compared to those observed with polymerization under inert conditions, the kinetics experiment without degassing revealed a shorter inhibition period and a higher apparent rate constant of propagation ($k_{p,app}$) denoted by the blue squares in Figure 2c,d. These findings indicate that the PET-RAFT activation step was accelerated in the presence of oxygen (Scheme 1a). This "oxygen-acceleration" behavior was also observed for other types of methacrylic monomers; however, oligo(ethylene glycol) methyl ether methacrylate (OEGMA) exhibited it most notably, as depicted in Figure 2e. It is worth noting that "oxygen-acceleration" behavior was recently reported by Boyer et al. and Kwon et al.[69,70] Without degassing and with excellent conversion and polymerization control (α = 97%, M_n = 28 600, $Đ$ = 1.08), block copolymer synthesis (PMMA-*b*-PBzMA) was accomplished, confirming the high vitality of the reaction under those conditions (Figure 2f).

Mechanism of Ag_2S NC-Mediated PET-RAFT Polymerization under Red-Light Illumination. Before expanding our investigation to aqueous conditions, illumination at different wavelengths, and use of different monomers, we conducted mechanistic studies to comprehend the origin of the unconventional RAFT agent selectivity of Ag_2S NCs and "oxygen-acceleration" behavior.

https://doi.org/10.1021/acscatal.2c04684
ACS Catal. 2023, 13, 665−680

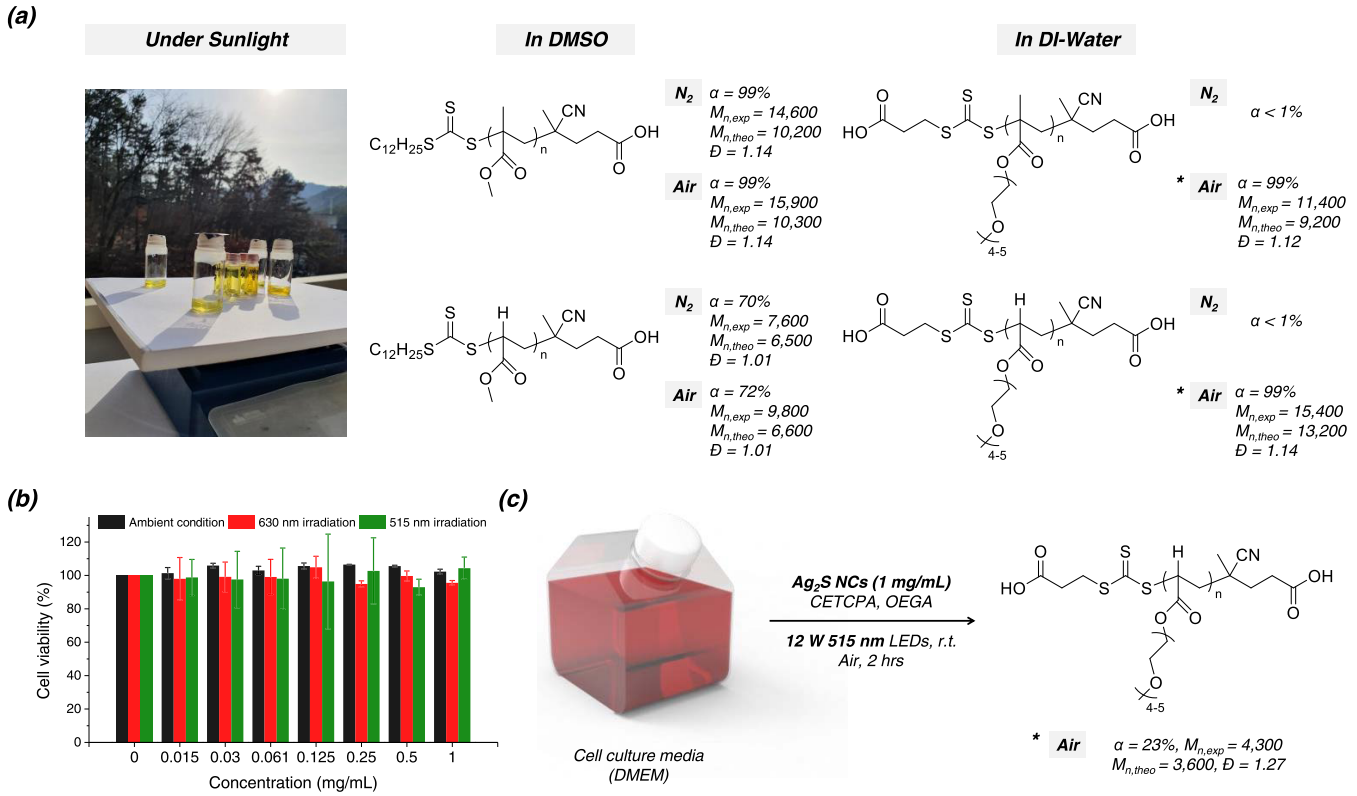

Figure 9. (a) Natural sunlight-driven PET-RAFT polymerization using Ag_2S NCs (350 μg/mL). (b) Cell viability assay of NIH 3T3 cells incubated with varying concentrations of Ag_2S NCs under ambient, 630 nm (24 h) and 515 nm irradiation (3 h). (c) Reaction scheme and result of PET-RAFT polymerization of OEGA using Ag_2S NCs in the cell culture media. *Target degree of polymerization is 30.

On the basis of an unambiguous mechanistic understanding of the PET-RAFT process, these phenomena can be understood. Nevertheless, despite recent intensive research on PET-RAFT,[13,14,71] the reaction mechanism remains unclear because it can involve multiple competing pathways, making investigations fundamentally challenging.[12,72,73] As depicted in Scheme 1a, one such pathway involves the transfer of electrons from an excited-state catalyst to a ground-state RAFT agent, resulting in the formation of an anionic intermediate, which then undergoes fragmentation to provide a propagating radical and anionic thiocarbonylthio (TCT) group. Photoinduced energy transfer is an alternative pathway wherein energy is transferred from an excited-state catalyst to a RAFT agent to excite the latter to an electronically excited state (Scheme 1b); Dexter energy transfer is considered to be of predominant relevance in this case.[74] Through the homolytic C−S bond cleavage of the resulting intermediate, active, propagating radicals are then produced. Direct photolysis of the RAFT agent can also occur under PET-RAFT conditions. The direct visible-light absorption by the RAFT agent, attributed to the n → π^* transition of the TCT moiety,[65] excites the agent to an excited state, which is followed by homolysis of the C−S bond to produce an active propagating radical (Figure S11).

As the RAFT agents, responsible for both initiation and chain-transfer processes, have relatively high oxidizing powers (and thereby less negative ground-state reduction potentials, $-0.8\ V < E^0_{red} < -0.4\ V$), low triplet energies ($1.5\ eV < E_{00}(T_1) < 1.8\ eV$), and visible-light absorption ($400\ nm < \lambda_{onset} < 600\ nm$) (see Table 1), most visible-light-absorbing PCs can induce polymerization through all of the aforementioned pathways, which considerably limits the understanding of the precise mechanism, even for systems using well-known photocatalysts such as $Ir(ppy)_3$ and $Ru(bpy)_3$, as recently reported by Boyer and Allonas[71,75] and Konkolewicz,[76] respectively; the ground-state reduction potentials, triplet energies, and absorption onsets of the selected RAFT agents and their single-monomer insertion adducts (i.e., CDTPA−MMA and CPADB−MMA, as described in Table 1) were evaluated either experimentally or computationally based on (time-dependent) density functional theory, (TD)DFT, as shown in Table 1. Fortunately, based on the photophysical and electrochemical properties of Ag_2S NCs shown in Table 1 and the excitation source of the 635 nm LED, the electron transfer pathway can be the only possible mechanistic pathway of PET-RAFT polymerization performed under our experimental conditions, allowing detailed studies on the unusual behaviors mentioned above.

As depicted in Figure 3a, it is assumed that the activation step of the electron transfer pathway of PET-RAFT involves stepwise dissociative electron transfer (DET).[77] In this instance, the electron transfer between the excited PC and the RAFT agent (S═(Z)CS−R) results in the formation of a radical anionic intermediate (S═(Z)CS−$R^{\bullet -}$), which proceeds via C−S bond cleavage to yield a propagating radical ($R^{\bullet}$) and an anionic TCT moiety (S═(Z)CS^-). To confirm this, the transfer coefficients (β) of CDTPA and CPADB were calculated using the difference between the peak potential (E_p) and the half-peak potential ($E_{p/2}$), as determined by cyclic voltammetry (Figure S6). The resulting values ($\beta_{CDTPA} = 0.34$ and $\beta_{CPADB} = 0.63$) are close to 0.5, and indicate that the RAFT agents react through stepwise DET and not concerted DET. In fact, the authors of a recent report by Moad et al.[78]

https://doi.org/10.1021/acscatal.2c04684
ACS Catal. 2023, 13, 665−680

also claimed that CDTPA and CPADB undergo stepwise reductive cleavage, although the reported transfer coefficients differed from our findings (β_{CDTPA} = 0.58 and β_{CPADB} = 0.66). Thus, we hypothesized that our counterintuitive observations were associated with the bond-dissociation process of the radical anion intermediate and not the initial electron transfer between the PC and the RAFT agent.

Origin of Different Reaction Patterns between PC and a RAFT Agent. We used QC modeling to better understand the cause of this peculiar RAFT agent selectivity (Figure 3). In the Supporting Information, the computational details are described. As depicted in Figure 3a, we divided the DET pathway into four consecutive steps: (i) photoinduced electron transfer from the catalyst to the RAFT agent (State A → State B), (ii) relaxation of the radical ion intermediate (State B → State C), (iii) C−S bond elongation to reach the transition state (State C → State D), and (iv) complete C−S bond cleavage (State D → State E). Thereafter, we recorded the free-energy profiles, shown in Figure 3b, along the reaction pathway. Intriguingly, the activation energies for the C−S bond dissociation of the relaxed radical anion (i.e., the energy difference between State C and State D) were determined to be 21.9 and 45.5 kJ/mol for CDTPA and CPADB, respectively, indicating that the C−S bond dissociation of the radical anion intermediate may be crucial for the observed RAFT agent selectivity of Ag_2S.

Figure 3c−e depicts the charge and structural analysis of all intermediates conducted to determine the cause of the higher energetic barrier for CPADB. The charge distribution of three distinct regions (i.e., Z, S═C−S, and R) of RAFT agents was evaluated. As shown in Figure 3c, the analysis demonstrates that, for both CDTPA and CPADB, the delivered electron prefers the S═C−S moiety over the Z group. Moreover, more charges are incurred in CDTPA than in CPADB. The bond-length analysis provided additional insight into the structural modifications occurring during dissociation (Figures 3d, S12, and S13). The C═S bond length was significantly longer in the relaxed radical anion intermediate formed by electron transfer from the catalyst than in the neutral RAFT agent. In addition, almost identical changes in the C═S bond length were observed for CDTPA and CPADB, indicating that both radical anion intermediates underwent almost identical levels of C═S bond cleavage.

The changes in the C−S bond length of the S═C−S moiety were then evaluated for both CDTPA and CPADB. A shorter C−S bond is anticipated in radical anion intermediates due to the resonance form of S═C−S with an additional electron. Although CDTPA followed this usual pattern, CPADB exhibited the opposite trend (Figure 3d). This is because, in CPADB, electron delocalization occurs at the benzene ring and C═S moiety rather than S═C−S, as the benzene ring and S═C−S are in the same plane (Figure 3e). This argument was also supported by the decrease in the C−Z bond length of the CPADB radical anion intermediate (Figure S14). In contrast, the delivered electrons in CDTPA are localized at S═C−S. In the transition state of both CDTPA and CPADB, the delivered electrons were located at S═C−S. As depicted in Figure 3e, the phenyl ring of CPADB began to rotate during bond dissociation, preventing the delocalization of electrons in the transition state. Figure S15 demonstrates that similar results were obtained from calculations for single-monomer-inserted CDTPA and CPADB (e.g., CDTPA−MMA and CPADB−MMA, respectively).

On the basis of our charge and structure analysis, we can hypothesize that the higher activation energy of (single-monomer-inserted) CPADB is due to the unique stability of the radical anion intermediate, which originates from the strong electron delocalization.[79] According to a recent report by Coelho et al.,[77] DET-RAFT of MMA in the presence of CPADB was successful at 30 °C (α = 39% and $Đ$ = 1.09), which does not correspond with our findings. The most likely cause is the excessive use of reducing agents (i.e., $Na_2S_2O_4$) in the aforementioned study, which led to a significant increase in the radical anion intermediate concentration and, consequently, in the number of radical species propagating.

Origin of the "Oxygen-Acceleration" Behavior. The "oxygen-acceleration" behavior of the Ag_2S NCs system was then investigated. Normal oxygen tolerance in PET-RAFT polymerization is accompanied by rate retardation and an increased inhibition period, suggesting a "pre-deoxygenation" mechanism. According to previous studies, reactive oxygen species (ROS) are initially generated by the PC via type I and/or type II mechanisms.[80] Subsequently, ROS are consumed by the oxidation of DMSO to dimethyl sulfone, which significantly reduces the concentration of dissolved oxygen in the reaction medium, thereby facilitating oxygen tolerance. In contrast to the normal oxygen tolerance behavior, Boyer et al. reported an oxygen-mediated reductive quenching process during PET-RAFT polymerization, where the polymerization rate was considerably enhanced in the presence of both oxygen and sacrificial reducing agents (e.g., tertiary amines) under red-NIR illumination.[69] Kwon et al. reported the "oxygen-acceleration" phenomenon during the PET-RAFT polymerization of different acrylic and acrylamide monomers in the absence of sacrificial reducing agents and the presence of the newly designed PC.[70] Both studies indicated that oxygen acts as a catalyst to facilitate the electron transfer between the PC in the excited state and the RAFT agent (Figure 4f). These recent studies and our kinetics experiments (Figure 2c) led us to hypothesize that molecular oxygen acts as an electron shuttle to speed up the activation step during PET-RAFT polymerization (Figure 4f).

Using the redox potentials of oxygen, RAFT agents, and Ag_2S NCs, we investigated the thermodynamic viability of our hypothesis. The oxygen ground-state reduction potential (E^0_{red}) was measured to be ∼−0.70 V versus SCE (at a normal ambient oxygen concentration of 20.9% v/v, Figure S6). This potential is greater than both the ground-state reduction potential of CDTPA (E^0_{red} = −0.78 V, Table 1) and the excited-state oxidation potential of Ag_2S NCs (E_{ox}* = −0.78 V, Table 1). These results indicate that the catalytic behavior of molecular oxygen is thermodynamically favorable. We performed DFT calculations to gain a deeper comprehension of the photoinduced electron transfer from Ag_2S NCs to molecular oxygen (Figures 4a,b and S16). We assumed that the oxygen molecule is adsorbed on the Ag_2S surface, where two spin-up electrons occupy the π* orbitals of the oxygen molecule to describe the ground-state configuration. Density of states (DOS) and orbital densities (squared Kohn−Sham orbitals) for spin-down electrons are depicted in Figure 4a,b, respectively. The valence band maximum (VBM) indicates that a small number of densities are distributed to molecular oxygen, whereas the oxygen molecule does not contribute to the conduction band (Figure 4a). In the ground state, the highest occupied molecular orbital (HOMO) exhibited delocalized electron densities over the Ag_2S NC and the

https://doi.org/10.1021/acscatal.2c04684
ACS Catal. 2023, 13, 665−680

oxygen molecule. The lowest unoccupied molecular orbital (LUMO) representing the conduction band minimum (CBM) of the Ag_2S NC was located primarily at the Ag_2S NC (Figure 4b). The two peaks at ~0.3 eV correspond to the π^* orbitals of the oxygen molecule, indicating that these orbitals are located between VBM and CBM. Therefore, the π^* orbitals of the oxygen molecule become energetically accessible when illuminated at 630 nm (1.97 eV). Based on the results of our QC calculations, we hypothesize that the photoinduced electron transfer from Ag_2S NC to oxygen occurs in three steps: (i) Ag_2S NC is excited by absorbing light with a wavelength of 630 nm, (ii) the excited electron is relaxed to CBM, and (iii) the electron in CBM of Ag_2S is transferred to one of the two empty π^* orbitals of the O_2 molecule (Figure S16).

To verify our hypothesis, a nitroblue tetrazolium chloride (NBT) assay was conducted to measure the production of superoxide radical anions ($O_2^{\bullet-}$), which play a crucial role in our proposed mechanism. In this assay, the tetrazolium dimer is converted by $O_2^{\bullet-}$ to bluish-purple-colored formazan (see Figures 4c and S17). After a few minutes of green (or red) LED illumination, the aqueous solution of Ag_2S NCs (350 μg/mL) and NBT (50 μM) changed the color from pale yellow to bluish purple. The UV−vis absorbance spectrum of the solution was recorded as a function of illumination time. The spectral shift corresponded to the color shift observed with the naked eye. A decrease in the absorption peak at 265 nm indicated the decomposition of the dimer, while the emergence of a new absorption peak at 490 nm indicated the formation of formazan. Additional control experiments in the absence of Ag_2S NCs revealed no color change in the solution under green (or red) LED illumination (Figure S18). Similarly, the UV−vis spectrum of the NBT solution did not change over time. The UV−vis spectrum of the Ag_2S NCs/NBT aqueous solution did not change with time in the absence of light, indicating that both the presence of Ag_2S NCs and illumination play crucial roles in the production of superoxide radical anions. To further verify the role of superoxide anions, we carried out polymerization of MMA with KO_2 as a superoxide anion source; since the solubility of KO_2 was not very good at DMSO, the polymerization proceeded in rather heterogeneous environments. Very interestingly, substantial conversions of ~40% were obtained in 24 h. The obtained polymers showed a molecular weight similar to the theoretically expected molecular weight and also substantially low dispersity, implying that the electron transfer between KO_2 and CDTPA might initiate the polymerization reaction (Figure S19).

While it has been confirmed that $O_2^{\bullet-}$ is produced under the reaction conditions, other ROS, such as singlet oxygen and hydroxyl radicals, were not formed (Figure 4d,e). The generation of hydroxyl radicals was examined using terephthalic acid (TA), which selectively reacts with hydroxyl radicals by forming 2-hydroxyterephthalic acid that exhibits a strong fluorescence peak at 425 nm (Figure 4e). For this assay, because of the poor water solubility of TA, a water−DMSO mixture (75:1, v/v) was used to prepare the solution of Ag_2S NCs (350 μg/mL) and TA (50 μM). The variation in the photoluminescence (PL) spectrum of the solution was recorded over time under green LED illumination. No fluorescence at 425 nm was observed over time, indicating that hydroxyl radicals were not produced in our reaction system. To confirm the biocompatibility of Ag_2S PC under illumination, we also examined the formation of singlet oxygen in DMSO using 9,10-dimethylanthracene (DMA), which can react with singlet oxygen by forming an endoperoxide moiety. Similar to the hydroxyl radical experiment, there was no change in the UV−vis spectrum over time under green LED illumination (Figure 4d).

Origin of Different Reaction Patterns between PC and Monomers. To investigate the compatibility of Ag_2S NCs with various monomers, PET-RAFT polymerization of acrylate and acrylamide monomers [in this case, methyl acrylate (MA)] in DMSO under 635 nm LED illumination was performed. CDTPA was chosen as the RAFT agent for the polymerization of MA because CPADB exhibited no activity during the PET-RAFT polymerization of MMA. Intriguingly, neither monomer polymerized after 24 h of illumination, regardless of the degassing process (Figure 5a), which was somewhat unexpected given that the propagation rate constant (k_p) of MA is significantly greater than that of MMA. Notably, PET-RAFT polymerization of MA under inert conditions showed no conversions even when illuminated by 6 W LEDs emitting at 515 nm (~5 mW/cm^2). Since the reduction potentials of CDTPA−MA and CDTPA−MMA are not significantly different, we hypothesized that the C−S bond dissociation of the radical anion intermediates was responsible for the difference in the reaction patterns of MA and MMA.

To comprehend the cause of this behavior, QC calculations were performed. The free-energy profiles of the reaction pathway between the electron transfer (State A → State B) and the complete C−S bond cleavage (State D → State E) are depicted in Figure 6a,b. C−S bond dissociation of radical anion intermediates (State C), as predicted, was the rate-determining step for both CDTPA−MMA and CDTPA−MA. In addition, the activation energy of CDTPA−MMA was calculated to be 13.5 kJ/mol, which is significantly less than the activation energy of CDTPA−MA (29.0 kJ/mol). Our hypothesis is supported by the significant difference between the activation energies of the two single-monomer-inserted moieties. The difference in activation energies may be attributable to the stability of the radical species generated (State E). The activation energy of the radicals generated from CDTPA−MMA (State E) was 8.1 kJ/mol less than the activation energy of the relaxed radical anion intermediate (State C). The activation energy of the CDTPA−MA radical (State E) was 6.6 kJ/mol higher than that of the radical anion intermediate (State C). To experimentally verify our hypothesis, we performed PET-RAFT polymerization of MA under inert conditions and 515 nm illumination at elevated temperatures (60 °C) (Figure 5a and Table S3). Indicating the existence of an activation barrier, the polymerization resulted in substantial conversion (43%) with excellent control ($Đ$ = 1.02). This result is also consistent with a very recent report from Boyer et al. wherein the rate of PET-RAFT polymerization of MA mediated by a metal naphthalocyanine-based PC under 780 nm illumination was significantly accelerated at moderately elevated temperatures.[81]

PET-RAFT Polymerization in DMSO under Blue- and Green-Light Illumination. First, we performed polymerization of (meth)acrylates under different wavelengths of light (i.e., blue, green, and sunlight). As predicted, the rate of MMA polymerization was significantly increased under green and blue illumination, whereas the polymerization process was poorly controlled (Table S4). Under blue LED illumination, the functionality of synthesized polymers was not adequately

https://doi.org/10.1021/acscatal.2c04684
ACS Catal. 2023, 13, 665−680

maintained (Figure S20). This suggests that high-energy illumination further activates the PET-RAFT electron transfer pathway as well as other reaction pathways (i.e., the energy transfer pathway and the photoiniferter process) that are forbidden under red-light illumination.[82] This observation was supported by the fact that successful polymerization occurred in the absence of Ag_2S NCs under green and blue LED illumination (Table S5). Contrary to what was observed under red-light illumination, polymerization reactions in the air were slower under these conditions than they were under inert conditions. Under such conditions, energy transfer and photoiniferter processes, in which oxygen cannot act as a catalyst, can be activated. However, this behavior is difficult to comprehend in its entirety; therefore, additional research is currently underway.

Next, we polymerized MA under green and blue LED illumination, which was significantly different from the MMA polymerization reaction (Figure 5a). Under green LED illumination, under inert conditions, there was no polymerization of MA, as was observed under red LED conditions. The polymerization in air resulted in a conversion of 81% adequate control ($Đ$ = 1.01). In this instance, "oxygen acceleration" was more pronounced than MMA polymerization under red LED illumination. Identical results were also observed for other acrylic monomers (Figure 5b). Based on the mechanistic studies described in the previous section, we attributed this behavior to the increase in excitation light energy (from red to green) and the catalytic role of oxygen, which accelerated the formation of radical anions. Consequently, the production of radical species significantly accelerated the rate of polymerization. This result agrees well with the previously cited DET-RAFT example by Coelho et al.[77]

In contrast to the polymerization under 515 nm illumination, the polymerization of MA occurred regardless of the presence of oxygen under 455 nm illumination (6 W LEDs providing ∼5 mW/cm^2). In this instance, a higher conversion rate was repeatedly attained when oxygen was present. This suggests that the "oxygen-acceleration" phenomenon occurs under 455 nm illumination, albeit to a lesser extent than under green LED illumination (Figure 5a). Under 455 nm illumination, the photoiniferter process occurs via direct photolysis, whereas under 515 nm illumination, it does not. In the absence of Ag_2S NCs, blue LED illumination during MA polymerization resulted in a significantly higher conversion of 93% with excellent control ($Đ$ = 1.01), whereas no polymer products were obtained under green LED illumination. These results demonstrably confirm our hypothesis (Table S6).

PET-RAFT of Methacrylic Monomers in an Aqueous Environment. After PET-RAFT polymerization of (meth)-acrylates in DMSO using Ag_2S NCs at different excitation wavelengths (i.e., red, green, and blue light), the reaction medium was changed to water as an eco-friendly solvent (Figure 7). Due to their high water solubility, we select 4-((((2-carboxyethyl)thio)carbonothioyl)thio)-4-cyanopentanoic acid (CETCPA) and (meth)acrylate, depicted in Figure 7a,b, as the RAFT agent and monomer, respectively. According to the chemical structures, the photophysical and electrochemical properties of CETCPA are very similar to those of CDTPA.

As depicted in Figures 7 and 8, the reaction pattern of the aqueous PET-RAFT polymerization was remarkably similar to that of the DMSO polymerization. Under red-light illumination, the polymerization of methacrylic monomers was successful (Figure 7a,d,e) and exhibited "oxygen-acceleration" behavior (Figure 7c,d). Under red-light illumination, no polymerization of acrylic monomers was observed, whereas blue-light illumination led to successful polymerization (Figure 8a). We discovered that the polymerization of the acrylic monomer under green-light illumination was extremely sensitive to the presence of oxygen, which is consistent with the outcomes of our experiments in DMSO (Figure 8a,b).

Sunlight-Driven PET-RAFT Polymerization. We conducted polymerization of four different monomer−solvent combinations (i.e., MMA−DMSO, MA−DMSO, OEGMA−water, and OEGA−water) under natural sunlight illumination (Figure 9). The reactions were conducted in the presence or absence of oxygen, with a total reaction time of 10 h and a final reaction temperature of 17 °C. As shown in Figure 9a,b, all monomer−solvent combinations resulted in successful polymerization reactions. We also observed the "oxygen-acceleration" behavior during polymerization, as predicted by our previous experiments. These results indicate that Ag_2S NCs are an effective full-spectrum PC for PET-RAFT polymerization performed under environmentally friendly and ambient conditions.

Biocompatibility of Ag_2S and PET-RAFT in a Cell Culture Environment. The photocatalytic performance of Ag_2S NCs over a broad range of illumination wavelengths in both organic and aqueous media, as well as their biocompatibility, make Ag_2S NCs a potential PC for photomediated polymerization reactions in biologically relevant media. Here, PET-RAFT polymerization was performed on OEGA in a solution with a composition similar to that of cell culture media (Dulbecco's modified Eagle medium (DMEM)): 4.5 g/L D-glucose, L-glutamine, and 110 mg/L sodium pyruvate. First, the biocompatibility of the synthesized Ag_2S NCs was evaluated (Figures 9b and S21). Up to 1 mg/mL Ag_2S NCs exhibited no cytotoxicity toward the selected three different cells (i.e. NIH 3T3, HeLa, and PC-3). We further observed a similar level of toxicity when the same experiment was repeated under continuous illumination from 630 nm (and 515 nm) LEDs, as expected (see Figure S22 for details of viability experiments with 515 nm light illuminations). It also should be noted that the photothermal effect of Ag_2S NCs was not observed in these experiments (Figure S23). We attributed this to the fact that Ag_2S NCs did not produce singlet oxygen, which dominates in photodynamic therapy (PDT) due to its high cytotoxicity.

To prevent adverse effects on the biological environment, the reaction time and monomer concentration were shortened (Table S7). Notably, the reaction system is oxygen tolerant and does not require deoxygenation of the medium or the addition of any harmful substances. Two hours of OEGA polymerization under 12 W 515 nm LED illumination resulted in a significant 23% conversion with adequate control ($Đ$ = 1.27), demonstrating the applicability of Ag_2S NCs as an effective PC for biocompatible PET-RAFT polymerization. Negative control experiments without Ag_2S NCs (Figures 9c and S24) yielded no polymerization products, confirming the role of Ag_2S NCs as a PC.

CONCLUSIONS

In conclusion, we discovered a biocompatible, water-dispersible, and full-spectrum PC that successfully mediated the aqueous/ambient PET-RAFT polymerization of various

https://doi.org/10.1021/acscatal.2c04684
ACS Catal. 2023, 13, 665−680

acrylic monomers in the absence of additives under the illumination of natural sunlight. Through indepth studies of the photocatalytic properties of Ag_2S NCs, we determined that the observed reactivity and biocompatibility were attributable to the sufficiently high reducing power and small band gap of the PC. In contrast to conventional PET-RAFT, which involves multiple competing pathways, the Ag_2S-mediated PET-RAFT reaction is driven solely by electron transfer under low-energy illumination as a result of the unique electronic structure of Ag_2S. Under these conditions, we observed unanticipated reaction patterns based on the combination of excitation light wavelength, monomer, and RAFT agent, as well as unconventional "oxygen-acceleration" behavior. Our experimental and theoretical studies suggest that the radical anion intermediates, generated by the photoinduced electron transfer between the excited-state PC and RAFT agent, play an essential role in the polymerization reaction and can provide a foundation for a better mechanistic understanding of the extremely complex PET-RAFT processes. Finally, we demonstrated that Ag_2S NCs can act as PCs and mediate PET-RAFT polymerization even in a cell culture environment. We believe this study offers intriguing insights into future environmentally friendly polymerization reactions.

■ ASSOCIATED CONTENT

Supporting Information

The Supporting Information is available free of charge at https://pubs.acs.org/doi/10.1021/acscatal.2c04684.

Instrument information for characterization of synthesized polymers and Ag_2S nanocrystals, procedures of polymerization, QC calculation details, reactive oxygen species (ROS) detection experiments, cell viability assay, and additional supporting figures and tables (PDF)

■ AUTHOR INFORMATION

Corresponding Authors

Seung Kyu Min − *Department of Chemistry, Ulsan National Institute of Science and Technology (UNIST), Ulsan 44919, Republic of Korea;* orcid.org/0000-0001-5636-3407; Email: skmin@unist.ac.kr

Seungho Cho − *Department of Materials Science and Engineering, Ulsan National Institute of Science and Technology (UNIST), Ulsan 44919, Republic of Korea;* orcid.org/0000-0001-7926-5674; Email: scho@unist.ac.kr

Min Sang Kwon − *Department of Materials Science and Engineering, Research Institute of Advanced Materials, Seoul National University, Seoul 08826, Republic of Korea;* orcid.org/0000-0002-1485-7588; Email: minsang@snu.ac.kr

Authors

Changhoon Yu − *Department of Materials Science and Engineering, Research Institute of Advanced Materials, Seoul National University, Seoul 08826, Republic of Korea*

Jaejung Song − *Department of Materials Science and Engineering, Ulsan National Institute of Science and Technology (UNIST), Ulsan 44919, Republic of Korea*

Tae In Kim − *Department of Chemistry, Ulsan National Institute of Science and Technology (UNIST), Ulsan 44919, Republic of Korea*

Yungyeong Lee − *Department of Materials Science and Engineering, Research Institute of Advanced Materials, Seoul National University, Seoul 08826, Republic of Korea*

Yonghwan Kwon − *Department of Materials Science and Engineering, Research Institute of Advanced Materials, Seoul National University, Seoul 08826, Republic of Korea; Department of Chemistry, Ulsan National Institute of Science and Technology (UNIST), Ulsan 44919, Republic of Korea*

Jongkyoung Kim − *Department of Materials Science and Engineering, Ulsan National Institute of Science and Technology (UNIST), Ulsan 44919, Republic of Korea*

Jeehun Park − *Department of Materials Science and Engineering, Research Institute of Advanced Materials, Seoul National University, Seoul 08826, Republic of Korea*

Jinho Choi − *Department of Materials Science and Engineering, Research Institute of Advanced Materials, Seoul National University, Seoul 08826, Republic of Korea*

Junsang Doh − *Department of Materials Science and Engineering, Research Institute of Advanced Materials, Seoul National University, Seoul 08826, Republic of Korea;* orcid.org/0000-0002-1483-2380

Complete contact information is available at: https://pubs.acs.org/10.1021/acscatal.2c04684

Author Contributions

‖C.Y., J.S., and T.I.K. contributed equally.

Notes

The authors declare no competing financial interest.

■ ACKNOWLEDGMENTS

The authors thank Dr. Johannes Gierschner and Dr. Reinhold Wannemacher at IMDEA Nanoscience for their helpful discussion. This work was supported by the New Faculty Startup Fund (0668-20200127) from the Seoul National University and the Basic Science Research Program through the National Research Foundation of Korea (NRF), which was funded by the Ministry of Science and ICT (MSIT) (2021R1A5A1030054 and 2022R1A2C2011627). The work from UNIST was supported by the 2022 Research Fund (1.220024.01) of UNIST, the NRF through grants funded by the Korean Government (MSIT; 2019R1A2C1007744, 2020R1A6A3A01099311, and 2022R1C1C1003654), and the Ministry of Trade, Industry, and Energy (MOTIE, 20015619).

■ REFERENCES

(1) Pan, X.; Tasdelen, M. A.; Laun, J.; Junkers, T.; Yagci, Y.; Matyjaszewski, K. Photomediated controlled radical polymerization. *Prog. Polym. Sci.* **2016**, *62*, 73−125.

(2) Chen, M.; Zhong, M.; Johnson, J. A. Light-controlled radical polymerization: Mechanisms, methods, and applications. *Chem. Rev.* **2016**, *116*, 10167−10211.

(3) Dadashi-Silab, S.; Doran, S.; Yagci, Y. Photoinduced electron transfer reactions for macromolecular syntheses. *Chem. Rev.* **2016**, *116*, 10212−10275.

(4) Corrigan, N.; Shanmugan, S.; Xu, J.; Boyer, C. Photocatalysis in organic and polymer synthesis. *Chem. Soc. Rev.* **2016**, *45*, 6165−6212.

(5) Bryden, M. A.; Zysman-Colman, E. Organic thermally activated delayed fluorescence (TADF) compounds used in photocatalysis. *Chem. Soc. Rev.* **2021**, *50*, 7587−7680.

(6) Niu, J.; Lunn, D. J.; Pusuluri, A.; Yoo, J. I.; O'Malley, M. A.; Mitragotri, S.; Soh, H. T.; Hawker, C. J. Engineering live cell surfaces with functional polymers via cytocompatible controlled radical polymerization. *Nat. Chem.* **2017**, *9*, 537−545.

(7) Corrigan, N.; Jung, K.; Moad, G.; Hawker, C. J.; Matyjaszewski, K.; Boyer, C. Reversible-deactivation radical polymerization (Controlled/living radical polymerization): From discovery to materials design and applications. *Prog. Polym. Sci.* **2020**, *111*, No. 101311.
(8) Corbin, D. A.; Miyake, G. M. Photoinduced organocatalyzed atom transfer radical polymerization (O-ATRP): Precision polymer synthesis using organic photoredox catalysis. *Chem. Rev.* **2022**, *122*, 1830−1874.
(9) Singh, V. K.; Yu, C.; Badgujar, S.; Kim, Y.; Kwon, Y.; Kim, D.; Lee, J.; Akhter, T.; Thangavel, G.; Park, L. S.; Lee, J.; Nandajan, P. C.; Wannemacher, R.; Milián-Medina, B.; Lüer, L.; Kim, K. S.; Gierschner, J.; Kwon, M. S. Highly efficient organic photocatalysts discovered via a computer-aided-design strategy for visible-light-driven atom transfer radical polymerization. *Nat. Catal.* **2018**, *1*, 794−804.
(10) Xu, J.; Jung, K.; Atme, A.; Shanmugam, S.; Boyer, C. A robust and versatile photoinduced living polymerization of conjugated and unconjugated monomers and its oxygen tolerance. *J. Am. Chem. Soc.* **2014**, *136*, 5508−5519.
(11) McKenzie, T. G.; Fu, Q.; Uchiyama, M.; Satoh, K.; Xu, J.; Boyer, C.; Kamigaito, M.; Qiao, G. G. Beyond traditional RAFT: Alternative activation of thiocarbonylthio compounds for controlled polymerization. *Adv. Sci.* **2016**, *3*, No. 1500394.
(12) Phommalysack-Lovan, J.; Chu, Y.; Boyer, C.; Xu, J. PET-RAFT polymerization: Towards green and precision polymer manufacturing. *Chem. Commun.* **2018**, *54*, 6591−6606.
(13) Shanmugam, S.; Xu, J.; Boyer, C. Photocontrolled living polymerization systems with reversible deactivations through electron and energy transfer. *Macromol. Rapid Commun.* **2017**, *38*, No. 1700143.
(14) Song, Y.; Kim, Y.; Noh, Y.; Singh, V. K.; Behera, S. K.; Abudulimu, A.; Chung, K.; Wannemacher, R.; Gierschner, J.; Lüer, L.; Kwon, M. S. Organic photocatalyst for ppm-level visible-light-driven reversible addition-fragmentation chain-Transfer (raft) polymerization with excellent oxygen tolerance. *Macromolecules* **2019**, *52*, 5538−5545.
(15) Tucker, B. S.; Coughlin, M. L.; Figg, A.; Sumerlin, B. S. Grafting-from proteins using metal-free PET−RAFT polymerizations under mild visible-light irradiation. *ACS Macro Lett.* **2017**, *6*, 452−457.
(16) Chen, M.; Gu, Y.; Singh, A.; Zhong, M.; Jordan, A. M.; Biswas, S.; Korley, L. T. J.; Balazs, A. C.; Johnson, J. A. Living additive manufacturing: Transformation of parent gels into diversely functionalized daughter gels made possible by visible light photoredox catalysis. *ACS Cent. Sci.* **2017**, *3*, 124−134.
(17) Shanmugam, S.; Xu, J.; Boyer, C. Living additive manufacturing. *ACS Cent. Sci.* **2017**, *3*, 95−96.
(18) Zhang, Z.; Corrigan, N.; Bagheri, A.; Jin, J.; Boyer, C. A versatile 3D and 4D printing system through photocontrolled RAFT polymerization. *Angew. Chem., Int. Ed.* **2019**, *58*, 17954−17963.
(19) Jung, K.; Corrigan, N.; Ciftci, M.; Xu, J.; Seo, S. E.; Hawker, C. J.; Boyer, C. Designing with light: Advanced 2D, 3D, and 4D materials. *Adv. Mater.* **2019**, *32*, No. 1903850.
(20) Nothling, M. D.; Fu, Q.; Reyhani, A.; Allison-Logan, S.; Jung, K.; Zhu, J.; Kamigaito, M.; Boyer, C.; Qiao, G. G. Progress and perspectives beyond traditional RAFT polymerization. *Adv. Sci.* **2020**, *7*, No. 2001656.
(21) Lee, Y.; Kwon, M. S. Emerging organic photoredox catalysts for organic transformations. *Eur. J. Org. Chem.* **2020**, *2020*, 6028−6043.
(22) Back, J. H.; Kwon, Y.; Cho, H.; Lee, H.; Ahn, D.; Kim, H. J.; Yu, Y.; Kim, Y.; Lee, W.; Kwon, M. S. Visible-light-curable acrylic resins toward UV-light-blocking adhesives for foldable displays. *Adv. Mater.* **2022**, No. 2204776.
(23) Kwon, Y.; Noh, Y.; Kim, D.; Lee, J.; Lee, Y.; Yu, C.; Roldao, J. C.; Feng, S.; Gierschner, J.; Wannemacher, R.; Kwon, M. S. Formation and degradation of strongly reducing cyanoarene-based radical anions towards efficient radical anion-mediated photoredox catalysis. *Nat. Commun.* (accepted).
(24) Thompson, R. C.; Moore, C. J.; vom Saal, F. S.; Swan, S. H. Plastics, the environment and human health: current consensus and future trends. *Phil. Trans. R. Soc. B* **2009**, *364*, 2153−2166.
(25) Anastas, P.; Eghbali, N. Green chemistry: principles and practice. *Chem. Soc. Rev.* **2010**, *39*, 301−312.
(26) Semsarilar, M.; Perrier, S. 'Green' reversible addition-fragmentation chain-transfer (RAFT) polymerization. *Nat. Chem.* **2010**, *2*, 811−820.
(27) Lee, Y.; Boyer, C.; Kwon, M. S. Visible-light-driven polymerization towards the green synthesis of plastics. *Nat. Rev. Mater.* **2022**, *7*, 74−75.
(28) Allison-Logan, S.; Fu, Q.; Sun, Y.; Liu, M.; Xie, J.; Tang, J.; Qiao, G. G. From UV to NIR: A full-spectrum metal-free photocatalyst for efficient polymer synthesis in aqueous conditions. *Angew. Chem., Int. Ed.* **2020**, *59*, 21392−21396.
(29) Xu, J.; Shanmugam, S.; Duong, H. T.; Boyer, C. Organophotocatalysts for photoinduced electron transfer-reversible addition−fragmentation chain transfer (PET-RAFT) polymerization. *Polym. Chem.* **2015**, *6*, 5615−5624.
(30) Wu, C.; Chen, H.; Corrigan, N.; Jung, K.; Kan, X.; Li, Z.; Liu, W.; Xu, J.; Boyer, C. Computer-guided discovery of a pH-responsive organic photocatalyst and application for pH and light dual-gated polymerization. *J. Am. Chem. Soc.* **2019**, *141*, 8207−8220.
(31) Xu, J.; Jung, K.; Boyer, C. Oxygen tolerance study of photoinduced electron transfer−reversible addition−fragmentation chain transfer (PET-RAFT) polymerization mediated by Ru(bpy)$_3$Cl$_2$. *Macromolecules* **2014**, *47*, 4217−4229.
(32) Tucker, B. S.; Coughlin, M. L.; Figg, A.; Sumerlin, B. S. Grafting-from protein using metal-free PET-RAFT polymerizations under mild visible-light irradiation. *ACS Macro Lett.* **2017**, *6*, 452−457.
(33) Shanmugam, S.; Xu, J.; Boyer, C. Aqueous RAFT photopolymerization with oxygen tolerance. *Macromolecules* **2016**, *49*, 9345−9357.
(34) Shen, L.; Lu, Q.; Zhu, A.; Lv, X.; An, Z. Photocontrolled RAFT polymerization mediated by a supramolecular catalyst. *ACS Macro Lett.* **2017**, *6*, 625−631.
(35) Huang, Y.; Li, X.; Li, J. L.; Zhang, B.; Cai, T. An environmentally benign and pH-sensitive photocatalyst with surface-bound metalloporphyrin for heterogeneous catalysis of controlled radical polymerization. *Macromolecules* **2018**, *51*, 7974−7982.
(36) Xu, S.; Yeow, J.; Boyer, C. Exploiting wavelength orthogonality for successive photoinduced polymerization-induced self-assembly and photo-crosslinking. *ACS Macro Lett.* **2018**, *7*, 1376−1382.
(37) Huang, Y.; Zhang, X. R.; Ye, S.; Li, J. L.; Li, X.; Cai, T. Robust hollow nanocomposites with ruthenium−bipyridine complexes for heterogeneous catalysis of logic-controlled RAFT polymerization. *Nanoscale* **2019**, *11*, 13502−13510.
(38) Yang, Y.; An, Z. Visible light induced aqueous RAFT polymerization using a supramolecular perylene diimide/cucurbit [7] uril complex. *Polym. Chem.* **2019**, *10*, 2801−2811.
(39) Jiang, J.; Ye, G.; Lorandi, F.; Liu, Z.; Liu, Y.; Hu, T.; Chen, J.; Lu, Y.; Matyjaszewski, K. Localized Surface Plasmon Resonance Meets Controlled/Living Radical Polymerization: An Adaptable Strategy for Broadband Light-Regulated Macromolecular Synthesis. *Angew. Chem., Int. Ed.* **2019**, *58*, 12096−12101.
(40) Li, X.; Ye, S.; Zhang, Y. C.; Zhao, H. P.; Huang, Y.; Zhang, B.; Cai, T. Magnetic Janus nanocomposites with iridium(III) complexes for heterogeneous catalysis of logic controlled RAFT polymerization using multiplexed external switching. *Nanoscale* **2020**, *12*, 7595−7603.
(41) Zhao, Y.; Shao, S.; Xia, J.; Huang, Y.; Zhang, Y. C.; Li, X.; Cai, T. Hydrophilic ultrafiltration membranes with surface-bound eosin Y for an integrated synthesis-separation system of aqueous RAFT photopolymerization. *J. Mater. Chem. A* **2020**, *8*, 9825−9831.
(42) Li, R.; An, Z. Achieving ultrahigh molecular weights with diverse architectures for unconjugated monomers through oxygen-tolerant photoenzymatic RAFT polymerization. *Angew. Chem., Int. Ed.* **2020**, *59*, 22258−22264.

https://doi.org/10.1021/acscatal.2c04684
ACS Catal. 2023, 13, 665−680

(43) Xia, L.; Cheng, B. F.; Zeng, T. Y.; Nie, X.; Chen, G.; Zhang, Z.; Zhang, W. J.; Hong, C. Y.; You, Y. Z. Polymer nanofibers exhibiting remarkable activity in driving the living polymerization under visible light and reusability. *Adv. Sci.* **2020**, *7*, No. 1902451.
(44) McClelland, K. P.; Clemons, T. D.; Stupp, S. I.; Weiss, E. A. Semiconductor quantum dots are efficient and recyclable photocatalysts for aqueous PET-RAFT polymerization. *ACS Macro Lett.* **2020**, *9*, 7−13.
(45) Olson, R. A.; Levi, J. S.; Scheutz, G. M.; Lessard, J. J.; Figg, C. A.; Kamat, M. N.; Basso, K. B.; Sumerlin, B. S. Macromolecular photocatalyst for synthesis and purification of protein−polymer conjugates. *Macromolecules* **2021**, *54*, 4880−4888.
(46) Huang, Y.; Li, X.; Zhang, Y. C.; Shi, Z.; Zeng, L.; Xie, J.; Du, Y.; Lu, D.; Hu, Z.; Cai, T.; Luo, Z. Aqueous protein−polymer bioconjugation via photoinduced RAFT polymerization using high loading heterogeneous catalyst. *ACS Appl. Mater. Interfaces* **2021**, *13*, 44488−44496.
(47) Li, Q.; Lu, Z.; Yang, H.; Cai, J.; Yin, X.; Zhao, Y.; Xiao, L.; Hou, L. Photoinduced organocatalyzed controlled radical polymerization feasible over a wide range of wavelengths. *Polym. Chem.* **2022**, *13*, 527−535.
(48) Guo, W. L.; Zhou, Y.; Duan, B.; Wei, W. F.; Chen, C.; Li, X.; Cai, T. Exploiting nanofibrous chitin microspheres as heterogeneous photocatalysts for high throughput. *Chem. Eng. J.* **2022**, *429*, No. 132120.
(49) Strandwitz, N. C.; Khan, A.; Boettcher, S. W.; Mikhailovsky, A. A.; Hawker, C. J.; Nguyen, T. Q.; Stucky, G. D. One- and two-photon induced polymerization of methylmethacrylate using colloidal CdS semiconductor quantum dots. *J. Am. Chem. Soc.* **2008**, *130*, 8280−8288.
(50) Dadashi-Silab, S.; Tasdelen, M. A.; Asiri, A. M.; Khan, S. B.; Yagci, Y. Photoinduced atom transfer radical polymerization using semiconductor nanoparticles. *Macromol. Rapid Commun.* **2014**, *35*, 454−459.
(51) Huang, Y.; Zhu, Y.; Egap, E. Semiconductor quantum dots as photocatalysts for controlled light-mediated radical polymerization. *ACS Macro Lett.* **2018**, *7*, 184−189.
(52) Wu, Z.; Fang, W.; Wu, C.; Corrigan, N.; Zhang, T.; Xu, S.; Boyer, C. An aqueous photo-controlled polymerization under NIR wavelengths: synthesis of polymeric nanoparticles through thick barriers. *Chem. Sci.* **2022**, *13*, 11519−11532.
(53) Yu, W.; Yin, J.; Li, Y.; Lai, B.; Jiang, T.; Li, Y.; Liu, H.; Liu, J.; Zhao, C.; Singh, S. C.; Chen, J.; Lin, B.; Idriss, H.; Guo, C. Ag_2S quantum dots as an infrared excited photocatalyst for hydrogen production. *ACS Appl. Energy Mater.* **2019**, *2*, 2751−2759.
(54) Yang, W.; Zhang, L.; Hu, Y.; Zhong, Y.; Wu, H. B.; Lou, X. W. Microwave-assisted synthesis of porous Ag_2S−Ag hybrid nanotubes with high visible-light photocatalytic activity. *Angew. Chem., Int. Ed.* **2012**, *51*, 11501−11504.
(55) Suresh, A. K.; Doktycz, M. J.; Wang, W.; Moon, J. W.; Gu, B.; Meyer, H. M.; Hensley, D. K.; Allison, D. P.; Phelps, T. J.; Pelletier, D. A. Monodispersed biocompatible silver sulfide nanoparticles: facile extracellular biosynthesis using the γ-proteobacterium, Shewanella oneidensis. *Acta Biomater.* **2011**, *7*, 4253−4258.
(56) Smirnov, M. S.; Buganov, O. V.; Tikhomoriv, S. A.; Ovchinnikov, O. V. Photoexcitation dynamics in hybrid associates of Ag_2S quantum dots with methylene blue. *J. Lumin.* **2021**, *232*, No. 117794.
(57) Jiang, P.; Li, S.; Han, M.; Liu, Y.; Chen, Z. Biocompatible Ag_2S quantum dots for highly sensitive detection of copper ions. *Analyst* **2019**, *144*, 2604−2610.
(58) Aydemir, D.; Hashemkhani, M.; Durmusoglu, E. G.; Acar, H. Y.; Ulusu, N. N. A new substrate for glutathione reductase: Glutathione coated Ag_2S quantum dots. *Talanta* **2019**, *194*, 501−506.
(59) Jiang, P.; Zhu, C. N.; Zhang, Z. L.; Tian, Z. Q.; Pang, D. W. Water-soluble Ag_2S quantum dots for near-infrared fluorescence imaging in vivo. *Biomaterials* **2012**, *33*, 5130−5135.
(60) Zhang, Y.; Hong, G.; Zhang, Y.; Chen, G.; Li, F.; Dai, H.; Wang, Q. Ag_2S quantum dot: A bright and biocompatible fluorescent nanoprobe in the second near-infrared window. *ACS Nano* **2012**, *6*, 3695−3702.
(61) León-Velázquez, M. S.; Irizarry, R.; Castro-Rosario, M. E. Nucleation and growth of silver sulfide nanoparticles. *J. Phys. Chem. C* **2010**, *114*, 5839−5849.
(62) Kryukov, A. I.; Zin'chuk, N. N.; Korzhak, A. V.; Kuchmii, S. Y.; Stroyuk, A. L. Optical and catalytic properties of Ag_2S nanoparticles. *J. Mol. Catal. A* **2004**, *221*, 209−221.
(63) Edvinsson, T. Optical quantum confinement and photocatalytic properties in two-, one- and zero-dimensional nanostructures. *R. Soc. Open Sci.* **2018**, *5*, No. 180387.
(64) Barman, S. R.; Shanthi, N.; Shukla, A. K.; Sarma, D. D. Order-disorder and electronic transitions in $Ag_{2+\delta}S$ single crystals studied by photoemission spectroscopy. *Phys. Rev. B* **1996**, *53*, 3746−3751.
(65) McKenzie, T. G.; Fu, Q.; Wong, E. H. H.; Dunstan, D. E.; Qiao, G. G. Visible light mediated controlled radical polymerization in the absence of exogenous radical sources or catalysts. *Macromolecules* **2015**, *48*, 3864−3872.
(66) Otsu, T.; Yoshida, M.; Tazaki, T. A model for living radical polymerization. *Macromol. Chem., Rapid Commun.* **1982**, *3*, 133−140.
(67) Jung, K.; Boyer, C.; Zetterlund, P. B. RAFT iniferter polymerization in miniemulsion using visible light. *Polym. Chem.* **2017**, *8*, 3965−3970.
(68) Yeow, J.; Chapman, R.; Gormley, A. J.; Boyer, C. Up in the air: oxygen tolerance in controlled/living radical polymerization. *Chem. Soc. Rev.* **2018**, *47*, 4357−4387.
(69) Wu, C.; Jung, K.; Ma, Y.; Liu, W.; Boyer, C. Unravelling an oxygen-mediated reductive quenching pathway for photopolymerisation under long wavelengths. *Nat. Commun.* **2021**, *12*, No. 478.
(70) Lee, Y.; Kwon, Y.; Kim, Y.; Yu, C.; Feng, S.; Park, J.; Doh, J.; Wannemacher, R.; Koo, B.; Gierschner, J.; Kwon, M. S. A water-soluble organic photocatalyst discovered for highly efficient additive-free visible-light-driven grafting of polymers from proteins at ambient and aqueous environments. *Adv. Mater.* **2022**, *34*, No. 2108446.
(71) Corrigan, N.; Xu, J.; Boyer, C.; Allonas, X. Exploration of the PET-RAFT initiation mechanism for two commonly used photocatalysts. *ChemPhotoChem* **2019**, *3*, 1193−1199.
(72) Allegrezza, M. L.; Konkolewicz, D. PET-RAFT polymerization: Mechanistic perspectives for future materials. *ACS Macro Lett.* **2021**, *10*, 433−446.
(73) Thum, M. D.; Wolf, S.; Falvey, D. E. State-dependent photochemical and photophysical behavior of dithiolate ester and trithiocarbonate reversible addition−fragmentation chain transfer polymerization agents. *J. Phys. Chem. A* **2020**, *124*, 4211−4222.
(74) Strieth-Kalthoff, F.; Glorius, F. Triplet energy transfer photocatalysis: Unlocking the next level. *Chem* **2020**, *6*, 1888−1903.
(75) Christmann, J.; Ibrahim, A.; Charlot, V.; Croutxé-Barghorn, C.; Ley, C.; Allonas, X. Elucidation of the key role of $[Ru(bpy)_3]^{2+}$ in photocatalyzed RAFT polymerization. *ChemPhysChem* **2016**, *17*, 2309−2314.
(76) Kuhn, L. R.; Allegrezza, M. L.; Dougher, N. J.; Konkolewicz, D. Using kinetic modeling and experimental data to evaluate mechanisms in PET-RAFT. *J. Polym. Sci.* **2020**, *58*, 139−144.
(77) Maximiano, P.; Mendonca, P. V.; Costa, J. R. C.; Haworth, N. L.; Serra, A. C.; Guliashvili, T.; Coote, M. L.; Coelho, J. F. J. Ambient temperature transition-metal-free dissociative electron transfer reversible addition−fragmentation chain transfer polymerization (DET-RAFT) of methacrylates, acrylates, and styrene. *Macromolecules* **2016**, *49*, 1597−1604.
(78) Strover, L. T.; Cantalice, A.; Lam, J. Y. L.; Postma, A.; Hutt, O. E.; Horne, M. D.; Moad, G. Electrochemical behavior of thiocarbonylthio chain transfer agents for RAFT polymerization. *ACS Macro Lett.* **2019**, *8*, 1316−1322.
(79) Shanmugam, S.; Xu, J.; Boyer, C. Light-regulated polymerization under near-infrared/far-red irradiation catalyzed by bacteriochlorophyll *a*. *Angew. Chem., Int. Ed.* **2016**, *55*, 1036−1040.
(80) Robertson, C. A.; Evans, D. H.; Abrahamse, H. Photodynamic therapy (PDT): A short review on cellular mechanisms and cancer

https://doi.org/10.1021/acscatal.2c04684
ACS Catal. 2023, 13, 665−680

research applications for PDT. *J. Photochem. Photobiol. B* **2009**, *96*, 1−8.
(81) Wu, Z.; Jung, K.; Wu, C.; Ng, G.; Wang, L.; Liu, J.; Boyer, C. Selective photoactivation of trithiocarbonates mediated by metal naphthalocyanines and overcoming activation barriers using thermal energy. *J. Am. Chem. Soc.* **2022**, *144*, 995−1005.
(82) Xu, J.; Shanmugam, S.; Corrigan, N. A.; Boyer, C.Catalyst-Free Visible Light-Induced RAFT Photopolymerization. In *Controlled Radical Polymerization: Mechanisms*, ACS Symposium Series; American Chemical Society, 2015; Vol. *1187*, pp 247−267.

https://doi.org/10.1021/acscatal.2c04684
ACS Catal. 2023, 13, 665−680

nature communications

Article

https://doi.org/10.1038/s41467-022-35774-5

Formation and degradation of strongly reducing cyanoarene-based radical anions towards efficient radical anion-mediated photoredox catalysis

Received: 26 August 2021

Accepted: 22 December 2022

Published online: 06 January 2023

Check for updates

Yonghwan Kwon[1,2], Jungwook Lee[1], Yeonjin Noh[1,2], Doyon Kim[2], Yungyeong Lee[1], Changhoon Yu[1], Juan Carlos Roldao[3,4], Siyang Feng[3], Johannes Gierschner[3] ✉, Reinhold Wannemacher[3] ✉ & Min Sang Kwon[1] ✉

Cyanoarene-based photocatalysts (PCs) have attracted significant interest owing to their superior catalytic performance for radical anion mediated photoredox catalysis. However, the factors affecting the formation and degradation of cyanoarene-based PC radical anion ($PC^{\bullet-}$) are still insufficiently understood. Herein, we therefore investigate the formation and degradation of cyanoarene-based $PC^{\bullet-}$ under widely-used photoredox-mediated reaction conditions. By screening various cyanoarene-based PCs, we elucidate strategies to efficiently generate $PC^{\bullet-}$ with adequate excited-state reduction potentials (E_{red}^{*}) via supra-efficient generation of long-lived triplet excited states (T_1). To thoroughly investigate the behavior of $PC^{\bullet-}$ in actual photoredox-mediated reactions, a reductive dehalogenation is carried out as a model reaction and identified the dominant photodegradation pathways of the $PC^{\bullet-}$. Dehalogenation and photodegradation of $PC^{\bullet-}$ are coexistent depending on the rate of electron transfer (ET) to the substrate and the photodegradation strongly depends on the electronic and steric properties of the PCs. Based on the understanding of both the formation and photodegradation of $PC^{\bullet-}$, we demonstrate that the efficient generation of highly reducing $PC^{\bullet-}$ allows for the highly efficient photoredox catalyzed dehalogenation of aryl/alkyl halides at a PC loading as low as 0.001 mol% with a high oxygen tolerance. The present work provides new insights into the reactions of cyanoarene-based $PC^{\bullet-}$ in photoredox-mediated reactions.

Over the last decade, visible light-driven photoredox catalysis that utilizes the energy of photons has risen to prominence in organic synthesis owing to its mild conditions, high tolerance to various functional groups, and unique operating mechanism[1–6]. Upon photoexcitation, a photoredox catalyst (PC) can participate in single-electron transfer (SET) events with substrates, consequently generating reactive radical intermediates from a variety of bench-stable substrates. This formerly inaccessible reaction strategy has enabled significant developments in radical chemistry for organic[7–13] and polymer synthesis[14–20].

To further enhance the efficiency and expand the reaction scope of visible light-driven photoredox catalysis, it is essential to maximize

A full list of affiliations appears at the end of the paper. ✉e-mail: johannes.gierschner@imdea.org; reinhold.wannemacher@imdea.org; minsang@snu.ac.kr

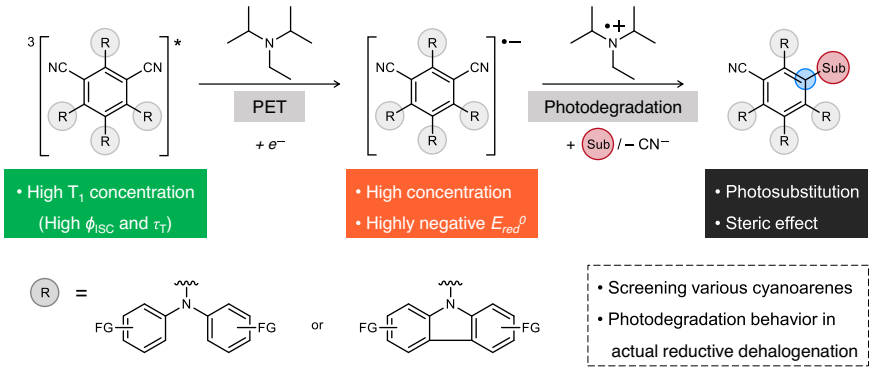

Fig. 1 | Schematic illustration of the current work. Reaction scheme of the formation and photodegradation of cyanoarene-based photocatalyst radical anion ($PC^{\bullet-}$). Here, ISC, T_1, PET, and Sub denote intersystem crossing, triplet excited state, photoinduced electron transfer, and substituent, respectively.

the reducing power and concentration of active PC species that activate the substrate of interest through an electron transfer (ET) process. This can mostly be facilitated in a reductive quenching cycle wherein a one-electron-reduced PC (i.e., $PC^{\bullet-}$) commonly acts as an active PC species because $PC^{\bullet-}$ usually exhibits a far longer lifetime than the optically excited PC species (i.e., $^{1,3}PC^{*}$) acting as an active PC intermediate in an oxidative quenching cycle[21]. Moreover, $PC^{\bullet-}$ is regarded as a core intermediate for the recently proposed multiphoton excitation catalysis mechanism based on consecutive photoinduced electron transfer (ConPET)[22–24] and electrophotocatalysis[25–27], therefore, merits special attention.

The concentration of $PC^{\bullet-}$ in the photostationary state and the ground state reduction potential of the PC (E_{red}^{0}(PC)) both play critical roles in photoredox-mediated catalytic reactions employing $PC^{\bullet-}$ as an active species[21]. A high concentration of $PC^{\bullet-}$ implies a high collision frequency with the substrate under illumination by visible light, which facilitates ET events. In addition, a more negative E_{red}^{0} indicates an increase in the driving force for ET, thus accelerating ET processes. To achieve a highly negative E_{red}^{0} of a PC, a high energy lowest unoccupied molecular orbital (LUMO) is required[15]. Furthermore, to ensure visible light absorption by such a PC, the energy of the highest occupied molecular orbital (HOMO) should scale with that of the LUMO; however, the accompanying decrease in E_{red}^{*} is detrimental to the photoinduced electron transfer (PET) between a PC and a reductant. In other words, it is very difficult to target PCs combining the following properties: (i) good visible light absorption, (ii) adequate initial PET with a sacrificial reductant, and iii) a highly negative reduction potential. Thus, the generation of $PC^{\bullet-}$ is normally targeted in PCs with a less negative reduction potential (e.g., perylene diimide[22,28], Acr-Mes $^{+}BF_4^{-}$[8,29], Rh6G[30], and $Ru(bpy)_3Cl_2$[7,31–33]) or under special reaction conditions[23,34,35] (Supplementary Table 1 in the Supplementary Information (SI)).

As exemplified by the recent reports by the groups of Zhang[36], Zeitler[37], Kwon[15], and others[11,38–44], cyanoarenes have emerged as attractive organic PCs. Such PCs exhibit excellent catalytic performances for a variety of visible light-driven organic reactions[38–40] and polymerizations[45–49]. Among them, 4DP-IPN and its analogs have attracted considerable interest owing to their superior catalytic performance for radical anion-mediated photoredox catalysis. For example, Wickens et al. reported the successful photocatalyzed reductive cleavage of strong C(sp^2)–N and C(sp^2)–O bonds by the electrochemically generated $4DP\text{-}IPN^{\bullet-}$[41]. More recently, the groups of Wickens[42] and Wu[43] used 4DP-IPN analogs as PCs to perform the phosphonylation, borylation, and hydroarylation of highly inactivated aryl chlorides. Through careful characterization of the radical anion of 4DP-IPN, they proposed that its high reducing power (E_{red}^{0} = −1.66 V vs SCE, all redox potentials in the current work are against saturated calomel electrode (SCE) unless otherwise noted) is the crucial factor. Meanwhile, recent studies on cyanoarene-based $PC^{\bullet-}$ have revealed that a photodegradation of PCs is involved in photoredox catalysis[50–53], which might induce unwanted catalytic activities of the photodegraded adducts. However, despite these research efforts, it is still unclear which factors affect the formation and degradation of the radical anion of cyanoarene-based PCs. This lack of understanding can lead to inefficiencies in radical anion-mediated photoredox reactions such as inappropriate choice of PC, excessive PC loading, and inadequate selection of the excitation source. However, no studies have focused on the in-depth investigation of the cyanoarene-based $PC^{\bullet-}$.

Herein, we investigate the formation and degradation of the cyanoarene-based $PC^{\bullet-}$ under widely-used photoredox-mediated reaction conditions (Fig. 1). Through the investigation of various cyanoarene-based PCs with different redox potentials and abilities to generate triplet excited states (T_1), we found that organic PCs exhibiting both the ultra-efficient generation of long-lived T_1 and adequately positive excited state reduction potentials (E_{red}^{*}(PC)) enable these PCs to efficiently form strongly reducing $PC^{\bullet-}$ under mild visible light illumination. During the screening of these cyanoarenes, we also found that the different photodegradation behaviors of PCs depend on their electronic and steric properties. We also identified a strong correlation between the photodegradation reaction of cyanoarenes and the abilities of PCs to be one-electron reduced. To further investigate the photodegradation behavior of $PC^{\bullet-}$ in actual photoredox catalysis, we carried out the reductive dehalogenation of aryl halides as a model reaction. From in situ monitoring of the reaction, we revealed that the dehalogenation and photodegradation of PCs are co-dependent on the rate of the ET process. Furthermore, we demonstrated the highly efficient dehalogenation of aryl/alkyl halides at a very small loading of 4DP-IPN with a high oxygen tolerance; it thus outperformed other conventional PCs that were used as controls.

Results

PET event between 4DP-IPN and sacrificial reducing agents

We first investigated the initial PET from amine-based sacrificial donors to 4DP-IPN; tertiary amines were used because they are the most commonly used sacrificial reducing agents. Given the ground state oxidation potentials of the prepared amines (E_{ox}^{0}(DIPEA) = 0.68 V, E_{ox}^{0}(TBA) = 0.88 V, and E_{ox}^{0}(TEA) = 0.96 V, where DIPEA, TBA, and TEA represent diisopropylethylamine, triethylamine, and tributylamine, respectively)[54,55], and the excited state reduction potential of the PC (E_{red}^{*}(4DP-IPN) = 0.63 V), the PET is expected to be very slow owing to its unfavorable thermodynamics. To monitor the PET, we conducted photoluminescence (PL) decay quenching experiments using time-correlated single-photon counting (TCSPC). The UV-Vis absorption and PL emission spectra of 4DP-IPN are shown in Supplementary Fig. 3. Under degassed conditions without a sacrificial electron donor, the decay lifetimes of the prompt and delayed components of 4DP-IPN

https://doi.org/10.1038/s41467-022-35774-5

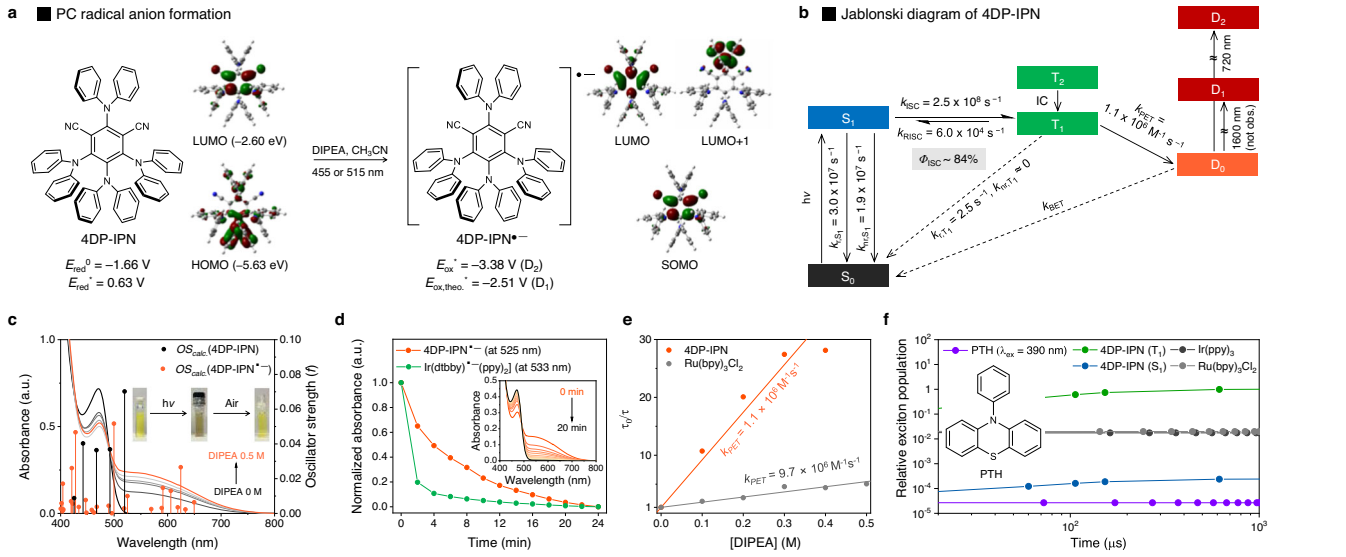

Fig. 2 | Characterization of 4DP-IPN and 4DP-IPN$^{\bullet-}$. a Reaction scheme of the formation of 4DP-IPN$^{\bullet-}$. The calculated frontier molecular orbitals (MO) topologies of 4DP-IPN and 4DP-IPN$^{\bullet-}$ are shown. Their excited state redox potentials (E_{red}^*(PC) and E_{ox}^*(PC$^{\bullet-}$)) were estimated from $E_{red}^* = E_{0\text{-}0} + E_{red}^0$ and $E_{ox}^*(PC^{\bullet-}) = -E_{0\text{-}0}(PC^{\bullet-}) + E_{red}^0(PC)$; $E_{0\text{-}0}$(PC) and $E_{0\text{-}0}$(PC$^{\bullet-}$) were evaluated by the onset of gated photoluminescence (PL) emission spectrum in CH_3CN at 65 K and the onset of UV-Vis absorption spectrum at room temperature (RT), respectively. **b** Jablonski diagram of 4DP-IPN. The rate constants of all photophysical processes were evaluated in the current work; here, IC, (R)ISC, D_0, and $S_1/T_1/D_n$ denote internal conversion, (reverse)intersystem crossing, doublet ground state and singlet/triplet/doublet excited state, respectively. **c** UV-Vis absorption spectra of 4DP-IPN (black line) and 4DP-IPN$^{\bullet-}$ (orange line) in CH_3CN; here, a.u. denotes arbitrary units. UV-Vis absorption spectra of 4DP-IPN$^{\bullet-}$ were taken right after illumination by two 3 W 515 nm LEDs for 1 min at RT. TD-DFT results (oscillator strengths) are shown as stick spectra. **d** Time-dependent changes of the UV-Vis absorbance of 4DP-IPN$^{\bullet-}$ at 525 nm and Ir(dtbby)$^{\bullet-}$(ppy)$_2$PF$_6$ at 533 nm (compare Supplementary Fig. 9). PC$^{\bullet-}$ was generated under the illumination of two 3 W 515 nm LEDs for 3 min (for 4DP-IPN) or two 3 W 455 nm LEDs for 1 min (for Ir(dtbby)(ppy)$_2$PF$_6$) at RT. Changes in the UV-Vis absorption spectrum of freshly generated 4DP-IPN$^{\bullet-}$ were recorded every 2 min under dark conditions (inset). **e** Stern–Volmer plots for the PL decays quenching of 4DP-IPN and Ru(bpy)$_3$Cl$_2$ in CH_3CN by DIPEA at RT. **f** Results of kinetics simulation of the relative excited state population of selected PCs (5.0×10^{-3} M) over time under continuous 455 nm (or 390 nm for 10-phenylphenothiazine (PTH)) irradiation (see the SI for the full details of the kinetics simulation).

were measured to be 3.3 ns and 104 μs, respectively (Supplementary Fig. 5). Adding tertiary amines significantly shortened the decay lifetimes of the delayed components (Supplementary Fig. 6), whereas those of the prompt components changed negligibly (Supplementary Fig. 7), implying that T_1 is mainly responsible for the PET events. In fact, the measured rate for PET is larger than the reverse intersystem crossing (RISC) rate and smaller than the ISC rate, further supporting this argument (Fig. 2b). Among the sacrificial donors, DIPEA exhibited the strongest quenching effect (Fig. 2e and Supplementary Fig. 6). The PET rate constants (k_{PET}) increased with an increasing thermodynamic driving force ($-\Delta G_{PET}$), consistent with Marcus normal region behavior (Supplementary Fig. 6)[56]. As a control, we performed a PL quenching experiment with DIPEA on Ru(bpy)$_3$Cl$_2$, which is widely used as a PC for reductive quenching photocatalytic cycles[31–33]. In the presence of the same amount of DIPEA, k_{PET} for Ru(bpy)$_3$Cl$_2$ (9.7×10^6 M^{-1} s^{-1}) was higher than that for 4DP-IPN (1.1×10^6 M^{-1} s^{-1}), consistent with the trend in the excited state reduction potentials of the PCs (E_{red}^*(Ru(bpy)$_3$Cl$_2$) = 0.77 V)[57].

Interestingly, for the same amount of DIPEA, the PL decay quenching in 4DP-IPN changed to a greater extent than that in Ru(bpy)$_3$Cl$_2$. This indicates that the rate of PET (v_{PET}) from DIPEA to the PC is faster in 4DP-IPN than that in Ru(bpy)$_3$Cl$_2$, although the thermodynamic driving force for PET is less favorable in 4DP-IPN. We attribute this finding to the highly efficient long-lived T_1 generation by 4DP-IPN. In fact, the excited state population of PC is a crucial factor for generating the PC$^{\bullet-}$ because the molar rate of PET, v_{PET} (in M s^{-1}), is described by

$$v_{PET} = k_{PET}[PC^*][Q] \quad (1)$$

where $[PC^*]$ is the concentration of the PC in the excited state and $[Q]$ is the concentration of the quencher (i.e., DIPEA). We then modeled the time-dependent excited state concentrations of selected PCs after turning on irradiation; this model was based on the rate law to estimate the PET ability of 4DP-IPN and to compare it to those of other well-known PCs (Fig. 2f; see also Supplementary Fig. 13 in the SI for details of the simulation and the rate equations employed). The rate constants used in the kinetics simulations were obtained from either our experiments or the literature. In the photostationary state, the concentration of 4DP-IPN molecules in T_1 was approximately 10^2 times higher than those of both Ru(bpy)$_3$Cl$_2$ and Ir(ppy)$_3$ and was approximately 10^5 times higher than that of 10-phenylphenothiazine (PTH), which has commonly been used as a highly reducing PC (E_{ox}^*(PTH) = –2.10 V)[58]. This indeed suggests that 4DP-IPN is superior for PET with sacrificial agents, despite its unfavorable thermodynamics.

Generation of PC$^{\bullet-}$ of cyanoarene-based PCs

The formation of the PC$^{\bullet-}$ of 4DP-IPN can be directly monitored by UV-Vis absorption spectroscopy. As the PC$^{\bullet-}$ is known to be sensitive to oxygen and moisture[8,59], all samples were prepared inside a glove box. A degassed solution of 4DP-IPN was first irradiated with a 515 nm light emitting diode (LED) for 1 min in the presence of an excess amount of DIPEA; in this context, it should be noted that exogenous tertiary amines have been reported to be able to suppress back electron transfer (BET) events[60]. The UV-Vis absorption spectra of the 4DP-IPN solution were recorded before and immediately after irradiation (Fig. 2c). Spectral changes were observed, in agreement with a color change that could be observed by the naked eye (Fig. 2c, inset). A decrease in the absorption peak at 470 nm implied the depletion of

4DP-IPN, while a new broad absorption band appeared at 500–750 nm, indicating the generation of 4DP-IPN$^{\bullet-}$; perfect isosbestic points (at 428 and 493 nm) also appeared for the reaction. Once the resulting PC$^{\bullet-}$ was exposed to air, close to 100% of the 4DP-IPN was rapidly regenerated, demonstrating the nearly perfect reversibility of this transformation (Supplementary Fig. 8a). The stability of the PC$^{\bullet-}$ was also measured by recording changes in the UV-Vis absorption spectrum of freshly generated PC$^{\bullet-}$ every 2 min under dark conditions (orange line in Fig. 2d). A gradual decay was observed in the dark over more than 20 min, which is approximately two times longer than that of Ir(dtbby)$^{\bullet-}$(ppy)$_2$PF$_6$ reported by König et al. under similar conditions (green line in Fig. 2d)[23]. This superior stability of 4DP-IPN$^{\bullet-}$ is likely due to retarded BET in the triplet contact radical ion pair involving the 4DP-IPN$^{\bullet-}$, which is related to the lack of heavy atoms and, thus, a decreased spin–orbit coupling.

The formation of the PC$^{\bullet-}$ was further confirmed by (time-dependent) density functional theory, (TD-)DFT, calculations (using the B3LYP functional, 6–311++G* basis set, and the polarizable continuum model, PCM, with acetonitrile as the solvent); such calculations provide insights into the underlying electronic situation. In the neutral form of 4DP-IPN (black line in Fig. 2c), the low-energy absorption band consisted of a number of transitions with partial charge transfer (CT) character and a relatively low oscillator strength f (Supplementary Fig. 14); for instance, S_1 was well described by a transition from the HOMO to the LUMO (HOMO→LUMO), as depicted in Fig. 2a. Furthermore, the TD-DFT calculations correctly reproduced the appearance of a red-shifted absorption band for the PC$^{\bullet-}$ (orange line in Fig. 2c), which was shown to consist of a multitude of CT and locally excited (LE) transitions with a small f; here, the D_2 state corresponded to the excitation from the singly occupied molecular orbital (SOMO) to the LUMO+1, which was of LE character but had a small differential overlap, thus generating a small f (Fig. 2a and Supplementary Fig. 14). Note, however, that the theoretical evidence clearly indicates the appearance of a near-infrared (NIR) band for the PC$^{\bullet-}$, which corresponded to the D_1 state (SOMO→LUMO; Fig. 2b and Supplementary Fig. 14), independent of the chosen DFT functional. At the B3LYP level of theory, it appeared at 1454 nm. We thus recorded the absorption spectrum in the NIR range to 1500 nm but did not find evidence for such absorption in this range (Supplementary Fig. 10). However, an absorption band might possibly have appeared at a wavelength >1500 nm and was therefore not detected. Nonetheless, note that the energy difference between the bands at 1450 and 1600 nm, for example, is only ~0.1 eV, which is within the error of the DFT calculations.

Next, we investigated the formation of PC$^{\bullet-}$ for a set of cyanoarene-based PCs with different redox potentials and abilities to generate T_1; nine additional PCs were synthesized with different donor moieties (Fig. 3 and Supplementary Fig. 11). In most cases, the low-energy absorption bands appeared to red-shift relative to those of the PC; even 4-p,p-DCDP-IPN shows broad absorption band in the NIR region (Fig. 3j). These results indicate the broad applicability of our strategy. Furthermore, to verify the relevance of T_1 for PC$^{\bullet-}$ formation, two 4DP-IPN analogs (4-p-MCDP-IPN and 4-o,p-DCDP-IPN) with better E_{red}^* (i.e., a lower HOMO) but a negligibly small concentration of T_1, were prepared (Fig. 3, Supplementary Fig. 5, and Supplementary Table 4); this finding might be due to fast RISC mediated by vibronic coupling[61], and further in-depth investigations are currently underway. Interestingly, PC$^{\bullet-}$ was not noticeably generated for such PCs in our experimental conditions, clearly confirming that the long-lived T_1 generation of a PC is crucial for the formation of PC$^{\bullet-}$. Nevertheless, in most strongly twisted donor–acceptor structures, ^{3}PC* is efficiently generated; furthermore, by changing the donor and/or acceptor moieties, the redox potentials are delicately controlled over a broad range, enabling the use of radical ions with tailored redox potentials for a variety of highly efficient conventional photoredox catalysis, multiphoton excitation catalysis, and photoelectrocatalysis[13,15].

Photodegradation behavior of 4DP-IPN

The PC$^{\bullet-}$ formation was determined to be sensitive to the wavelength and intensity of irradiation. Spectral changes similar to those in the solutions of 4DP-IPN and DIPEA under 515 nm irradiation were observed when irradiated with a 455 nm LED for 1 min; however, the spectrum did not fully recover even after exposure to air, implying that the PC is likely to be degraded by 455 nm irradiation (Supplementary Fig. 8). In fact, continuous 455 nm LED irradiation over 5 min resulted in the photodegradation of 4DP-IPN (Fig. 4a and Supplementary Fig. 8c). These results suggest that the PC$^{\bullet-}$ can be efficiently generated under 455 nm LED irradiation, although followed by molecular degradation or unwanted chemical reactions[50–53].

We carefully monitored the degradation of 4DP-IPN in the presence of the sacrificial reductant (i.e., DIPEA) alone under both 455 and 515 nm LED irradiation, and the degradation under 455 nm illumination was much faster than that under 515 nm illumination. This can possibly be ascribed to differences in the absorption efficiencies ($\varepsilon = 9.0 \times 10^3\ M^{-1}\ cm^{-1}$ at 455 nm and $\varepsilon = 4.5 \times 10^2\ M^{-1}\ cm^{-1}$ at 515 nm). As illustrated in Fig. 4a, 4DP-IPN decomposed into two green luminescent compounds. After scaling up the reaction, we successfully isolated the photodegraded adducts. Intensive structural characterization via 1D/2D NMR analyses and mass spectroscopy clearly confirmed that one of the two CN groups of 4DP-IPN was substituted with a methyl group or hydrogen atom to yield 4DP-Me-BN (major product) and 4DP-H-BN (minor product), respectively (Supplementary Figs. 20, 21).

Control experiments were performed in combination with DFT calculations to investigate the mechanistic pathway of the 4DP-IPN degradation under the given conditions (Supplementary Figs. 18 and 19). Interestingly, no degradation could be identified by thin-layer chromatography (TLC) in the absence of DIPEA (Supplementary Fig. 18a), suggesting that DIPEA plays an important and specific role in the photodegradation process of 4DP-IPN. We thus assumed that long-lived 4DP-IPN$^{\bullet-}$ first formed in the presence of DIPEA, followed by the methyl and hydrogen substitution reaction of the PC$^{\bullet-}$. Here, the methyl and hydrogen seem to have been provided through the β-scission of the one-electron-oxidized adduct of DIPEA (DIPEA$^{\bullet+}$). In fact, the C–C (and C–H) bonds located in the β-position of DIPEA$^{\bullet+}$ are well known to be substantially weaker than those of neutral DIPEA; hence, β-scission normally occurs to generate the radical species[42,62–66], which was also well reproduced by our DFT calculations (Fig. 4b). Moreover, the possibility that the methyl and hydrogen originated from the solvent (CH_3CN) could be ruled out because in deuterated acetonitrile (CD_3CN), the CH_3 substitution reaction was still observed instead of the CD_3 substitution (Fig. 4a).

We further investigated the photodegradation of other cyanoarene-based PCs. As illustrated in Fig. 5, very interesting patterns emerged, which relied on the electronic properties (i.e., propensity for PC$^{\bullet-}$ formation) and structural features (i.e., steric environments nearby the CN group) of PCs. As in 4DP-IPN, methyl substitution at one of the two CN groups was observed for 3DP-Cz-IPN and 3DP-DCDP-IPN, both of which have similar electronic and structural properties compared with 4DP-IPN (Fig. 5a). However, in 4Cz-IPN and 4tCz-IPN, ethyl substitution occurred with a small amount of methyl substitution, suggesting that the steric environment near the CN group is a crucial factor in the substitution reaction (Fig. 5b). The ethyl group likely originates from the C–N bond cleavage of DIPEA$^{\bullet+}$ assisted by a 1,2-methyl shift. Indeed, the use of diisopropylmethylamine instead of DIPEA generated a CH_3-substituted adduct as a major product, which clearly supports our hypothesis.

Figure 5c shows the results of photodegradation experiments for the PCs in which PC$^{\bullet-}$ was not properly formed. No photodegradation was observed for 3DP-DMDP-IPN or 4-o,p-DCDP-IPN, whereas complex

https://doi.org/10.1038/s41467-022-35774-5

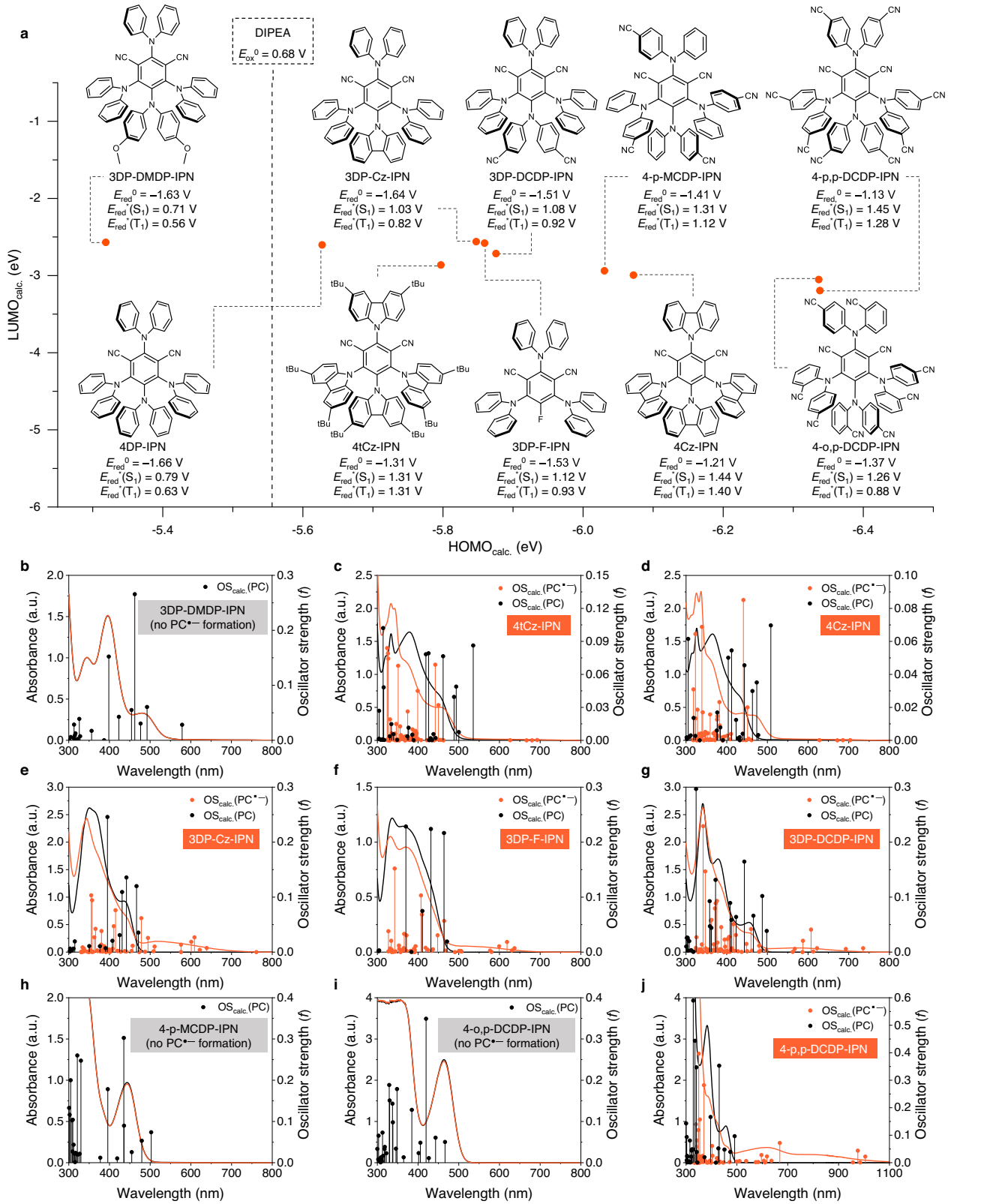

Fig. 3 | Formation of $PC^{\bullet-}$ of various cyanoarene-based PCs. a Chemical structures of selected cyanoarene-based PCs and their calculated HOMO and LUMO energies. UV-Vis absorption spectra of selected PC (black line) and $PC^{\bullet-}$ (orange line). It should be noted that the PCs prepared here contain six completely new compounds (3DP-DMDP-IPN, 3DP-Cz-IPN, 3DP-DCDP-IPN, 4-p-MCDP-IPN, 4-o,p-DCDP-IPN, and 4-p,p-DCDP-IPN). All ground state reduction potentials of PCs (E_{red}^0(PC)) were measured in the current work and their excited state reduction potentials (E_{red}^*(PC)) were estimated from $E_{red}^* = E_{0\text{-}0} + E_{red}^0$; $E_{0\text{-}0}(S_1)$ and $E_{0\text{-}0}(T_1)$ were evaluated by the onset of PL emission and gated PL emission, respectively, in CH_3CN at 65 K (except for 4tCz-IPN in DMF). UV-Vis absorption spectra were taken from the degassed solutions of PCs (1.0×10^{-4} M) and DIPEA (0.5 M) in CH_3CN right after illumination of two 3 W 455 nm LEDs for 1 min at RT, **b** 3DP-DMDP-IPN, **c** 4tCz-IPN, **d** 4Cz-IPN, **e** 3DP-Cz-IPN, **f** 3DP-F-IPN, **g** 3DP-DCDP-IPN, **h** 4-p-MCDP-IPN, **i** 4-o,p-DCDP-IPN, and **j** 4-p,p-DCDP-IPN. All solutions were prepared in a glove box and fully degassed. TD-DFT calculation results (oscillator strengths) are shown as stick spectra.

https://doi.org/10.1038/s41467-022-35774-5

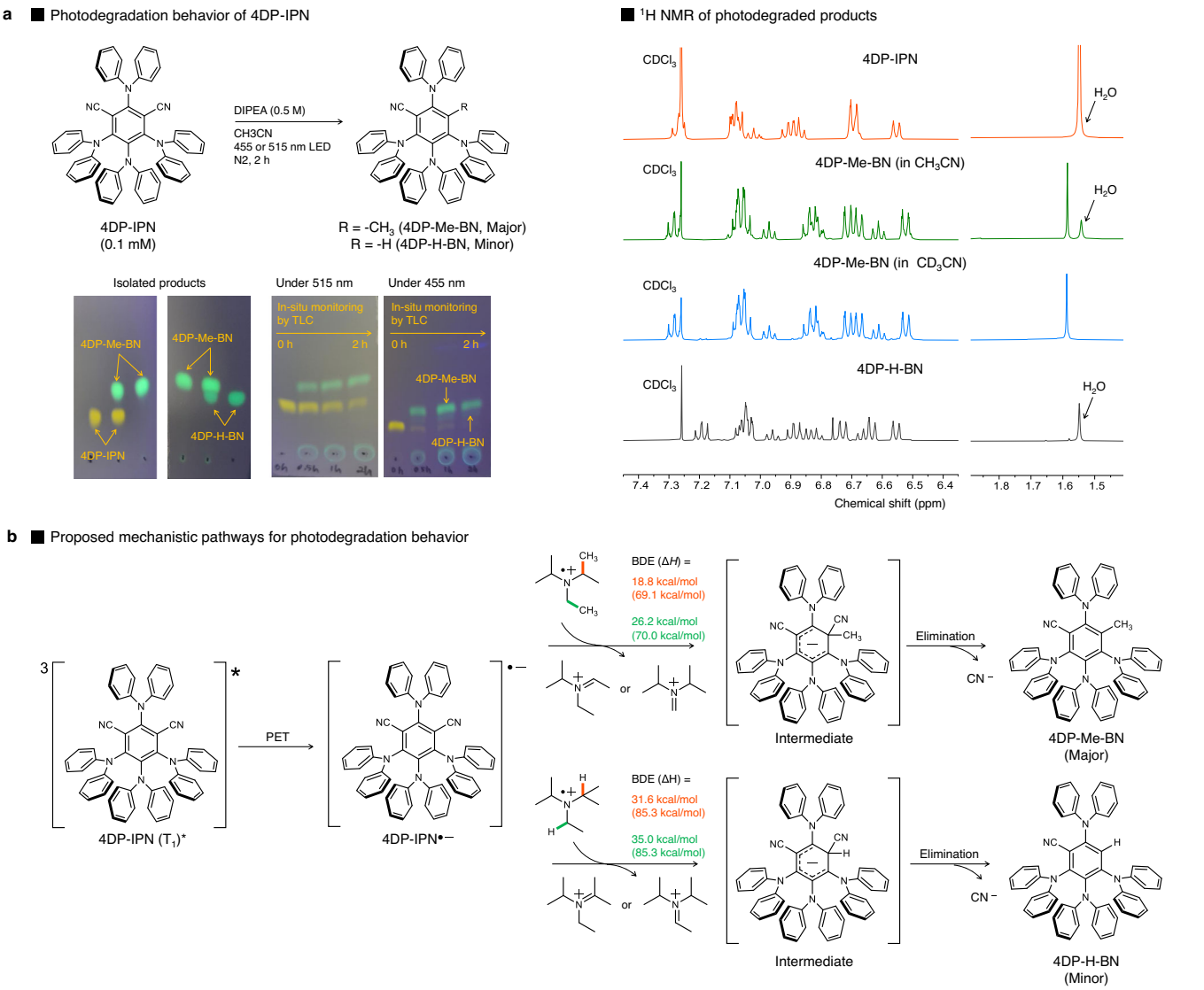

Fig. 4 | Photodegradation behavior of 4DP-IPN. a Reactions were performed with 4DP-IPN (1.0×10^{-4} M) and DIPEA (0.5 M) in CH_3CN under the illumination of two 3 W 515 nm LEDs or two 3 W 455 nm LEDs at RT. PC degradations were monitored in situ by TLC with eluent conditions (CH_2Cl_2:hexanes, 7:3 v/v). The photodegraded products were isolated by column chromatography, and ^1H NMR spectra confirmed that a methyl (and hydrogen) substitution reaction occurred at the CN position of 4DP-IPN to yield 4DP-Me-BN (and 4DP-H-BN). **b** Proposed mechanistic pathway for the photodegradation behavior of 4DP-IPN in the presence of DIPEA and DFT calculations for the bond dissociation energies (Δ*H*) in $DIPEA^{•+}$; the values in parenthesis correspond to the calculated bond dissociation energies in DIPEA.

degradation mixtures were formed in 4-p-MCDP-IPN. These results imply that in such PCs, no well-defined degradation pathway through the $PC^{•-}$ intermediate exists, and thus, the photodegradation behavior is determined by the intrinsic photostability of the PCs. Finally, we examined the photodegradation behavior of 3DP-F-IPN and 4-p,p-DCDP-IPN, which effectively generated $PC^{•-}$ and contain additional labile groups such as C–F bonds or other types of C–CN bonds. Complex reaction mixtures formed for both PCs, which was probably due to the degradation of these labile groups (Fig. 5d). Further in-depth investigations are currently underway to fully understand the photodegradation behaviors of cyanoarene-based PCs.

Dehalogenation of activated aryl/alkyl halides

Based on the experimental results discussed above, we assumed that the supra-efficient $PC^{•-}$ generation of 4DP-IPN and its highly negative E_{red}^0 of −1.66 V would enable the very efficient dehalogenation of aryl/alkyl halides. To that end, we first examined the feasibility of reducing 4-bromobenzonitrile ($E_{red}^0 = -1.83$ V), which was chosen as a substrate owing to its moderate reactivity, thereby allowing us to compare the catalytic performance of 4DP-IPN with those of well-known PCs. The reaction conditions were optimized by irradiating a mixture of 4-bromobenzonitrile, 4DP-IPN (0.005 mol%), and tertiary amines in degassed acetonitrile with a 455 nm LED light at room temperature. Although no conversion was achieved in the presence of five equivalents of TEA, the reduction product, benzonitrile, was obtained in 100% yield after 8 h using ten equivalents of DIPEA (Supplementary Table 5). This result is consistent with the PL quenching experiments, clearly indicating that the efficient generation of $PC^{•-}$ is a key factor in proceeding with the dehalogenation reaction. Notably, 455 nm LED irradiation gave better results (i.e., faster reaction kinetics) than 515 nm LED irradiation, which seems to contradict the UV-Vis absorption results concerning the photodegradation of the $PC^{•-}$. This inconsistency was most likely due to the fact that the ET between the $PC^{•-}$ and the substrate occurred much faster than the photodegradation of the $PC^{•-}$. To confirm our hypothesis, we investigated the photodegradation behavior of 4DP-IPN in actual reactions to dehalogenate various aryl halides (Fig. 6a) in which ten equivalents of DIPEA were used as a sacrificial agent. Aliquots of each reaction mixture were taken

https://doi.org/10.1038/s41467-022-35774-5

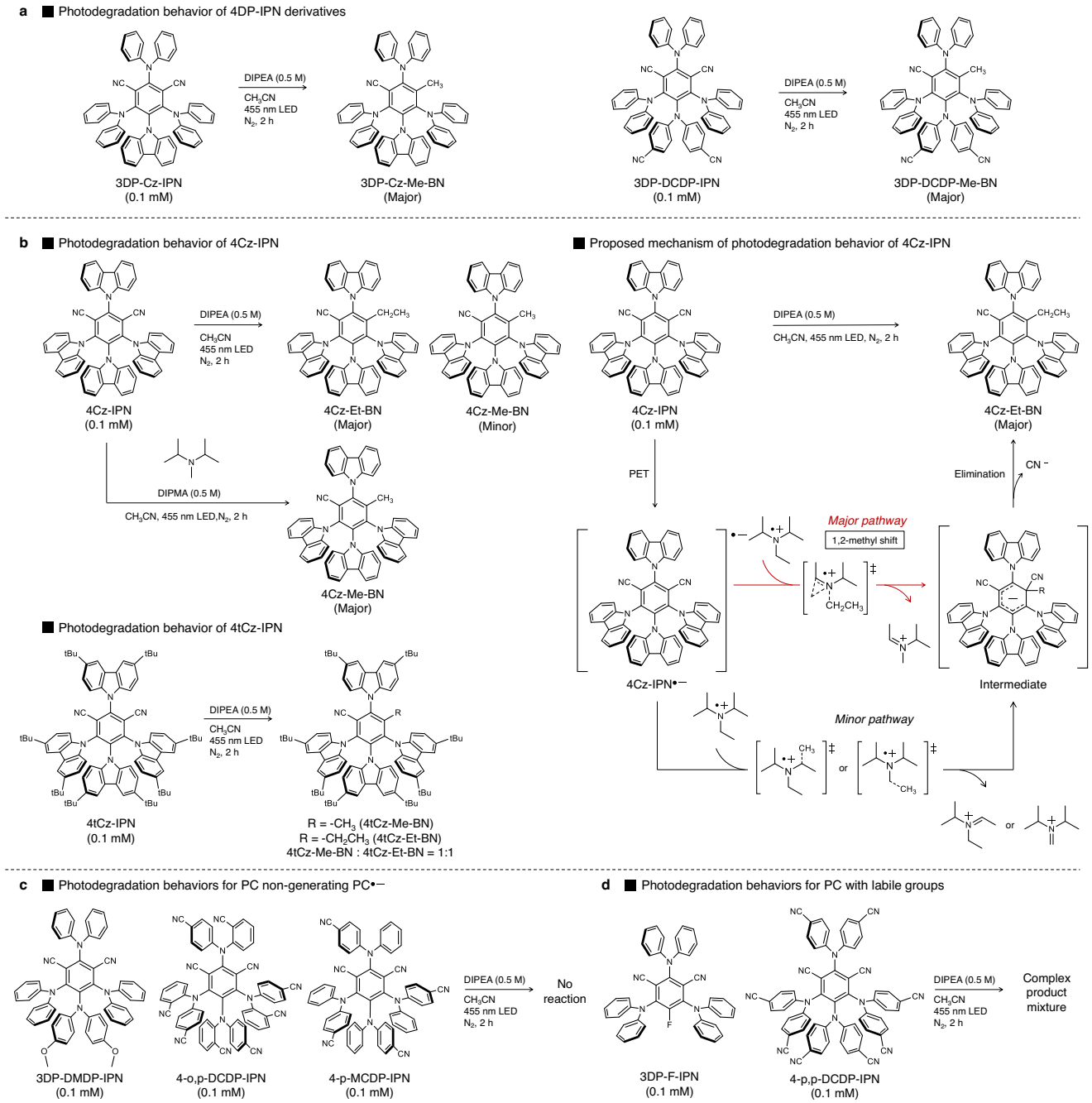

Fig. 5 | Photodegradation behaviors of various cyanoarene-based PCs. a Photodegradation behavior of 3DP-Cz-IPN and 3DP-DCDP-IPN. **b** Photodegradation behaviors of 4Cz-IPN and 4tCz-IPN and the proposed mechanism of photodegradation in the presence of DIPEA and DIPMA as a reducing agent. **c** Photodegradation behavior of PCs non-generating $PC^{\bullet-}$. **d** Photodegradation behaviors of PCs with labile groups. For the characterizations of the isolated products, see Supplementary Figs. 20–26 in the SI.

at a given time to monitor the progress of the reactions as well as the PC degradation. As only a small amount of PC (here, 1 mol%) was used, the degradation of the PC was monitored by TLC, whereas the reaction was tracked by ^{1}H NMR.

As shown in Fig. 6a: Reaction A, an 100% yield was obtained for 4-bromobenzonitrile in 1.5 h, while only a trace amount of the photodegradation product, 4DP-Me-BN, appeared; this implies that 4DP-IPN is an active PC for the dehalogenation of 4-bromobenzonitrile. More interestingly, the degradation of the PC was significantly retarded during the dehalogenation reaction compared to that in the presence of DIPEA alone (Fig. 6a: TLC). This was presumably due to the fact that the PC degradation competes with the dehalogenation reaction, as described in Fig. 6c. In other words, in the presence of 4-bromobenzonitrile, the ET from $4DP\text{-}IPN^{\bullet-}$ to 4-bromobenzonitrile seemed to be significantly faster than (i) the formation of $4DP\text{-}IPN^{\bullet-}$ and (ii) the substitution reaction to form 4DP-Me-BN, which results in a substantial delay in the PC degradation. In fact, faster PC degradation occurred in the dehalogenation reactions of more challenging substrates (i.e., 4-chlorobenzonitrile, 4-iodoanisole, and 4-bromoanisole in Fig. 6a: Reaction B, C, and D, respectively), further supporting our hypothesis.

In a further step, we examined the catalytic activity of the PC degradation adduct, 4DP-Me-BN (Fig. 6b), using 1 mol% of 4DP-Me-BN to proceed with the dehalogenation reactions of 4-bromobenzonitrile and 4-bromoanisole; note that the reactions proceeded under the

https://doi.org/10.1038/s41467-022-35774-5

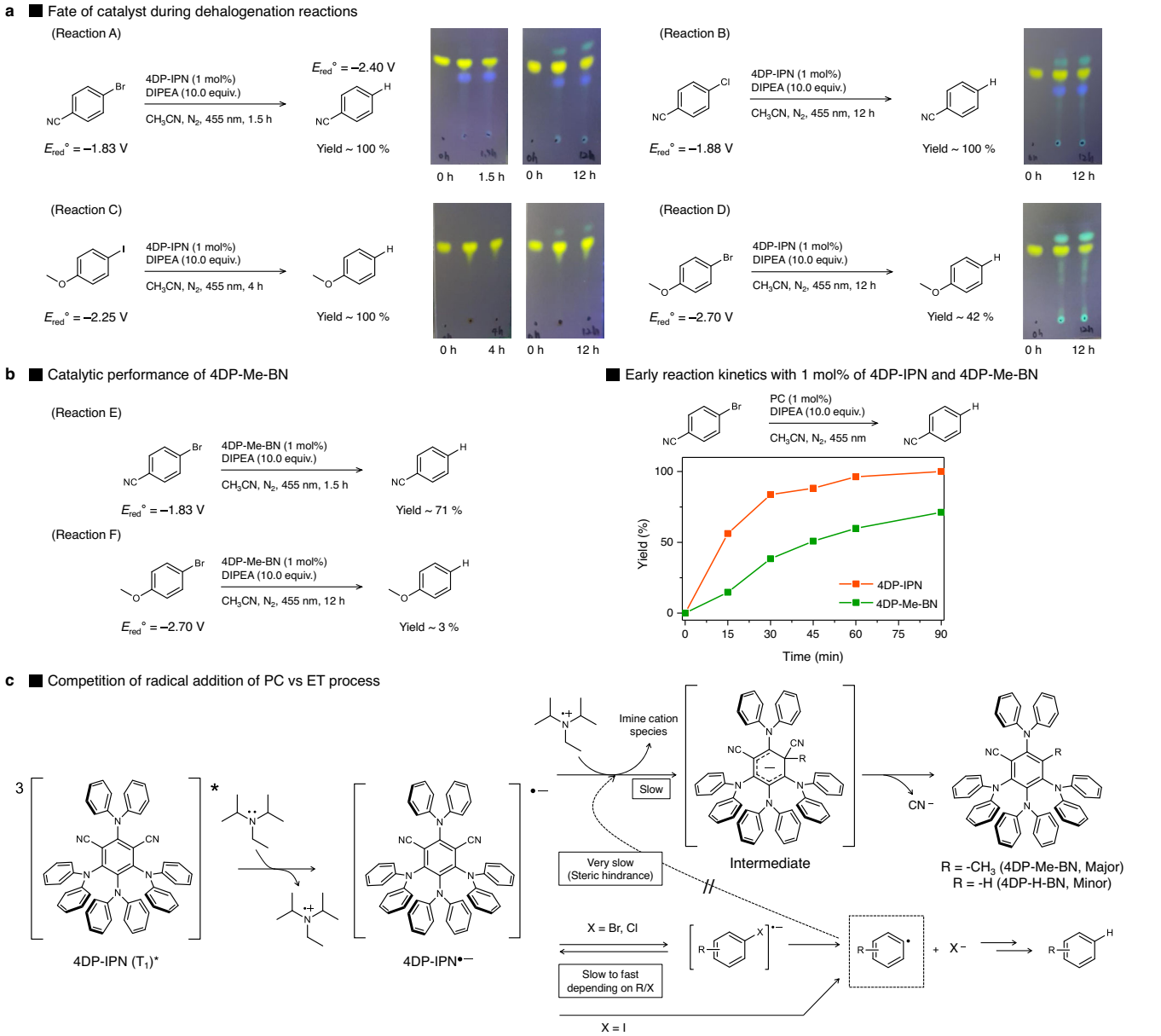

Fig. 6 | Photodegradation of 4DP-IPN in actual dehalogenation reactions. a Fate of catalyst during dehalogenation reactions. Reactions were performed with substrates (0.1 M), DIPEA (10.0 equiv.), and 4DP-IPN (1 mol%, 1.0×10^{-3} M) in CH_3CN (1 mL) under the illumination of two 3 W 455 nm LEDs for several hours at RT. Yields were determined by ^1H NMR using 1,3,5-trimethoxybenzene as an internal standard. PC degradation was monitored by in situ TLC with eluent conditions (EA:hexanes, 1:4 v/v). All redox potential values were obtained from the literature where the potential values were measured against the standard calomel electrode (SCE)[67,72,73]. **b** Catalytic performance of 4DP-Me-BN. Reactions were performed under the same conditions as in **a**. Early reaction kinetics of the dehalogenation reactions with 4DP-IPN (orange line) and 4DP-Me-BN (green line) were monitored on a 2 mL scale; the yields were determined by ^1H NMR using 1,3,5-trimethoxybenzene as an internal standard. **c** Proposed mechanistic pathways for the photodegradation of 4DP-IPN in the presence of aryl halides.

same conditions. With 4DP-Me-BN (4DP-IPN) as a PC, 71% (100%) and 3% (42%) yields were obtained for 4-bromobenzonitrile and 4-bromoanisole, respectively, indicating the lower catalytic performance of 4DP-Me-BN. Reaction kinetics studies of 4-bromobenzonitrile further confirmed the lower catalytic activity of 4DP-Me-BN than that of 4DP-IPN (Fig. 6b, right). More interestingly, when the continuous irradiation was prolonged to 12 h after the completion of the dehalogenation reaction of 4-bromobenzonitrile, only a small amount of the PC degradation adduct appeared, suggesting that the PC degradation was still retarded in the absence of 4-bromobenzonitrile (Fig. 6a: Reaction A, TLC). This might have been due to the fact that the reaction product, benzonitrile ($E_{red}° = -2.40$ V)[67], can act as an electron acceptor instead of 4-bromobenzonitrile, competing with the PC degradation process.

Finally, the molecular origin of the lower catalytic activity of 4DP-Me-BN was studied. According to DFT calculations, the substitution of CN by CH_3 did not significantly change the overall three-dimensional structure with respect to that of 4DP-IPN, thus still providing a strongly twisted donor–acceptor conformation (Fig. 7a). Nevertheless, the electronic structure substantially changed in 4DP-Me-BN. The substitution of the strongly electron-withdrawing CN group with the weakly electron-donating CH_3 in the central acceptor moiety increased both the HOMO and LUMO energies. However, the increase of 0.47 eV in the LUMO energy was considerably larger than that of the HOMO energy (0.11 eV) because the acceptor (where the LUMO is located; see Figs. 2a and 7a) was directly affected by CH_3 substitution, while the HOMO (mainly located on the donor) was only indirectly affected by

https://doi.org/10.1038/s41467-022-35774-5

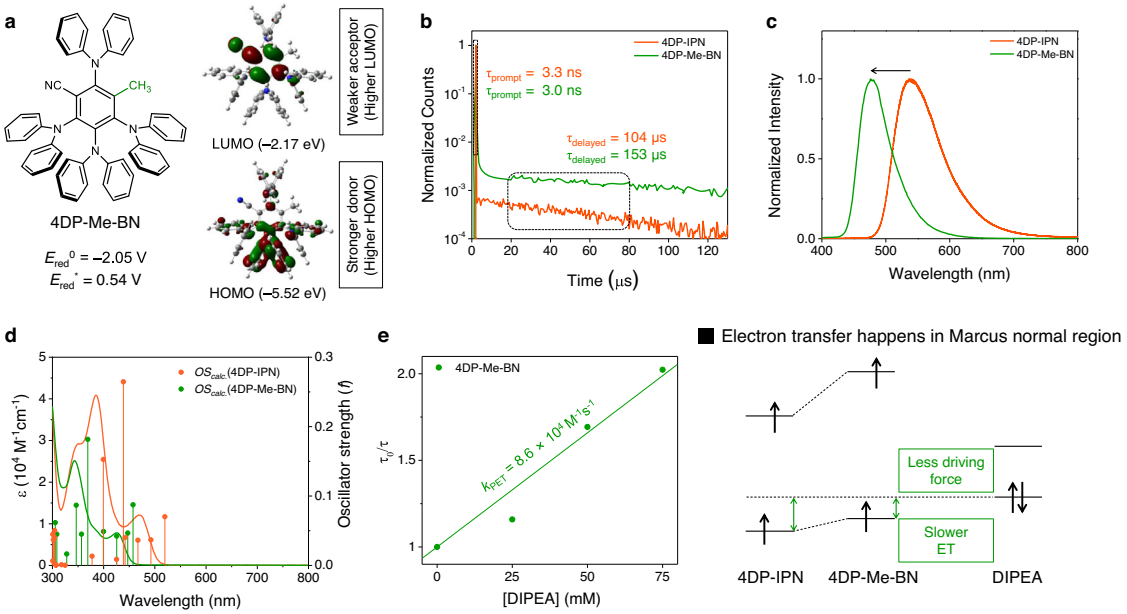

Fig. 7 | Characterization of 4DP-Me-BN. a Calculated energies and topologies of the frontier MO of 4DP-Me-BN. **b** PL decay of 4DP-IPN (1.0×10^{-5} M; orange line) and 4DP-Me-BN (1.0×10^{-5} M; green line) in CH_3CN at RT. **c** Steady-state PL emission spectra of 4DP-IPN (1.0×10^{-5} M; orange line) and 4DP-Me-BN (1.0×10^{-5} M; green line) in CH_3CN at RT. **d** UV-Vis absorption spectra of 4DP-IPN (1.0×10^{-5} M; orange line) and 4DP-Me-BN (1.0×10^{-5} M; green line) in CH_3CN at RT. TD-DFT results (oscillator strengths) are shown as stick spectra. **e** Stern–Volmer plots for the PL quenching of 4DP-Me-BN (1.0×10^{-5} M) in CH_3CN by DIPEA at RT. Stern–Volmer plots were obtained from PL decays of 4DP-Me-BN, excitation at λ_{ex} = 377 nm, and detection at λ_{det} = 470 nm.

the inductive effect caused by the decrease in the electron-withdrawing power of the acceptor unit.

Photophysical and electrochemical measurements of PCs species are well in accordance with their DFT calculations. Strongly delayed fluorescence with a long decay lifetime of 153 μs was seen in 4DP-Me-BN (Fig. 7b), indicating an intact thermally activated delayed fluorescence cycle not too different from that in 4DP-IPN. The UV-Vis absorption and PL emission spectra of 4DP-Me-BN showed a distinct blue shift with respect to those of 4DP-IPN (Fig. 7c, d), confirming the steeper increase in the LUMO energy upon CH_3 substitution than that of the HOMO. Finally, the lower excited state reduction potential (E_{red}^* = 0.54 V) and ground state reduction potential (E_{red}^0 = −2.05 V) of 4DP-Me-BN compared to those of 4DP-IPN (Supplementary Fig. 3) were also well supported by the DFT results, which revealed that 4DP-Me-BN exhibited higher HOMO and LUMO energies.

The fact that the catalytic performance of 4DP-Me-BN was worse than that of 4DP-IPN might be surprising, considering that 4DP-Me-BN has a (i) highly negative reduction potential, (ii) decent long-lived T_1 generation, and (iii) greatly improved stability. However, we concluded that the catalytic activity might have been impaired by i) the very low light absorption of 4DP-Me-BN ($\varepsilon = 1.1 \times 10^3$ $M^{-1}cm^{-1}$ at 455 nm), as observed in the UV-Vis absorption spectrum (Fig. 7d), and (ii) a decrease in the PET rate between 4DP-Me-BN and DIPEA owing to the lowered excited state reduction potential of 4DP-Me-BN. In fact, the k_{PET} of 4DP-Me-BN in the presence of DIPEA measured by a PL quenching experiment was 8.6×10^4 $M^{-1}s^{-1}$, approximately one order of magnitude lower than that of 4DP-IPN, which was consistent with Marcus normal region behavior described above (Fig. 7e), thus supporting our hypothesis.

Using the optimized conditions, we screened different PCs. As shown in Table 1, 4DP-IPN outperformed the other PCs used for comparison. $Ru(bpy_3)Cl_2$ and $Ru(phen)_3(PF_6)_2$, which are commonly used as PCs for reductive cycles, gave very low yields of 13 and 0%, respectively, even at high catalyst loadings of 5 mol%; this might have been caused by the less negative reduction potential of the catalysts ($E_{red}^0(Ru(bpy)_3^{2+})$ = −1.33 V and $E_{red}^0(Ru(phen)_3^{2+})$ = −1.36 V) compared to that of 4DP-IPN (−1.66 V)[57]. Rh6G and PDI employed as PCs for ConPET showed yields of 2 and 4%, respectively, at 5 mol% PC loadings. Although the one-electron-reduced forms of those PCs are known to have highly negative excited state oxidation potentials ($E_{ox}^*(PDI^{\bullet-})$ = −1.87 V and $E_{ox}^*(Rh6G^{\bullet-})$ = −2.40 V)[28,30], the excited state populations of $Rh6G^{\bullet-}$ and $PDI^{\bullet-}$ were low because of their short excited state lifetimes; this might have led to inefficient ET with 4-bromobenzonitrile and hence very low yields. On the other hand, $Ir(ppy)_3$, known as a PC for oxidative cycles[9], showed decent catalytic activity, but to give comparable yields, it required 100 times higher PC loading (0.5 mol%) compared to that of 4DP-IPN. The higher required catalyst loading might have been due to the relatively shorter excited state lifetime of $Ir(ppy)_3$ compared with that of $4DP\text{-}IPN^{\bullet-}$, despite the highly negative excited state oxidation potential of $Ir(ppy)_3$ ($E_{ox}^*(Ir(ppy)_3)$ = −1.73 V). Finally, the reaction scope was explored in the presence of 4DP-IPN (0.05–0.005 mol%) for a range of differently substituted aryl/alkyl halides with ground state reduction potentials of less than −2.2 V, which gave corresponding reduction products in nearly quantitative yields (Fig. 9, Activated aryl/alkyl halides).

Oxygen tolerance

At a higher 4DP-IPN concentration of 0.05 mol%, the reaction of 4-bromobenzonitrile gave a quantitative yield without degassing (Fig. 8b), which enabled a facile gram-scaled reaction under ambient conditions without any preceding degassing (Fig. 9). To understand the origin of this high oxygen tolerance, the kinetics of the reaction with and without degassing were monitored. An inhibition period clearly appeared under non-degassed conditions but not under fully degassed conditions (Fig. 8c). These results imply that dissolved oxygen in the mixture solutions was fully consumed before starting the reductive dehalogenation reaction. According to the previous reports[68–70], oxygen could be consumed through the generation of reactive oxygen species (i.e., singlet oxygen and superoxide anion) and their subsequent reaction with DIPEA and/or its cationic intermediates. The kinetics of the photoredox catalytic reactions of 4-bromobenzonitrile with and without degassing process were then

https://doi.org/10.1038/s41467-022-35774-5

Table 1 | Results of reductive dehalogenation of 4-bromobenzonitrile with a variety of PCs

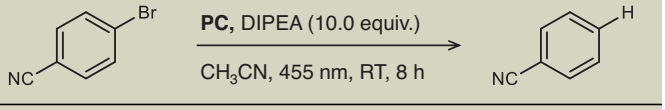

Entry	PC	Loading (mol%)	Yield (%)
1	–	–	0
2	$Ru(bpy)_3Cl_2$	5	13
3	$Ru(phen)_3(PF_6)_2$	5	0
4	Rh6G	5	2
5[a]	PDI	5	0
6[a,b]		5	4
7	4Cz-IPN	5	75
8[a]	$Ir(ppy)_3$	5	100
9		0.5	100
10		0.05	26
11		0.005	0
12	4DP-IPN	5	100
13		0.5	100
14		0.05	100
15		0.005	100
†16[c]		0.005	0
†17[d]		0.005	0

Reactions were performed with 4-bromobenzonitrile (0.1 M), PC (5–0.005 mol%), and DIPEA (10.0 equiv.) in CH_3CN (1 mL) under the illumination of two 3 W 455 nm LEDs for 8 h at RT. All solutions were prepared inside a glove box and degassed by bubbling with Ar. Yields were determined by GC-FID.

†1H NMR using 1,3,5-trimethoxybenzene as an internal standard.

[a]Reaction performed in DMF due to solubility.

[b–d]Control experiments were performed [b]with TEA instead of DIPEA, [c]in the absence of DIPEA, or [d]in the dark conditions.

simulated using the mechanistic model described in Fig. 8a (see Supplementary Fig. 15 and Supplementary Table 7 in the SI for details of the kinetics simulation); all parameters including the rate constants used in the kinetics simulations were obtained from the experiments or from the literature. As shown in Fig. 8c (green line with open squares), the experimental trends were quite well reproduced by the kinetics simulations, supporting our hypothesis. Although these trends were well simulated, a substantial discrepancy appeared between the simulated and experimental kinetics, which was likely due to the fact that ET was overestimated, and BET was not considered in the model. In fact, the nonlinearity observed in the experimental kinetics was adequately reproduced in the simulations by considering the adequate BET for a slower ET (Fig. 8c; green line with open circles). However, significant discrepancies were still observed for dehalogenation reactions in the presence of oxygen (Fig. 8c, right). This is probably due to the depletion of the tertiary amines by reactive oxygen species, which is not considered in model[69,70]. indeed, in air, the oxygen tolerance was determined depending on the amount of DIPEA (Supplementary Table 8).

The experimental results thus far suggest that the dehalogenation of activated aryl/alkyl halides at very low PC loadings and the high oxygen tolerance arise from the highly efficient generation of both the long-lived T_1 of 4DP-IPN and the $PC^{\bullet-}$ with a highly negative E_{red}^0(4DP-IPN) of −1.66 V. In particular, high $PC^{\bullet-}$ concentrations apparently led to the highly efficient dehalogenation of the halides by overcoming the potential barrier of ~0.5 V without involving the ConPET process. In fact, the addition of 4-bromobenzonitrile into the solution of 4DP-$IPN^{\bullet-}$ induced the perfect regeneration of 4DP-IPN, clearly indicating that direct ET occurs between 4DP-$IPN^{\bullet-}$ and 4-bromobenzonitrile, and thus, that ConPET was not involved in this case (Supplementary Fig. 12).

Dehalogenation of inactivated aryl/alkyl halides

Finally, the dehalogenation of inactivated aryl/alkyl halides was explored. The E_{red}^0 values of the substrates were ranged from −2.2 to −3.0 V, which were expected to be difficult to overcome by conventional photoredox catalysis. However, despite the very high potential energy barrier, moderate to high yields were mostly attained at higher PC loadings (5–0.5 mol%). We thus presumed that ConPET was involved in the dehalogenation of inactivated halides. In fact, the excited state oxidation potential of 4DP-$IPN^{\bullet-}$ was estimated to be −3.38 V according to Eq. (2), which corresponds to the D_2 state; relying on Koopmans theorem, this corresponds to an energy of −1.30 eV. According to the (TD-)DFT calculations, the D_1 state could also contribute to ConPET. However, considering the energies and corresponding reducing powers (i.e., E_{ox}^*(4DP-$IPN^{\bullet-}$ at D_1) = −2.51 V), the D_2 state was likely to be responsible for ConPET. In fact, the excited state lifetime of D_2 was expected to be sufficiently long, as the energy gap between D_2 and D_1 (0.87 eV from $E_{theo}(D_1–D_2) = E_{0\text{-}0,exp}(PC^{\bullet-}) - E_{theo}(D_0–D_1)$, Supplementary Fig. 14) was similar to that between D_1 and D_0 (0.85 eV, Supplementary Fig. 14); this should effectively slow down the internal conversion from D_2 and thus enhance the D_2 lifetime, not considering here any barriers to internal conversion via conical intersections, which could additionally stabilize the D_2 state.

$$E_{ox}^*(PC^{\bullet-}) = -E_{0-0}(PC^{\bullet-}) + E_{red}^0(PC) \quad (2)$$

Thus, the excited state oxidation potential of 4DP-$IPN^{\bullet-}$ was high enough to reduce the inactivated aryl/alkyl halides. Despite similar reduction potentials, aryl chloride gave a lower yield than aryl bromide, even with higher PC loadings (i.e., chlorobenzene vs 4-bromoanisole, see Fig. 9). This might be attributed to the slow bond dissociation of the aryl chloride anion owing to the strong C–Cl bond, facilitating BET from the aryl chloride anion to PC or DIPEA derivatives.

The participation of ConPET in the case of 4-bromoanisole was corroborated by the following semi-quantitative quenching experiments (Supplementary Fig. 12). In fact, the addition of an excess amount of 4-bromobenzonitrile (E_{red}^0 = −1.83 V) to the preformed solution of 4DP-$IPN^{\bullet-}$ distinctly changed the color from dark green to yellow in a few seconds, which is indicative of the regeneration of 4DP-IPN. In contrast, the solution of 4DP-$IPN^{\bullet-}$ showed no evident color change in the presence of excess 4-bromoanisole (E_{red}^0 = −2.70 V). This suggests that fast ET between 4DP-$IPN^{\bullet-}$ and 4-bromoanisole might be ruled out and that a multiphoton excitation process (i.e., ConPET) might be involved. However, given the low to moderate yields of inactivated aryl chlorides, it seems that the ConPET process was not very efficient here (Fig. 9). This was presumably due to the short excited state lifetime of 4DP-$IPN^{\bullet-}$, which was supported by the fact that steady-state PL emission was not observed for the solution of 4DP-$IPN^{\bullet-}$ (Supplementary Fig. 10). Of course, other possible pathways, such as a halogen atom transfer (XAT) by α-aminoalkyl radicals recently proposed by Leonori et al.[71], cannot be excluded. Further investigation of the excited state dynamics of $PC^{\bullet-}$ and related ConPET processes is underway.

Discussion

We investigated the formation and degradation of one-electron reduced cyanoarene-based PCs under widely-used photoredox-mediated reaction conditions and found that the cyanoarenes exhibiting both ultra-efficient generation of long-lived T_1 and adequately positive E_{red}^* enabled these PCs to efficiently form $PC^{\bullet-}$ under mildly visible light illumination. We further investigated (i) the photodegradation of various cyanoarene-based PCs with

https://doi.org/10.1038/s41467-022-35774-5

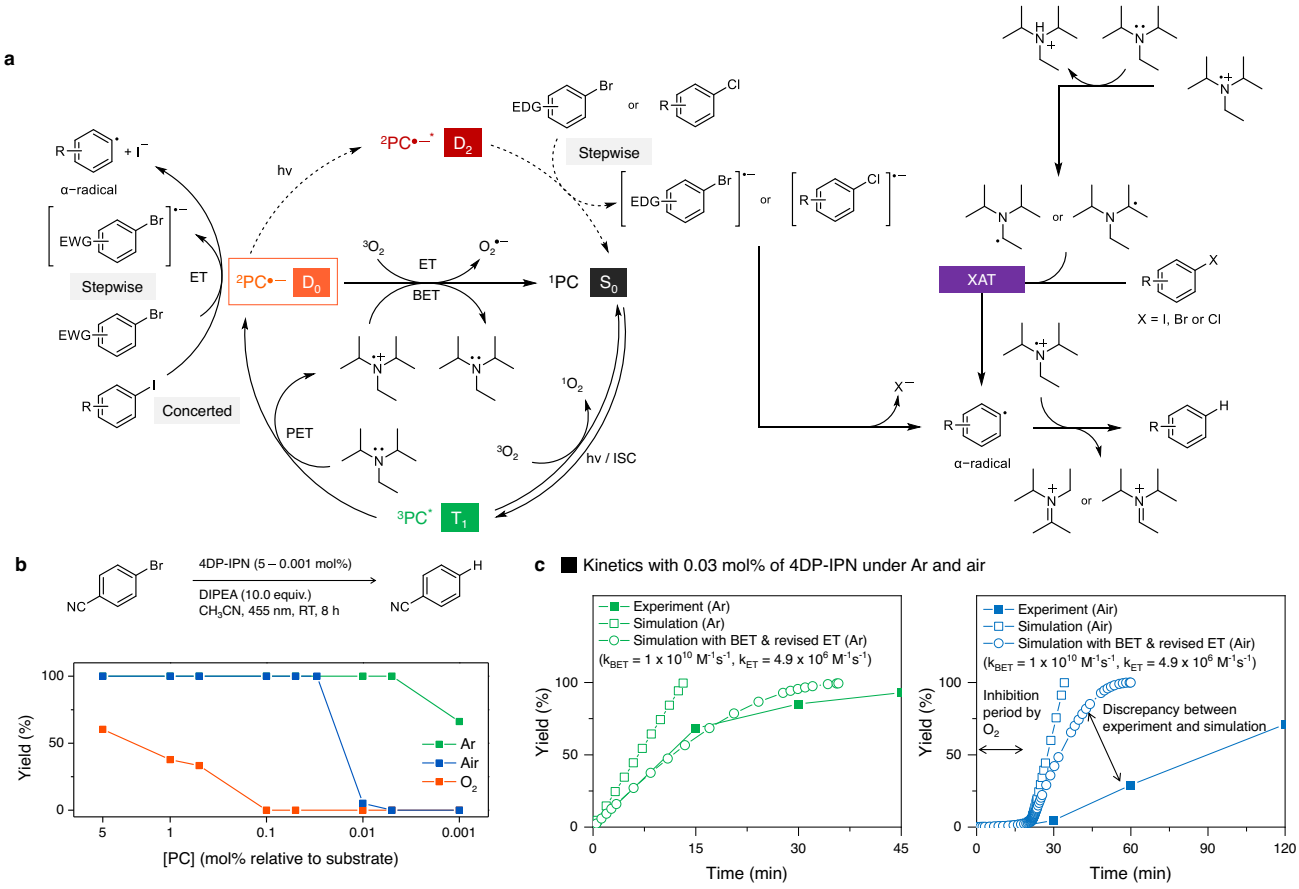

Fig. 8 | Oxygen tolerance in the dehalogenation reactions. a Proposed mechanism of the photocatalyzed reductive dehalogenation of aryl halides mediated by $^2PC^{\bullet-}$. Here, (B)ET and XAT denote (back)electron transfer and halogen atom transfer, respectively. **b** Effect of oxygen for the reductive dehalogenation of 4-bromobenzonitrile with 4DP-IPN as a PC in the presence of Ar (green-filled squares), air (blue-filled squares), and O_2 (orange-filled squares). Reactions were performed with 4-bromobenzonitrile (0.1 M), DIPEA (10.0 equiv.), and 4DP-IPN (5–0.001 mol%) in CH_3CN under the illumination of two 3 W 455 nm LEDs for 8 h. **c** Experimental (filled squares) and simulated (empty squares) reaction kinetics of photoredox-mediated reductive dehalogenation of 4-bromobenzonitrile with 4DP-IPN (0.03 mol%) under Ar and air atmospheres in a closed glass vial; simulated (empty circles) reaction kinetics indicate that the BET process ($k_{BET} = 1 \times 10^{10}\ M^{-1}\ s^{-1}$) and a slower ET process ($k_{ET} = 4.9 \times 10^6\ M^{-1}\ s^{-1}$) are involved. Kinetics simulations were performed based on the proposed mechanism described in Supplementary Fig. 15. The rate constants for all processes were evaluated from experiments or calculations (see Supplementary Fig. 15 and Supplementary Table 7 for the full details of the kinetics simulation).

different electronic and steric properties and (ii) the photodegradation of 4DP-IPN in actual dehalogenation reactions with different substrates, providing significant insights into the photoredox catalysis carried out by cyanoarene-based PCs. Based on the in-depth analysis of photodegradation behaviors, we also demonstrated highly efficient reductive dehalogenation, indicating that it is possible to significantly reduce PC loading when photodegradation processes are not involved. We believe that our work will provide a better understanding of the formation, degradation, and photochemical/electrochemical features of $PC^{\bullet-}$. Moreover, our results pave the way to in-depth knowledge of the reductive cycles and the stability of PCs in purely organic PC-driven photoredox catalysis, which can be applied to address many challenging issues in a variety of photoredox-mediated organic reactions and polymerizations.

Methods

General procedure for generation of $PC^{\bullet-}$

Inside the glove box, a sealable quartz cuvette was charged with PC (1.0×10^{-4} M) and DIPEA (0.5 M) in 3 mL of anhydrous CH_3CN. After that, the quartz cuvette was capped with a screw cap and sealed with parafilm. Subsequently, the reaction was carried out under the illumination of two 3 W 455 or 515 nm LEDs for 1 min at RT. After illumination, UV-Vis absorption spectra of the illuminated solutions were measured immediately. In preparation for the reaction, pre-prepared stock solutions of the PCs were used for higher reproducibility of results.

General procedure for PC photodegradation

Outside the glove box, a 20 mL glass vial equipped with a stirring bar was charged with PC (1.0×10^{-4} M) and DIPEA (0.5 M) in 1 mL of anhydrous CH_3CN as a solvent. Then, the vial was capped with a rubber septum or screw cap and sealed with parafilm. The reaction batches were purged with N_2 (99.999%) for 30 min. Subsequently, the reaction was carried out for 2 h under the illumination of two 3 W 455 nm LEDs at RT. Without the work-up process, the aliquots of the crude reaction mixture were diluted by CH_2Cl_2 and monitored by TLC. In preparation for the reaction, pre-prepared stock solutions of the PCs were used for higher reproducibility of results. For the scale-up reaction of photodegradation, a 20 mL glass vial equipped with a stirring bar was charged with PC (1.0×10^{-2} M) and DIPEA (1 M) in 5–6 mL of anhydrous CH_3CN as a solvent. Then, the vial was capped with a rubber septum or

https://doi.org/10.1038/s41467-022-35774-5

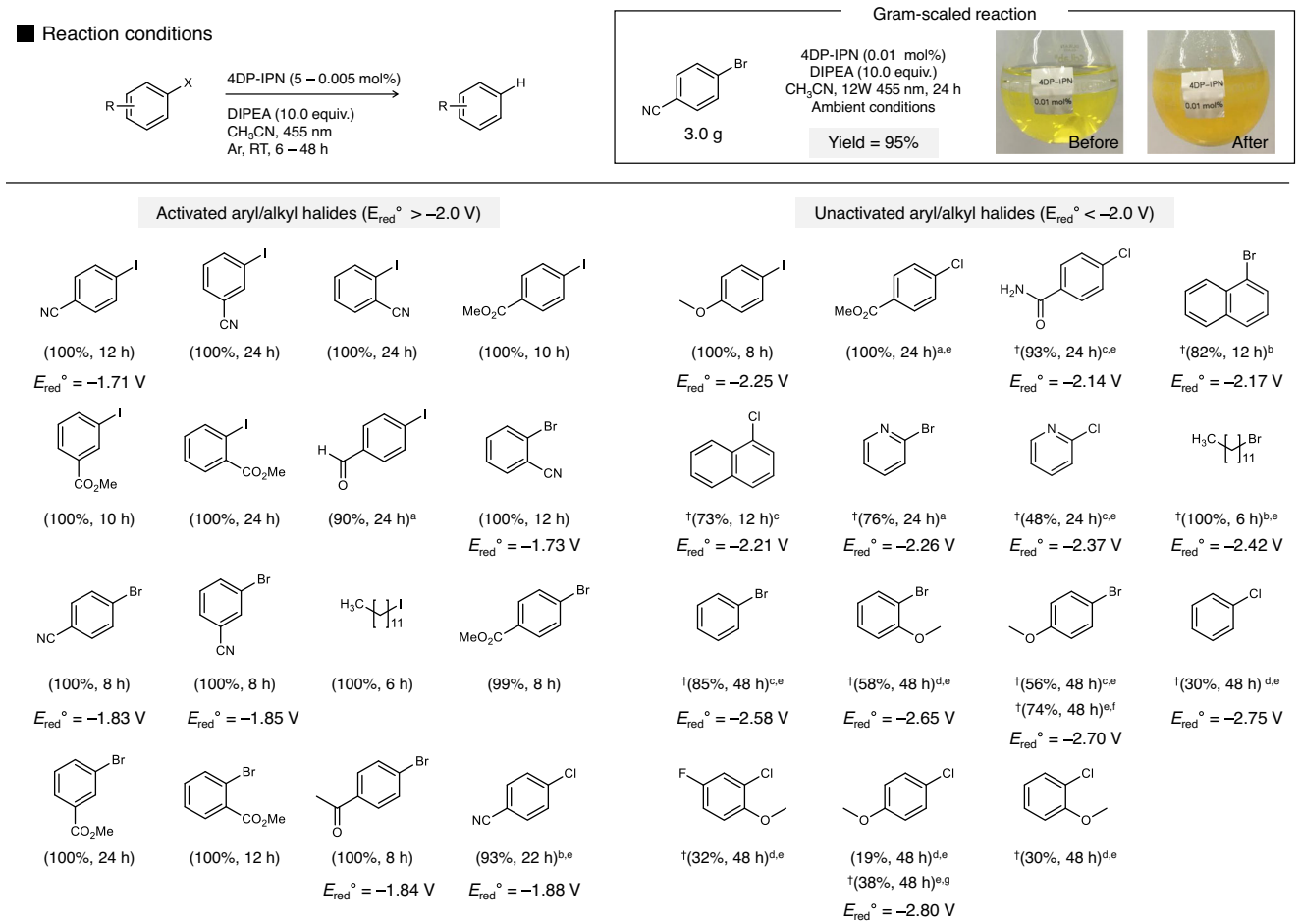

Fig. 9 | Results of reductive dehalogenation of various aryl/alkyl halides in the presence of 4DP-IPN as a PC. Reactions were performed with substrates (0.1 M), DIPEA (10.0 equiv.), and 4DP-IPN (0.005 mol%) in CH_3CN (1 mL) under the illumination of two 3 W 455 nm LEDs for 6 to 48 h at RT. The gram-scaled reaction was performed with 4-bromobenzonitrile (3.0 g, 16.48 mmol), DIPEA (10.0 equiv.), and 4DP-IPN (0.01 mol%) in CH_3CN (30 mL) with irradiation by four 3 W 455 nm LEDs under ambient conditions without any degassing. Reactions were performed with [a]0.01 mol%, [b]0.05 mol%, [c]0.5 mol%, and [d]5 mol% 4DP-IPN, and [e]illumination by four 3 W 455 nm LEDs. Injection of a total of [f]1.5 mol% and [g]3 mol% 4DP-IPN divided over three additions every 16 h during the course of the reaction. Yields were determined by GC-FID or [†]^{1}H NMR using 1,3,5-trimethoxybenzene as an internal standard. All redox potential values were obtained from the literature, where the potential values were measured against the SCE[72–77].

screw cap and sealed with parafilm. Subsequently, the reaction was carried out for 2 h under the illumination of four 3 W 455 nm LEDs at RT without degassing process[53]. Afterward, the reaction mixture was evaporated under low pressure and the concentrated crude products were further purified by column chromatography on silica gel.

General procedure for photoredox reductive dehalogenation

Inside the glove box, a 20 mL glass vial equipped with a stirring bar was charged with aryl halides (0.1 mmol), DIPEA (174 µL, 1 mmol), PC (5–0.001 mol% to relative aryl halides), 1,3,5-trimethoxybenzene (33.6 mg, 0.2 mmol) as an internal standard for GC-FID and ^{1}H NMR, and anhydrous CH_3CN (1 mL, 0.1 M of aryl halides) as solvent. After, the vial was capped with a rubber septum or screw cap and sealed with parafilm. The reaction batches were purged with Ar (99.9999%) (or with air or with O_2 (99.995%)) for 30 min outside the glove box. Subsequently, the reaction was carried out for hours under the illumination of two 3 W 455 nm LEDs at RT. Without a work-up process, the aliquots of the crude reaction mixture were analyzed by GC-FID or ^{1}H NMR to obtain yields of dehalogenated products. In preparation for the reaction, pre-prepared stock solutions of the PCs were used for the higher reproducibility of results.

Data availability

The authors declare that the data supporting the findings of this study are available within the paper and its Supplementary Information.

References

1. Romero, N. A. & Nicewicz, D. A. Organic photoredox catalysis. *Chem. Rev.* **116**, 10075–10166 (2016).
2. Prier, C. K., Rankic, D. A. & MacMillan, D. W. C. Visible light photoredox catalysis with transition metal complexes: applications in organic synthesis. *Chem. Rev.* **113**, 5322–5363 (2013).
3. Yoon, T. P., Ischay, M. A. & Du, J. Visible light photocatalysis as a greener approach to photochemical synthesis. *Nat. Chem.* **2**, 527–532 (2010).
4. Narayanam, J. M. R. & Stephenson, C. R. J. Visible light photoredox catalysis: applications in organic synthesis. *Chem. Soc. Rev.* **40**, 102–113 (2011).
5. Buzzetti, L., Crisenza, G. E. M. & Melchiorre, P. Mechanistic studies in photocatalysis. *Angew. Chem. Int. Ed.* **58**, 3730–3747 (2019).
6. Nicewicz, D. A. & Nguyen, T. M. Recent applications of organic dyes as photoredox catalysts in organic synthesis. *ACS Catal.* **4**, 355–360 (2014).

7. Nicewicz, D. A. & MacMillan, D. W. C. Merging photoredox catalysis with organocatalysis: the direct asymmetric alkylation of aldehydes. *Science* **322**, 77–80 (2008).
8. MacKenzie, I. A. et al. Discovery and characterization of an acridine radical photoreductant. *Nature* **580**, 76–80 (2020).
9. Nguyen, J. D., D'Amato, E. M., Narayanam, J. M. R. & Stephenson, C. R. J. Engaging unactivated alkyl, alkenyl and aryl iodides in visible-light-mediated free radical reactions. *Nat. Chem.* **4**, 854–859 (2012).
10. Cybularczyk-Cecotka, M., Szczepanik, J. & Giedyk, M. Photocatalytic strategies for the activation of organic chlorides. *Nat. Catal.* **3**, 872–886 (2020).
11. Bryden, M. A. & Zysman-Colman, E. Organic thermally activated delayed fluorescence (TADF) compounds used in photocatalysis. *Chem. Soc. Rev.* **50**, 7587–7680 (2021).
12. Kim, H. & Lee, C. Visible-light-induced photocatalytic reductive transformations of organohalides. *Angew. Chem. Int. Ed.* **51**, 12469–12472 (2012).
13. Lee, Y. & Kwon, M. S. Emerging organic photoredox catalysts for organic transformations. *Eur. J. Org. Chem.* **2020**, 6028–6043 (2020).
14. Wu, C., Liu, W., Lim, C. H., Miyake, G. & Lim, C. H. Rational design of photocatalysts for controlled polymerization: effect of structures on photocatalytic activities. *Chem. Rev.* **122**, 5476–5518 (2021).
15. Singh, V. K. et al. Highly efficient organic photocatalysts discovered via a computer-aided-design strategy for visible-light-driven atom transfer radical polymerization. *Nat. Catal.* **1**, 794–804 (2018).
16. Lee, Y. et al. A water-soluble organic photocatalyst discovered for highly efficient additive-free visible-light-driven grafting of polymers from a protein at ambient and aqueous enviornments. *Adv. Mater.* **34**, 2108446 (2022).
17. Lee, Y., Boyer, C. & Kwon, M. S. Visible-light-driven polymerization towards the green synthesis of plastics. *Nat. Rev. Mater.* **7**, 74–75 (2021).
18. Fors, B. P. & Hawker, C. J. Control of a living radical polymerization of methacrylates by light. *Angew. Chem. Int. Ed.* **51**, 8850–8853 (2012).
19. Theriot, J. C. et al. Organocatalyzed atom transfer radical polymerization driven by visible light. *Science* **352**, 1082–1086 (2016).
20. Xu, J., Jung, K., Atme, A., Shanmugam, S. & Boyer, C. A robust and versatile photoinduced living polymerization of conjugated and unconjugated monomers and its oxygen tolerance. *J. Am. Chem. Soc.* **136**, 5508–5519 (2014).
21. Glaser, F., Kerzig, C. & Wenger, O. S. Multi-photon excitation in photoredox catalysis: concepts, applications, methods. *Angew. Chem. Int. Ed.* **59**, 10266–10284 (2020).
22. Ghosh, I., Ghosh, T., Bardagi, J. I. & König, B. Reduction of aryl halides by consecutive visible light-induced electron transfer processes. *Science* **346**, 725–728 (2014).
23. Giedyk, M. et al. Photocatalytic activation of alkyl chlorides by assembly-promoted single electron transfer in microheterogeneous solutions. *Nat. Catal.* **3**, 40–47 (2020).
24. Bardagi, J. I., Ghosh, I., Schmalzbauer, M., Ghosh, T. & König, B. Anthraquinones as photoredox catalysts for the reductive activation of aryl halides. *Eur. J. Org. Chem.* **2018**, 34–40 (2018).
25. Barham, J. P. & König, B. Synthetic photoelectrochemistry. *Angew. Chem. Int. Ed.* **59**, 11732–11747 (2020).
26. Wu, S., Kaur, J., Karl, T. A., Tian, X. & Barham, J. P. Synthetic molecular photoelectrochemistry: new frontiers in synthetic applications, mechanistic insights and scalability. *Angew. Chem. Int. Ed.* **61**, e202107811 (2022).
27. Cowper, N. G. W., Chernowsky, C. P., Williams, O. P. & Wickens, Z. K. Potent reductants via electron-primed photoredox catalysis: unlocking aryl chlorides for radical coupling. *J. Am. Chem. Soc.* **142**, 2093–2099 (2020).
28. Zeman, C. J., Kim, S., Zhang, F. & Schanze, K. S. Direct observation of the reduction of aryl halides by a photoexcited perylene diimide radical anion. *J. Am. Chem. Soc.* **142**, 2204–2207 (2020).
29. Tlili, A. & Lakhdar, S. Acridinium salts and cyanoarenes as powerful photocatalysts: opportunities in organic Synthesis. *Angew. Chem. Int. Ed.* **133**, 19678–19701 (2021).
30. Marzo, L., Ghosh, I., Esteban, F. & König, B. Metal-free photocatalyzed cross coupling of bromoheteroarenes with pyrroles. *ACS Catal.* **6**, 6780–6784 (2016).
31. Narayanam, J. M. R., Tucker, J. W. & Stephenson, C. R. J. Electron-transfer photoredox catalysis: development of a tin-free reductive dehalogenation reaction. *J. Am. Chem. Soc.* **131**, 8756–8757 (2009).
32. Tucker, J. W., Nguyen, J. D., Narayanam, J. M. R., Krabbe, S. W. & Stephenson, C. R. J. Tin-free radical cyclization reactions initiated by visible light photoredox catalysis. *Chem. Commun.* **46**, 4985–4987 (2010).
33. Nguyen, J. D., Tucker, J. W., Konieczynska, M. D. & Stephenson, C. R. J. Intermolecular atom transfer radical addition to olefins mediated by oxidative quenching of photoredox catalysts. *J. Am. Chem. Soc.* **133**, 4160–4163 (2011).
34. Cole, J. P. et al. Organocatalyzed birch reduction driven by visible light. *J. Am. Chem. Soc.* **142**, 13573–13581 (2020).
35. Ghosh, I., Shaikh, R. S. & König, B. Sensitization-initiated electron transfer for photoredox catalysis. *Angew. Chem. Int. Ed.* **56**, 8544–8549 (2017).
36. Luo, J. & Zhang, J. Donor-acceptor fluorophores for visible-light-promoted organic synthesis: photoredox/Ni dual catalytic C(sp3)-C(sp2) cross-coupling. *ACS Catal.* **6**, 873–877 (2016).
37. Speckmeier, E., Fischer, T. G. & Zeitler, K. A toolbox approach to construct broadly applicable metal-free catalysts for photoredox chemistry: deliberate tuning of redox potentials and importance of halogens in donor-acceptor cyanoarenes. *J. Am. Chem. Soc.* **140**, 15353–15365 (2018).
38. Shang, T. Y. et al. Recent advances of 1,2,3,5-tetrakis(carbazol-9-yl) –4,6-dicyanobenzene (4CzIPN) in photocatalytic transformations. *Chem. Commun.* **55**, 5408–5419 (2019).
39. Liu, Y. et al. 4CzIPN-tBu-catalyzed proton-coupled electron transfer for photosynthesis of phosphorylated N-heteroaromatics. *J. Am. Chem. Soc.* **143**, 964–972 (2021).
40. Singh, P. P. & Srivastava, V. Recent advances in using 4DPAIPN in photocatalytic transformations. *Org. Biomol. Chem.* **19**, 313–321 (2021).
41. Chernowsky, C. P., Chmiel, A. F. & Wickens, Z. K. Electrochemical activation of diverse conventional photoredox catalysts induces potent photoreductant activity. *Angew. Chem. Int. Ed.* **60**, 21418–21425 (2021).
42. Chmiel, A. F., Williams, O. P., Chernowsky, C. P., Yeung, C. S. & Wickens, Z. K. Non-innocent radical ion intermediates in photoredox catalysis: parallel reduction modes enable coupling of diverse aryl chlorides. *J. Am. Chem. Soc.* **143**, 10882–10889 (2021).
43. Xu, J. et al. Unveiling extreme photoreduction potentials of donor-acceptor cyanoarenes to access aryl radicals from aryl chlorides. *J. Am. Chem. Soc.* **143**, 13266–13273 (2021).
44. Shi, Q. et al. Visible-light mediated catalytic asymmetric radical deuteration at non-benzylic positions. *Nat. Commun.* **13**, 1–9 (2022).
45. Al Mousawi, A. et al. Carbazole derivatives with thermally activated delayed fluorescence property as photoinitiators/photoredox catalysts for LED 3D printing technology. *Macromolecules* **50**, 4913–4926 (2017).
46. Song, Y. et al. Organic photocatalyst for ppm-level visible-light-driven reversible addition-fragmentation chain-transfer (raft) polymerization with excellent oxygen tolerance. *Macromolecules* **52**, 5538–5545 (2019).

47. Back, J. H. et al. Visible light curable acrylic resins toward UV-light blocking adhesives for foldable displays. *Adv. Mater.* 2204776 (2022).
48. Back, J. H. et al. Synthesis of solvent-free acrylic pressure-sensitive adhesives: via visible-light-driven photocatalytic radical polymerization without additives. *Green. Chem.* **22**, 8289–8297 (2020).
49. Back, J. et al. Adhesives via photoredox-mediated radical polymerization. *Molecules* **26**, 385–396 (2021).
50. Meng, Q. Y., Schirmer, T. E., Berger, A. L., Donabauer, K. & König, B. Photocarboxylation of benzylic C-H bonds. *J. Am. Chem. Soc.* **141**, 11393–11397 (2019).
51. Donabauer, K. et al. Photocatalytic carbanion generation-benzylation of aliphatic aldehydes to secondary alcohols. *Chem. Sci.* **10**, 5162–5166 (2019).
52. Kong, D. et al. Fast carbon isotope exchange of carboxylic acids enabled by organic photoredox catalysis. *J. Am. Chem. Soc.* **143**, 2200–2206 (2021).
53. Grotjahn, S. & König, B. Photosubstitution in dicyanobenzene-based photocatalysts. *Org. Lett.* **23**, 3146–3150 (2021).
54. Kohtani, S., Mori, M., Yoshioka, E. & Miyabe, H. Photohydrogenation of acetophenone using coumarin dye-sensitized titanium dioxide under visible light irradiation. *Catalysts* **5**, 1417–1424 (2015).
55. Adenier, A., Chehimi, M. M., Gallardo, I., Pinson, J. & Vilà, N. Electrochemical oxidation of aliphatic amines and their attachment to carbon and metal surfaces. *Langmuir* **20**, 8243–8253 (2004).
56. Silverstein, T. P. Marcus theory: thermodynamics CAN control the kinetics of electron transfer reactions. *J. Chem. Educ.* **89**, 1159–1167 (2012).
57. Koike, T. & Akita, M. Visible-light radical reaction designed by Ru- and Ir-based photoredox catalysis. *Inorg. Chem. Front.* **1**, 562–576 (2014).
58. Discekici, E. H. et al. A highly reducing metal-free photoredox catalyst: design and application in radical dehalogenations. *Chem. Commun.* **51**, 11705–11708 (2015).
59. Lewis, F. D. Proton-transfer reactions of photogenerated radical ion pairs. *Acc. Chem. Res.* **19**, 401–405 (1986).
60. Zhao, H. & Leonori, D. Minimization of back-electron transfer enables the elusive Sp3 C–H functionalization of secondary anilines. *Angew. Chem. Int. Ed.* **60**, 7669–7674 (2021).
61. Etherington, M. K. et al. Revealing the spin–vibronic coupling mechanism of thermally activated delayed fluorescence. *Nat. Commun.* **7**, 1–7 (2016).
62. Wayner, D. D. M., Dannenberg, J. J. & Griller, D. Oxidation potentials of α-aminoalkyl radicals: bond dissociation energies for related radical cations. *Chem. Phys. Lett.* **131**, 189–191 (1986).
63. Beatty, J. W. & Stephenson, C. R. J. Amine functionalization via oxidative photoredox catalysis: Methodology development and complex molecule synthesis. *Acc. Chem. Res.* **48**, 1474–1484 (2015).
64. Wang, J. & Zheng, N. The cleavage of a C-C bond in cyclobutylanilines by visible-light photoredox catalysis: development of a [4+2] annulation method. *Angew. Chem. Int. Ed.* **54**, 11424–11427 (2015).
65. Wang, Q. & Zheng, N. A photocatalyzed synthesis of naphthalenes by using aniline as a traceless directing group in [4 + 2] annulation of amino-benzocyclobutenes with alkynes. *ACS Catal.* **7**, 4197–4201 (2017).
66. Staveness, D. et al. Providing a new aniline bioisostere through the photochemical production of 1-aminonorbornanes. *Chem* **5**, 215–226 (2019).
67. Roth, H. G., Romero, N. A. & Nicewicz, D. A. Experimental and calculated electrochemical potentials of common organic molecules for applications to single-electron redox chemistry. *Synlett* **27**, 714–723 (2016).
68. Hayyan, M., Hashim, M. A. & Alnashef, I. M. superoxide ion: generation and chemical implications. *Chem. Rev.* **116**, 3029–3085 (2016).
69. Pan, Y. et al. Graphene oxide and rose bengal: oxidative C–H functionalisation of tertiary amines using visible light. *Green. Chem.* **13**, 3341–3344 (2011).
70. Baciocchi, E., Del Giacco, T. & Lapi, A. Quenching of singlet oxygen by tertiary aliphatic amines. Structural effects on rates and products. *Helv. Chim. Acta* **89**, 2273–2280 (2006).
71. Constantin, T. et al. Aminoalkyl radicals as halogen-atom transfer agents for activation of alkyl and aryl halides. *Science* **367**, 1021–1026 (2020).
72. Houser, K. J., Bartak, D. E. & Hawley, M. D. Electrochemical studies of the formation and decomposition of the fluorobenzonitrile radical anions. *J. Am. Chem. Soc.* **95**, 6033–6040 (1973).
73. Rondinini, S., Mussini, P. R., Muttini, P. & Sello, G. Silver as a powerful electrocatalyst for organic halide reduction: the critical role of molecular structure. *Electrochim. Acta* **46**, 3245–3258 (2001).
74. Enemærke, R. J., Christensen, T. B., Jensen, H. & Daasbjerg, K. Application of a new kinetic method in the investigation of cleavage reactions of haloaromatic radical anions. *J. Chem. Soc. Perkin Trans. 2* **1**, 1620–1630 (2001).
75. Isse, A. A., Durante, C. & Gennaro, A. One-pot synthesis of benzoic acid by electrocatalytic reduction of bromobenzene in the presence of CO_2. *Electrochem. Commun.* **13**, 810–813 (2011).
76. Gavioli, G. B., Borsari, M. & Fontanesi, C. Theoretical study of the electroreduction of halogenated aromatic compounds. Part 2. - Bromine and chlorine derivatives in different organic solvents. *J. Chem. Soc. Faraday Trans.* **89**, 3931–3939 (1993).
77. Poizot, P., Laffont-Dantras, L. & Simonet, J. The one-electron cleavage and reductive homo-coupling of alkyl bromides at silver-palladium cathodes. *J. Electroanal. Chem.* **624**, 52–58 (2008).

Acknowledgements

We thank Prof. Soo Young Park, Prof. Ki Tae Nam, and Prof. Chulbom Lee for sharing instruments. This work was supported by the TJ Park Science Fellowship of POSCO TJ Park Foundation and by the Basic Science Research Program through the National Research Foundation of Korea (NRF), which was funded by the Ministry of Science and ICT (MSIT) (2021R1A5A1030054 and 2022R1A2C2011627). The work at IMDEA was supported by the Spanish Ministry for Science (MINECO/MICINN–FEDER projects CTQ2017–87054 and RTI2018-097508-B-I00) by the "Severo Ochoa" program for Centers of Excellence in Research and Development (MINECO grant SEV–2016–0686 and MICINN grant CEX2020-001039-S), European Union structural funds and Comunidad de Madrid NMAT2D-CM Program (P2018/NMT-4511), and Campus of International Excellence UAM + CSIC.

Author contributions

Y.K. and M.S.K. were responsible for the initial conception of the project. Y.K., J.G., R.W., and M.S.K were involved in the discussion of the photophysics and photochemical reactions and were responsible for writing and editing the final manuscript. Y.K. performed most of the experiments and wrote the initial draft of the manuscript. J. L., Y.L., and C.Y. assisted in the synthesis of cyanoarene compounds. Y.N. and D.K. assisted in the dehalogenation reaction. S.F. and R.W. performed CW and gated photoluminescence measurements at variable temperatures and analyzed the data. Y.K. performed DFT calculations supported by J.C.R. Y.K. performed the kinetic simulation under supervision from R.W. and M.S.K. All the authors discussed the results and commented on the manuscript. J.G., R.W., and M.S.K. supervised the project.

Competing interests

The authors declare no competing interests.

Additional information

Supplementary information The online version contains supplementary material available at https://doi.org/10.1038/s41467-022-35774-5.

Correspondence and requests for materials should be addressed to Johannes Gierschner, Reinhold Wannemacher or Min Sang Kwon.

Peer review information *Nature Communications* thanks Max Kudisch, and the other, anonymous, reviewers for their contribution to the peer review of this work. Peer reviewer reports are available.

[1]Department of Materials Science and Engineering, Seoul National University, Seoul 08826, Republic of Korea. [2]Department of Materials Science and Engineering, Ulsan National Institute of Science and Technology (UNIST), Ulsan 44919, Republic of Korea. [3]Madrid Institute for Advanced Studies, IMDEA Nanoscience, Calle Faraday 9, Campus Cantoblanco, Madrid 28049, Spain. [4]Donostia International Physics Center (DIPC), Manuel Lardizabal Ibilbidea 4, San Sebastián 20018, Spain. ✉e-mail: johannes.gierschner@imdea.org; reinhold.wannemacher@imdea.org; minsang@snu.ac.kr